Superconducting quadrupoles magnets for the large hadron collider luminosity upgrade

Franck Borgnolutti

Franck Borgnolutti. Superconducting quadrupoles magnets for the large hadron collider luminosity upgrade. Other. Institut National Polytechnique de Lorraine, 2009. English. NNT : 2009INPL070N . tel-01748771

Institut National Polytechnique de Lorraine
Ecole Doctorale Informatique – Automatique – Electronique - Mathématiques
Département de formation doctorale Electrotechnique – Electronique
Laboratoire Environnement et Minéralurgie

et

Università degli Studi di Milano
Fisica Applicata
Fisica, Astrofisica e Fisica Applicata

THÈSE

Présentée en vue de l'obtention du grade de

Docteur de l'Institut National Polytechnique de Lorraine
et de
Dottore di Ricerca dell'Università degli Studi di Milano

Préparée au CERN/TE/MSC

Par

Franck BORGNOLUTTI
Ingénieur ENSEM

Aimants Quadripolaires Supraconducteurs pour l'Augmentation de la Luminosité du Grand Collisionneur de Hadrons

Thèse soutenue publiquement le 5 novembre 2009

Directeurs de Thèse :
Professeur Alain MAILFERT, INPL (Nancy)
Professeur Lucio ROSSI, CERN (Genève)

Encadrement :
Docteur Ezio Todesco, CERN (Genève)

Jury :
Professeur Alain MAILFERT, INPL (Nancy)
Professeur Lucio ROSSI, CERN (Genève)
Professeur Giovanni BELLOMO, Laboratoire LASA (Segrate)
Docteur Arnaud DEVRED, ITER Organisation (Cadarache)
Docteur Jean-Luc DUCHATEAU, CEA (Cadarache)
Professeur Denis NETTER, INPL (Nancy)

Acknowledgments

I first want to warmly acknowledge Dr. Ezio Todesco. He has been my supervisor during these three years. I thank him for encouraging me to be thorough while allowing me an independent style of working. His availability to answer my questions and his deep knowledge of magnet technology and accelerator physics made my efforts much easier. I really appreciated his friendship and I hope I will have the opportunity to work with him again.

I would like to thank Prof. Alain Mailfert for inspiring me to become a physicist. His courses in electromagnetism and superconductivity given at ENSEM raised my enthusiasm for superconducting magnets. Despite the distance and his very time-demanding occupations he manifested a lot of interest in my work and never stopped proposing innovative ideas.

I would also like to express my gratitude to Prof. Lucio Rossi who offered me the opportunity to do my Ph. D. thesis at CERN and who accepted to be my thesis co-director. He and Prof. Alain Mailfert made it possible for me to graduate from the "Università degli study di Milano" and the "Institut National Polytechnique de Lorraine".

Thank to Paolo Fessia for his valuable help on the design of the new inner triplet quadrupole. It has been a pleasure and a rewarding experience to work with him.

Thanks also to all my colleagues from the TE-MSC group, particularly to those of the MDA section. The good atmosphere and the enthusiasm of all these persons made my stay at CERN an enjoyable moment.

I would also like to thank Glyn Kirby for his precious help on technical issues, Bernhard Auchmann for the Roxie Support, and Stephan Russenschuck for his help on magnet design.

I have to thank Giovanni Bellomo, Jean-Luc Duchateau and Denis Netter for accepting to be members of the jury. A special thank to Arnaud Devred for his presence in the jury and for his relevant and very helpful advises on my thesis report.

I also want to thank Jens, who helps me improving my spoken English, and Tiina for her good mood. Thank also to Sebastien and all other persons I forgot mentioning.

Je voudrais également remercier Thierry, pour être la quand il le faut.

Je remercie profondément mes parents, ainsi que tous mes frères et sœur. Je leur dédie cette thèse.

Enfin, je remercie Nicole pour sa présence de chaque instant.

Contents

RESUME EN FRANÇAIS 8

I. INTRODUCTION 17

II. SUPERCONDUCTING MAGNETS FOR PARTICLES ACCELERATOR.. 20

- **II.1 Particle accelerator 20**
  - II.1.1 Particle accelerator for high energy physics 20
  - II.1.2 Layout of the Large Hadron Colider (LHC) 21
  - II.1.3 Relevant quantity for accelerator magnets.. 23
- **II.2 Field computation in particles accelerators magnets 24**
  - II.2.1 Basic equations 24
  - II.2.2 Solution of the Laplace's equation 26
  - II.2.3 High energy accelerator magnets.. 28
  - II.2.4 Magnetic field in an infinitely long accelerator magnet.. 29
  - II.2.5 Field harmonics definition 31
  - II.2.6 Impact of field errors on accelerator performance.. 33
- **II.3 Electromagnetic design of quadrupole magnets in 2D 34**
  - II.3.1 Winding configuration.. 34
  - II.3.2 Field calculation of quadrupole based on cos2θ design by means of Fourier series 36
  - II.3.3 Iron yoke 40
- **II.4 Superconducting materials 42**
  - II.4.1 Superconductivity 42
  - II.4.2 Nb-Ti and Nb_3Sn.. 43
  - II.4.3 Superconducting cables 45
- **II.5 Current and temperature margin 46**
- **II.6 Mechanical structure of Nb-Ti quadrupole magnets 49**
- **II.7 Upgrade of the LHC Interaction regions.. 50**
- **II.8 Issues of the thesis 52**

III. ANALYTIC ESTIMATES OF THE MAGNETIC ENERGY IN SUPERCONDUCTING QUADRUPOLES.. 54

- **III.1 Magnetic energy definition.. 54**
- **III.2 Ironless and non graded quadrupole 55**
- **III.3 Comparison of analytical versus numerical estimate for realistic lay-outs. 58**
- **III.4 Magnetic energy at critical current density.. 60**
- **III.5 Graded coils.. 61**
- **III.6 Iron yoke contribution.. 63**
- **III.7 Longitudinal magnetic force 66**
- **III.8 Summary.. 70**

IV. COIL MISS-POSITIONING AND FIELD HARMONICS ERRORS 72

IV.1 Field quality measurements 72
IV.2 Source of field harmonic errors 74
IV.3 Uncertainty in the field harmonic errors 76
IV.4 A Review of the method used to estimate the reproducibility of coil positioning through magnetic measurements 78
IV.5 Estimate of the amplitude of the blocks displacement in Nb3Sn magnets 86
  IV.5.1 Analysis of the HFDA dipole 86
  IV.5.2 Analysis of the TQ quadrupole 88
IV.6 Uncertainty of the field errors in superconducting quadrupoles 91
IV.7 Summary 95
V. ELECTROMAGNETIC DESIGN OF THE QUADRUPOLE FOR THE UPGRADE OF THE LHC INTERACTION REGION 98
V.1 A novel method for coil optimization 98
  V.1.1 Outline 98
  V.1.2 Analytical model 99
  V.1.3 Multipoles optimization 104
  V.1.4 Estimate of the short sample gradient 116
  V.1.5 Estimate of the forces 118
  V.1.6 Coil cross-section with Rutherford cables 120
V.2 Application to the MQXC design 120
  V.2.1 Specification of the MQXC cables 120
  V.2.2 Sector coil case 121
  V.2.3 Layout with Rutherford cables and iron yoke 126
  V.2.4 The iron yoke 128
  V.2.5 Summary of the magnetic performance 131
  V.2.6 Layer jump and splice 133
  V.2.7 Design of the coil head 134
V.3 Field quality study 137
V.4 Summary 138
CONCLUSION 140
REFERENCES 143
APPENDIX A 149
APPENDIX B 151
APPENDIX C 152
APPENDIX E 154
APPENDIX F 156
NOMENCLATURE 169

Résumé en Français

Les accélérateurs de particules sont des outils essentiels pour l'étude et la compréhension de la matière à l'échelle subatomique. Les résultats expérimentaux obtenus par ces machines couplées aux théories développées au fils des décennies ont conduit à l'élaboration d'une théorie connue sous le nom de modèle standard. Développé dans les années soixante-dix, le modèle standard est une théorie qui décrit les forces faibles, fortes et électromagnétiques, ainsi que l'ensemble des particules supposées élémentaires qui constituent la matière. Il a été jusqu'à ce jour été utilisé par les physiciens comme un moyen de comprendre les lois qui régissent le monde subatomique et a permit de prédire un certain nombres de phénomènes physiques avant que ceux-ci ne soient observés dans des accélérateurs de particules. Le modèle va une nouvelle fois être mis à l'épreuve dans ce qui sera le plus puissant accélérateur de particules jamais construit et dans lequel une énergie de collision record de 14 TeV entre deux faisceaux de particules devrait être atteinte en 2010: le grand collisionneur de hadron, ou LHC (Large Hadron Collider).

Le LHC est un accélérateur circulaire de type synchrotron de 27 km de circonférence enfoui a 100 m sous la frontière Franco-suisse située prés de Genève. Actuellement en fin de construction, le LHC sera utilisé pour accélérer et guider deux faisceaux de particules de la famille des hadrons. Les faisceaux vont circuler en sens opposé dans deux tubes concentriques de 56 mm de diamètre et a une vitesse très proche de la vitesse de la lumière, et vont se rencontrer en quatre points appelés points de collisions. En ces points, le produit issu des collisions sera analysé par des détecteurs. Pour guider les particules, le LHC utilise des aimants dipolaires basés sur la technologie supraconductrice niobium-titane (Nb-Ti) refroidi à 1.9 K. Le champ magnétique intense (8.3 T) généré dans l'ouverture de ces aimants et le grand rayon de courbure de l'anneau du LHC (4.3 km) permettent de maintenir radialement chaque faisceau sur son orbite jusqu'à une énergie maximale de 7 TeV par faisceau. Outre l'énergie, le second paramètre d'importance dans un collisionneur est la luminosité définie en chaque point de collision par le nombre de collisions par seconde. Pour accroitre la probabilité d'observer des événements rares comme l'hypothétique boson de Higgs, particule essentielle dans la théorie du modèle standard mais qui n'a jamais été observée, probabilité qui d'après les physiciens devrait être d'environ un pour deux milliard de collisions il est nécessaire d'avoir le plus grand nombre possible de collisions, et donc la plus grande luminosité possible. Un des paramètres clés permettant d'agir sur la luminosité est la qualité des aimants quadripolaires d'insertion placés de part et d'autre de chaque point de collision et assemblés en cellule de quatre aimants. Leur rôle est de focaliser les faisceaux de particules de façon à obtenir des dimensions transverses de faisceaux au point de collision les plus petites possibles, et donc d'avoir une grande luminosité. Les aimants quadripolaires utilisés dans le LHC sont, comme les dipôles d'arc du LHC, basés sur la technologie supraconductrice Nb-Ti refroidis à 1.9 K. Le gradient de l'induction magnétique intégré sur la longueur magnétique de l'aimant (ou gradient intégré), qui est la grandeur de référence pour un quadripôle, généré à courant nominal dans l'ouverture de 70 mm des aimants quadripolaires d'insertion du LHC est de 1370 T pour deux des quatre aimants (MQXA) et de 1182 T pour les deux autres (MQXB). Les deux types d'aimants MQXA et MQXB fournissent le même gradient de 215 T/m dans la section transverse mais diffère en longueur magnétique (6.37 m contre 5.50 m respectivement). Cela permet d'obtenir une dimension transverse moyenne du faisceau aux points de collision de l'ordre de 17 µm. La proximité des aimants quadripolaires d'insertion avec les points de collisions soumet ceux-ci à de fortes doses de radiations qui endommagent les câbles supraconducteurs constituant les bobines, réduisant leur performance et leur durée de vie. Cette dernière est estimée à environ sept années. Le remplacement de ces aimants se fera dans le cadre du projet appelé « phase 1 de l'augmentation de la luminosité du LHC ». Ce projet à pour but d'obtenir une luminosité 2 à 3 fois supérieure à la valeur actuelle. Pour atteindre la nouvelle valeur de la luminosité, une partie du facteur d'accroissement devra être obtenue par les nouveaux quadripôles d'insertion. Les bobines de ces derniers, principalement pour des raisons de coûts et de temps que nécessiterait le développement d'un nouveau câble supraconducteur, seront basées sur les câbles de réserves des dipôles d'arc du LHC et devront fournir un gradient nominal de 120 T/m dans une ouverture de 120 mm. Les quatre aimants d'insertion qui forment une cellule focalisante seront identiques en section transverse et en longueur magnétique (entre 7 et 10 m). Avec ces nouveaux quadripôles, le diamètre moyen du faisceau au point de collision sera d'environ 12 µm. La nécessité d'avoir des aimants à grandes ouvertures réside dans le fait que la dimension moyenne du faisceau au point de collision est en première approximation inversement proportionnelle à la dimension moyenne du faisceau dans les aimants d'insertion. Cependant, la limitation en courant due à la propriété des matériaux supraconducteurs utilisés dans les bobines des aimants ne permet pas d'avoir des ouvertures supérieures à 120 mm avec la technologie Nb-Ti. En effet, le gradient maximum que l'on peut espérer obtenir dans l'ouverture d'un quadripôle décroit en première approximation avec l'inverse de l'ouverture. Par conséquent, pour obtenir les valeurs requises de gradient intégré on doit augmenter la longueur des quadripôles. Pour des raisons d'encombrement, la taille de ces derniers est limitée a l'espace disponible de part et d'autre des détecteurs. Pour la phase 1 de l'augmentation de la luminosité, une optimisation poussée de la zone d'interaction a permis d'augmenter l'espace dédié aux quadripôles d'insertion de 32.7 m à 42.5 m. Après la phase 1 viendra la phase 2 de l'augmentation de la luminosité du LHC. Celle-ci, à l'étude depuis 2004, consistera à remplacer les aimants d'insertion de la phase 1 (qui auront été dimensionnés de façon à utiliser au mieux la technologie Nb-Ti) par des aimants quadripolaires plus performants basés sur la technologie niobium-étain (Nb_3Sn). Le changement de matériau supraconducteur devrait permettre, selon les premières estimations, d'augmenter la luminosité nominale actuelle par un facteur 10 (un facteur 3-5 par rapport à la phase 1). Des efforts importants pour le développement de câbles en Nb_3Sn, notamment sur le problème lié a la dégradation des performances critiques provoquée par la friabilité du niobium-étain, ont été réalisés dans le cadre du projet des États-Unis LARP (Large Accelerator Research Program). Dans ce contexte et pour la première fois dans l'histoire du Nb_3Sn, une série de 10 aimants quadripolaires avec des bobines en niobium-étain a été construite et testée.

Cette thèse a comme objectif principal le dimensionnement de la section transverse des bobines supraconductrices des aimants quadripolaires d'insertion pour la phase 1 de l'augmentation de la luminosité du LHC. La grande dimension requise pour l'ouverture des quadripôles, sans égale au vu de l'état de l'art, soulève les questions suivantes: est-il techniquement possible de réaliser un tel aimant? Si oui, comment trouver celui qui optimise au mieux les différentes contraintes posées par le cahier des charges ? Il est d'autant plus difficile de répondre à ces questions que les matériaux utilisés sont supraconducteurs. Ils sont caractérisés par une surface critique en dessous de laquelle doit se trouver le point nominal de fonctionnement de l'aimant. Ainsi, une hypothétique loi d'échelle des grandeurs électriques ou mécaniques permettant de statuer sur la faisabilité d'un aimant doit prendre en compte, pour une température donnée, la loi (j_c,B) du matériau supraconducteur considéré. Un autre point d'importance pour les aimants d'accélérateurs est la qualité du champ magnétique. Une bonne qualité de champ est vitale pour la stabilité du faisceau de particules, et donc pour le fonctionnement d'un accélérateur. Cependant, le changement de technologie supraconductrice prévu pour la phase 2 de l'augmentation de la luminosité, nécessaire au vu des limites atteintes pour cette application par le Nb-Ti, soulève un nouveau problème lié au processus de fabrication et d'assemblage d'une bobine Nb_3Sn qui diffère de celui utilisé pour une bobine Nb-Ti: est-il possible d'atteindre dans des aimants Nb_3Sn une qualité de champ au moins aussi bonne que pour du Nb-Ti? Cette question concerne aussi bien les aimants quadripolaires que dipolaires. En effet, le VLHC (le très grand collisionneur de hadrons), hypothétique successeur du LHC, devrait utiliser des aimants dipolaires en Nb_3Sn pour courber le faisceau. Dans cette thèse nous tenterons d'apporter, et ce en utilisant le plus possible des calculs analytiques, une réponse à ces questions. La réflexion sur les aimants d'accélérateur et plus particulièrement sur certains phénomènes observés sur les mesures magnétiques réalisées dans des séries de quadripôles nous à aussi amené à des résultats analytiques basés sur les statistiques et permettant d'expliquer l'origine de ces phénomènes. L'obtention de ces résultats a été permise par l'existence et la disponibilité de mesures magnétiques réalisées dans des séries de quadripôles utilisées dans plusieurs accélérateurs de particules. Cette approche statistique du traitement des données magnétiques a aussi permis de remettre en cause certains concepts utilisés jusqu'à maintenant, et ce sans justification, comme par exemple le concept d'incertitude de la moyenne des harmoniques de champs dans une série d'aimants.

A l'étape préliminaire du dimensionnement d'un aimant d'accélérateur il est d'une grande importance de disposer de lois simples permettant de rapidement estimer et avec une bonne précision les principales grandeurs électriques et mécaniques d'un aimant dont on connaîtrait seulement les principaux paramètres. Ces lois permettent de rapidement statuer sur la faisabilité de l'aimant sans avoir à recourir à des techniques de modélisation numériques qui sont longues et fastidieuses à mettre en œuvre et n'apportent en général qu'une précision de deuxième ordre. De telle lois pour le gradient magnétique ainsi que pour les forces de Laplace exercées dans le plan transverse d'un bobinage quadripolaire de type cosinus 2 thêta (approximation d'une répartition en courant dont la densité varie en cosinus 2 thêta autour de l'ouverture de l'aimant, thêta étant la position angulaire) on déjà été établies dans le passé. Cependant, une loi similaire permettant d'estimer l'énergie magnétique et qui est un élément essentiel dans le calcul et le dimensionnement des protections d'un aimant en cas de quench n'a encore jamais établie. Nous proposons ici une formule simple permettant de calculer l'énergie magnétique stockée dans un quadripôle d'accélérateur dont les bobines seraient de type cosinus 2 thêta. La formule est composée de trois termes : un terme principal obtenu de façon entièrement analytique et donnant l'énergie magnétique dans un aimant quadripolaire composé de bobines faites de secteurs concentriques dans lesquelles la densité de courant est uniforme, un coefficient correcteur lui aussi obtenu de façon analytique et permettant de tenir compte de la présence d'une culasse ferromagnétique infiniment perméable, et un deuxième coefficient correcteur permettant de tenir compte d'une non-uniformité de la densité de courant dans les bobines et cette fois-ci obtenu à partir d'une analyse numérique réalisée sur plusieurs aimants existant. Pour rendre possible une approche analytique du problème on ne considère ici que le cas où le quadripôle est infiniment long. Cette dernière approximation est justifiée par le fait que les dimensions transverses des aimants d'accélérateur sont habituellement petites devant leur longueur. Par exemple, pour les aimants actuels d'insertion du LHC le diamètre intérieur et extérieur des bobines est de 35 et 82 mm respectivement, alors que la longueur magnétique est de plusieurs mètres. Dans ce cas l'énergie magnétique est donnée en joule par unité de longueur. Le premier terme de la formule l'énergie est obtenu en intégrant sur la surface transverse des bobines le produit scalaire du potentiel vecteur et de la densité de courant circulant dans les bobines. L'intégration est grandement simplifiée du fait que les bobines sont composées de secteurs concentriques. En effet, ceci permet de ré-exprimer la densité de courant et le potentiel vecteur à partir de leur développement en séries de Fourier. La formule de l'énergie magnétique obtenue consiste en une somme infinie de termes : à chaque harmonique de courant correspond une partie de l'énergie magnétique totale. A partir de cette expression on montre que le fondamental de courant est responsable pour environ 98-99 % de l'énergie magnétique totale. Une comparaison entre modèle analytique et quadripôles réels utilisés dans des accélérateurs de particules montre que le modèle analytique le plus représentatif du modèle réel est le cas ou le quadripôle est fait de bobines composées d'un seul secteur de dimension angulaire 30°. La comparaison analytique/numérique est rendue possible grâce au concept d'épaisseur de bobine équivalente: elle est définie comme l'épaisseur que devrait avoir la bobine d'un aimant qui serait fait d'un secteur de dimension angulaire de 30º et qui aurai la même surface de conducteur dans le plan transverse que la bobine réelle. L'erreur associée dans la détermination de l'énergie est de l'ordre de 10 % pour la trentaine d'aimants considérés. L'énergie magnétique est trouvée proportionnelle au rayon d'ouverture de la bobine à la puissance quatre. Un couplage de la formule analytique avec la loi (jc,B) du supraconducteur utilisé (Nb-Ti ou Nb_3Sn) et à température donnée a permis de mettre en évidence pour un domaine d'épaisseur de bobine compris entre 0.2 et 1.2 fois le rayon d'ouverture une augmentation quasi exponentielle de l'énergie avec le gradient (à rayon d'ouverture fixe). Le coefficient correcteur permettant de prendre en compte la présence d'une culasse ferromagnétique a été obtenu analytiquement à l'aide de la méthode des courants images dans le cas ou la perméabilité magnétique de la culasse est infinie. Une comparaison entre modèle numérique et modèle analytique montre que l'accord analytique/numérique est aussi de l'ordre de 10 %. Enfin, dans le cas ou la bobine est traversée par deux différentes densités de courant nous proposons un coefficient correcteur obtenu semi-semi-analytiquement en analysant une dizaine de quadripôles utilisant cette méthode. La encore, l'estimation l'énergie est réalisée avec une précision de 10 %.

La connaissance de l'énergie magnétique d'un aimant permet non-seulement de dimensionner le système d'alimentation électrique mais offre aussi la possibilité d'avoir accès aux forces magnétiques qui contraignent le bobinage dans les trois directions de l'espace. Les forces magnétiques radiales et azimutales dans la section transverse de l'aimant sont bien connues, mais ce n'est pas le cas des forces magnétiques longitudinales qui tendent à allonger les enroulements. Ces forces augmentent avec l'énergie et peuvent être un facteur limitant dans la course aux grandes ouvertures. C'est notamment le cas pour le Nb_3Sn du fait de sa sensibilité à la déformation. Dans ce cas particulier la connaissance de la force magnétique appliquée dans les têtes est très importante. Il a déjà été établi à l'aide du théorème des travaux virtuels et en l'absence de culasse ferromagnétique que l'énergie magnétique par unité de mètre est aussi la force magnétique appliquée sur chacune des extrémités d'un aimant. Dans cette thèse nous montrons, à l'aide du tenseur des contraintes de Maxwell que c'est aussi vrai pour le cas particulier ou le fer est infiniment perméable et est beaucoup plus long que la bobine. Nous montrons également que la force magnétique du cas précédent est aussi la force maximale que l'on peut espérer avoir pour un aimant. En effet, en utilisant le tenseur des contraintes de maxwell nous montrons que la force est nécessairement plus faible lorsque le fer à une dimension longitudinale du même ordre de grandeur ou est plus petit que les bobines.

La seconde étape dans la conception d'un aimant supraconducteur consiste à élaborer un design détaillé de la bobine a partir des paramètres principaux obtenu à l'aide des lois d'échelles. Pour la phase 1 de l'augmentation de la luminosité, les lois d'échelles on permis de déterminer que pour générer un gradient de 120 T/m dans une ouverture de 120 mm et en utilisant les câbles supraconducteurs du LHC il suffisait d'une bobine faite de deux couches de conducteurs. La loi pour l'énergie magnétique décrite précédemment prévoit pour cet aimant une énergie stockée à courant nominal d'environ 0.4 MJ/m, et une force longitudinale maximale appliquée sur une moitié de la bobine de 0.4 MN (0.1 MN pour chacune des quatre bobines constituant le quadripole). Pour le design détaillé, une nouvelle contrainte forte est à prendre en compte: la qualité du champ magnétique. Pour un quadripôle celle-ci est habituellement considérée comme acceptable lorsque les harmoniques de champs permis par la symétrie quadrupolaire sont plus petits que 1 unité, c'est-à-dire plus petit que 10^{-4} fois le champ principal. Pour arriver à ce résultat on construit des bobines composées de plusieurs blocs de conducteurs (habituellement des câbles de type Rutherford) espacé par des espaceurs en cuivre. Il n'y a pas de règles générales pour définir le nombre de blocs constituant une bobine. Pour un quadripôle, on cherche habituellement à annuler les trois premiers harmoniques de champ autorisé par la symétrie quadripolaire : b_6, b_{10} et b_{14}. Pour les nouveaux quadripôles d'insertion du LHC il a été décidé que chaque couche de conducteur devait être composée de deux blocs (quatre blocs au total). Cette configuration à l'avantage de fournir suffisamment de degrés de libertés (qui sont les angles des secteurs de bobines et, dans une moindre mesure, la rotation des blocs) pour optimiser la qualité du champ magnétique, mais pas trop non plus pour ne pas compliquer la bobine, et par conséquent en augmenter le coût de réalisation. La difficulté du design réside dans l'identification des dimensions et positions des blocs de conducteurs. Ceux-ci doivent non seulement permettent de générer une bonne qualité de champ magnétique, mais aussi maximiser le gradient magnétique. Ceci est solution d'un problème inverse en magnétostatique et ne peut par conséquent pas être résolu directement. La complexité de la bobine (bobines faites de blocs, blocs fait de câbles et câbles fait de brins) nécessite l'utilisation de logiciel d'aide à la conception d'aimants et conduit à des calculs numériques longs qui ne permettent pas de couvrir l'ensemble du domaine des solutions possibles. Pour un temps de calcul raisonnable on ne peut analyser qu'une infime partie des solutions possibles. Les méthodes couramment utilisées pour l'optimisation des bobines d'aimants d'accélérateurs reposent sur des algorithmes stochastiques, comme par exemple les algorithmes génétiques, et ne permettent pas d'affirmer que l'optimum trouvé est un optimum global. Nous proposons ici, pour augmenter la probabilité de trouver un design optimum, une nouvelle approche : dans un premier temps on considère que les blocs de conducteurs constituant la bobine sont des secteurs concentriques placés autour de l'ouverture et parcouru par une densité de courant uniforme. Cette approximation présente l'avantage de pouvoir décomposer la densité de courant circulant dans les secteurs en séries de Fourier. Les harmoniques de champ peuvent être très rapidement calculés à l'aide d'un ordinateur. Pour un ordinateur standard (processeur pentium 4) et en utilisant le logiciel de calcul numérique « matlab », les temps de calculs n'excèdent pas quelques dizaines de microsecondes (a comparer au quelques dizaines de millisecondes requises par les logiciels d'aide a la conception d'aimants qui prennent en compte tous les détails de la bobine). La rapidité dans le calcul des harmoniques rend possible un scan des positions et dimensions angulaires des blocs avec un pas très fin sur le domaine de toutes les solutions possibles. Pour un temps de calcul inférieur à 24 heures il est possible d'optimiser une bobine quadripolaire constituée au maximum de 5 blocs. Le nombre de configurations de blocs analysé est alors de quelque milliards. Parmi tout les cas analysés on tire un nombre limité de solutions uniformément réparties sur tout le domaine des solutions possibles et générant des harmoniques de champ en accord avec les spécifications. Ensuite, pour chacune des solutions donnant une bonne qualité de champ, la connaissance analytique de l'induction magnétique généré en tout point de l'espace par la bobine quadripolaire, entouré ou non par une culasse magnétique de perméabilité infinie, permet de calculer le maximum de la valeur absolue de l'induction sur chacun des blocs. A partir de là, il est aisé de déterminer les grandeurs qui permettent de choisir la bobine quadripolaire qui correspondent au mieux aux spécifications. Ces grandeurs sont en général le courant critique, le gradient magnétique à courant critique, et le volume de supraconducteur. Cette méthode d'optimisation a été applique à la conception du design magnétique des nouveaux quadripôles d'insertion du LHC. Le scan angulaire a été réalisé en moins de 5 heures et a conduit à l'évaluation de 450 millions de différentes configurations de blocs parmi lesquelles seules 200 ont montré une qualité de champ acceptable. Les spécifications pour l'optimisation de la bobine sont : maximiser le gradient magnétique, minimiser le courant critique et la quantité de matériau supraconducteur utilisé. Pour chacun des 200 cas, nous avons calculé le courant critique, le gradient à courant critique, et le volume de la bobine. Ceci a permis d'identifier une configuration de bobine qui, en plus de satisfaire aux contraintes posées dans le cahier des charges, est facilement réalisable. Ensuite, pour passer du model analytique qui consiste en un ensemble d'angles au modèle réel ou les blocs de conducteur sont fait d'empilement de câbles il faut calculer le nombre de tours de câbles qui approxime au mieux chacun des blocs. L'inévitable distorsion de champ résultant de la dimension finie de câbles et due au fait que l'empilement de câble n'est pas tout à fait un pur secteur peut être corrigé en ré-optimisant la position des blocs et en autorisant des petites rotations de ceux-ci. Cette seconde étape dans la conception de l'aimant a été réalisée à l'aide du logiciel d'aide à la conception d'aimant pour accélérateur ROXIE. L'optimisation fine de la qualité du champ magnétique dans l'ouverture de l'aimant à été faite à partir d'une matrice de sensibilité construite autour des positions de blocs déterminées analytiquement, et tient compte de la présence d'une culasse ferromagnétique. Le gradient nominal est de 118.7 T/m pour un courant nominal de 12.7 kA. Il est à noter qu'un travail indépendant considérant cette fois ci non pas une bobine constituée de quatre blocs mais de six et reposant entièrement sur une optimisation numérique réalisé avec ROXIE et au moyen d'un algorithme génétique a obtenu comme solution optimale une bobine générant un gradient seulement 1 % plus grand que celui obtenue avec notre solution de quatre blocs. Ceci met bien en évidence que notre méthode permet de trouver une solution optimale. Pour une raison de simplicité de bobine (quatre blocs au lieu de six), notre solution a été retenue pour la réalisation et un modèle court devrait voir le jour courant 2010. Pour ce design nous avons aussi étudié le côté non-connexion des têtes de bobine pour lequel nous avons proposé un design techniquement réalisable et qui permet de minimiser les harmoniques dans cette zone. Ce travail a été entièrement réalisé avec ROXIE.

Une fois le design d'un aimant terminé, le concepteur de l'aimant se doit de fournir aux physiciens des accélérateurs une estimation des erreurs attendues sur les harmoniques du champ magnétique. Cette estimation permet de dire si la qualité du champ est suffisamment bonne pour assurer la stabilité du faisceau, ou non, et ce avant même la réalisation de prototypes. Parmi les nombreuses sources d'erreurs présentes dans un aimant d'accélérateur supraconducteur, nous nous intéresserons tout particulièrement aux erreurs dites géométriques. Les erreurs géométriques ont pour origines les tolérances mécaniques sur les composants et dans le processus d'assemblage de l'aimant et sont responsables pour la majeure partie de l'incertitude sur des harmoniques de champ. Les tolérances mécaniques fixent une limite sur la qualité de champ magnétique qu'il est possible d'atteindre dans un aimant d'accélérateur. Les erreurs géométriques de champ varient d'un aimant à un autre et sont généralement trouvées pour une série d'aimants identiques (aimants qui diffère seulement par les tolérances) distribués suivant une loi gaussienne. Dans ce cas, les erreurs géométriques de champ sont définies par leur valeur moyenne et leur dispersion (ou sigma). La méthode couramment utilisée pour estimer le sigma de l'erreur pour chaque harmonique consiste en une simulation de Monte-Carlo ou l'on suppose la totalité des erreurs de champ due à des erreurs aléatoires de positionnement des blocs de conducteurs constituant la bobine, *i.e.,* les blocs sont supposés infiniment rigides. Les blocs de conducteurs sont déplacés à partir de leur position d'origine suivant les trois types de déplacements possible dans le plan transverse de l'aimant, à savoir une rotation autour du centre de l'ouverture, une translation radiale, et une rotation des blocs autour de leur centre de gravité. L'amplitude du déplacement pour chacun des blocs est tirée au hasard dans une distribution gaussienne caractérisée par une dispersion définie au préalable. Une fois tous les blocs constituant la bobine déplacés, on calcule les harmoniques du champ magnétique. La même opération est répétée entre 100 et 1000 fois de sorte que l'on ait suffisamment de données pour obtenir une bonne estimation du sigma de l'erreur de chaque harmonique. Le model magnétique utilisé est un model 2D qui néglige, à juste titre pour un aimant d'accélérateur caractérisé par des dimensions transverses petites devant la longueur magnétique, l'impact des têtes de bobines. Par conséquent, les résultats obtenus sont une estimation des erreurs de champ intégrées sur la longueur magnétique de l'aimant. La valeur *rms* de l'amplitude du déplacement des blocs est un paramètre important dans l'estimation des erreurs de champ. Des valeurs de références pour des aimants en Nb-Ti ont été obtenues dans le passé grâce à une méthode inverse qui permet d'estimer l'amplitude des déplacements de conducteurs à partir des mesures magnétiques intégrées réalisées dans plusieurs séries d'aimants. La méthode repose sur la même simulation de Monte-Carlo que celle décrite précédemment. La différence est qu'ici on cherche la valeur *rms* du déplacement qui permet d'approcher au mieux les erreurs de champ mesurées. Elles ont été estime entre 10 et 30 μm. Ces valeurs de références sont caracteristique des aimants Nb-Ti dipolaires et quadrupolaire construit durant les quinze dernières années. Ces valeurs ont été obtenues pour une technologie mature et pour une production stable de plusieurs dizaines voir centaines d'unités du même aimant. Pour des aimants plus âgés, l'amplitude des déplacements de blocs à été estimé entre 0.040 mm et 0.065 mm.

La construction récente de deux séries de six aimants en Nb_3Sn (une série de quadripôles et une série de dipôles) offre pour la première fois l'opportunité d'estimer la précision atteinte dans le positionnement des blocs dans des aimants quadripolaires et dipolaires basés sur la technologie supraconductrice Nb_3Sn. Les deux séries d'aimants sont des model courts (1 m de long) de 43.5 mm d'ouverture pour les six dipôles (appelés HFDA), et de 90 mm d'ouverture pour les six quadripôles (appelés TQ). Les résultats obtenus donnent une amplitude du déplacement des blocs dans les dipôles de 0.13 mm, et de 0.14 mm dans les quadripôles. Dans le premier cas, le résultat obtenu est en bon accord avec des mesures de positionnement des blocs réalisé avec un système optique. Ceci conforte la pertinence du procédé utilisé. L'écart entre les valeurs obtenues pour des aimants Nb-Ti et des aimants Nb3Sn sont due au fait que l'on compare des petites séries de model R&D d'aimant avec des productions de mass. Il est par conséquent prématuré de conclure que la technologie Nb3Sn fournie intrinsèquement une moins bonne qualité de champ que le Nb-Ti. Il y a un facteur 5 à 10 d'amélioration à potentiellement gagné sur l'amplitude de la dispersion des blocs. Nous avons aussi analysé la variabilité dans le positionnement des blocs le long de l'axe des aimants Nb_3Sn. Ceci à été rendu possible grâce à l'existence de mesures magnétiques réalisées le long de l'axe. Comme pour les aimants longs en Nb-Ti, la variabilité dans le positionnement des blocs le long de l'axe est trouvé un ordre de grandeur plus petit que la variabilité d'un aimant à l'autre. De plus, la dispersion de long de l'axe de 0.03 mm obtenue pour le quadripôle TQ est similaire a ce que qui à été obtenu pour les aimants dipolaires en Nb-Ti du LHC. Ceci met en évidence que la précision dans le positionnement des blocs le long de l'axe d'un aimant en Nb3Sn a atteint les standards de la technologie Nb-Ti.

Cependant, l'hypothèse forte utilisée pour la simulation de Monte-Carlo et selon laquelle les erreurs géométriques de champ sont entièrement due à un déplacement aléatoire de chaque bloc indépendamment des autres blocs ne colle pas totalement avec les mesures magnétiques. En effet, l'hypothèse précédente conduit a une décroissance logarithmique de la dispersion des harmoniques avec l'ordre des harmoniques (harmoniques normaux et tournés identique), alors qu'en réalité on observe un schéma différent: les harmoniques normaux et tournés d'ordre 3, 5, 7, … ont même valeur, les harmonique normaux et tournés sont généralement différents pour les ordres 4, 8, 10, …, et les harmoniques autorisés ont généralement une valeur bien plus grande que ceux non autorisés du même ordre. Pour comprendre ce phénomène encore inexpliqué à cette date, nous nous sommes appuyés sur une méthode directe qui consiste à calculer la dispersion de chaque harmonique lorsque les blocs de conducteur sont déplacés suivant quatre modes de déplacement réalistes pour un quadripôle. Le premier de ces modes considère le cas ou tous les blocs constituants une bobine sont indépendants les un des autres, le deuxième mode suppose un couplage des défauts dans chacune des quatre bobines formant un quadripôle, le troisième mode considère un déplacement aléatoire des plans médian de la bobine quadripolaire, et enfin, le quatrième mode considère un couplage de tous les blocs. A l'aide de calculs statistiques on montre que la dispersion des harmoniques suivant les quatre modes de déplacement plausible est compatible avec les mesures magnétiques.

Enfin, nous avons aussi traité un autre sujet relatif à la qualité du champ magnétique : l'incertitude de la moyenne de l'erreur des harmoniques de champ non autorisés par la symétrie quadripolaire. De part le design, les harmoniques non autorisés sont nuls. Cependant, lorsque l'on analyse les mesures magnétiques on trouve généralement une valeur non-nulle. Ceci peut être expliqué soit par des erreurs systématiques dans la bobine résultant en erreurs de champ systématique qui, dans une série d'aimants, s'additionneraient, ou alors par un effet statistique lié au nombre limité d'aimant dans la série. Pour trancher sur l'origine de l'incertitude de la moyenne nous avons utilisé les mesures magnétiques réalisées sur 11 séries d'aimant quadripolaire en Nb-Ti utilisé dans le LHC et dans RHIC. Pour chaque série nous avons analysé si la moyenne des harmoniques de champ intégré est compatible avec l'hypothèse d'une moyenne nulle. Les résultats obtenus montrent que c'est en général le cas, sauf pour les harmoniques a_6, a_{10}, b_4 et b_8. Notons que pour des raisons de précision de mesures, seul les harmoniques de rang inferieur à 10 sont considérés. Une partie de la moyenne de a_6 et a_{10} est due à l'asymétrie du coté connexion des têtes de bobines. Pour les harmoniques b_4 et b_8 on observe que l'incertitude sur la moyenne n'est pas compatible l'hypothèse d'une moyenne nulle seulement dans les quadripôles qui ont une culasse ferromagnétique faite de deux pièces à la place des quatre pièces nécessaires pour satisfaire la symétrie quadripolaire.

I. Introduction

Particle accelerators are essential tools for our understanding of the smallest constituents of the matter. Experimental results obtained by these machines coupled with theories set up over the years accumulated to what is today known as “the Standard Model” [88]. Developed in the early 1970s, the Standard Model has been so far used by physicists as a mean of understanding laws of sub-nuclear physics. The model will be tested at unprecedented energies in the CERN Large Hadron Collider (LHC), the largest and strongest particle accelerator ever built.

The LHC is a circular accelerator which steers and collides two counter-rotating protons beams in four collision points; in these points, detectors are placed to analyze the products emerging from the collisions. To reach its designed collision energy of 14 TeV (7 TeV per beam), the LHC is equiped with superconducting dipole and quadrupole magnets based on the Nb-Ti technology. Having an operational temperature of 1.9 K, the dipoles, used to bend the beams, provide a nominal magnetic field of 8.3 T [63]. Arc quadrupoles, used to assure the beams stability, operate also at 1.9 K and have a peak field on their conductor of 6.85 T [63]. Beside the energy, the other important parameter for a collider is its luminosity. It is defined as the rate of collisions between particles. A large luminosity is necessary to increase the probability of occurrence of rare events such as the generation of the Higgs boson [1], a fundamental, but still undiscovered, particle predicted by the standard model. The luminosity is partly determined by the properties of the quadrupole magnets placed on each part of the experiments, which are used to focus beams at the collision point. In the LHC, the focusing is realized by an arrangement of four 70-mm-aperture Nb-Ti quadrupoles providing 215 T/m in operational condition, called inner triplet quadrupoles. Because of the high radiation doses emerging from the collision, it is expected that the lifetime of the inner triplet quadrupoles will be of the order of 7 years [62]. Their replacement will be done in the framework of the “LHC Upgrade phase-I” project approved by the CERN Council in December 2007 and aiming at increasing the luminosity of the LHC by a factor 2-3 with respect to the nominal luminosity. To achieve this goal, the new inner triplet quadrupoles, which will partly contribute to this increase, will have to be of larger aperture than the present baseline. They will provide an estimated gradient of 120 T/m within a coil of inner diameter of 120 mm. This will be achieved by a 2-layers-coil based on the so-called $\cos 2\theta$ design using the 15 mm wide Nb-Ti spare cables of the LHC arc dipoles [67]. The four quadrupoles constituting the triplet will be of the same cross-section but will differ in length.

A phase-II upgrade of the LHC, foreseen at the horizon of 2020, aims at increasing the luminosity by a factor 10 with respect to the present baseline. Part of this increase will be obtained again by replacing the Nb-Ti quadrupoles of the inner triplet of the phase-I upgrade by quadrupoles with larger aperture (at least 130 mm) based on the Nb_3Sn technology. In this context the US-LARP (Large Accelerator Research Program) program launched in 2004 develops the Nb_3Sn technology for insertion quadrupoles. A few Nb_3Sn quadrupole short models have already been built and tested [76] [44] [22].

At the early stage of the choice of the electromagnetic design of a superconducting accelerator quadrupole, such as those for the phase-I upgrade of the LHC, it is interesting to have a first insight of the main parameters such as the short sample gradient, the magnetic forces in the coil or the electromagnetic stored energy without requesting the use of a full design of the magnet. A formula giving the short sample gradient and current in a quadrupole as a function of the main parameters such as the coil inner radius, the coil width and the type of superconducting material was worked out in [71]. Following a similar approach, in [47] it has been established a semi-analytical formula allowing estimating the maximal stress in the coil generated by large electromagnetic forces in superconducting quadrupoles. However, the magnetic stored energy in a quadrupole magnet which is an important parameter for the quench calculation and for designing its quench protection has not been yet expressed analytically. In this thesis we worked out such a formula. The equation is obtained from the Fourier decomposition of a uniform current density flowing in a quadrupole with coils made of one 30 ° sector and is then extended to include the case of a graded coil, *i.e.* whose the current density is larger in the outer part of the coil. The effect of an infinitely permeable iron around the coil on the magnetic energy is also taken into account by mean of an analytical corrective coefficient, and the iron saturation impact on the stored energy is investigated through numerical study. To validate our approach we compared the analytical formula of the stored energy with numerical computations performed on 31 real quadrupole coils.

To avoid as much as possible beam orbit perturbations, the magnetic field provided by the dipoles and quadrupoles constituting the accelerator ring are required to have a high level of homogeneity. In superconducting magnets, the main source of field distortion is due to mechanical tolerances in the coil components or in the magnet assembly. The field distortion can be expressed through harmonic coefficients of series expansion of the magnetic field within the magnet aperture. Typically, field harmonics errors have to be smaller than 10^{-4} times the main dipolar or quadrupolar field. From the spread of the field harmonic errors measured in a series of magnets it is possible, through a Monte-Carlo simulation, to estimate the precision reached in the reproducibility in the coil positioning [11] [45]. This method has been applied on several series of Nb-Ti dipoles and quadrupoles built for particle accelerators. This gave a *rms* value in the precision of the coil positioning ranging from 0.010 mm to 0.030 mm. However, due to the lack of series of identical magnets, this has not been done yet in Nb_3Sn magnets. In this thesis we propose to take the opportunity of two small series of Nb_3Sn dipole and quadrupole magnets recently built in the framework of the Fermilab National Accelerator Laboratory (FNAL) core program (dipoles) and of the LHC Accelerator Research Program (LARP) (quadrupoles) to estimate for the first time the precision in the reproducibility in the coil positioning of Nb_3Sn magnet. This is the second original result of this thesis.

The field quality in a quadrupole magnet is intrinsically linked to its electromagnetic design, which is the solution of an inverse problem in magneto-static consisting in finding current distributions generating pure quadrupolar fields. The typical current distribution for quadrupole accelerator magnets is obtained approximating a $\cos 2\theta$ current distribution by blocks of keystoned cables arranged around the magnet aperture [81]. The number of blocks, their number of cable turns, and their position are chosen so as to (i) minimize harmonics allowed by the quadrupolar symmetry and to (ii) fit the best with the specifications *e.g.* gradient, current, amount of cables… An exhaustive scan of all the possible arrangements of blocks is usually not possible because of the huge computational time it would need and the coil optimization is usually done by means of optimization algorithm like genetic algorithm [74]. In this thesis we propose a novel method to optimize the cross-section of cos2θ-type superconducting quadrupole magnets and we apply it to the design of the new inner triplet quadrupole for the phase-I of the LHC upgrade. The method consists in considering quadrupoles with coils made of sectors instead of blocks of cables so as to be able to use the Fourier series of the magnetic field. This allows, for coils made of up to five sectors, to perform an exhaustive scan of all possible configurations of sectors dimensions and position, guaranteeing that the found solution is a global one and not a local one. Those satisfying the field quality specifications are kept and are sorted out according the relevant short samples current and gradient parameters. The knowledge of the magnetic field everywhere also allows calculating the net magnetic forces in the sectors constituting the winding.

The plan of the work is the following: in chapter II we introduce some general concept that will be used in our research. The original part of the work carried out in the in this thesis starts in Chapter III where we work out a general formula allowing estimating the magnetic energy stored in superconducting quadrupoles and we investigate on its domain of applicability through numerical cross-check. In chapter IV we estimate the precision of the reproducibility in the coil positioning in Nb_3Sn dipole and quadrupole magnets. Finally, in chapter V we present the novel optimization method of electromagnetic quadrupole design we used for the design of the new quadrupole for the LHC phase-I upgrade.

II. Superconducting magnets for particles accelerator

II.1 Particle accelerator

II.1.1 Particle accelerator for high energy physics

The purpose of an accelerator of charged particles is to direct a particle's beam of a given energy against a target. Low energy accelerators are used to investigate the nuclear structure while high energy accelerators produce new varieties of particles and study their properties. The energy of an accelerator is usually given in eV, one eV being equal to the kinetic energy gain by an electron when it accelerates through an electrostatic potential difference of one volt. Among the family of high energy accelerators, capable of producing beams above 1 GeV, one can distinguish two main categories: linear accelerators (linac) and synchrotrons. In a linear accelerator particles travel along a straight line, while in a synchrotron particles travel along a circular orbit, thus allowing to store and use the beam at any time. The classical scheme of one beam of high energy particles hitting a nucleus of a fixed target is not the most efficient because some of the collision energy is wasted when the fixed particle gets kinetic energy from the high velocity particles. To get the maximum energy one has to collide particles of opposite momentum. This is what is achieved in a **collider,** where particles beams are accelerated and collide head on.

In general, circular accelerators like colliders are made of arcs separated by straight sections called **insertion regions**. Arcs are needed to bend the beam and insertion regions are used to house among other, acceleration cavities. In a collider, collisions take place in insertions regions. The point where the collision occurs is called **interaction point** and is denoted by **IP**. In a collider one can distinguish three main families of magnet: the **arc dipole** magnets used to bend the beam in the arc regions, the **arc quadrupole** magnets used to assure the beam stability, and the **insertion region magnets** (quadrupoles and dipoles) use to prepare the beam for the collision.

The energy of a beam circulating in an accelerator is intrinsic to the dimension of the accelerator and to the strength of the magnetic field used to maintain the beam on the reference orbit. The energy [GeV] of one beam is given by

$$E \approx 0.3BR, \tag{1}$$

where B [T] is the magnetic field generated by the dipole (see Figure 1) in the arc and oriented perpendicularly to the beam trajectory, and R [m] is the radius of curvature. Note that R is usually smaller than the radius of the accelerator because of the presence of the insertion regions, and because arcs are not entirely filled with dipoles magnets. One way to reach high energies is the use of superconductivity: it allows the production of intense magnetic field while having limited power consumption (with respect to that of normal magnets). For that reason many colliders rely on superconductivity.

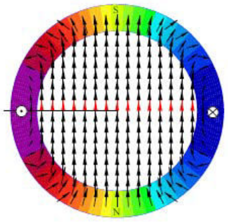

Figure 1 – Dipolar-type magnetic field [74].

In the collider family, one distinguishes the single-ring collider where particles of opposite charge circulate in the same pipe, and the twin-ring collider where particles of the same charge circulate in two pipes. In this thesis we will often refer to superconducting magnets used or only designed either for single-ring collider (Tevatron [101]) or in double-ring colliders (HERA [39], SSC [87], RHIC [53], and LHC [86]).

II.1.2 Layout of the Large Hadron Colider (LHC)

The LHC, located at CERN, on the border between France and Switzerland, near Geneva, is a superconducting synchrotron that has been designed to accelerate and store hadron beams in a ring of 27 km of circumference up to energy of 7 TeV. Clockwise and anti-clockwise beams will circulate at nearly the speed of light in two separated pipes and will collide in four experiments named ALICE [3], ATLAS [8], CMS [31] and LHCb [64], and with a maximum collision energy of 7+7 TeV.

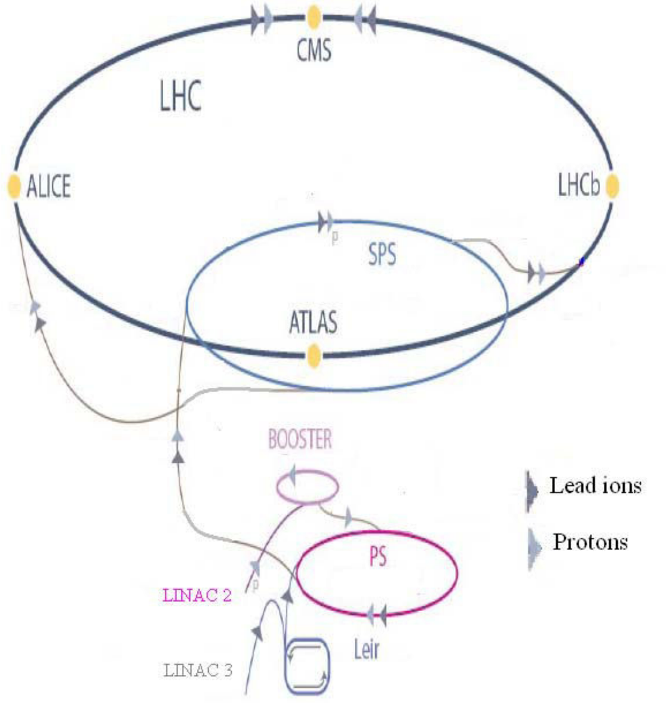

Figure 2 – The LHC injector complex of protons and lead ions.

To investigate the smallest constituents of matter, the LHC will make to collide either two beams of protons, which will represent 90% of the collisions, or lead irons. The injector complex of the LHC is shown in Figure 2. About 90 % of the collisions will be proton-proton collisions. They are extracted from a hydrogen source at a kinetic energy of 100 eV. Then, after being grouped in buckets, protons are accelerated through a ~80 m long Linac (Linac 2) up to energy of 50 MeV before being injected in the 157 m of circumference Proton Synchrotron Booster (PSB) aiming at increasing the beam energy up to 1.4 Gev. In the PSB, the velocity of the proton beams already reaches 91.6 % of the speed of light. From the PSB, particles are transferred to the 628 m of circumference Proton Synchrotron (PS) where the protons energy is increased up to 28 GeV. The final accelerating step before injection in the LHC ring takes place in 6.9 km of circumference Super Proton Synchrotron which allows increasing the beams energy from 28 GeV to 450 GeV. The injection finishes when all bunches of protons fill the two tubes of the LHC ring. Finally the energy is raised up to 7 TeV and the two beams are collided.

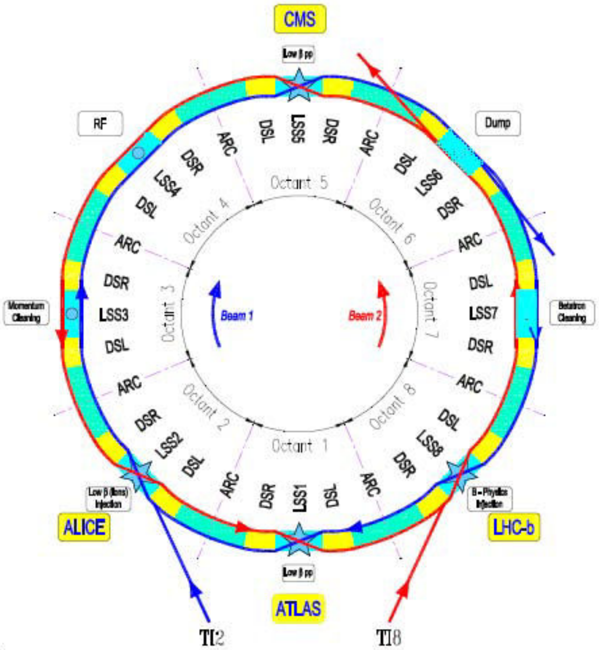

Figure 3 – Layout of the LHC: The two beams path and the four interaction points.

The control of the beams trajectories and stabilities in the LHC ring (see Figure 3) is achieved by means of 1232 superconducting dipoles providing a magnetic field of 8.33 T, and of 360 superconducting arc quadrupoles generating a field gradient of 223 T/m. an example of quadrupolar field is given in Figure 4.

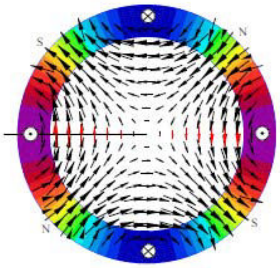

Figure 4 – Quadrupolar-type magnetic field [74].

In addition to that, about 4000 corrector magnets are positioned all along the ring. On each side of the experiments are located specific magnets aiming at preparing beams for the collision (see Figure 5). Among these magnets are the so-called inner triplet quadrupoles used to reduce the beam size at the collision point so as to increase the probability on the number of events. Part of the work done in this thesis is on the design of a new inner triplet quadrupole for the LHC.

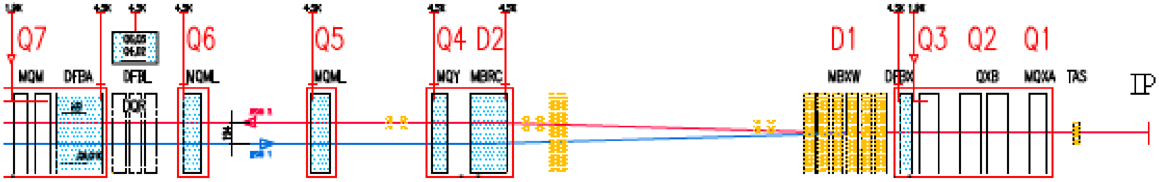

Figure 5 – Schematic layout of the left side of an interaction region. The magnets denoted with D are dipoles, while those denoted with Q are quadrupoles. The interaction point is denoted by IP. Quadrupoles of the inner triplet are denoted by Q1, Q2 and Q3. Note that Q3 is made of 2 quadrupoles.

II.1.3 Relevant quantity for accelerator magnets

Let us consider a particle of charge q travelling at the velocity $\vec{v}$ in a magnetic field $\overrightarrow{B}$. The force applied by the magnet on the particle is given by

$$\vec{f} = q\vec{v} \times \vec{B}. \tag{2}$$

Developing X gives

$$\vec{f} = \begin{pmatrix} f_x \\ f_y \\ f_z \end{pmatrix} = q \begin{pmatrix} B_z v_y - B_y v_z \\ B_x v_z - B_z v_x \\ B_y v_x - B_x v_y \end{pmatrix}, \tag{3}$$

where B_x, B_y and B_z are the x, y and z-components of the magnetic field. Similarly, v_x, v_y and v_z are the x, y and z-components of the particle velocity.

Let us now assume that the particle runs parallel to the axis of an accelerator magnet defined here as the z-axis of the rectangular coordinate (x,y,z) *i.e.* $v_x \sim v_y \sim 0$ and $v_z \sim c$ (c being the speed of light). This assumption is reasonable since the particle deviation from the reference orbit is small.

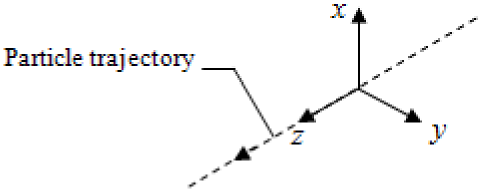

Figure 6 – Particle trajectory in the rectangular coordinate system (O,x,y,z).

With this assumption the force applied on a particle force applied on the particle rewrites

$$\vec{f} = \begin{pmatrix} f_x \\ f_y \\ f_z \end{pmatrix} = qv_z \begin{pmatrix} -B_y \\ B_x \\ 0 \end{pmatrix}, \tag{4}$$

where B_x and B_y are the z and y-components of the magnetic field. The first consequence is that the z-component of the magnet field (B_z) does not interact with the particle: what is important are the transverse components (B_x and B_y) of the magnetic field.

The momentum given by the magnetic field to the particle between the time t_1 and t_2 is

$$\Delta\vec{P} = \int_{t_1}^{t_2} \vec{f}dt \tag{5}$$

Assuming that v_z does note varies between t_1 and t_2 and noting that $dt = dz/v_z$ allows rewrite Eq. (5)

$$\Delta\vec{P} = \frac{1}{v_z}\int_{z_1}^{z_2} \vec{f}dz\,, \tag{6}$$

where z_1 and z_2 are the positions of the particle at $t=t_1$ and $t=t_2$, respectively. Decomposing Eq. (6) according to its x and y-components, and substituting $\vec{f}$ by Eq. (4) gives

$$\Delta P_x = -q\int_{z_1}^{z_2} B_x dz \qquad \text{and} \qquad \Delta P_y = q\int_{z_1}^{z_2} B_y dz. \tag{7}$$

In practice, the quantities which are the most relevant when dealing about the magnets of an accelerator (dipole, quadrupole, …) are the integrated components of the magnetic field.

II.2 Field computation in particles accelerators magnets

II.2.1 Basic equations

Although the magnetic field in accelerator magnets is time dependent, in any case the time constant of the field variation is large so we can consider it as a magneto-static problem. Maxwell's equations in magneto-static are

$$\nabla.\vec{B} = 0 \tag{8}$$

$$\nabla \times \vec{H} = \vec{J} \tag{9}$$

$\vec{B}$ [T] is the magnetic flux density (or magnetic induction) and $\vec{H}$ [Am^{-1}] is the magnetic field. Furthermore, $\vec{B}$ and $\vec{H}$ are linked by

$$\vec{B} = \mu_0\left[\vec{H} + \vec{M}(\vec{H})\right], \tag{10}$$

where $\vec{M}$ [Am^{-1}] is the magnetization of the material and μ_0 is the magnetic permeability of the vacuum [Hm^{-1}]. The relation between $\vec{M}$ and $\vec{H}$ is given by the material properties *e.g.,* diamagnetic, paramagnetic or ferromagnetic. Note that $\vec{M} = 0$ in the vacuum. Expression (10) can be re-written by means of the magnetic permeability tensor $\bar{\bar{\mu}}$ in the particular case where $\vec{M}$ varies linearly with $\vec{H}$, *i.e.,* if the material considered is linear,

$$\vec{B} = \bar{\bar{\mu}}\vec{H}. \tag{11}$$

If, in addition to be linear, the medium is also isotropic, the relation (11) reduces to

$$\vec{B} = \mu_0(1 + \chi)\vec{H} \tag{12}$$

$$\vec{B} = \mu_0\mu_r\vec{H}, \tag{13}$$

where χ [dimensionless] is the magnetic susceptibility of the medium and μ_r [dimensionless] is the relative magnetic permeability of the medium (relative with respect to that of vacuum). From now and throughout the whole thesis, we will only consider linear and isotropic magnetic media when carrying out analytical calculation of the magnetic flux density in the absence or presence of ferromagnetic materials (Eq. (13)).

The nullity of divergence $\vec{B}$ implies that $\vec{B}$ can be expressed in term of the potential vector $\vec{A}$ [Tm^{-1}]

$$\vec{B} = \nabla \times \vec{A}. \tag{14}$$

Assuming that divergence $\vec{A}$ is null (Coulomb gauge), and combining Eqs. (14) and (13) in Eq. (9) one gets the Poisson's equation

$$\Delta\vec{A} = -\mu_0\mu_r\vec{J}. \tag{15}$$

In space free of current, Eq. (9) reads

$$\nabla \times \vec{H} = \vec{0}; \tag{16}$$

this implies that, in a region free of currents, $\vec{H}$ can be expressed in term of the magnetic scalar potential V_m, expressed in [A] and defined as

$$\vec{H} = -\nabla V_m. \tag{17}$$

The surfaces on which V_m is constant are orthogonal to the magnetic flux lines. Combining Eqs. (17) and (13) and substituting it in Eq. (8) while assuming an homogenous and linear material leads to the Laplace's equation

$$\Delta V_m = 0. \tag{18}$$

One has to notice that V_m is single-valued only on simply-connex domains.

II.2.2 Solution of the Laplace's equation

Neglecting the magnetic field provided by the particle beam, the aperture of an accelerator magnet is free from charges and currents. Therefore, we can consider the magnetic potential scalar V_m defined in Eqs. (17) and (18). In the cylindrical coordinate system (O,r,θ,z), the Laplace equation to which $V_m(r,\theta,z)$ satisfies (Eq. (18)) reads

$$\frac{1}{r}\frac{\partial}{\partial r}\left(r\frac{\partial V_m}{\partial r}\right)+\frac{1}{r^2}\frac{\partial^2 V_m}{\partial \theta^2}+\frac{\partial^2 V_m}{\partial z^2}=0. \tag{19}$$

The above equation can be solved by means of the separation of variables method leading to express V_m as

$$V_m = R(r)\Theta(\theta)Z(z). \tag{20}$$

The winding of an accelerator magnet of axis z is symmetric about z=0 and has a periodicity in θ. One can therefore assume that that V_m is finite at $r = 0$, that $V_m(-z)=V_m(z)$ and that there is a periodicity of V_m in θ. Under these assumptions the general solution of V_m is [34]

$$V_m(r,\theta,z)=\sum_{n=0}^{\infty}\sum_{p=0}^{\infty}\left(\frac{r}{R_{ref}}\right)^{n+2p}\left[k_{np}^{S}(z)\cos(n\theta)-k_{np}^{N}(\mathrm{z})\sin(n\theta)\right] \tag{21}$$

with

$$k_{np}^{S}(z)=\frac{(-1)^p n!\,{R_{ref}}^{2p}}{2^{2p}p!\,(n+p)!}\frac{d^{2p}}{dz^{2p}}[k_{n0}^{S}(z)] \tag{22}$$

and

$$k_{np}^{N}(z)=\frac{(-1)^p n!\,{R_{ref}}^{2p}}{2^{2p}p!\,(n+p)!}\frac{d^{2p}}{dz^{2p}}[k_{n0}^{N}(z)]. \tag{23}$$

The positive integer n is the harmonic order of the Fourier expansion of V_m. The constant R_{ref} is a fixed reference radius arbitrary chosen and the functions k_{n0}^{S} and k_{n0}^{N} depend only on the winding features. The components of the magnetic field can be obtained substituting Eq. (21) in Eq. (17).

As shown in section II.1.3, the important feature in an accelerator magnet is the integrated magnetic field, *i.e.,* the magnetic field integral is obtained integrating the magnetic field over the length of the magnet. Since the z-dependent functions in Eq. (21)

are decoupled from the r and θ-dependent functions, we can introduce an integrated magnetic potential scalar $V_m^L(r,\theta)$ (expressed in [Am]) as the integral of $V_m(r,\theta,z)$ over z, and for z extending from -∞ to +∞. When carrying out the integration, all terms with $m>0$ vanish [34] and $V_m^L(r,\theta)$ becomes

$$V_m^L(r,\theta) = \int_{-\infty}^{+\infty} V_m(r,\theta,z)dz = \sum_{n=0}^{\infty}\left(\frac{r}{R_{ref}}\right)^n [K_n^S\cos(n\theta) - K_n^N\sin(n\theta)] \quad (24)$$

where

$$K_n^S = \int_{-\infty}^{+\infty} k_{n0}^S(z)\,dz \quad and \quad K_n^N = \int_{-\infty}^{+\infty} k_{n0}^N(z)\,dz. \quad (25)$$

The r and θ-components of the integrated magnetic field will be then calculated substituting Eq. (24) in eq. (17).

Let us now assume that the harmonic function $V_m^L(r,\theta)$ is the imaginary component of an analytic function $\bar{W}^L(r,\theta)$ defined as

$$\bar{W}^L(r,\theta) = F_m^L(r,\theta) + iV_m^L(r,\theta), \quad (26)$$

where $F_m^L(r,\theta)$, the conjugate harmonic function of $V_m^L(r,\theta)$, is shown to be the z-component of the magnetic vector potential $\vec{A}(r,\theta,z)$ integrated over z and for z extending from -∞ to +∞

$$F_m^L(r,\theta) = \frac{1}{\mu_0}\int_{-\infty}^{+\infty} A_z(r,\theta,z)dz. \quad (27)$$

Note that $F_m^L(r,\theta)$ and $V_m^L(r,\theta)$ satisfy to the Cauchy-Riemann equations. The expression of $F^L{}_m$ (in [Am]) reads

$$F_m^L(r,\theta) = \sum_{n=0}^{\infty}\left(\frac{r}{R_{ref}}\right)^n [-K_n^N\cos(n\theta) - K_n^S\sin(n\theta)]. \quad (28)$$

Substituting Eqs. (24) and (28) in Eq. (26) allows expressing $\bar{W}^L(r,\theta)$

$$\bar{W}^L(r,\theta) = \sum_{n=0}^{\infty}\left(\frac{r}{R_{ref}}\right)^n [\cos(n\theta) + i\sin(n\theta)](-K_n^N + iK_n^S). \quad (29)$$

Let us re-express Eq. (29) using the complex variable $\bar{z} = x + iy = re^{i\theta}$

$$\bar{W}^L(r,\theta) = \sum_{n=0}^{\infty} \left(\frac{\bar{z}}{R_{ref}}\right)^n (-K_n^N + iK_n^S). \tag{30}$$

Due to the analycity of $\bar{W}^L$ it has been shown in [65] that one can define a complex integrated magnetic induction B^L (expressed in [Tm]) as

$$-\mu_0 \frac{d\bar{W}^L}{d\bar{z}} = B_y^L + iB_x^L = \bar{B}^L, \tag{31}$$

where ${B_x}^L$ and B_y^L are the x and y-components of $\bar{B}^L$. The integrated magnetic induction $\bar{B}^L$can be re-writen

$$\bar{B}^L(r,\theta) = -\mu_0 \sum_{n=1}^{\infty} \left(\frac{\bar{z}}{R_{ref}}\right)^{n-1} \left(\frac{n}{R_{ref}}\right) (-K_n^N + iK_n^S). \tag{32}$$

In the accelerator community we use to re-write Eq. (32) as

$$\bar{B}^L = \sum_{n=1}^{+\infty} (B_n^L + iA_n^L) \left(\frac{\bar{z}}{R_{ref}}\right)^{n-1}, \tag{33}$$

where A_n^L and B_n^L are the so-called **skew** and **normal integrated** harmonic components. They are expressed in [Tm] and are defined as

$$B_n^L = \mu_0 \left(\frac{n}{R_{ref}}\right) K_n^N \quad \text{and} \quad A_n^L = -\mu_0 \left(\frac{n}{R_{ref}}\right) K_n^S. \tag{34}$$

Note that A_n^L, coefficient of order n in the development of the integrated induction B^L, is not a vector potential.

II.2.3 High energy accelerator magnets

Most of magnets used in particles accelerator of high energy are dipoles to bend the particles beam and quadrupoles to focus the beam. Due to the limitation of the performances of the superconducting materials, magnets have to be long enough to provide the required bending and focusing strength defined as the integrated induction and integrated gradient. For instance, in the LHC machine the integrated induction (bending strength) for the main dipoles is 120 Tm. The maximal induction provided is 8.3 T in an aperture diameter of 56 mm [63], this leads to a magnet length of 14.3 m. Similarly, the needed integrated gradient (focusing strength) in the main quadrupoles is 690 T. The maximal gradient provided in the 3.1 m long quadrupole is 223 T/m in an aperture diameter of 56 mm [63]. With theses dimensions, *i.e.,* long axial dimensions with respect to the transverse dimensions, it is clear that one can consider that the magnetic induction in the straight part is similar to what one would have for a magnet of similar cross-section but of infinite length. For that reason, the computation of the magnetic field in the magnet body is usually done assuming that the coil is infinitely long into the *z* direction. This assumption has the advantages of simplifying the magnetic flux density computation in the magnet body and of enabling bi-dimensional analytical calculation. The magnetic field provided by the coil ends and the current leads is computed separately by means of numerical codes, *e.g.*, Roxie [73]. In the following we only consider 2D problem with uniform current density in *z*. A 3D view of a quadrupole coil is shown in Figure 7.

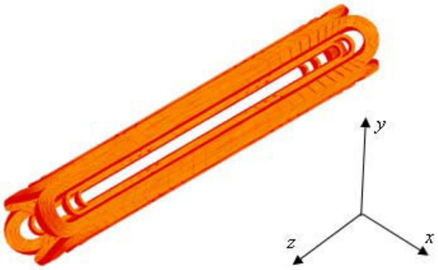

Figure 7 – Quadrupole coil of a superconducting accelerator magnet.

II.2.4 Magnetic field in an infinitely long accelerator magnet

Let us condsider a current distribution in the cylindrical coordinate system *(O,r,θ,z)* such that it does not depend on the *z* variable and it has only a *z*-component

$$\vec{J}(r,\theta) = j_z(r,\theta)\,\vec{z}. \tag{35}$$

As the problem is invariant by translation along the *z*-axis, *e.g.*, an infinitely long magnet in *z*, the dependence of V_m on *z* cancels and all the terms in *p* disappear, and thus Eq. (21) re-writes

$$V_m(r,\theta) = \sum_{n=0}^{\infty} \left(\frac{r}{R_{ref}}\right)^n [k_n^S \cos(n\theta) - k_n^N \sin(n\theta)], \tag{36}$$

where $k^S{}_n$ and $k^N{}_n$ are coefficients obtained from the solution of the bi-dimensional Laplace's equation

$$\Delta V_m(r,\theta) = 0. \tag{37}$$

Classically in magneto-static [40], when considering lines currents running only along *z*, we define an analytical function $\overline{W}$ where V_m is its imaginary component

$$\overline{W}(r,\theta) = F_m(r,\theta) + iV_m(r,\theta), \tag{38}$$

and F_m is

$$F_m(r,\theta) = \frac{1}{\mu_0} A_z(r,\theta), \tag{39}$$

where $A_z(r,\theta)$ is the only component different from zero of the vector potential $\vec{A}$. It is of the form

$$A_z(r,\theta) = \mu_0 F_m(r,\theta) = \sum_{n=0}^{\infty} \left(\frac{r}{R_{ref}}\right)^n \left[-k_n^N \cos(n\theta) - k_n^S \sin(n\theta)\right]. \tag{40}$$

If the current distribution is known, the vector potential $A_z(r,\theta)$ may be obtained from the Biot and Savart law

$$A_z(r,\theta) = \iint_S \left[\int_{-\infty}^{+\infty} j_z(r_p,\theta_p) \frac{1}{\|PM\|} dz_p\right] r_p dr_p d\theta_p, \tag{41}$$

where S is the cross-sectional area [in the plan (O,r,θ)] of the current carrying structure within which flows the current density $j_z(r_p,\theta_p)$. $P(r_p,\theta_p,z_p)$ is a given point belonging to the current carrying structure and $M(r,\theta)$ is the point where the vector potential $A_z(r,\theta)$ is computed.

Let us re-express Eq. (38) using the complex variable $\bar{z} = x + iy = re^{i\theta}$

$$\bar{W}(r,\theta) = \sum_{n=0}^{\infty} \left(\frac{\bar{z}}{R_{ref}}\right)^n (k_n^S + ik_n^N). \tag{42}$$

The magnetic induction $\bar{B}$, which is also analytical, can be derived from above equation by means of

$$-\mu_0 \frac{d\bar{W}}{d\bar{z}} = B_y + iB_x = \bar{B}, \tag{43}$$

where B_x and B_y are the x and y-components of $\bar{B}$. $\bar{B}$ can be re-writen

$$\bar{B}(r,\theta) = \sum_{n=1}^{\infty} \left(\frac{\bar{z}}{R_{ref}}\right)^{n-1} \left(\frac{n}{R_{ref}}\right) (k_n^S + ik_n^N). \tag{44}$$

We use to re-write $\bar{B}$ as

$$\bar{B} = \sum_{n=1}^{+\infty} (B_n + iA_n) \left(\frac{\bar{z}}{R_{ref}}\right)^{n-1}. \tag{45}$$

As previously, the accelerator community use the coefficients A_n and B_n, expressed in [T] and called **skew** and **normal harmonic** coefficients respectively. Note that A_n, coefficient of order n in the development of the complex induction $\bar{B}$, is not a vector potential. The complex number $B_n + iA_n$ is usually denoted by

$$\bar{C}_n = B_n + iA_n. \tag{46}$$

It is worth noting that Eq. (33) and Eq. (45) are similar except that in Eq. (33) we use the integrated induction B^L [Tm] while in Eq. (45) we use the induction B [T]. For an infinitely long magnet $\bar{B}$ can be considered as B^L per unit length. **Thus, a bi-dimensional harmonic approach can be used either with $\bar{B}$ for infinitely long magnets or with $\bar{B}^L$ for real magnets of finite length.**

II.2.5 Field harmonics definition

Let us here consider the bi-dimensional problem invariant along z in the rectangular coordinate system (*O,x,y,z*). The analyticity of the complex induction $\bar{B}$ defined in Eq (43), easily verified by means of the Maxwell's equations, implies that $\bar{B}$ can be expanded into a Taylor's series in any disk where $\bar{B}$ is analytic, *i.e.,* there is neither currents nor magnetic media within the disk. If the disk origin is chosen as the origin *O* of the (*O,x,y*) plan and considering the European notation, *i.e.,* the harmonic order *n* starts from *n* = 1, one has

$$\bar{B}(\mathrm{z}) = \sum_{n=1}^{\infty} R_{ref}^{n-1} \frac{1}{n!} \frac{\partial^n \bar{B}(\bar{z})}{\partial \bar{z}^n}\bigg|_{z=0} \left(\frac{z}{R_{ref}}\right)^{n-1}, \tag{47}$$

where the reference radius R_{ref} is typically chosen to be around 2/3 of the magnet aperture radius. The skew and normal harmonic coefficients A_n and B_n defined in Eq. (45) and given at the reference radius R_{ref} read

$$\bar{C}_n = B_n + iA_n = R_{ref}^{n-1} \frac{1}{n!} \frac{\partial^n \bar{B}(\bar{z})}{\partial \bar{z}^n}\bigg|_{z=0}. \tag{48}$$

In the American community, author sometimes prefer re-write Eq. (45) as:

$$\bar{B} = \sum_{n=0}^{\infty} (B_n + iA_n) \left(\frac{z}{R_{ref}}\right)^{n}. \tag{49}$$

To pass from the EU to the US notation

$$\bar{C}_n^{EU} = \bar{C}_{n-1}^{US}. \tag{50}$$

From now and throughout the whole thesis we only refer the European notation, *i.e.,* the multipole order *n* start from *n* = 1 [Eq. (45)].

The aim of a $2N$-poles magnet is to produce a pure $2N$-polar magnetic field. It is therefore convenient to introduce c_n, the normalized induction at the reference radius

$$\bar{B}(\mathrm{z}) = 10^{-4} B_N \sum_{n=1}^{\infty} \bar{c}_n \left(\frac{z}{R_{ref}}\right)^{n-1} \tag{51}$$

with

$$\bar{c}_n = b_n + i a_n = 10^{-4} \frac{\bar{C}_n}{B_N}, \tag{52}$$

and where B_N is the normal coefficient of a $2N$-poles magnet given at the reference radius R_{ref}. The 10^4 term has been added for practical purpose so that c_n is given in units of 10^{-4}. The Coefficients b_n and a_n are the normalized normal and skew harmonic coefficients given in units of 10^{-4}. Note that in a dipole the main field is B_1, and in a quadrupole the field gradient denoted by G and expressed in [Tm^{-1}] is given by

$$G = \frac{B_N}{R_{ref}}. \tag{53}$$

It is worth noting that by linearity the harmonic coefficient C_n due to a winding composed of k conductors is obtained from

$$\bar{C}_n = \sum_{l=1}^{k} \bar{C}_n^l, \tag{54}$$

where $C_n^{\,l}$ is the complex harmonic coefficient due to the conductor l. This remark does not stand for the normalized coefficient $\bar{c}_n$ which is not linear.

As previously said, we are mostly interested in the integral of the field harmonics over the length of the magnet since their value are representative of the overall focusing or bending strength of the magnet and of the possibly unwanted field strength due to distortion of the original magnetic induction caused, for instance, by defects on the magnet components or on the coils positioning. Let us consider a $2N$-poles magnet e.g. N=1 for a dipole and $N = 2$ for a quadrupole. According to the notation adopted for the integrated skew and normal harmonic components in Section II.2.2 (A_n^L and B_n^L), the **integrated normalized multipoles**, denoted by a_n^L and b_n^L and expressed in units, are calculated by means of

$$a_n^L = 10^4 \frac{A_n^L}{B_N^L} \quad \text{and} \quad b_n^L = 10^4 \frac{B_n^L}{B_N^L}. \tag{55}$$

In the literature we usually find the equivalent equation [25]

$$a_n^L = \frac{\int_{-\infty}^{+\infty} a_n(z) B_N(z)\, dz}{L_m B_N(0)} \quad \text{and} \quad b_n^L = \frac{\int_{-\infty}^{+\infty} b_n(z) B_N(z)\, dz}{L_m B_N(0)}, \tag{56}$$

with z the position along the magnet axis and $B_N(0)$ the main field harmonic in the center of the magnet, *i.e.,* $z = 0$. L_m is the so-called magnetic length of the magnet which is usually smaller than the physical length of the magnet. The magnetic length is calculated for the main field harmonic (*i.e.* B_1 for a dipole, B_2 for a quadrupole, …) by means of [25]

$$L_m = \frac{\int_{-\infty}^{+\infty} B_N(z)\, dz}{B_N(0)}. \tag{57}$$

II.2.6 Impact of field errors on accelerator performance

Particles travelling in a circular accelerator or storage ring have to make a large number of revolutions. In order to keep particles as close as possible to the reference orbit, focusing forces acting perpendicularly to the reference orbit are required (see Figure 8). They are achieved by FODO cells composed of a focusing quadrupole (F), a defocusing quadrupole (D) and a non-focusing element O which could be either a dipole or a drift space. The focusing quadrupole focus the beam in one plan but defocus it in the other, and inversely for the defocusing one. The overall focusing action of the beam in the two transverse plans of a FODO cell has been first established in 1957 in [33]. Note that a FODO cell in the horizontal plan becomes a DOFO cell in the vertical plan (horizontal and vertical plans are perpendicular to the orbit path). The feature of FODO cells is that they make particles oscillate in the transverse plane around the reference orbit. These oscillations are called betatron oscillations. For instance, the horizontal displacement $x(s)$ from the design orbit of a particle running along s, the path length of the design orbit, is described by [81]

$$x(s) = a_x \sqrt{\beta_x(s)} \cos[\varphi_x(s) + \varphi_x^0], \tag{58}$$

where $\varphi_x(s)$ is the phase advance in the horizontal plan

$$\varphi_x(s) = \int \frac{ds}{\beta_x(s)} \tag{59}$$

and $\beta_x(s)$ is the so-called beta function defined in meter. The beta function is obtained solving the non linear differential equation given by the sequence of magnets, *i.e.,* the lattice structure. Constants φ_x^0 and a_x are given by initial conditions.

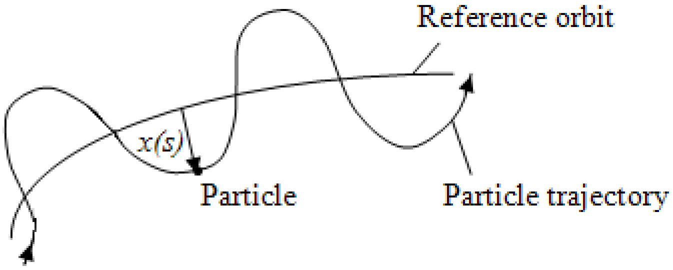

Figure 8 – Particle trajectory in the *x* or horizontal plane. Oscillations about the design orbit are called betatron oscillations.

From the beta function β_x one can calculate Q_x, the number of betatron oscillations in the horizontal plane per revolution [81]

$$Q_x = \frac{1}{2\pi}\oint \frac{ds}{\beta_x(s)} \tag{60}$$

The number Q_x is a very important parameter in accelerator physics. It has to be carefully chosen so that the length of the design orbit is not an integer value of the betatron oscillations *i.e.,* the oscillation close upon itself after one revolution. If Q_x is an integer value, any dipole-type field distortion would excite coherently the particles from turn to turn and it would end in the loss of the beam. On the other hand, if Q_x is not an integer value, the dipole field error would excite the particles at different phases from turn to turn resulting to an average deviation of zero. Similarly, a quadrupolar field error-type would excite particles for half integer values of Q_x, and sextupole correctors would excite third integer values, and so on. Similarly to the horizontal plane, one can define the vertical displacement of the particle $y(s)$ by means of the beta function $\beta_y(s)$ and of the phase $\varphi_y(s)$. As for the horizontal plane, Q_y has to be different from an integer. Magnetic field error of the type skew, *e.g.,* a dipole magnet tilted around its axis, generated together with error of the type normal, leads to couple Q_x and Q_y

$$gQ_x + hQ_y = p. \tag{61}$$

Parameters g and h are integer values. To prevent resonances, integer values of p are forbidden up to a given order. A quadrupole magnet which has its normalized field harmonic components (a_n and b_n) of any order, except for n=2, below one unit is usually seen to be acceptable from the field quality point of view.

II.3 Electromagnetic design of quadrupole magnets in 2D

II.3.1 Winding configuration

Current density distributions in quadrupoles magnets are solutions of an inverse problem consisting in finding sources of current generating a pure quadrupolar field, *i.e.,* all multipoles are zero except B_2. There are, in theory, an infinite number of solutions to inverse problems. However, in addition to generate a pure quadrupolar magnetic field in their aperture, superconducting accelerator quadrupoles winding must allow to easily implement a retaining system which has to withstand the large electromagnetic forces. In the past, two main types of winding generating a pure quadrupolar field and satisfying to the mechanical constrains had been identified: the so-called cos(2θ)-type [27] consisting of a cylindrical tube with a current density proportional to cos(2θ), where θ is the azimuthal angle (see Figure 9, left) and the intersecting ellipse-type [12] [92] obtained by constant current densities flowing in the intersection of two identical ellipses oriented perpendicularly to each other (see Figure 9, right).

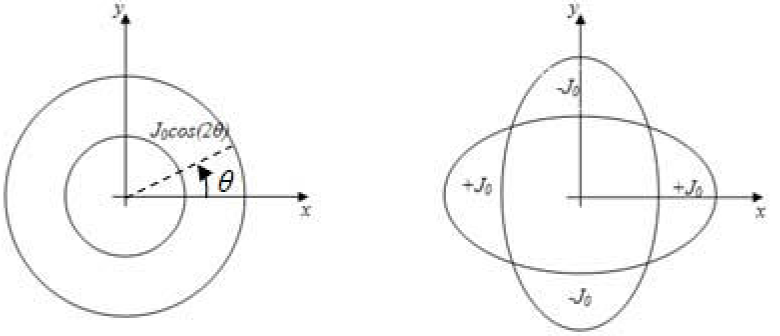

Figure 9 – Cos2θ-type and intersecting ellipse-type coil allowing generating a pure quadrupolar field in their aperture.

So far, the most widely used winding-type in superconducting accelerator has been the cos2θ-type. It has the advantage to be well and easily approximated by an assembly of pure sector coil blocks, *i.e.,* sector coil delimited by lines going through the origin, powered with constant current densities. The cosθ and the cos2θ-type designs have been successfully used for the first time in the superconducting dipoles and quadrupoles of the Tevatron accelerator in 1984 [101].

More recently, in 2006, it has been theoretically shown in [77]-[78] the existence of a more general winding shape generating an ideal quadrupolar field. The shape of the quadrupole winding is delimited by inner and outer lines, named r_1 and r_2 respectively and parameterized in θ

$$r_1(\theta) = \frac{ab}{[a^4 + (b^4 - c)cos^2\theta + (c - a^4)cos^4\theta]^{1/4}} \tag{62}$$

$$r_2(\theta) = \frac{ab}{[a^4 + (b^4 - c)sin^2\theta + (c - a^4)sin^4\theta]^{1/4}}, \tag{63}$$

where constant a, b and c refer to the shape of the winding. Note that one retrieves the intersecting ellipses shape when

$$c = a^4 + (b^2 - a^2)^4. \tag{64}$$

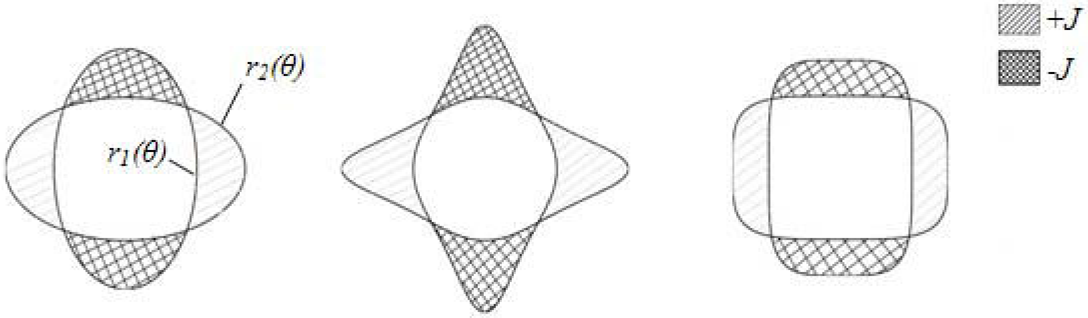

Figure 10 – Example of coil shape allowing generating a pure quadrupolar field : elliptic shape (left), star-like shape (middle) and Panofsky-like shape (right) [78].

II.3.2 Field calculation of quadrupole based on cos2θ design by means of Fourier series

The cross-section of a quadrupole can be well approximated by a given number of sectors carrying a constant current density (see Figure 11). The need of having more than one sector is due to the constraint of generating a pure field component (quadrupole in this case): the quadrupolar symmetry naturally cancels all unwanted field harmonics except normal harmonic of order 6, 10, 14,… called **allowed harmonics**. A quadrupole made of simple 30° sector coil (see Figure 11, left) sets to zero the first non-zero normal harmonic, *i.e.,* the multipole b_6 in Eq. (52), which is not enough to meet the beam dynamics requirements. Lay-outs with two sectors having appropriate angles can set to zero also normal multipoles of order 10 and 14, *i.e.,* b_{10} and b_{14}, (see Figure 11 middle), thus providing sufficiently pure fields to satisfy the beam dynamics specifications [71]. Here we recall analytical equations of the vector potential and of the magnetic field produced everywhere by a quadrupole with coils made of sectors [6]. These expressions will be used in Section III to calculate the magnetic energy in quadrupoles, and in a new method set up in Section V.1 to design superconducting quadrupoles.

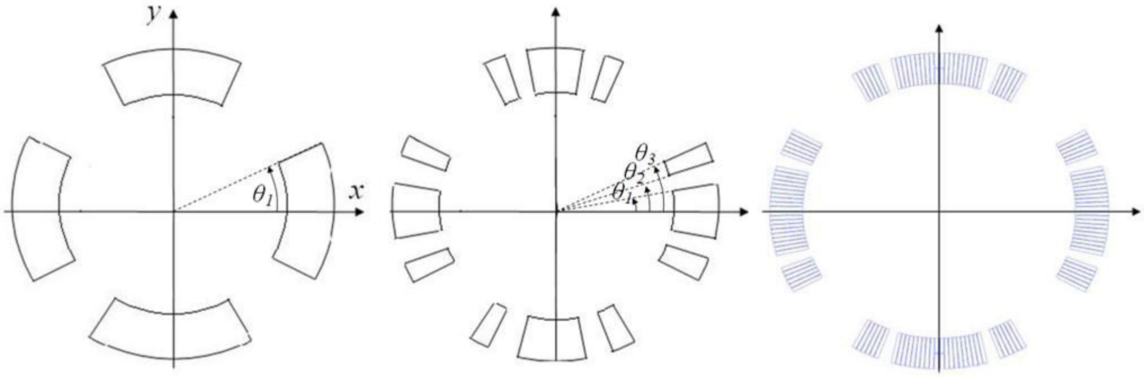

Figure 11 – Quadrupole made of one (left) or two (middle) pure sectors blocks and cross-section of the RHIC main quadrupole (right).

Any quadrupole with coils made of sectors carrying a constant current density j_0 can be modeled by a thick winding powered by a sum of sinusoidal current densities with different amplitudes and pulsations

$$j(\theta) = \sum_{n=1}^{\infty} j_n(\theta) \tag{65}$$

where

$$j_n(\theta) = j_0 \alpha_n \cos(n\theta) \tag{66}$$

where there is no constant term because for a quadrupole the average current density is null, and the sine terms are absent due to the coil symmetry. The coefficient α_n is given by

$$\alpha_n = \frac{1}{\pi} \int_0^{2\pi} \frac{j(\theta)}{j_0} \cos(n\theta)\, d\theta. \tag{67}$$

For instance, the α_n coefficient of a coil made by a single sector of angular dimension θ_1 (see Figure 11, left) reads

$$\alpha_n = \frac{2}{n\pi} \sin(n\theta_1) \left[1 + \cos(n\pi) - 2\cos\left(n\frac{\pi}{2}\right)\right], \tag{68}$$

and for a coil made of two sector delimited by the angles θ_1, θ_2 and θ_3 (see Figure 11, middle) it reads

$$\alpha_n = \frac{8}{n\pi} [\sin(n\theta_1) + \sin(n\theta_3) - \sin(n\theta_2)]. \tag{69}$$

For any coil with quadrupolar symmetry (as for instance the lay-outs shown in Figure 11), the coefficient α_n is different from zero only for n=2,6,10,14,..., *i.e.,* for allowed multipoles.

Let us now consider a quadrupole with coil made of sectors of inner radius R_1 and outer radius R_2 (see Figure 12). The analytical expression of the harmonic of rank n of the vector potential produce by the harmonic of current j_n at the point P of coordinates (r,θ) can be expressed by means of

$$A_{z,n}(r,\theta) = D_n(r) j_n(\theta). \tag{70}$$

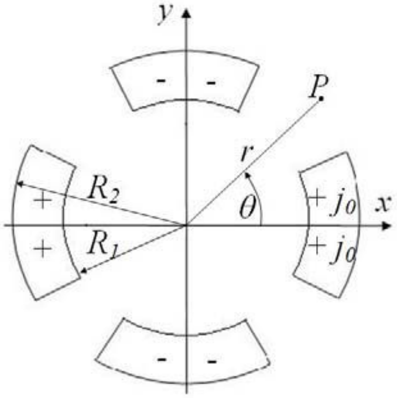

Figure 12 – Cross-section of a quadrupole with coils made of one pure sector.

One has to distinguish three zones where the vector potential has different expressions matching at the zones interfaces:

- **For *r* < *R*₁**

For n=2

$$D_2(r) = \frac{\mu_0}{4} r^2 \ln\left(\frac{R_2}{R_1}\right) \tag{71}$$

and for n>2

$$D_n(r) = -\frac{\mu_0}{2}\frac{r^n}{n(n-2)}\left(\frac{1}{{R_2}^{n-2}} - \frac{1}{{R_1}^{n-2}}\right). \tag{72}$$

- **For *R*₁ < *r* < *R*₂**

For n=2

$$D_2(r) = \frac{\mu_0}{4}\left(\frac{1}{4r^2}\left[r^4 - {R_1}^4\right] + r^2 ln\left(\frac{R_2}{r}\right)\right) \tag{73}$$

and for n>2

$$D_n(r) = \frac{\mu_0}{2n}\left(\frac{1}{n+2}\left[r^2 - \frac{{R_1}^{n+2}}{r^n}\right] + \frac{1}{n-2}\left[r^n - \frac{r^n}{{R_2}^{n-2}}\right]\right). \tag{74}$$

- **For *R*₂ < *r***

For any n

$$D_n(r) = \frac{\mu_0}{n(n+2)}\frac{1}{r^n}\left({R_2}^{n+2} - {R_1}^{n+2}\right). \tag{75}$$

The magnetic flux density created in each of the three zone is derived from $\vec{B} = \vec{\nabla} \times \vec{A}$

$$B_{n,r}(r,\theta) = \frac{1}{r}\frac{\partial A_{n,z}}{\partial \theta} \tag{76}$$

$$B_{\theta,r}(r,\theta) = \frac{\partial A_{n,z}}{\partial r}. \tag{77}$$

- **For *r* < *R₁***

For *n*=2

$$B_{2,r}(r,\theta) = -\frac{\mu_0 j_0 a_2}{2} r\ln\left(\frac{R_2}{R_1}\right)\sin{(2\theta)} \tag{78}$$

$$B_{2,\theta}(r,\theta) = -\frac{\mu_0 j_0 a_2}{2} r\ln\left(\frac{R_2}{R_1}\right)\cos{(2\theta)} \tag{79}$$

and for *n*>2

$$B_{n,r}(r,\theta) = \frac{\mu_0 j_0 a_n}{2}\frac{r^{n-1}}{(n-2)}\left(\frac{1}{{R_2}^{n-2}} - \frac{1}{{R_1}^{n-2}}\right)\sin(n\theta) \tag{80}$$

$$B_{n,\theta}(r,\theta) = \frac{\mu_0 j_0 a_n}{2}\frac{r^{n-1}}{(n-2)}\left(\frac{1}{{R_2}^{n-2}} - \frac{1}{{R_1}^{n-2}}\right)\cos(n\theta). \tag{81}$$

- **For *R₁* < r < *R₂***

For *n*=2

$$B_{2,r}(r,\theta) = -\frac{\mu_0 j_0 a_n}{2}\left[\frac{1}{4}\left(r - \frac{{R_1}^4}{r^3}\right) + rln\left(\frac{R_2}{r}\right)\right]\sin(2\theta) \tag{82}$$

$$B_{2,\theta}(r,\theta) = -\frac{\mu_0 j_0 a_n}{2}\left[\frac{1}{4}\left(\frac{{R_1}^4}{r^3} - r\right) + rln\left(\frac{R_2}{r}\right)\right]\cos(2\theta) \tag{83}$$

and for *n*>2

$$B_{n,r}(r,\theta) = -\frac{\mu_0 j_0 a_n}{2}\left[\frac{1}{n+2}\left(r - \frac{{R_1}^{n+2}}{r^{n+1}}\right) - \frac{1}{n-2}\left(\frac{r^{n-1}}{{R_1}^{n-2}} - r\right)\right]\sin(n\theta) \tag{84}$$

$$B_{n,\theta}(r,\theta) = -\frac{\mu_0 j_0 a_n}{2n}\left[\frac{1}{n+2}\left(2r + n\frac{{R_1}^{n+2}}{r^{n+1}}\right) - \frac{1}{n-2}\left(n\frac{r^{n-1}}{{R_1}^{n-2}} - 2r\right)\right]\cos(n\theta). \tag{85}$$

- **For *R₂* < r**

For any *n*

$$B_{n,r}(r,\theta) = -\frac{\mu_0 j_0 a_n}{2(n+2)}\frac{1}{r^{n+1}}\left[{R_2}^{n+2} - {R_1}^{n+2}\right]\sin(n\theta) \tag{86}$$

$$B_{n,\theta}(r,\theta)=\frac{\mu_0 j_0 a_n}{2(n+2)}\frac{1}{r^{n+1}}\left[{R_2}^{n+2}-{R_1}^{n+2}\right]\cos(n\theta). \tag{87}$$

II.3.3 Iron yoke

Accelerator magnets are usually surrounded by an iron yoke in order to shield both the magnet aperture from external magnetic perturbations and the area surrounding the magnet from the magnetic field produced by the coil. The iron also has the advantage to enhance the magnetic field within the magnet aperture. The iron yoke is also sometimes used to partly support electromagnetic forces acting on the coil. The magnetic field produced in the vacuum, within the coil and in the yoke by the coil + yoke, can be calculated in the basic case where all the media considered are linear. [37]. It is obtained solving the Poisson's and Laplace's equations

$$\Delta A_z+\mu_0 J_z=0 \qquad \text{within the winding} \tag{88}$$

$$\Delta A_z=0 \qquad \text{in the void and in the iron yoke,} \tag{89}$$

and using the boundary conditions at the interface between void and yoke.

Analytical calculation of the magnetic field is possible only for particular geometries of the yoke as for instance a circular tube surrounding the coil. Otherwise numerical computations are necessary. In the particular case where the outer radius of the tube extends to the infinite, the calculation of the magnetic field within the yoke aperture can be done using of the well-known "current image" method [81]. In this case, the magnetic field contribution of an iron yoke of inner radius R_{ir} and of relative magnetic permeability μ_r and surrounding a current line located in $\bar{z}_0=x_0+iy_0$ can be analytically calculated substituting the yoke by a virtual current line located in $\bar{z}_0'$ and carrying a current I' defined as

$$\bar{z}_0'=\frac{{R_{ir}}^2}{{\bar{z}_0}^*} \qquad \text{and} \qquad I'=\frac{\mu_r-1}{\mu_r+1}I. \tag{90}$$

Similarily, to analytically evaluate the induction enhancement due to the presence of an iron yoke of inner radius R_{ir} around a sector coil of inner and outer radii R_1 and R_2 within which flow a current density j, one can consider that the contribution of the yoke to the magnetic field is equivalent to that of a virtual sector coil of inner and outer radii R_1' and R_2', and powered with a current density j' (see Figure 13) defined as

$$R_1'=\frac{R_{ir}^2}{R_2} \qquad \text{and} \qquad R_2'=\frac{R_{ir}^2}{R_1} \tag{91}$$

and

$$j'=\frac{\mu_r-1}{\mu_r+1}\frac{(R_1R_2)^2}{R_{ir}^4}j. \tag{92}$$

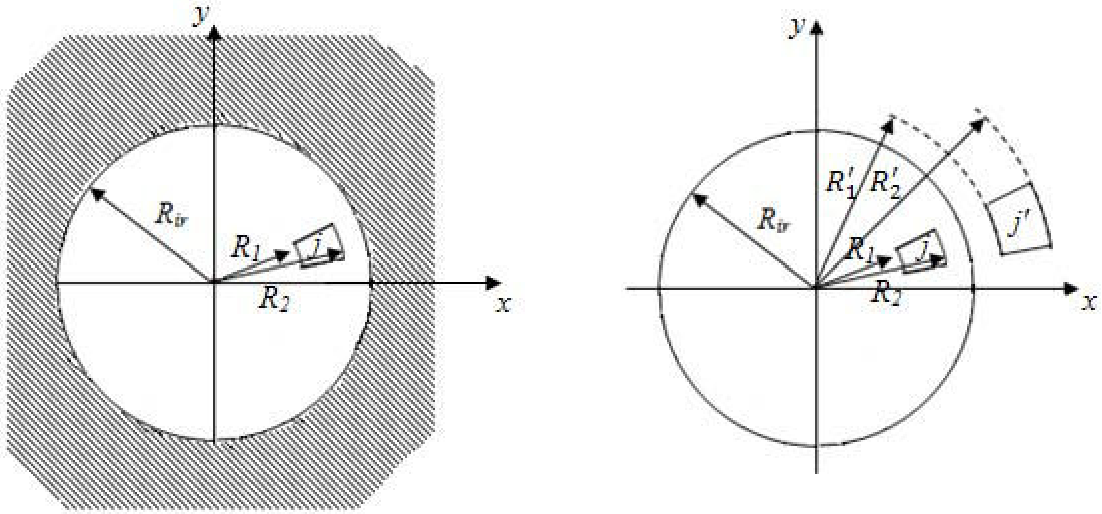

Figure 13 – Left: sector coil surrounded by an unsaturated iron yoke of uniform permeability μ_r. Right: model based on the current image method to calculate the contribution of the iron yoke to the magnetic field within the yoke inner radius R_{ir}.

Eqs. (91) and (92), derived from the "current image" method, will be used to estimate the enhancement of the stored energy in a quadrupole magnet (see Chapter III), and to calculate the yoke contribution to the short sample gradient in the coil optimization method set up in Chapter V.

As previously said, the presence of an iron yoke is that, at fix current, it enhances the field harmonic coefficients (see Section II.2.5) provided by the coil. For instance, let us consider a quadrupole made of pure sector coils of inner and outer radii R_1 and R_2 (see for instance Figure 12), and providing the harmonic coefficients A_n^{coil} and B_n^{coil}. The field harmonic enhancement due to the presence of an unsaturated iron yoke of inner radius R_{ir} can be estimated by means of [36]

$$\frac{A_n^{coil}+A_n^{iron}}{A_n^{coil}}=\frac{B_n^{coil}+B_n^{iron}}{B_n^{coil}}=1+\frac{\mu_r-1}{\mu_r+1}\left(\frac{R_1R_2}{{R_{ir}}^2}\right)^n, \tag{93}$$

where A_n^{iron} and B_n^{iron} are due to the iron yoke. One can see that the smaller is the yoke radius, the larger is the contribution of the yoke to the field harmonics. The relative contribution of the iron yoke to the harmonics can be, in theory, at max 100 % if R_1 and R_{ir} tend toward R_2 i.e. the coil is an infinitely thin sheet of current on which lays the iron yoke. For physical reasons $(R_1R_2)<R_{ir}^2$. Therefore, the relative field harmonic contribution due to the presence of the yoke decreases when n increases.

The iron starts to saturate at around 1.5 T. This limits the iron contribution to the magnetic field and it produces additional unwanted distortion of the magnetic field within the aperture. If the yoke has the same symmetry as the magnet, then only allowed multipoles are affected by the yoke saturation. For a quadrupole the thickness e of the iron needed to limit the fringe field outside the yoke can be estimated from [6]

$$e = \frac{G\,R_1^2}{2\,B_s}, \tag{94}$$

where R_1 is the coil inner radius, B_s the field density at which the yoke saturate (~1.5 T), and G is the field gradient within the aperture.

II.4 Superconducting materials

II.4.1 Superconductivity

Practical superconductors used in large magnets are characterized by their critical surface which depend on the current density, on the magnetic field and on the temperature. Any point belonging to the critical surface can be identified by the three parameters (T_c, B_c, J_c) where T_c is the critical temperature, B_c the upper critical magnetic field and J_c the critical current density. Below the critical surface the material is in the superconducting state featuring a null resistivity. For a given temperature and magnetic field, the superconducting/normal transition occurs when the transport current becomes larger than the current carrying capability allowed by the superconducting state. For instance, the critical current of a Nb-Ti material can be as large as 1500 Amm^{-2} at 10 T and 1.9 K.

Two types of superconductors, named type I, *e.g.,* mercury and tin, and type II, *e.g.,* niobium-titanium (Nb-Ti) and niobium-tin (Nb-Sn), have been identify. Superconductors of type I have a rather small critical field (usually <0.1 T) which make their use in high field magnets impractical. Superconductors of type II remain superconducting at much higher field (~15 T for Nb-Ti) and are therefore well suited for high field magnets. Type II superconductors are characterized by two critical magnetic fields B_{c1} and B_{c2}. Below B_{c1}, which is of the order of 0.1 T, the superconductor is in the Meissner phase, *i.e.,* magnetic flux lines cannot enter the superconductor save on a very small depth. In superconducting magnet, the magnetic field in the coil is usually much larger than B_{c1} and thus the magnetic flux lines penetrate the superconductor through quantified flux tubes (2.07×10^{-15} Wb) called **vortex**. Between B_{c1} and B_{c2} the superconductor is said to be in the mixed state and above B_{c2} it is in the normal state. The transport current carried by the superconductor displaces the vortex. This phenomenon, called **flux flow**, produces heat generation and limits the current carrying capability of the superconductor. The method used to prevent vortex displacements is called **flux pinning** and consists for the Nb-Ti into inserting impurities (grain boundary for the Nb_3Sn) in the superconductor crystal lattice. The fluxoid distribution among pining site depends on the applied magnetic field.

Two main types of superconductors have been developed for high field magnet applications: the Nb-Ti and the Nb_3Sn. Note that both Nb-Ti and Nb_3Sn superconductors belong to the Low Temperature Superconductor (LTS) family featuring a critical temperature at zero magnetic field of about 9 K for the Nb-Ti and 18 K for the Nb_3Sn. Superconductors of the High Temperature Superconductor (HTS) family feature a critical temperature much higher than for LTS (up to 150 K), but have not yet been used for accelerator magnets.

II.4.2 Nb-Ti and Nb_3Sn

The **Nb-Ti** has the advantage to be ductile and easily manufactured. It is well suitable for magnet applications with induction ranging from 2 to 10 T. The **Nb_3Sn** provides better superconducting performances than the Nb-Ti, *i.e.,* higher j_c, B_c and T_c, and allows to operate at fields in excess of 12 T [61]. However, once reacted, the manufacturing of the Nb_3Sn is difficult because of the brittleness of the material and the superconducting properties are strain sensitive [41] [42]. In addition to that, the Nb_3Sn requires a long heat treatment at high temperature and gas inert ovens.

The parameterizations of the critical surfaces of Nb-Ti and Nb_3Sn materials have been obtained by fitting experimental measurements.

- ***<u>Nb-Ti</u>***

The critical current density j_c defined in Eq. (95) and given at a magnetic field B and a temperature T is related to metallurgic and thermal processes aimed at creating flux pinning. Its empirical fit worked out in [23] L. Bottura, et al., "*Field errors decay and "snap back" in LHC model dipoles*", IEEE Trans. On App. Supercond., Vol. 7, No. 2, pp 602-605, 1997.

[24] is

$$j_C(B,T) = j_{Cref}\frac{D_{Nb-Ti}}{B}\left[\frac{B}{B_{C2}(T)}\right]^{\beta_1}\left[1-\frac{B}{B_{C2}(T)}\right]^{\beta_2}\left[1-\left(\frac{T}{T_{C0}}\right)^{1.7}\right]^{\beta_3}. \tag{95}$$

Typical fitting values for LHC strands are j_{cref} = 1500 Amm^{-2}, $D_{Nb-Ti} = 31.4$ T, $\beta_1 = 0.63$, $\beta_2 = 1.0$ and $\beta_3 = 2.3$. B_{C2} is the critical magnetic field at the temperature T and at zero current. At a given temperature B_{C2} accounts for the nucleation of the superconducting phase, *i.e.,* creation of Cooper pairs. It is defined as

$$B_{C2}(T) = B_{C20}\left[1-\left(\frac{T}{T_{C0}}\right)^{1.7}\right], \tag{96}$$

where B_{C20} and T_{C0} are the critical magnetic field at zero temperature (about 14.5 T), and the critical temperature at zero field (about 9.2 K).

- ***Nb$_3$Sn***

In addition to be dependent on the the magnetic field *B* and the temperature *T*, the critical current density j_c in Nb$_3$Sn material depends also on the strain ε. According to [85] (quoted by Devred in [36]) j_c can be fitted by

$$j_c(B,T,\varepsilon) = \frac{D(\varepsilon)}{\sqrt{B}}\left[1-\frac{B}{B_{C2}(T,\varepsilon)}\right]^2\left[1-\left(\frac{T}{T_{C0}(\varepsilon)}\right)^2\right]^2. \tag{97}$$

As for the Nb-Ti, the critical field density B_{C2} [Eq. (98)] accounts for the nucleation of the superconducting phase. It depends on *T* and *ε* and can be estimated by

$$\frac{B_{C2}(T,\varepsilon)}{B_{C20}(\varepsilon)} = \left[1-\left(\frac{T}{T_{C0}(\varepsilon)}\right)^2\right]\left\{1-0.31\left(\frac{T}{T_{C0}(\varepsilon)}\right)^2\left[1-1.77ln\left(\frac{T}{T_{C0}(\varepsilon)}\right)\right]\right\}, \tag{98}$$

where B_{C20} is the critical magnetic field at zero temperature and at the strain *ε*. It can be estimated by

$$B_{C20}(\varepsilon) = B_{C20m}(1-\beta|\varepsilon|^{1.7}), \tag{99}$$

where B_{C20m} is the critical magnetic field at zero temperature, and zero strain. The parameter *β* [dimensionless] has to be taken equal to 900 for a compressive strain, and to 1250 for a tensile strain.

The critical temperature T_{C0} at zero magnetic field and at the strain *ε* can be estimated by

$$T_{C0}(\varepsilon) = T_{C0m}(1-\beta|\varepsilon|^{1.7})^{1/3}, \tag{100}$$

where T_{C0m} is the critical temperature at zero magnetic field, and zero strain. The parameter *D* in the relation (97) is given by

$$D(\varepsilon) = D_{Nb_3Sn}(1-\beta|\varepsilon|^{1.7})^{1/2}, \tag{101}$$

where the fitting parameter D_{Nb_3Sn} depends on the chosen wire (it is not an intrinsic property). It is usually of the order of 12000 $AT^{1/2}mm^{-2}$ for a very conservative j_c value at 4.2 K and 12 T of 750 Amm^{-2}. In recent years, j_c values in excess of 2500 A/mm have been routinely achieved (D_{Nb_3Sn}= 40000).

Expressions (95) and (97) have been used to calculate the dependence of the temperature margin on the nominal current and the nominal peak field in the coil (see Section II.5).

More practical fit functions giving the critical current versus the applied magnetic field at fixed temperature have been worked out in [71]. They propose a linear fit for the Nb-Ti and for applied magnetic field B larger than 5 T at 1.9 K, and larger than 2 T at 4.2 K.

$$j_c = c(B^*_{c2}-B), \tag{102}$$

where B_{c2}^* it the critical field at zero current. B_{c2}^* is of ~10 T at 4.2 K and ~13 T at 1.9 K, whereas the slope c ~ 6×10^8 [AT^{-1}m^{-2}] is independent of the temperature.

Still in [71], it has been proposed a new function to fit the critical current j_c of Nb$_3$Sn superconductor as a function of the magnetic field B

$$j_c = c\left(\frac{b}{B} - 1\right), \tag{103}$$

where typical values for a wire having 3000 [Amm^{-2}] at 4.2 K and 12 T are c = 4.0×10^9 [Tm^{2}A^{-1}] and b = 21 T (at 4.2 K) or b = 23 T (at 1.9 K).

II.4.3 Superconducting cables

The cables usually used in superconducting cosθ-type accelerator magnets are called **Rutherford-type cables**. They are made from 20-40 strands of diameter around 1 mm, twisted together and shaped into a flat cable of two layers. In order to well fit the sector coil shape of cosθ-type magnets when being stacked, cables are slightly keystoned, *i.e.*, the cable is actually not rectangular but trapezoidal. Strands forming the cable consist in superconducting filaments of diameter typically of the order of tens of micro-meter embedded in a normal metal matrix, usually high purity copper (see Figure 14). Small sizes of the filaments are required to get rid of instabilities in the superconductor (flux jump) which would limit the superconducting performances of the cable [100]. To estimate the critical diameter of superconducting filament one commonly refers to the so-called adiabatic stability criterion and dynamic stability criterion [38]. The normal matrix plays several key roles. It acts as a stabilizer against flux jump, it provides mechanical stability, and it is used to take over the current in case of quench in order to protect the superconducting filaments from deleterious damages [100]. To prevent generation of large currents induced in the filaments and in the strands by a time varying magnetic field which can degrade the superconductor performances, filaments within a wire and wires within the cable are twisted together.

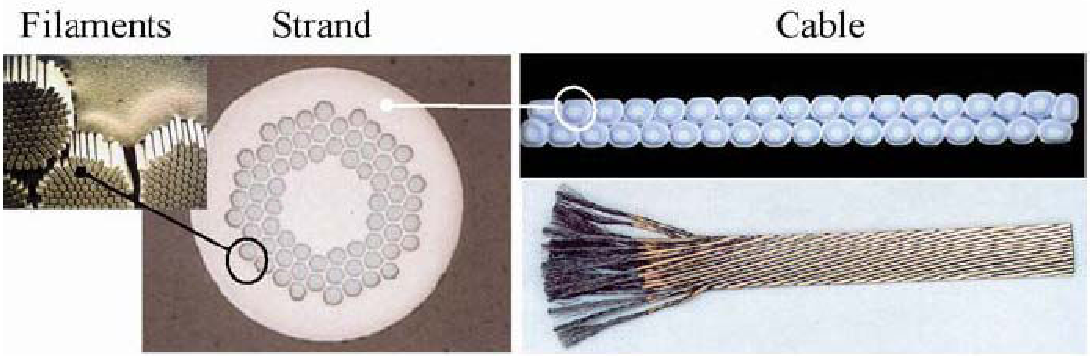

Figure 14 - Left: LHC superconducting strand made of around 8000 NbTi filaments embedded in a copper matrix forming the strand – center. Right: Rutherford cable: cross section (top); (bottom) conductor windings [9].

The insulation of Nb-Ti cables is usually realized by means of two layers of polyimide tapes overlapping by 50 % and wrapped around the cable, and surrounded by another polyimide tape [63] (see Figure 15).

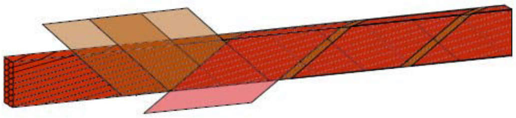

Figure 15 – Insulation scheme of the Nb-Ti cable of the LHC [30].

The important parameter for a magnet designer is the overall current density j carried by the insulated cable. It is defined as

$$j = kj_{sc}, \tag{104}$$

where j_{sc} is the effective current density flowing within the superconducting filaments and k [dimensionless] a dilution factor taking into account the cable void, the copper and the insulation of the cable. The parameter k is defined as [71]

$$k = \frac{S_{strand}}{S_{cable}} \frac{1}{1 + \nu_{cu-sc}}, \tag{105}$$

with S_{strand} and S_{cable}, the cross-sectional areas of the strands in the conductor and of the insulated conductor respectively. The parameter υ_{cu-sc} is the copper to superconductor ratio of a strand with typical values in between 1 and 2. The dilution factor k, also called filling factor, is usually in the range [0.2;0.35]. For instance, the cable of the main quadrupoles of the LHC has a filling factor of 0.254 [63].

II.5 Current and temperature margin

In operational conditions superconducting magnets are powered with a current lower than their short sample current in order to prevent a quench of the magnet in case of conductor motion [35] or when energy due to beam losses is deposited onto the superconducting coil [99]. The relative difference between the operational current I_{op} and the short sample current I_{ss} is called current margin Eq. (106) (see Figure 16). Similarly, we define the operational peak field in the coil B_{op} and the short sample field in the coil B_{ss}. The current margin is defined as:

$$m = \frac{I_{ss} - I_{op}}{I_{ss}}, \tag{106}$$

and is expressed in percentage. One has to note that we could also define the magnetic field density margin but it is out of interest since it would be of the same value than the current margin because of the linearity of the load line, yoke saturation excluded.

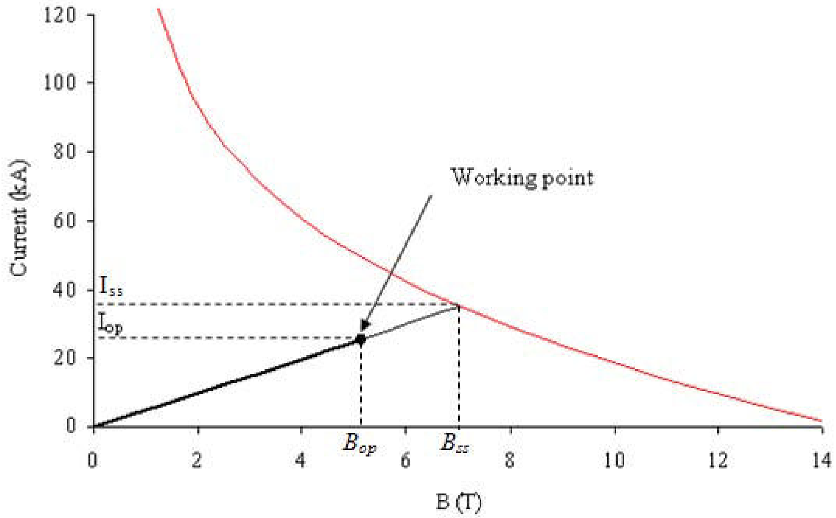

Figure 16 – Arbitrary load line (black) and critical surface (red) in the current/magnetic field plan. The critical surface corresponds to the inner layer cable of the LHC main dipole at 1.9 K.

What is of importance is not the current margin itself since we do not expect to power the magnet beyond its nominal current but the associated temperature margin $T_m(I_{op},B_{op})$ (see Figure 17). Indeed, heat deposited or dissipated into the superconducting coil increases locally the temperature and brings the working point close to the critical surface, and possibly cross it provoking the quench of the magnet. The temperature margin is defined, for given operational current I_{op} and magnetic peak field density in the coil B_{op}, as the increase of temperature which would lead the magnet to cross the critical surface.

$$T_m\left(I_{op},B_{op}\right) = T_c\left(I_{op},B_{op}\right) - T_{op}. \tag{107}$$

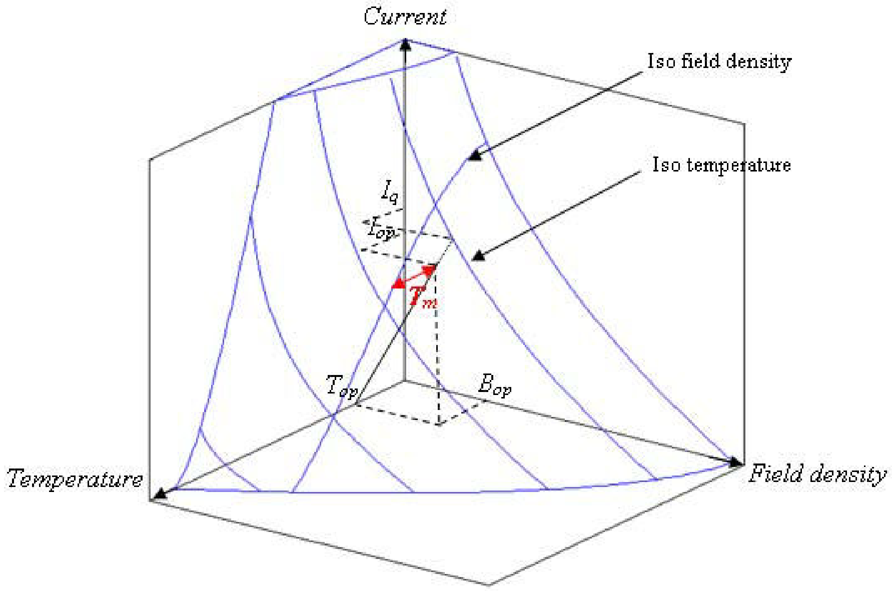

Figure 17 – Critical surface of the Nb-Ti LHC main dipole cable and arbitrary load line. The temperature margin is denoted T_m. The load line lies in the current/field density plane.

The dependence of the temperature margin T_m on I_{op} and B_{op} cannot be expressed through a simple equation. Instead, we propose to numerically compute the temperature margin associated to a current and an applied magnetic field both taken with 20 % margin with respect to the critical surface. The 20% margin is out of physical meaning but is usually considered as a safe value for accelerator magnet working either at 1.9 K or 4.2 K. For instance, the LHC main dipole and main quadrupole are designed to work with 14 % and 20 % margin on the current respectively [63]. Main dipoles and quadrupoles of the HERA particles accelerator work with 23 % and 28 % margin respectively [66]. Results obtained for Nb-Ti and Nb_3Sn materials at 1.9 K and 4.2 K, through numerical analysis of Eq. (95) and (97) respectively, are shown in Figure 18 where temperature margins have been plotted versus the operational field B_{op}. For the Nb-Ti we assumed a critical current density in the superconductor of 3000 A/mm^2 at 4.2K and 5T, or at 1.9 K and 8 T. For the Nb_3Sn we assumed a very conservative value of 750 A/mm2 at 4.2K and at 12 T , or at 1.9 K and 13.5 T. In addition, for the Nb_3Sn a compressive strain of -0.25 % has been considered.

From Figure 18 and assuming 20 % margin on the current one observes that:

- T_m ~ 1.1 K for the Nb-Ti at 4.2 K.
- T_m ~ 2.0 K for the Nb-Ti at 1.9 K.
- T_m ~ 3.5 K for the Nb_3Sn at 4.2 K.
- T_m ~ 4.7 K for the Nb_3Sn at 1.9 K.

In Figure 18 one also notices that the temperature margin depends on the operational magnetic field. The temperature margin increases with the magnetic field for the Nb-Ti, while it decreases for the Nb_3Sn. The maximal variation in the temperature margin calculated for the range of magnetic field of the Figure 18 is:

- $\Delta T_m = +0.18$ K (+17 %) for Nb-Ti at 4.2 K.
- $\Delta T_m = +0.29$ K (+15 %) for Nb-Ti at 1.9 K.
- $\Delta T_m = -0.46$ K (-12 %) for Nb_3Sn at 4.2 K.
- $\Delta T_m = -0.82$ K (-16 %) for Nb_3Sn at 1.9 K.

One has to notice that we cannot directly compare the T_m at 1.9 K with the T_m at 4.2 K because the characteristics (specific heat, thermal conductivity) of the materials which composed the cable (Nb-Ti, copper) and of the helium are strongly dependant on the temperature and thus affect the relevant energy margin parameter [52]. However, for a given temperature in the superconductor one can see from Figure 18 that magnets featuring a low current and a high field in the coil will get a slightly larger temperature margin than magnets working at high current and low field.

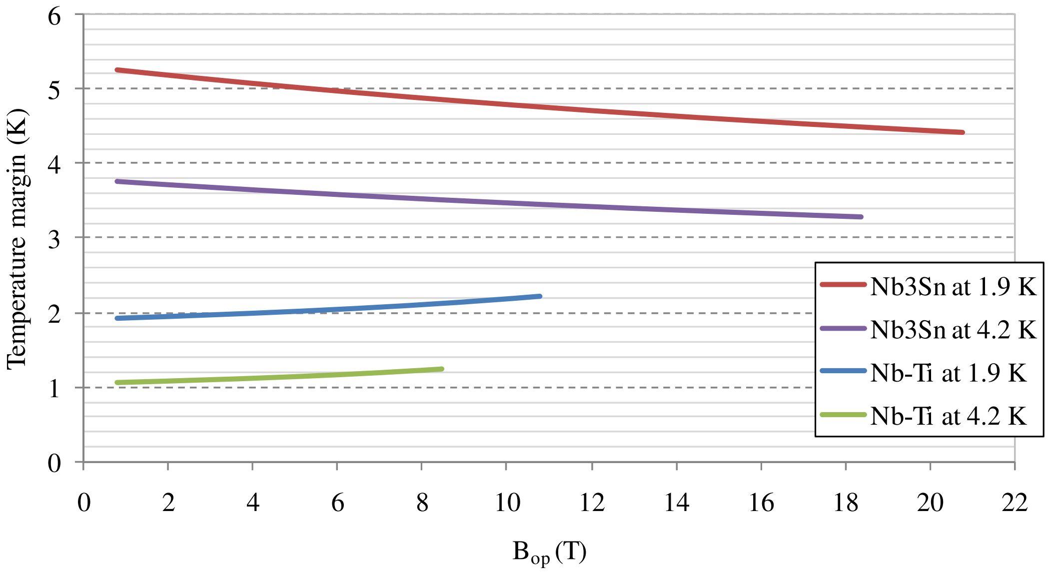

Figure 18 - Dependence of the temperature margin with the applied magnetic field B_{op} in Nb-Ti and Nb_3Sn materials. The applied magnetic field is taken with 20% margin on the short sample field.

II.6 Mechanical structure of Nb-Ti quadrupole magnets

Accelerator magnets are made of an assembly of several components. The four superconducting coils (1) forming the quadrupole winding are held together by means of laminated stainless-steel collars (2) surrounded by laminated iron yokes (3), and encircled by a shrinking cylinder (4) (see Figure 19). The assembly of these four elements is called a **cold-mass,** *i.e.,* the part of the magnet that has the same temperature than the coil. Note that sometime, like in the Tevatron magnets, the iron yoke is not part of the cold mass [32].

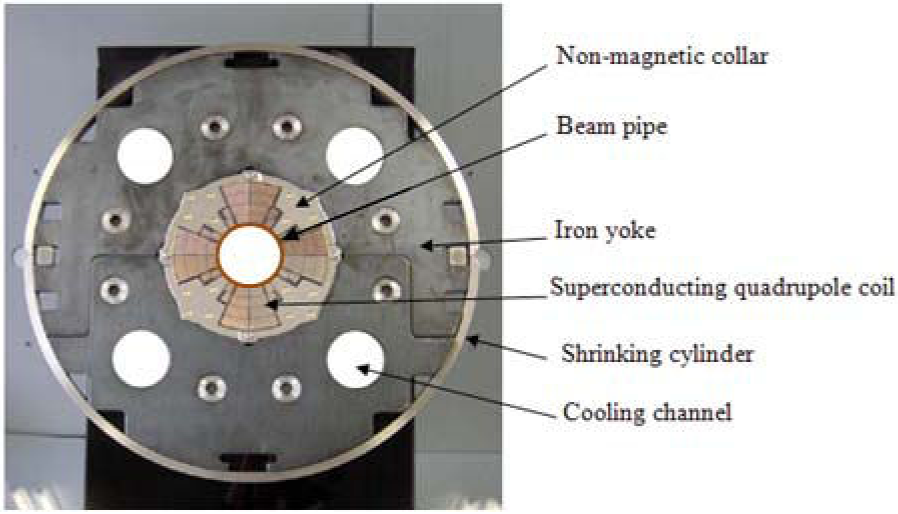

Figure 19 – Cross-sectional view of the cold mass of the LHC MQXA quadrupole [63].

Collars, which are usually made of stainless steel laminations, are used as mechanical support against the large electromagnetic forces taking place in the coils which tend to push the coils outward. It also provides the azimuthal pre-stress in the coil necessary to prevent the coil poles to be detached from the collar poles during cool down or when energizing the magnet. To summarize, the role of the collar is to provide a rigid structure to the coil so as to fix the coil dimensions. A close control of the coil dimensions is mandatory for a good field quality.

The iron yoke, in addition to what has been said in Section II.3.3, can also sometimes have a structural function in case where the collar is not or only partly self-supported: it contributes to increase the rigidity of the coil support structure and limit radial displacement. To achieve this role, it has to be in contact with the collars. For instance, the LHC MQXA [2] quadrupole shown in Figure 19 uses partly the iron yoke as a retaining structure, while the mechanical support of the LHC MQ quadrupole coil is entirely provided by collars [62], and in this case there is a gap between collars and the yoke.

The shrinking cylinder is usually composed of two half shells of stainless-steel welded around the yoke with high tension. It gives the rigidity of the cold mass. It is also used as helium container. The helium volume is separated from the beam vacuum by means of the beam pipe passing through the magnet aperture.

The cold-mass is inserted into a cryostat consisting of a vacuum vessel and a support structure. The supercritical helium at 4.2 K (Tevatron, HERA and RHIC), or the pressurized superfluid helium at 1.9 K (LHC) [63], can freely flow in the coil and in between the yoke and collar laminations. The heat flux generated in the cold-mass (coil movement, beam losses, …) is removed by means of cooling channels of two-phases helium passing through the iron yoke and transporting helium at almost constant temperature.

II.7 Upgrade of the LHC Interaction regions

On each side of the four experiments of the LHC is located a set of four quadrupoles, called inner triplet quadrupoles. From the optical point of view, one has a sequence of three magnets with opposite gradient (F-D-F cell). The central one is split into two: this is why we have four magnets. Their role is to squeeze and focus the beam at the interaction point of each experiment resulting in an enhancement of the **luminosity** of the collision. The luminosity, denoted by L [$\mathrm{cm}^{-2}\mathrm{s}^{-1}$] and depending only on beam parameters (and not on the physics of the interaction), is defined as the probability of number of events in a collision [63]

$$L = \frac{f_{rev}\gamma}{4\pi\varepsilon_n\beta^*}(N_b)^2 n_b F, \tag{108}$$

where N_b is the number of particles per bunch, n_b the number of bunches per beam, f_{rev} the revolution frequency, γ the relativistic gamma factor, ε_n the normalized transverse beam emittance, and F [dimensionless] a geometric luminosity reduction factor owing to the crossing angle at the collision point. The parameter β^* [cm] is the beta function (introduced in section II.2.6 as β_x and β_y) at the collision point. It is an image of the transverse size of the beam at the collision point and its value is related to the inner triplet quadrupoles layout (also called low-β insertion). The actual inner triplet used in the LHC is made of two types of 70 mm aperture diameter quadrupoles denoted by MQXA [2] and MQXB [21] based on the Nb-Ti technology and built in the framework of a US-Japan collaboration. Both provide a nominal gradient of 215 Tm^{-1}. This leads to a minimal β^* value of 55 cm resulting to a maximal luminosity value at the interaction points of 10^{34} cm^{-2}s^{-1} [63]. A schematic view of the layout of the actual inner triplet is shown in Figure 20.

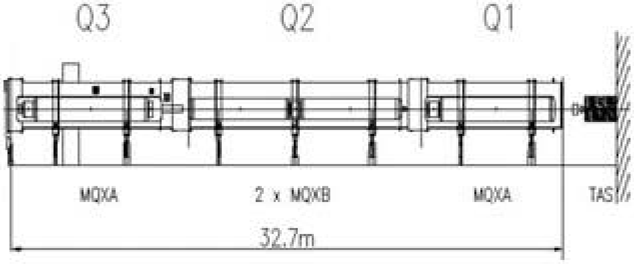

Figure 20 – Schematic view of the actual inner triplet quadrupole of the LHC [67].

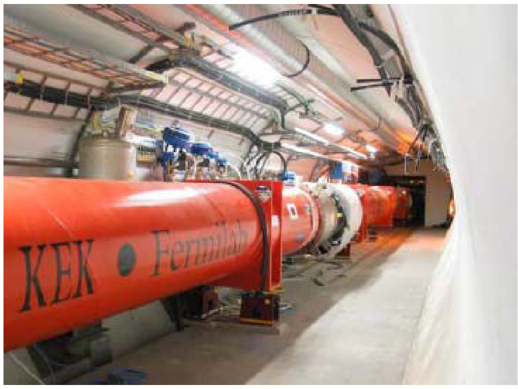

Figure 21 – inner triplet quadrupoles in the LHC interaction region [72].

The maximum of luminosity is achieved in the ATLAS and CMS experiments and results in high radiation dose absorbed by the inner triplet quadrupoles. According to the estimate, this limits their life time to around 7 years [83]. The replacement of the quadrupoles will be the opportunity to increase the luminosity of the LHC. The project, called LHC Phase-I upgrade, aims at increasing the luminosity by a factor 2-3 with respect to the nominal luminosity of 10^{34} cm^{-2}s^{-1}. Part of this increase is obtained through a reduction of β^* from 55 to 25-30 cm [67], the other part being obtained increasing the beam current. Several studies on a new inner triplet aiming at reducing β^* while maximizing the use of the existing infrastructure have been done in [14] [19] [20] [60] [68]. The retained solution is a ~ 45.2 m long triplet (see Figure 22) made of four 120 mm aperture quadrupoles based on the Nb-Ti cable of the LHC main dipole cable [63]. In this thesis we will present a design for the quadrupole coil.

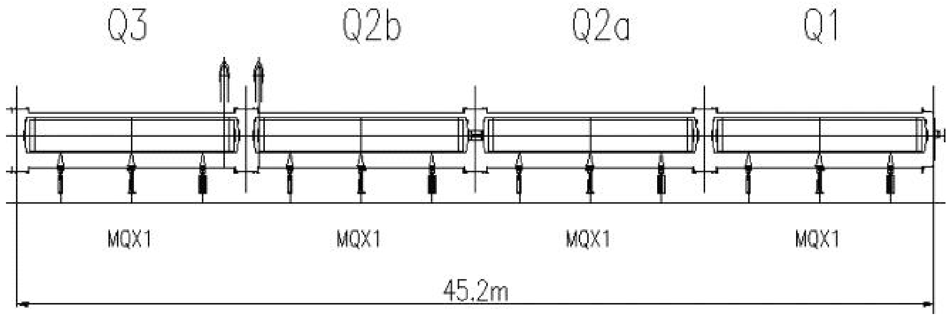

Figure 22 – Schematic view of the new inner triplet for the upgrade of the LHC interaction region [67].

II.8 Issues of the thesis

In this section we summarize the main problems that has to be solved to provide better design of superconducting quadrupole magnets.

Particle physics impose stringent constraint on the quality of the magnetic field produced by the different magnets constituting an accelerator. The quality of the magnetic field is usually characterized by spatial harmonics of the magnetic field expressed in unit of 10^{-4} times the main field at a given “reference radius”.

Conception and characterization of quadrupole magnets has to satisfy specifications on the main field (dipolar, quadrupolar,…) and on the field harmonic content. It is an inverse problem in magneto-static (aiming at finding current distributions generating a given magnetic field or magnetic field gradient in a given domain), which have an infinite number of solutions. This “infinity” can be reduced taking into account supplementary constraints such as materials properties (here superconductor and ferromagnetic), the amount of conductor available, the support structure to contain electromagnetic forces, the cost, … Conductor arrangements are the main elements one has to consider to satisfy the specifications on the magnetic field. An important part of this thesis will focus on the research of conductor arrangements aiming at designing a new quadrupole for the upgrade of the LHC interaction regions.

Moreover, large accelerators such like the LHC need series production of several hundred of “identical” magnets differing only by mechanical tolerances in the coil components or in the magnet assembly. Data accumulated by all the different laboratories on magnetic measurements performed on these magnet series allow statistical analysis of the field harmonics. The issue is to link the spread of the measurements with the precision on conductor positioning. This enables setting up specification on future realizations. This is also inverse problem of the magneto-static where the combination of statistical methods and of the harmonics analysis can lead to an improvement of the performances in future magnets. In this thesis, we address this issue through existing tools set up in the past and by means of analytical calculations aimed at linking the spread in the field error measured in a magnet series with the spread in the position of the conductor within the coil.

Superconducting magnets (dipoles, quadrupoles,…) are essential in the functioning of a particle accelerator and have to be electrically supplied in a reliable way. The magnetic energy at maximal magnetic field in each magnet has to be known to dimension the power supply and the coil protection system. In this thesis, a simple formula enabling an estimate of the magnetic energy as a function of the main parameters of the coil (coil dimensions, current density) will bring to light simple “scaling laws” giving the energy.

At last, it appears useful to improve the knowledge on quadrupole magnets and on their modes of conception using as much as possible analytical methods, which enables outlining the most important geometrical and electrical parameters.

III. Analytic estimates of the magnetic energy in superconducting quadrupoles

The magnetic energy stored in a superconducting accelerator magnet is an important parameter for the quench calculations and for designing the quench protection system [27] [81] [100]. However, an analytical calculation is rather difficult due to the complicated geometry of the coil and the evaluation is usually done with numerical codes [73] [97]. During the conceptual design phase it can be useful to have simple approximated expressions of the magnetic energy as a function of the main features of the quadrupole lay-out (magnet aperture, coil width, grading, iron yoke dimensions). Here we explore the possibility of giving such approximated formula, and their validity limits.

After recalling the magnetic energy definition, we derive an equation for an ironless quadrupole with uniform current density made of sector coils (Section III.2). A comparison of numerical computations and analytical estimates of the magnetic energy in real quadrupoles is made in section III.3. The formula is then extended to include the case of graded coils, *i.e.,* coils with non-uniform current density (Section III.5), and the impact of an unsaturated ferromagnetic iron around the coils (Section III.6). We also investigate the iron saturation effect through a numerical analysis. The study of 31 realistic quadrupole cross-sections shows that this approach enables an estimate of the magnetic energy of a quadrupole coil within 10% accuracy.

III.1 Magnetic energy definition

In the absence of non-linear magnetic material, the magnetic energy U_t produced by any winding can be obtained by integrating the scalar product between the magnetic induction $\vec{B} = \mu\vec{H}$ and the magnetic field $\vec{H}$ all over the space Ω_∞

$$U_t = \frac{1}{2}\iiint\limits_{\Omega_\infty} \vec{B}.\vec{H}\, d\Omega. \tag{109}$$

Substituting $\vec{H}$ in Eq. (109) by $\vec{B}/\mu$ gives

$$U_t = \frac{1}{2}\iiint\limits_{\Omega_\infty} \frac{\left|\vec{B}\right|^2}{\mu}\, d\Omega. \tag{110}$$

An equivalent approach makes use of the potential vector $\vec{A}$ defined as $\vec{B} = \nabla \times \vec{A}$

$$U_t = \frac{1}{2}\iiint\limits_{\Omega_\infty} \vec{A}.\vec{J}\, d\Omega = \frac{1}{2}\iiint\limits_{\Omega} \vec{A}.\vec{J}\, d\Omega. \tag{111}$$

Expression (111) is easier to implement since the integration is carried out over the finite window domain *Ω* where the current density is non-zero. The gauge invariance of the vector potential does not alter the validity of the relation (111). Throughout the section, we will use the I.S., thus expressing the current density *j* in [Am^{-2}], the distances in [m], and the energy in [J]. In high energy accelerator magnets, the transverse dimensions are usually small with respect to the axial one and therefore we can consider the magnet as infinitely long in the *z* direction. Neglecting the coil ends, one has that (i) the current density and the vector potential are parallel to the *z* axis, (ii) the magnetic field has components only in the transverse plane (*x*,*y*), and (iii) the magnetic energy per meter along *z* is given by:

$$U = \frac{1}{2}\iint_S A_z(x,y) j_z(x,y)\,dx\,dy\,, \tag{112}$$

where *S* is the cross-sectional area of the winding. Given the symmetry of the magnet, it is convenient to use in the transverse plane polar coordinates (*r*,*θ*) instead of the Cartesian ones *(x,y)*.

III.2 Ironless and non graded quadrupole

Let us now consider an infinitely long ironless quadrupole made of one layer of sector coil of inner and outer radius R_1 and R_2, respectively (see for instance Figure 23). The current density *j* flowing in the winding is assumed to be uniform.

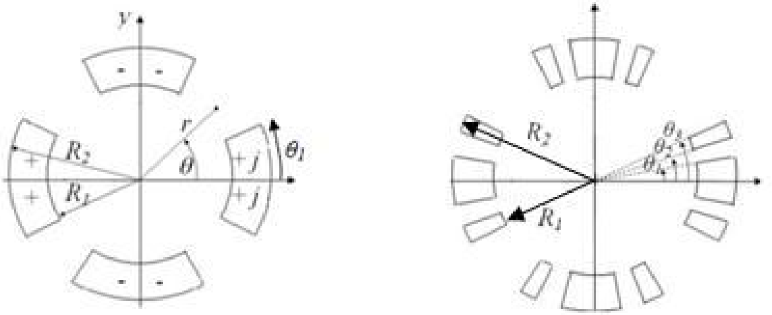

Figure 23 – Quadrupole made of one (left) or two (right) single sector coils.

As it has been shown in section II.3.2, the current density *j* flowing in the coils can be expanded in Fourier series

$$j(\theta) = \sum_{n=1}^{\infty} j_n(\theta), \tag{113}$$

where

$$j_n(\theta) = j\alpha_n \cos(n\theta), \tag{114}$$

and where the coefficient α_n is the harmonic coefficient of the Fourier series of *j*. Expression of α_n for a quadrupole with coils made of either one or two sectors coil are given in Eqs. (68) and (69), respectively. We recall here their expressions. For a quadrupole with coils made of a single sector of angle θ_1 as shown in Figure 23 (left) one has

$$\alpha_n = \frac{2}{n\pi}\sin(n\theta_1)\left[1+\cos(n\pi)-2\cos\left(n\frac{\pi}{2}\right)\right], \tag{115}$$

and for a quadrupole with coils made of two sectors delimited by the angles θ_1, θ_2 and θ_3 as shown in Figure 23 (right), α_n reads

$$\alpha_n = \frac{8}{n\pi}[\sin(n\theta_1)+\sin(n\theta_3)-\sin(n\theta_2)]. \tag{116}$$

The vector $A_z(r,\theta)$ produced by j at the position (r,θ) in the winding can also be expanded in Fourier series (see section II.3.2)

$$A_z(r,\theta) = \sum_{n=1}^{\infty} A_{z,n}(r,\theta), \tag{117}$$

where $A_{z,n}(r,\theta)$ is the vector potential given by a pure current harmonic of rank n inside the winding

$$A_{z,n}(r,\theta) = D_n(r)j_n(\theta). \tag{118}$$

The function D_n(r) is given by Eq. (73) for $n = 2$, and by Eq. (74) for $n > 2$.

To calculate the magnetic stored energy in a quadrupole made of pure sector coil one has to substitute expressions of the current (113) and of the vector potential (117) in Eq. (112). Since the harmonic functions are orthogonal, one has that

$$U = \frac{1}{2}\int_0^{2\pi}\int_{R_1}^{R_2}\sum_l A_{z,l}\sum_m j_m ds = \frac{\pi}{2}j_0^2\sum_n \alpha_n^2\int_{R_1}^{R_2} D_n(r)rdr \tag{119}$$

and therefore,

$$U = \sum_n U_n \equiv \frac{\pi}{2}j_0^2\sum_n \alpha_n^2\int_{R_1}^{R_2} D_n(r)rdr. \tag{120}$$

Substituting D_n by expression (73) for $n = 2$, and by expression (74) for $n > 2$ in (120), carrying out the integration and introducing the coil width $w=R_2-R_1$, one obtains an explicit expression for the magnetic energy coefficients

$$U_n = \frac{\pi\mu_0 j_0^2\alpha_n^2}{4n}R_1^4 f_n\left(\frac{w}{R_1}\right). \tag{121}$$

For $n = 2$ and $t = w/R_1$, the function f reads

$$f_2(t) = \frac{1}{8}[(1+t)^4 - 1] - \frac{1}{2}\ln(1+t) \tag{122}$$

and for n>2 one has

$$f_n(t) = \frac{1}{(n+2)(n-2)}\left[\frac{2}{(1+t)^{n-2}} - (1+t)^4 - 1 + \frac{n}{2}((1+t)^4 - 1)\right]. \tag{123}$$

The magnetic energy associated to the first harmonic of current is U_2:

$$U_2 = \frac{\pi\mu_0 j_0^2 \alpha_2^2}{8} R_1^4 f_2\left(\frac{w}{R_1}\right). \tag{124}$$

We now estimate the quantity of the energy carried by U_2 with respect to the total energy U as a function of w/R_1. In Figure 24 we study the function U_2/U for the [0-30º] sector coil (see Figure 23, left) which enables a cancellation of the first non-zero 12th pole and for four cases enabling a cancellation of both the 12th pole and the 20th pole, made of two blocks separated by a copper wedge (see Figure 23, right), and limited by the angles [0-12º, 18-30º], [0-18º, 22-32º], [0-24º, 30-36º] and [0-26º, 36-44º]. For w/R_1 larger than 0.2 (as in most superconducting magnets) the first harmonic U_2 accounts for 98%-99% of the total energy.

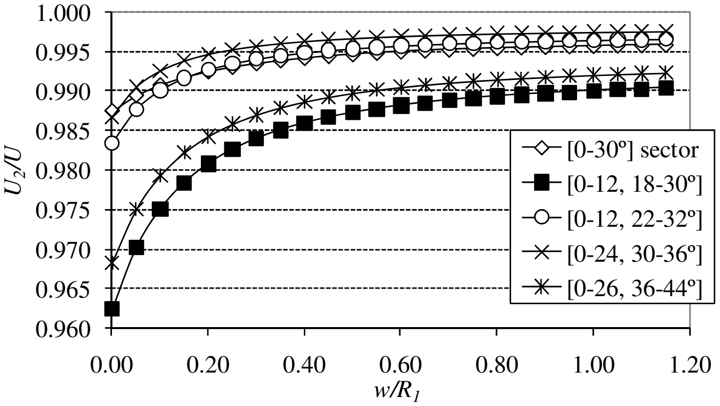

Figure 24 - Ratio between the magnetic energy produced by the main harmonic (n = 2) and the total energy versus coil width w over aperture radius R_1 for five different sector coils.

We can now link the gradient with the magnetic energy produced by the main harmonic of current given by (15). The field gradient of a sector coil is [71]:

$$G = \frac{\mu_0 j_0 \alpha_2}{2}\ln\left(1 + \frac{w}{R_1}\right) \tag{125}$$

and therefore the magnetic energy at a given w/R_1 ratio is proportional to the square of the gradient and the fourth power of the aperture radius:

$$U_2 = \frac{R_1^4 \pi G^2}{2\mu_0} h\left(\frac{w}{R_1}\right) \tag{126}$$

where the geometric function h, depending on the ratio t of coil width to aperture radius, is

$$h(t) = \frac{f_2(t)}{[\ln(1+t)]^2}. \tag{127}$$

The function *h* versus *t* is plotted Fig. 4. It is worth to mention that *h* is greater than 1.

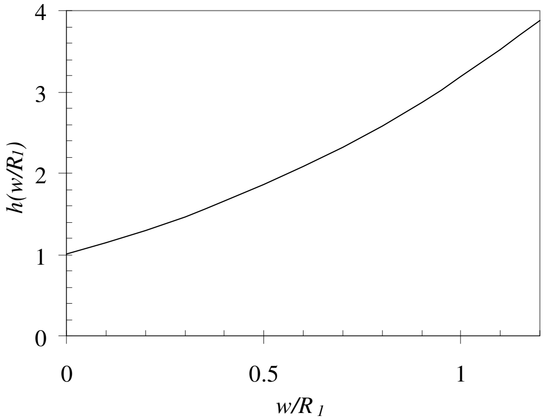

Function h defined in Eq. (127) versus *w/R₁*.

III.3 Comparison of analytical versus numerical estimate for realistic lay-outs

We now compare the numerical computation of the magnetic energy done using the numerical code [73] to the analytical estimate (124) for several realistic coil lay-outs; assuming that there is no iron yoke and that the current density *j* in the coils is uniform (no grading). The input parameters for the estimate (124) are the coil inner radius R_1 and the cross-sectional area *S* of the cable in the coil

. They are used to calculate the equivalent coil width w_{eq} [see Eq. (128)] defined as the 30° sector coil having the same inner radius R_1 and cross-sectional area *S* than the generic coil considered (see Figure 25)

$$w_{eq} = \left(\sqrt{1 + \frac{3S}{2\pi R_1^2}} - 1\right) R_1. \tag{128}$$

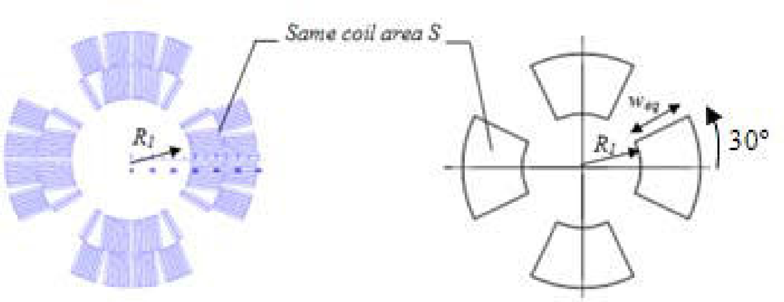

Figure 25 – Coil of the LHC MQ quadrupole (left), and equivalent quadrupole made of 30º sector coils of width w_{eq} (right).

To estimate the stored energy in a real quadrupole coil we substitute w_{eq} to w in Eq. (124). We consider 31 quadrupoles, all based on the cos 2θ lay-out. Some of them are used in particles accelerators such as the Intersection Storage Ring [13], the Tevatron [32], the Large Electron Positron collider [48], HERA [66], the Relativistic Heavy Ion Collider [4], and the Large Hadron Collider [28]. Others have been designed in the framework of the LHC luminosity upgrade: MQY 90/100/110 [69] and MQXC [14] and have been designed for the phase one of the LHC luminosity upgrade (Nb-Ti); HQ1, HQ2 [76], 90mm 2/4 Layers [44] and IRQ 90/100/110 [104], have been designed for the phase two of the LHC luminosity upgrade (Nb_3Sn). The TQ magnet [22] is a Nb_3Sn short model quadrupole built in the framework of the US LHC Accelerator Research Program (LARP). The quadrupoles lay-outs named Ap. 50/100/150/200mm have been sketched for a field quality study in superconducting quadrupoles [10]. LHC MQ+1 and LHC MQ+2 denote an LHC MQ coil with one or two additional layers, sketched to analyze coils with very large w/R_1. Please note that the current grading is removed from graded magnets, *i.e.,* the same current density is assumed to flow in both layers.

For these magnets, we compared the stored energy numerically computed and analytically determined with (124) (See Figure 26). All values agree within 10%, and 2/3 of them agree within 5%. It was also found that single 30° sector coil provides a better agreement than coils with two sectors.

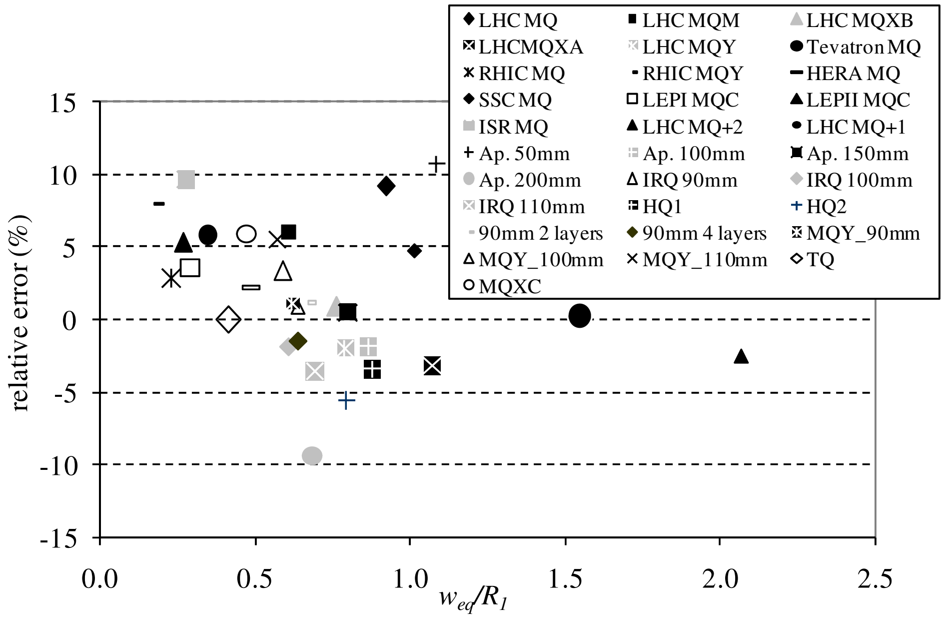

Figure 26 - Agreement between numerical estimate of magnetic energy and analytical estimate for a 30° sector coil based on Eq. (124).

III.4 Magnetic energy at critical current density

In superconducting magnets, the current density in the coils cannot exceed the critical current density of the superconductor corresponding to the peak field in the coil. Here we will compute the magnetic energy when the current density is set at its critical value. To do that we will use formulae worked out in [71] and enabling an estimate of the short sample current density j_{ss} in a Nb-Ti or Nb_3Sn ironless quadrupole coil made from sector coils. They have been summarized in Appendix A. For a Nb-Ti quadrupole, the formula is

$$j_{ss} = \frac{kcB_{c2}^*}{1 + kcR_1\left(a_{-1}\frac{R_1}{w} + 1 + a_1\frac{w}{R_1}\right)\gamma_0 \ln\left(1 + \frac{w}{R_1}\right)}, \tag{129}$$

where B_{c2}^* is the critical field, c is the slope of the superconductor critical surface in the plane (j,B), and k is the filling factor of the cable which takes into account the presence of copper, void, and insulation in the coil. We assume that $B_{c2}^* \sim 10$ T at 4.2K and ~ 13 T at 1.9 K and that $c \sim 6 \times 10^8$ [A/(Tm^2)] is independent of the temperature. For a single 30º sector coil, one has $\gamma_0 \sim 6.93 \times 10^{-7}$[A/(Tm^2)] (derived from analytical calculation), and $a_{-1} = 0.04$ and $a_1 = 0.11$ (obtained from a numerical fit).

Similarly, the expression for the short sample current in a Nb_3Sn quadrupole made of sector coils is [71]

$$j_{ss} = \frac{kc}{2}\left(\sqrt{\frac{4b}{kcR_1\left(a_{-1}\frac{R_1}{w}+1+a_1\frac{w}{R_1}\right)\gamma_0 \ln\left(1+\frac{w}{R_1}\right)}+1}-1\right). \qquad (130)$$

where typical values for a cable having 3000 [Amm^{-2}] are c = 4.0×10^{9} and b = 21 T (at 4.2 K) or b = 23 T (at 1.9 K).

Substituting the current density j in (126) either by the critical current density in a Nb-Ti coil (129) or in a Nb$_3$Sn coil (130), we obtain the energy as a function of the coil lay-out at the short sample current. As superconducting magnets are usually powered with about 20% operational margin from the short sample current, we computed the magnetic energy at the nominal current defined as 80% of the critical current. Plots of the magnetic energy versus the operational gradient for different magnet apertures in a semi-logarithmic scale are given in Figure 27. For each aperture radius, the coil width is varied from R_1/6 to 1.2R_1, according to the stat of the art. One observes that for a fixed aperture the energy is close to be the exponential of the gradient, thus giving straight lines in a semi-logarithmic plot.

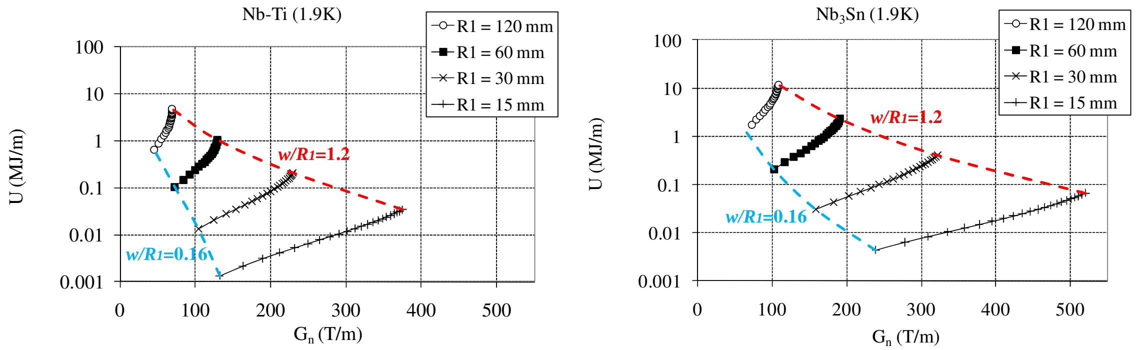

Figure 27 - Analytical estimate of the stored energy (MJ/m) in quadrupoles with Nb-Ti (left) and Nb$_3$Sn (right) at 1.9 K, filling factor of 0.3, powered at 80% of their short sample current and with aperture radii varying from 15 to 20 mm. On each curve, the ratio w/R_1 varies from 0.16 to 1.2.

III.5 Graded coils

The grading method consists in setting a higher current density in the outer layers, where the peak field is lower. This technique is widely used in superconducting accelerator magnets made of two or more layers. For graded magnets the previous approach cannot be directly used. Here we propose a heuristic corrective coefficient allowing taking into account the grading effect in the usual case where one has only two different current densities j_1 and j_2. The grading parameter is defined by:

$$g = \frac{j_2}{j_1} \qquad \text{with} \qquad g > 1. \qquad (131)$$

The average current density value j flowing through the overall coil cross-sectional area $S=S_1+S_2$ is:

$$j = \frac{j_1 S_1 + j_2 S_2}{S}, \tag{132}$$

where S_1 and S_2 are defined as the area of the inner and of the outer layer respectively. We express j as a function of g:

$$j = j_1 \left[1 + \frac{S_2}{S}(g-1)\right]. \tag{133}$$

Since the magnetic energy is proportional to j^2, we expect that the variation caused by current grading is proportional to:

$$x \equiv \left[1 + \frac{S_2}{S}(g-1)\right]^2. \tag{134}$$

Indeed, this is the case: in Figure 28 we show the numerical evaluation based on the numerical code [73] of the increase of the magnetic energy due to the grading in 11 quadrupoles presented in Section III.3. The increase is linear with the variable x.

$$\frac{U_g}{U_{ng}} = d(x-1) + 1, \tag{135}$$

where the fit gives d=1.167, U_g denotes the energy of the graded quadrupole, and U_{ng} the energy in the quadrupole when the grading is removed.

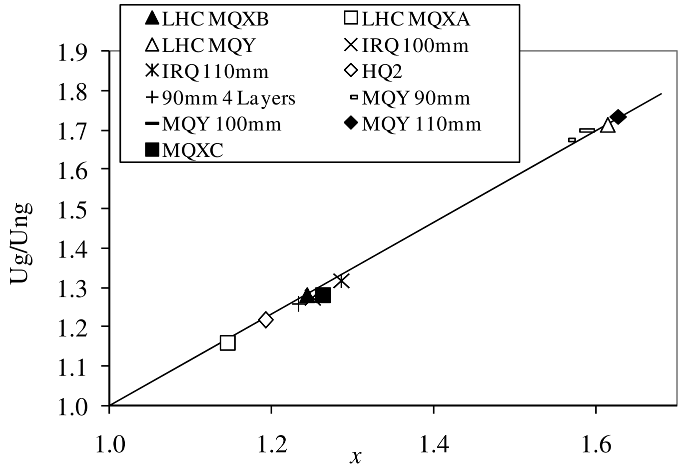

Figure 28 – Increase of magnetic energy due to grading as a function of x as defined in (134).

One can therefore obtain the following heuristic law allowing estimating the stored energy in graded quadrupoles:

$$U_g = U_2[d(x-1) + 1] \tag{136}$$

Comparison of (136) to numerical results including grading gives an agreement within 8 % (see Figure 29).

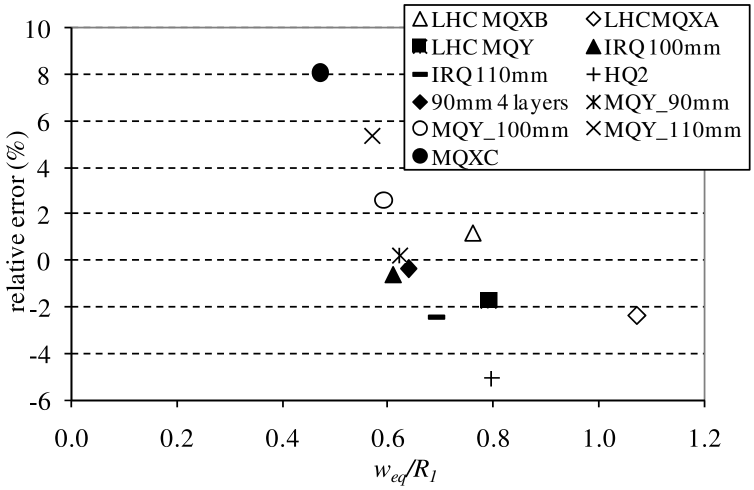

Figure 29 – Agreement between numerical computations of the magnetic energy in graded coils and estimates based on (136).

III.6 Iron yoke contribution

In this section, analytical calculations are performed considering an infinitely long cylindrical iron yoke of inner radius R_{ir} and of infinite permeability. The impact of the saturation on the magnetic energy is then evaluated through a numerical analysis. Analytical expressions of the *z*-component of the vector potential within the winding are obtained by means the current image method presented in Section II.3.3. The expression of A_z inside the winding can be split in two parts $A_z = A_c + A_i$, where A_c is the vector potential created by the coil alone [given in (120)], *i.e.*, when there is no iron, and A_i is the supplementary vector potential due to the iron yoke. As for A_c, the vector potential A_i can be expressed in a Fourier series

$$A_i(r,\theta) = \sum_{n=1}^{\infty} A_{i,n}(r,\theta) \tag{137}$$

where the harmonic of vector potential of rank *n* reads

$$A_{i,n}(r,\theta) = \frac{\mu_0 \alpha_2 j}{2n(n+1)} \frac{r^n}{R_{ir}^{2n}} R_1^{n+2} \left[\left(1+\frac{w}{R_1}\right)^{n+2} - 1\right] \cos(n\theta), \tag{138}$$

and where $w=R_2-R_1$. The total stored energy U_{tot} is obtained integrating the scalar product between the total vector potential $A_z = A_c + A_i$, and the current density in the winding. Therefore, the total energy can be written as a sum of two terms:

$$U_{tot} = U_c + U_i \tag{139}$$

where U_c is the stored energy created by the coil alone, and U_i is the supplementary energy due to the iron yoke contribution to the vector potential.

Considering only the main harmonic of the current, *i.e,* n=2, one has $U_c=U_2$ (see (124)); the expression of U_i is given by integrating the scalar product of the potential vector $A_{i,n}$ [expression (140) and n=2] and the current density in the winding over the winding cross-section S:

$$U_i = \frac{1}{2}\iint_S A_{i,2} j_2 dS, \tag{140}$$

where j_2 is the main harmonic of the current density in the winding:

$$j_2 = j\alpha_2 \cos(2\theta) \tag{141}$$

and therefore U_i is:

$$U_i = \frac{\pi}{128}\mu_0 j^2 {\alpha_2}^2 R_1^4 \left(\frac{R_1}{R_{ir}}\right)^4 [(1+t)^4 - 1]^2, \tag{142}$$

where $t=w/R_1$. We now express the ratio between the magnetic energy with iron yoke and without iron yoke as:

$$\frac{U_{tot}}{U_c} = 1 + \frac{U_i}{U_c}. \tag{143}$$

The ratio U_{tot}/U_c depends only on $t=w/R_1$ and on the forth power of R_1/R_{ir} :

$$\frac{U_{tot}}{U_c} = 1 + \frac{1}{8}\left(\frac{R_1}{R_{ir}}\right)^4 \frac{[(1+t)^4 - 1]^2}{\frac{1}{4}[(1+t)^4 - 1] - \ln(1+t)}. \tag{144}$$

In the range of t used in accelerator magnets, one can fit the complicated expression with a second order polynomial

$$\frac{U_{tot}}{U_c} = 1 + \left(\frac{R_1}{R_{ir}}\right)^4 (a_1 t^2 + b_1 t + c_1) \tag{145}$$

with a_1=8.52, b_1=-0.80 and c_1=1.56. For cross-checking the validity of this equation, we compare the semi-analytical formula (144) with the numerical computation [73] of the U_{tot}/U_c ratio carried out for 8 not graded magnets (upper part of Table 1) and 5 graded magnets (lower part of Table 1) surrounded either by an unsaturated yoke of relative permeability μ>>1 or a real iron yoke. Also in this case, the $t=w/R_1$ ratio used in Eq. (144) is replaced by the w_{eq}/R_1 ratio according to the definition (128).

Table 1 - Comparison of the U_{tot}/U_c ratio between analytical formula (145) and numerical computation performed both with an unsaturated yoke and with a real yoke. Non-graded magnets are gathered in the upper part of the table, and graded magnets in the lower part.

	U_{tot}/U_c			relative error (%)		
	Numerical no saturation	Numerical with saturation	Analytical	Ana/Num unsat	Ana/Num sat.	Num unsat/sat
RHIC MQY	1.43	1.43	1.43	-0.2	-0.2	0.0
RHIC MQ	1.52	1.52	1.50	-1.3	-1.3	0.0
ISR MQ	1.42	1.34	1.38	-2.5	3.4	6.0
Tevatron MQ	1.10	1.10	1.09	-0.5	-0.1	0.4
HERA MQ	1.18	1.17	1.16	-1.6	-1.4	0.2
LHC MQM	1.12	1.12	1.11	-0.9	-0.8	0.1
ssc MQ	1.12	1.12	1.10	-1.8	-1.9	0.0
LHC MQ	1.10	1.10	1.09	-1.4	-1.4	0.0
MQXC	1.29	1.21	1.27	-1.0	4.9	5.9
LHC MQXB	1.16	1.14	1.12	-3.0	-1.2	1.8
LHC MQY	1.18	1.18	1.14	-3.8	-4.0	0.0
HQ2	1.15	1.10	1.12	-2.7	2.0	4.8
LHC MQXA	1.32	1.19	1.22	-7.6	2.6	11.1

Let us consider the unsaturated case, for both the not graded (Table 1, upper part) and the graded magnets (Table 1, lower part), the effect of the iron yoke on the stored energy is predicted within 3 % using the analytical formula (144) (except for the LHC MQXA). Note that the formula always underestimates the ratio U_{tot}/U_c and that the iron contribution to the magnetic energy can be large (for example, ~50% in the RHIC MQ). In Figure 30 we plotted the relative increase of the energy due to the presence of an iron yoke versus the coil aspect ratio by means of the formula (144). One notices that for a quadrupole made with a current sheet and immediately surrounded by iron, the contribution of the iron to the energy reaches its maximum value of 100%.

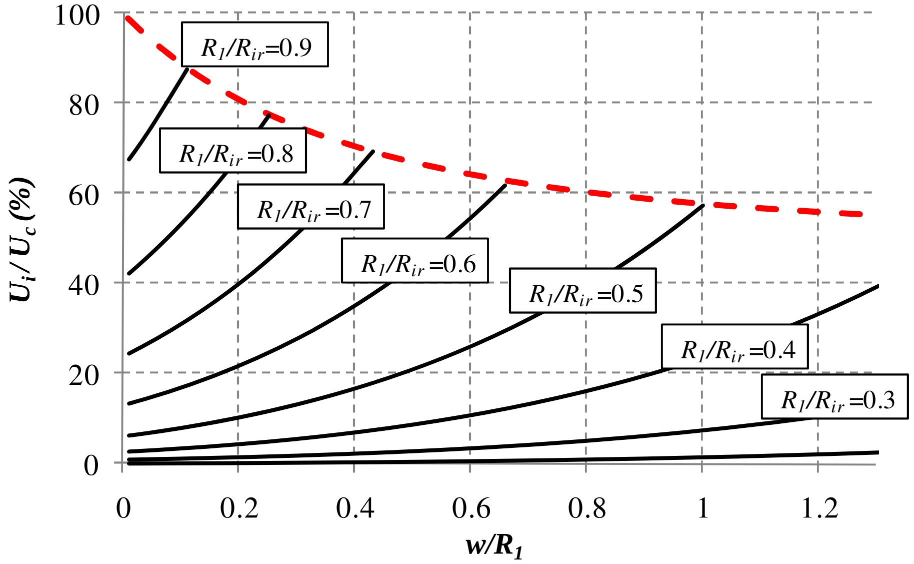

Figure 30 – Relative increase of the energy when adding an infinitely permeable iron yoke of inner radius R_{ir}. The current is kept constant. The red dotted line corresponds to the physical limit where the iron yoke lies on the outer radius of the coil.

As expected, the saturation of the iron yoke leads to a lower stored energy compared to what we have for an unsaturated yoke (see Table 1, last column). The decrease of the energy due to the iron saturation does not exceed ~5%, except for the MQXA where it is of 11%. In Figure 31 we compare the analytical estimate of the stored energy in superconducting quadrupoles graded (filled markers) or not (empty markers), and surrounded by an iron yoke using (124), (136) and (144), with a numerical computation [73] in case of a real iron yoke. The relative error is within 5% for 2/3 of the cases, and within 13% for the others.

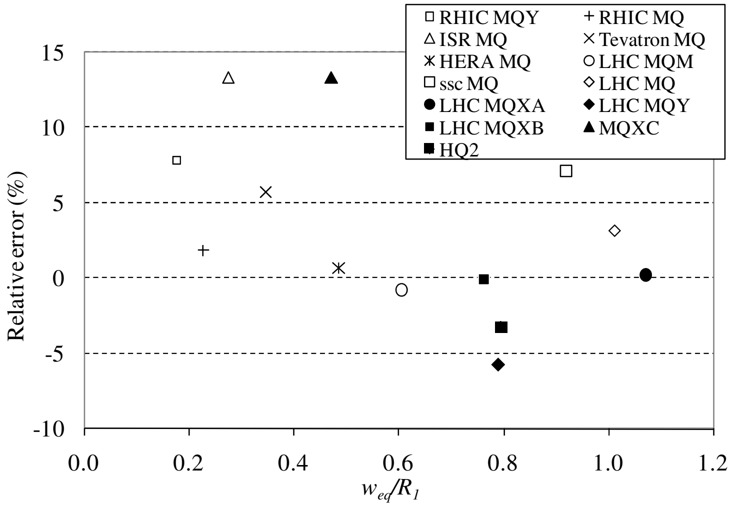

Figure 31 - Energy agreement between numerical computations of the stored energy in real quadrupoles (with real saturated iron) and analytical estimates based on Eq. (144).

III.7 Longitudinal magnetic force

The longitudinal electromagnetic force in superconducting accelerator magnets are of importance because they take place in the coil heads (see Figure 32), a very sensitive part of the magnet to quenches due to the difficulty to support the conductors and, for Nb_3Sn cables, due to the degradation of the superconducting performances of the cables owing to the cables bending.

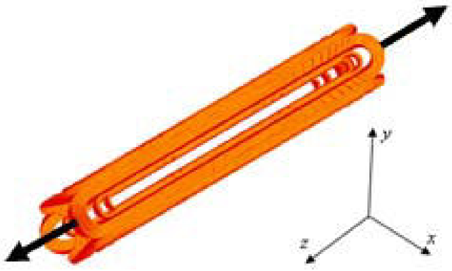

Figure 32 – Longitudinal magnetic force applied on a coil ends of a quadrupole.

Asner elaborated in [7] a semi-analytical method to estimate the magnetic force in the coil ends of superconducting magnets. The method, which request the use of numerical integration assumes that the end field has two components, one linear, bi-dimensional (straight part) and the second due to half a solenoid (coil head). A much simpler method developed in the past and based on the virtual work theorem allows estimating the net axial Lorentz force in superconducting and ironless quadrupole magnets. The expression of the axial force is obtained assuming a virtual axial elongation of the straight part of the coil while keeping a constant current:

$$F_z = \left.\frac{\partial W_m}{\partial z}\right|_{z=0} \tag{146}$$

where W_m [J] is the total stored energy of the coil. The force F_z is in [N] if $\partial W_m/\partial z$ is in [J/m] and its sign depends on the direction of the coil elongation ∂z: F_z is positif if ∂z is oriented in the same direction than the z-axis, and is negative otherwise. Therefore, the formula (124) derived in Section III.2 and giving the stored energy [J/m] per unit length of ironless quadrupole magnets and denoted by U_2 is also the net force applied on the magnet ends

$$F_z = U_2 \quad \text{if } \overrightarrow{\partial z}.\vec{z} > 0 \qquad \text{or} \qquad F_z = -U_2 \quad \text{if } \overrightarrow{\partial z}.\vec{z} < 0. \tag{147}$$

The longitudinal magnetic force applied on the end of a quadrupole winding with coils made of 30º sectors has been plotted in (see Figure 33). These plots are similar to those of the magnetic energy shown in Figure 27.

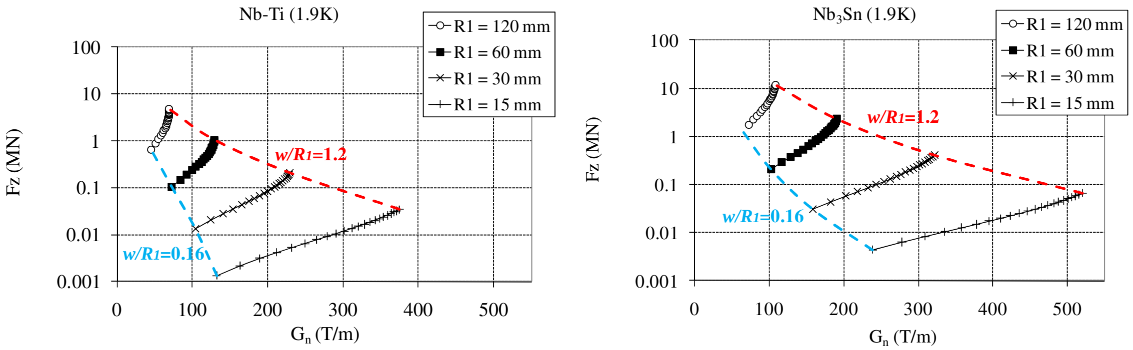

Figure 33 – Total magnetic force applied on one end of superconducting quadrupoles with Nb-Ti (left) and Nb$_3$Sn (right) at 1.9 K, filling factor of 0.3, powered at 80 % of their sample current and with aperture radii varying from 15 to 120 mm. one each curve, the ratio w/R1 varies from 0.16 to 1.2. These plots are similar to the plots of the magnetic energy in Figure 27.

Here we propose to investigate the magnetic end force when the coil is surrounded by an unsaturated iron yoke. To do that, we use the Maxwell stress tensor formula defined as [40]

$$\vec{F}_m = \oiint_S \left[\vec{B}(\vec{n}.\vec{B}) - \frac{1}{2}B^2\vec{n}\right] dS. \tag{148}$$

and giving the net magnetic force $\vec{F}_m$ applied on a conductor or a magnetic body enclosed within the surface *S*. The vector $\vec{n}$ is a unitary vector normal to the surface element *dS* and oriented outwardly with respect to the volume delimited by the surface *S*, and $\vec{B}$ denote for the magnetic field produced by sources located inside or outside the volume delimited by *S*.

Let us first consider a quadrupole coil of finite length *L* surrounded by a circular iron yoke of inner radius R_f and of infinite length in *z* (Figure 34). The magnetic permeability of the yoke is assumed infinite so that the magnetic flux lines penetrate the yoke perpendicularly to its surface.

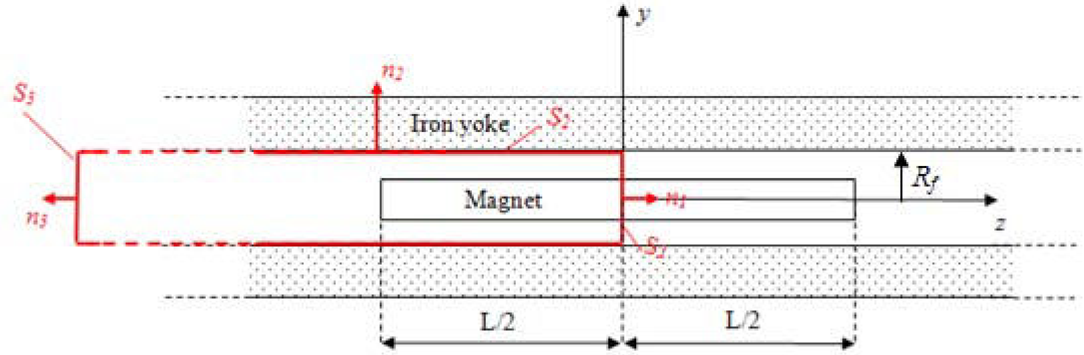

Figure 34 – Long qudrupole coil within an infinitly long iron yoke. The surface in red is used to calculate of the longitudinal force applied on half of the magnet by means of the Maxwell stress tensor. The iron is assumed to have an infinite permeability.

Let us apply the Maxwell stress tensor to the closed surface delimited by the red line in Figure 34. The closed surface is composed of the surfaces S_1 and S_3 (disks of radius R_{ir}) and S_2 (cylinder of radius R_{ir}). The longitudinal net magnetic force $F_z^{(1)}$ applied on half of the magnet is obtained summing up magnetic forces $\vec{F}_{z,1}$, $\vec{F}_{z,2}$ and $\vec{F}_{z,3}$ applied on the surfaces S_1, S_2 and S_3 respectively

$$F_z^{(1)} = \sum_{k=1}^{3} F_{z,k}, \tag{149}$$

where the magnetic force $\vec{F}_k$ applied on the surface S_k is obtained from

$$F_{z,k} = \frac{1}{\mu_0} \iint\limits_{S_k} \left[\vec{B}\left(\vec{n}_k . \vec{B}\right) - \frac{1}{2} B^2 \vec{n}_k \right] . \vec{z}\, dS_k. \tag{150}$$

Because of the infinite permeability of the iron which makes magnetic flux lines entering the yoke perpendicularly to the yoke surface one has $F_{z,2} = 0$. The magnetic force $F_{z,3}$ is also zero because the surface S_3 is set far from the magnet end so that the magnetic field on S_3 is zero. Taking into account that the magnetic field in the plane (*O*,*x*,*y*) has only in-plane components, the total longitudinal force applied on half the magnet writes:

$$F_z^{(1)} = F_{z,1} = -\frac{1}{\mu_0}\iint_{S_1} \frac{1}{2} B^2 dS_1. \tag{151}$$

Note that the force is negative because we considered the left half part of the coil ($\vec{z}$ oriented from left to right). For a coil length L long enough the magnetic flux density produced in the plan (O,x,y) is of the same value than what one would have for an infinitely long coil. In that case, Eq. (151) also gives the magnetic stored energy per unit length of magnet (since the magnetic permeability has been assumed infinite, all the magnetic energy is located within the yoke aperture, *i.e.,* no magnetic energy located in the iron yoke)

$$F_z^{(1)} = -U_{tot}, \tag{152}$$

where U_{tot} [J/m] is given by Eq. (144).

Usually, in superconducting accelerator magnets the longitudinal length iron yoke is of the same order than the length of the coil. Again in this case the longitudinal force applied on half the magnet can be expressed by means of the Maxwell stress tensor. One has to consider a close surface (see Figure 35, red lines) on which we apply the Maxwell stress tensor. The cross-sectional surface S_1 perpendicular the z axis, the surface S_2 (cylinder) lying on the yoke inner surface, the surface S_3 (ring) lying on the yoke end, the surface S_4 (cylinder) lying on the yoke outer surface, the surface S_5 (ring extending to the infinite) and the surface S_6 which closed the domain at the infinite.

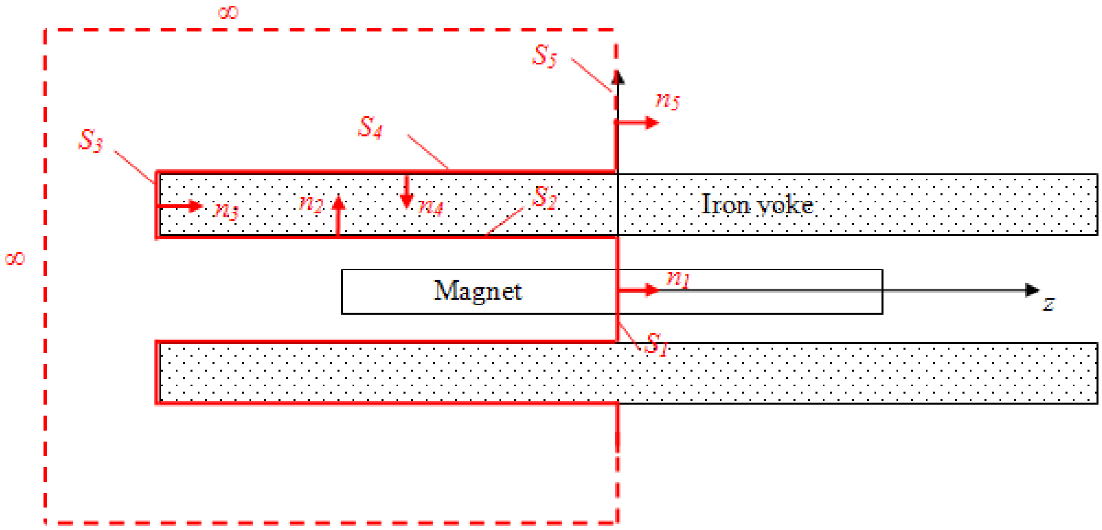

Figure 35 – Accelerator magnet surrounded by an iron yoke of finite length and of infinite permeability.

The total longitudinal force $F_z^{(2)}$ acting on half the coil end is obtained summing up the axial components of the magnetic force calculated on each of the 6 sub-surfaces (S_1 to S_6)

$$F_z^{(2)} = \sum_{k=1}^{6} F_{z,k}. \tag{153}$$

The magnetic forces $F_{z,2}$ and $F_{z,4}$ applied on the surface S_2 and S_4 are zero because of the infinite permeability of the iron which makes the magnetic flux line entering the yoke perpendicularly to its surface. We assume that the iron yoke traps all the magnetic flux lines so that $F_{z,5} = 0$. We also assume that the magnetic field is zero at the infinite which gives $F_{z,6} = 0$. Therefore, expression (153) reduces to

$$F_z^{(2)} = F_{z,1} + F_{z,3}. \tag{154}$$

The yoke and the coil are assumed to be very long with respect to the transverse dimensions of the coil. Hence, the axial force $F_{z,1}$ applied on the surface S_1 is of the same value than the total axial force applied on the end of a magnet surrounded by an infinitely long iron yoke, *i.e.,* $F_z^{(1)}$. Therefore Eq. (154) re-writes

$$F_z^{(2)} = F_z^{(1)} + F_{z,3} \tag{155}$$

where $F_{z,3}$ is given by

$$F_{z,3} = \frac{1}{\mu_0} \iint_{S_3} \left[\vec{B}\left(\vec{n}_3.\vec{B}\right) - \frac{1}{2} B^2 \vec{n}_3 \right].\vec{z}\, dS_3. \tag{156}$$

Because magnetic flux lines are perpendicular to S_3 expression (156) reduces to

$$F_{z,3} = \frac{1}{\mu_0} \iint_{S_3} \frac{1}{2} B^2 dS_3 \tag{157}$$

The integral of B^2 over the surface S_3 is positive since the integral of a positive function is positive. One notice that $F_{z,3}$ (Eq. (157)) is of opposite sign than $F_z^{(1)}$ (Eq. (151)). Therefore, according to Eq. (155) one can draw the conclusion: **The longitudinal magnetic force applied on the magnet ends is maximal when the iron yoke is infinitely long.**

III.8 Summary

We used the Fourier decomposition to evaluate the magnetic stored energy of a quadrupole made of sector coils as a simple function of the coil width and of the aperture (120). We showed that the ratio between the total stored energy and the energy produced by the first harmonic of current depends only on the ratio of coil width to the aperture radius. We also showed that the stored energy in a quadrupole made of sector coil is well approximated by the first harmonic of the energy (124). To link the analytical formula

(124) to a real quadrupole cross-section we defined the 30° sector coil equivalent through (128). Using this approach, the lay-out details as the number of blocks, and their angular position of a real coil, are ignored. The analytical equation allows predicting the magnetic energy within 10% (Figure 26).

The approach was generalized (136) to take into account of grading, which can contribute to a large amount of the stored energy (for instance, 42% for the MQY). Also in this case, the energy is foreseen through the semi-analytical formula within 10% (Figure 29). A third coefficient allowing taking into account of the contribution of an unsaturated iron yoke of infinite permeability is given (144). A comparison of the stored energy in real quadrupoles computed numerically (*i.e.,* real cross-section, real iron yoke and grading) and the analytical estimates of the energy through ((124), (136) and (144) shows agreement within 10% (Figure 31).

The knowledge of the magnetic energy also allows calculating the inductance of the quadrupole. Moreover, it is known that when there is no iron yoke and for sufficiently long quadrupole the energy per unit length of magnet gives the longitudinal Lorentz force acting upon the coil ends. We showed that this also the case when an infinitely permeable iron yoke is set around the coil, but not for finite values of the permeability. Finally we analytically showed by means of the Maxwell stress tensor that for an infinitely permeable iron yoke of smaller longitudinal length than the coil the magnetic force is necessarily smaller than what one would have for a yoke much longer that the coil.

IV. Coil miss-positioning and field harmonics errors

In the early stage of a magnet design it is important to give a reliable estimate of the expected field harmonic errors. This helps accelerator designers to determine if the estimated field errors are acceptable for the beam stability or not, and, if not, to dimension magnet correctors. The following convention will be used in defining field harmonics [81]

$$B_y + \mathrm{i}B_x = 10^{-4} B_N \sum_{n=1}^{\infty} (b_n + ia_n) \left(\frac{\bar{z}}{R_{ref}} \right)^{n-1}, \tag{158}$$

where B_N, expressed in [T], is the main component of the magnetic field at the reference radius R_{ref}. Coefficients b_n and a_n are the normalized normal and skew multipoles (normalized with respect to B_N) and are expressed in [units]. B_x and B_y are the x and y-components of field at the position $\bar{z} = x + iy$ in the magnet aperture. We remind the reader that multipoles allowed by symmetries in the current distribution of a dipole are b_1, b_3, b_5, …, and are b_2, b_6, b_{10}, … in a quadrupole.

Throughout this chapter we will focus on the spread of the reproducibility of the field harmonic errors due to geometric errors. Geometric errors are due to mechanical tolerances in the coil components or in the magnet assembly and limit the possibility to reach a high field quality in the magnet.

We first present the method commonly used to measure the harmonic content of the magnetic field in an accelerator magnet (Section IV.1), and we list the sources of possible field errors in Section IV.2. In Section IV.3 we introduce the concept of uncertainty in the measured field errors. We then recall the standard way used to estimate the random part of the spread in the coil position from the measured sigma of the geometric field errors (Section IV.4) and we apply it, for the first time, to series of Nb_3Sn dipole and quadrupole magnets manufactured in the past few years (section IV.5). A comparison of the obtained results with what has been obtained for magnets based on the mature Nb-Ti technology is done. Finally, we investigate the spread of the mean of the field errors through magnetic measurement performed on 11 series of Nb-Ti quadrupole magnets (Section IV.6) used in the LHC (7) and in the RHIC (4) machines. The goal of this study is to check if the measured mean values of the integral of the non-allowed harmonics are caused by systematic defect in the coil which adds up coherently or if it is due to statistical effect related to the number of magnets in the series.

IV.1 Field quality measurements

The measurement of the field harmonics of a superconducting accelerator magnet is usually done by means of a **rotating pick-up coil (or magnetic mole)** consisting into a cylinder made of non-magnetic materials and housing flat copper coils. The measurement consists in rotating the magnetic mole in the magnet aperture while supplying the magnet coil with a steady current. The harmonic content of the magnetic field is then obtained analyzing the Fourier expansion of the voltage induced in the mole winding [93].

Typical values of the field harmonic in a superconducting magnet are of the order of 10^{-4} times the main field. To be able to achieve such a precision in the measurement, the magnetic moles are manufactured and assembled with stringent tolerances on their components dimensions. Effects of defects in the measuring coil (vibration in the rotational motion of the coil, twist of the coil,…) on the harmonic content have been extensively studied in the past [34] and lead to the elaboration of more accurate measuring system like the so-called bucking coil [93]. Moreover, in order to get rid out of external sources of field errors such as the earth field and the yoke residual magnetization at low field, the field harmonics are calculated from the average of measurements performed with a positive and a negative current in the magnet coil. The latter method is only applied at warm since the field generated by the coil is small; at cold the sign of the current is not changed. Typically, series of ten measurements are performed: five with a positive current in the magnet coils, and five with a negative one. The possible offset between the mole axis (taken as the origin for the field harmonics) and the magnetic center of the magnet is taken into account by means of the "feed down" method based on cancelling two non-allowed harmonics in the measured spectrum [25]. The precision of magnetic measurements achieved by magnetic moles used for the LHC magnets is of about 1 unit for the main component and in between 0.01 and 0.001 units for harmonic of higher order [26]. Such a precision allows measuring harmonics up to order 10-12, higher order being out of interest since they are naturally small.

Magnetic measurements are performed at different steps of the magnet production to detect assembly errors or faulty components. For instance, for the LHC magnets, 2 measurements were performed at room temperature: the first one on the collared coil and the second one on the cold mass. For long magnets, as the LHC main dipole (15 m), the magnetic mole is usually smaller than the magnet and thus the magnetic measurement is obtained from a scan of the entire magnet. The interesting feature of the scan is that it provides magnetic measurements along the magnet length which can be used to estimate the coil waviness along the magnet axis [11].

After being assembled in its cryostat, the field harmonics of the magnet are again measured as explained before, but this time at low temperature and after a first cycle where the current is ramped up (from zero current to nominal current) and down. Magnetic measurements are performed on the second current cycle, for different current values. An example of magnetic measurement performed at 1.9 K in the TQS02b magnet is shown in Figure 36.

In this chapter, we analyze the geometric errors in the cold-mass. The field harmonic error measured at warm temperature is entirely provided by geometric errors in the cold-mass. At cold, the field error due to geometric errors is calculated at a chosen current where the yoke is not yet saturated, and where the persistent (see Section IV.2) currents are low. It is obtained from the average of the two measurements of the harmonic of the ramp-up and ramp-down of the load line branches. For instance, in the Figure 36 we show the geometric errors of b_6 (1) (in case the calculated value of b_6 is nil). The error due to the yoke saturation is also shown (2).

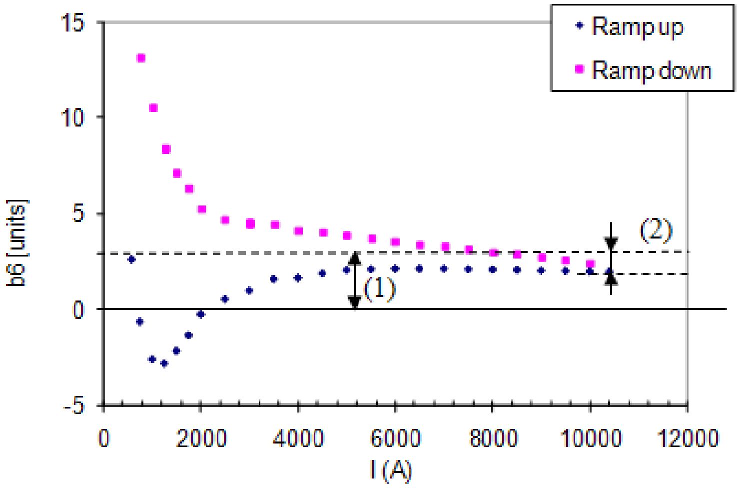

Figure 36 – Measurement of b_6 after a pre-cycle in the TQS02b quadrupole magnet. The hysteresis results from superconductor magnetization and the distortion at large current (> 5000A) results from iron saturation. Parts of the field error due to geometric errors (1) and due the saturation of the iron (2) are shown.

IV.2 Source of field harmonic errors

Field harmonic errors in superconducting magnets, defined as the discrepancy of the harmonics from the ideal field, can be classified into four main categories [36]: (1) geometric errors on the cold mass, (2) errors related to the iron saturation, (3) errors due to persistent currents, and (4) errors due to eddy currents.

- **Geometric errors**

In superconducting magnets, geometric errors inducing distortions of the magnetic field in the magnet aperture are all localized in the cold-mass, *i.e.,* in the coil, collars and iron yoke. They are due to tolerances on the dimensions of the components and in the assembly procedures. Moreover, at high field, the large magnetic forces in the coil can also be responsible for changing the shape of the coil; this is one of the reasons why superconducting magnet coils need to be pre-stressed. Below is a non-exhaustive list of possible sources of geometric errors on the cold-mass:

- Uncertainty on the dimensions of the coil components *e.g*. copper wedges and coil-blocks.
- Uncertainty on the dimensions of the collars.
- Uncertainty in the coil dimensions due to geometric error in the curing mould.
- Uncertainty on the coil-blocks positioning during the magnet assembly.
- Uncertainty on the size of the coil after pre-loading.

- Uncertainty on the iron yoke dimensions or position with respect to the coil.

The contribution of geometric error in the yoke to the content of the field errors is usually negligible with respects to other geometric defects. Therefore, in first approximation one can consider that the entire geometric field error has for origin defects in the coil. Typical tolerances in the coil components and in the assemble procedures are specified to be within 0.025 mm, except for the thickness of the insulated cable were the tolerances are generally one order of magnitude better [50].

- **Iron saturation**

The magnetic permeability of the iron yoke can be considered as very large and uniform as long as the magnetic flux density in the iron is less than 2 T. As a result, the iron yoke contribution to the magnetic field is an offset in the allowed harmonics independent of the current in the magnet coil. However, for magnetic flux density in the iron larger than 2 T, the magnetic permeability drops and the yoke contribution to the magnetic field does not vary linearly with the current anymore. This results in a current dependent distortion of the field harmonics. The iron saturation is pretty reproducible, and therefore, its contribution to the random part of the field harmonic errors is small.

- **Errors due to persistent currents**

Persistent currents are due to currents induced in the superconducting filaments when exposed to a varying magnetic field [81]. Since they flow in the superconductor, they can circulate as long as the superconductor is in the superconducting state. At low field, like during the injection phase, they can produce large distortion of the multipoles allowed by the magnet symmetry. Their amplitude, which depends on the history of the magnet powering cycle and on the size of the filaments, decreases with an increasing magnetic field. They are negligible at high field.

Note that another class of effect related to the filaments magnetization and called “decay and snap-back” is source of errors in the magnetic field. A decay of the magnetic field occurs at low field and during long periods of constant current. The drift of the magnetic field disappears as soon as the current ramp restarts. See [23] [52] for more details.

- **Errors due to eddy currents**

Eddy currents are induced in a superconducting cable by a time varying magnetic field and circulate through inter-filaments and inter-strands resistances of the cable. The amplitude of the eddy current depends on the magnetic field ramp rate, and on the cables geometry (the twist pitch), and on the electrical characteristic of the strands (matrix resistance) and cables (inter-strand resistance) [81].

IV.3 Uncertainty in the field harmonic errors

It is well known that the major part of the uncertainty in the field harmonic errors comes from geometric errors [50] on the coil dimensions and position, the others types of errors listed in section IV.2 being much more reproducible. The predominance of geometric errors in the uncertainty with respect to others class of errors can be observed from the correlation of the field harmonic errors measured in a set of identical magnets at warm (room temperature), where geometric errors are the main responsible for the variability of the field errors, and at cold temperature [10].

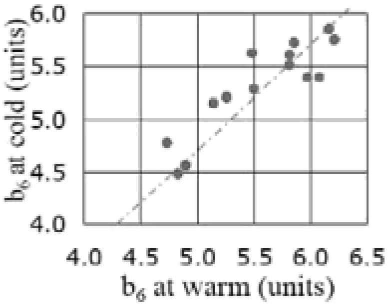

Figure 37 – Warm-cold correlation of the b_6 harmonic measured in 14 LHC MQ quadrupoles [82].

In a series of identical magnets, the uncertainty of the measured field errors (mainly due to geometric errors) is usually characterized by a **random component** (or **standard deviation of the field error** or **sigma of the field error**), denoted by σa_n and σb_n, and a **mean value (or systematic error)**, denoted by $<a_n>$ and $<b_n>$. For instance, the standard deviation and mean values of the skew harmonic of order n measured on L nearly identical magnets (they differ only from tolerances on the geometry of the coil and of its components) are calculated according to

$$\sigma a_n = \sqrt{\frac{1}{L}\sum_{i=1}^{L}\left(a_{i,n}\right)^2 - (< a_n >)^2} \quad \text{and} \quad < a_n >= \frac{1}{L}\sum_{i=1}^{L} a_{i,n}\,, \tag{159}$$

where $a_{i,n}$ is the skew harmonic of order n measured on the magnet number i belonging to the set of L magnets.

The discrepancy between the expected field harmonic errors, denoted by a_n^e and b_n^e and obtained from numerical computations, and the systematic errors obtained from measurement is called the **uncertainty in the mean**. It is denoted by δa_n or δb_n, and is calculated from

$$\delta a_n =< a_n > -a_n^e \quad \text{and} \quad \delta b_n =< b_n > -b_n^e \tag{160}$$

Note that the systematic non-allowed harmonics are usually zero. In Figure 38 are reported measurements of the a_4 harmonic coefficient performed at room temperature and with a rotating coil on 400 arc quadrupoles of the LHC. The mean value of the field error on a_4 is of 0.4 units and the standard deviation at one sigma (σa_4) is of 1.7 units. Because of the quadrupolar symmetry the systematic value of a_4 is zero. Therefore, the uncertainty in the mean (δa_4) is also of 0.4 units.

The uncertainty in the harmonic measurements owing to the measuring system is usually smaller than 0.01 units [26]. This allows measuring harmonic mean values up to the order 10 and sigma values (which are usually larger than mean values for non-allowed harmonics) up to order 10-12.

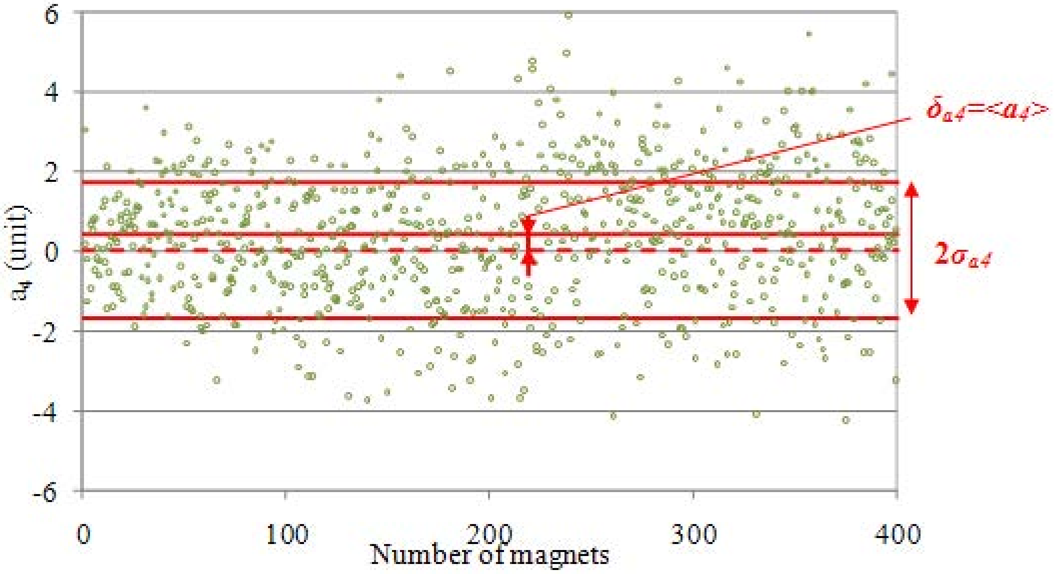

Figure 38 – Skew harmonic of order 4 measured in the 400 quadrupoles MQ of the LHC (markers). Means (solid red line) and standard deviation at one sigma (dashed red line).

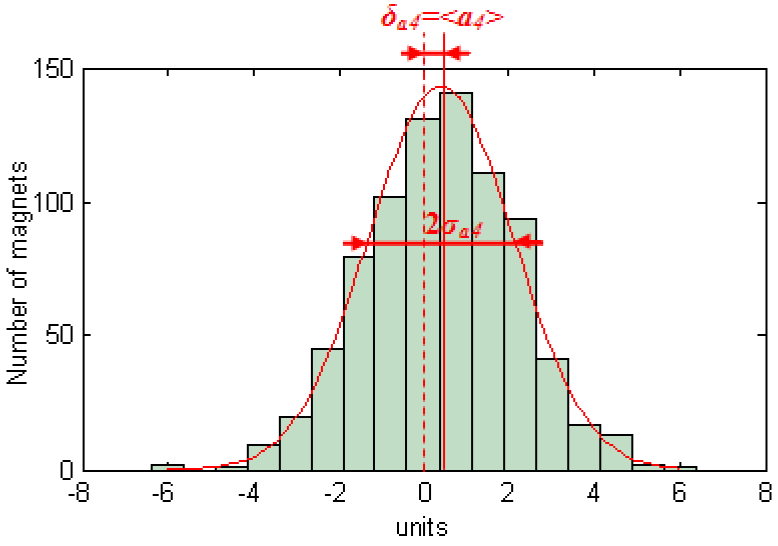

Figure 39 – Definition of the standard deviation and of the uncertainty in the mean through measurement of the multipole a_4 in 400 LHC MQ quadrupoles.

In a large series production one cannot tune each magnet independently from one another and therefore the uncertainty of the mean and the random component of the field error have to be as small as possible.

IV.4 A Review of the method used to estimate the reproducibility of coil positioning through magnetic measurements

A standard way of estimating the random component of the field quality in a superconducting magnet (dipole, quadrupole,…) is based on a Monte-Carlo simulation [11] [45] [50] [54] [55]. Each coil block constituting the winding is moved independently along the three degrees of freedom, *i.e.,* radial movement, azimuthal movement, and tilt (see Figure 40). Three independent random numbers are drawn for each coil block, with the same amplitude. To be more precise, let (r,θ) be the coordinates of the block baricentre, and ρ the distance of the block corner from the baricentre. The block will be moved by

$$\Delta r = \frac{d}{\sqrt{3}}\varepsilon_1 \qquad \Delta\varphi = \frac{d}{\sqrt{3}}\frac{1}{r}\varepsilon_2 \qquad \Delta\alpha = \frac{d}{\sqrt{3}}\frac{1}{\rho}\varepsilon_3 \tag{161}$$

where ε_1, ε_2 and ε_3 are three independent dimensionless random variables with zero average and sigma equal to one, and d is the *rms* value of the displacement. We used Gaussian random variables to simulate components and assembly tolerances; in principle, a uniform distribution can also be considered.

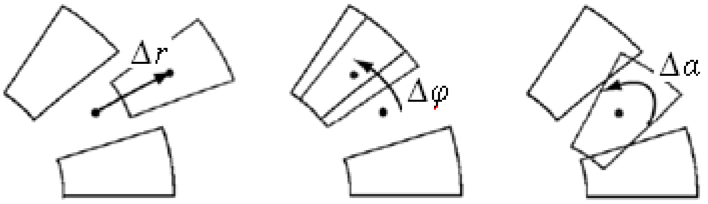

Figure 40 – Displacements associated with the position of a block in the coil transverse cross-section [9].

Once such random movements are assigned to the cross-section, the magnetic field is computed for this new configuration which is supposed to simulate a real coil including the manufacturing and assembling imperfections. The field is then represented according to the standard multipolar expansion defined in section II.2.5 and in Eq. (158). The simulation is repeated for 100-1000 cases, and an average $\mu_n(d)$ and standard deviation $\sigma_n(d)$ of the field harmonics is estimated for a given amplitude d. The standard deviation $\sigma_n(d)$ represents the impact of the spread d of the coil position on the field harmonics.

It has been shown in [79] that the spread in the multipoles is proportional to the spread in the position d within the interesting domain (d=0.01 to 0.2 mm). Moreover, it has also been shown that normal and skew components of the same order have a similar spread (within a few percent) and that the spread in the multipoles roughly decays with the multipole order n as $(R_{ref}/r)^n$, where r is the aperture radius, as expected by the Biot-Savart law [79]. For instance, the sigma of the field error obtained from simulation in the LHC arc dipole and quadrupole for two different values of d is shown in Figure 41.

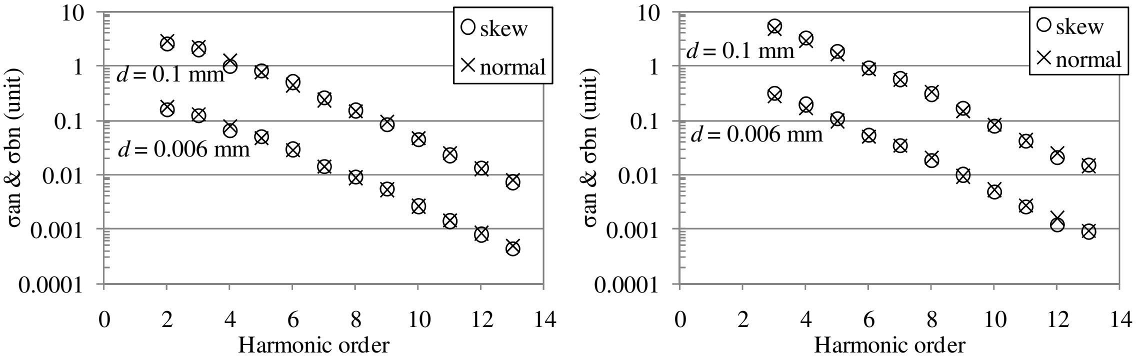

Figure 41 – Numerical estimate (markers) of geometric random multipoles due to random block displacements of different amplitude *d* for the blocks of the LHC arc dipole (left) and arc quadrupoles (right).

To summarize, in a semi-logarithmic plot σ_n versus multipole order n as shown in Figure 41, the Monte-Carlo results will be close to straight lines. By comparing with the sigma obtained from magnetic measurements (markers in Figure 42, for instance), one can evaluate the best value of *d* that accounts for the measured spread. The fit has to be done in the semi-logarithmic scale otherwise the higher order contribution is negligible [11] [55]. The comparison of the data with simulation usually points out a knee in the measurement data, which is considered as the finite resolution of the measurements. For this reason, one has to perform the fit using data up to a given multipolar order, which is usually ranging between 8 and 12. In Figure 42 we show the case of the LHC interaction region quadrupole MQXA, where the noise of the measurement is about 0.007 units and the truncation order for the fit has been set to 8.

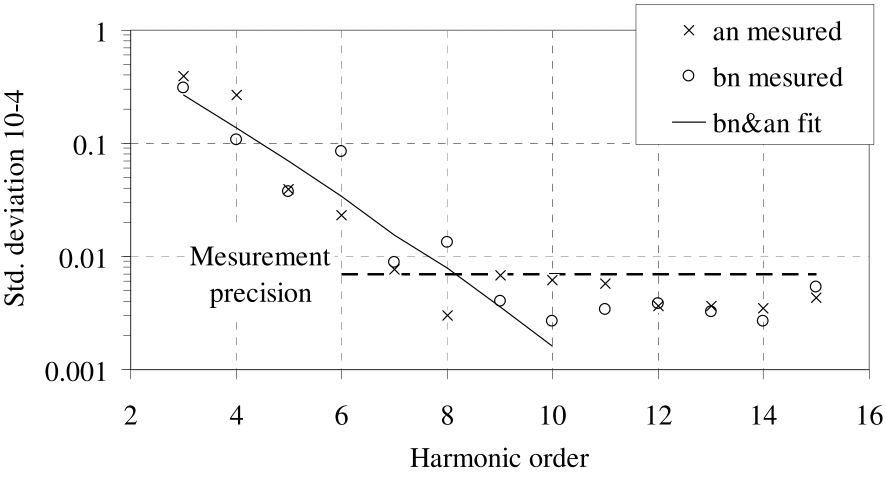

Figure 42 – Standard deviation of the multipoles measured in the LHC MQXA quadrupoles (markers), and best fit simulated for a random displacement of the coils of 0.011 mm (lines). The measurement precision is shown to be about 0.007 units (dashed line).

R.*m.s.* coil displacements estimated form integrated magnetic measurements performed over the production of Nb-Ti dipole magnets for Tevatron, HERA, RHIC and LHC are given in [11] (see Table 2). Displacements range from 0.065 mm in Tevatron to 0.016 mm in RHIC, *i.e.,* a gain of factor four has been achieved by this technology over 30 years. The level of complexity of the coil design is also important: the double layer, six blocks, 30 mm width coil in the LHC dipoles has a larger spread than the single layer, four blocks, 10 mm width coil in the RHIC dipoles.

Table 2 – Estimate of the reproducibility of the coil positioning in the production of superconducting dipoles for four particle accelerators [11].

Magnet	d (mm)
Tevatron	0.065
HERA	0.041
RHIC	0.016
LHC	0.025

For the Nb-Ti quadrupoles in RHIC and LHC, results are summarized in Table 3. The spread ranges from 0.01 mm to 0.03 mm. Also in this case it was shown that the spread along the axis is negligible with respect to the spread from coil to coil [11].

Table 3 – Estimate of the reproducibility of the coil positioning in the production of superconducting quadrupoles for RHIC and LHC.

Magnet	d (mm)
RHIC MQ	0.022
RHIC MQY	0.018
LHC MQ	0.029
LHC MQY	0.025
LHC MQXA	0.010
LHC MQXB	0.016

Moreover, the spread of the integral harmonics over a set of homogeneous magnets built on the same design, and the corresponding spread in the coil position as given in Table 3, depends on two components. The first one is the spread along the magnet axis, integrated over the total magnet length. This spread depends on the magnet length, and becomes negligible for very long magnets as the LHC dipoles.

The second component is due to the coil itself: this does not vary along the coil length, but it rather depends on assembly features that are common to the coil as a whole and differ from coil to coil (as for instance the curing cycle or the collaring). This second component does not depend on the magnet length.

The spread of the integral harmonics over a set of magnets will be the sum of the spread along the axis, plus the spread from coil to coil. For the long magnets given in Table 3, the second component is overwhelming. For example, in the LHC 14.3-m-long dipoles the spread along the axis measured with 125-mm-long mole correspond to about 0.030 mm of spread in the coil position. In the hypothesis of a Gaussian distribution of the spreads along the axis, this gives a negligible contribution (about 0.003 mm) to the spread along 14.3 m. For a 1-m-long model of the LHC dipole, the contribution of the spread along the axis would be 0.012 mm, i.e. still small but not negligible with respect to 0.025 mm spread from coil to coil.

To summarize, some care should be taken when carrying out this analysis to be sure that the spread along the axis and the magnet length are taken into account, and that the correct physical interpretation is given to these quantities computed from measurements and simulations.

So far we have assumed that the spread of the normal and skew harmonic of the same order are of the same value. This is not completely true. Indeed, in measured data one usually observe that the spread in the field error is not necessarily the same for normal and skew multipoles of the same order as it is shown for instance in Figure 43 for the LHC main dipole (left) and LHC main quadrupoles (right). Measured data in real magnets usually exhibit the following pattern:

- **In dipoles** allowed multipoles always have a larger spread than the non-allowed ones of the same order, *i.e.*, $\sigma_{b3} > \sigma_{a3}$, $\sigma_{b5} > \sigma_{a5}$,....

- **In quadrupoles** one notices that (i) the sigma of odd normal and skew multipoles tends to be of the same value (*i.e.*, $\sigma_{a3} = \sigma_{b3}$, $\sigma_{a5} = \sigma_{b5}$,…), while (ii) the sigma of even normal multipoles tends to differ from that of skew multipoles (*i.e.*, $\sigma_{a4} \neq \sigma_{b4}$, $\sigma_{a6} \neq \sigma_{b6}$, $\sigma_{a8} \neq \sigma_{b8}$,…), and that (iii) allowed multipoles always have a larger spread than the non-allowed ones of the same order, *i.e.*, $\sigma_{b6} > \sigma_{a6}$, $\sigma_{b10} > \sigma_{a10}$, ….

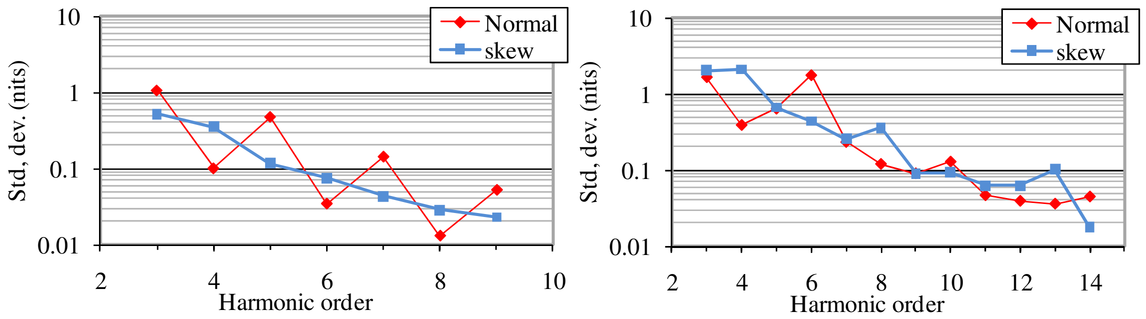

Figure 43 – Standard deviation of the multipoles measured in the LHC main dipoles (left) and in the LHC main quadrupoles (right). Data points have been linked by straight so as to make the field harmonic pattern more visible.

This shows that in reality coil displacements are not completely randomly distributed and that it may have coupling within the quadrupole coil. Because of that, the spread of the sigma of the different multipoles around the quasi-linear fit obtained from simulations leads to error associated to the estimate of *d* is the order of 20% to 60% [11].

Coil displacements leading to the measured pattern of the field errors are solutions of an inverse problem and consequently have an infinite number of possible solutions. In

[54] [55], the pattern of the sigma of the field error in dipoles and quadrupoles has been parameterized by means of two (dipole) or three (quadrupole) parameters, each one accounting for one of the two (dipole) or three (quadrupoles) symmetries exhibited by the current distribution in the magnet coil. More recently, in [11] and for dipoles magnets it has been proposed to consider multipoles families separately, *i.e.,* a_{2n+1}, a_{2n}, b_{2n+1} and b_{2n}., and to fit each family independently from one another by means of coupled modes of coil displacements as shown in Figure 44. This enables to provide different estimates of the spread *d*, for each family of multipoles.

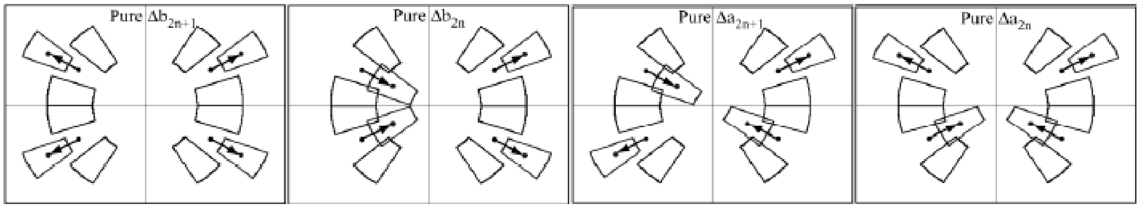

Figure 44 – Dipole coil imperfections generating multipole families [11]

For instance, according to Table 4, in RHIC and LHC the odd normal multipoles (*i.e.,* the “allowed ones”) correspond to a spread of around 0.050 mm, whereas the other ones range between 0.005 to 0.030 mm [11]. The same method will be used for the dipoles in Section IV.5.1.

Table 4 – Estimate of the reporductibility of the coil positioning in the production of superconducting dipoles (in mm) for 4 high energy particle accelerators, average values and split among the different multipole families [11].

Magnet	b_{2n+1}	b_{2n}	a_{2n+1}	a_{2n}
Tevatron	0.128	0.052	0.070	0.052
HERA	0.122	0.020	0.024	0.058
RHIC	0.052	0.006	0.008	0.032
LHC	0.054	0.001	0.018	0.026

We propose here to explain the origin of the pattern of the sigma of the field error in quadrupoles by using a direct method assuming four realistic modes of random displacements of the coils. Three of them are shown in Figure 46. Definitions of the vocabulary and of the coil numbering system used in the following are defined in Figure 45.

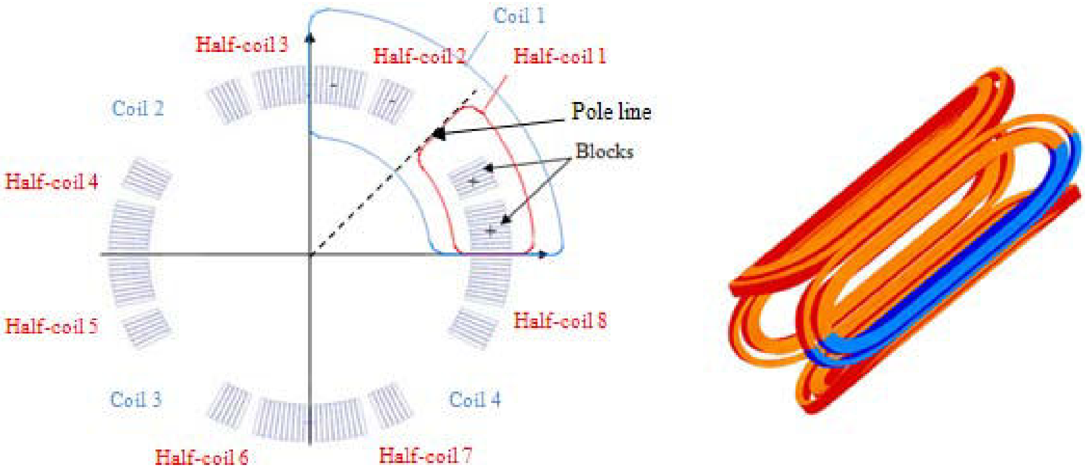

Figure 45 - Left: Definition of a coil, a half-coil and a block in a quadrupole. Signs indicate the current direction. Right: Isometric front view of a quadrupole winding. One of the 8 half-coil forming the quadrupole coil is in blue.

The four modes of realistic displacements considered are:

- Random displacement of the 8 half-coils independently from one to another.

- Coupled random displacement of the two half-coils constituting a coil so that the symmetry of the coil with respect to the pole line is always respected. Displacements of half-coils from one coil to another are decoupled. See for instance Figure 46 left.

- Random displacement of the mid-planes all independent from one another (since in reality one cannot control its location). See for instance Figure 46, 2nd from the left.

- Random displacement of the 8 half-coils assuming a perfect coupling so that the quadrupolar symmetry is always respected. This could be induced by the uncertainty in the collar inner radius or the uncertainty in the azimuthal length of the coil (see Figure 46 right).

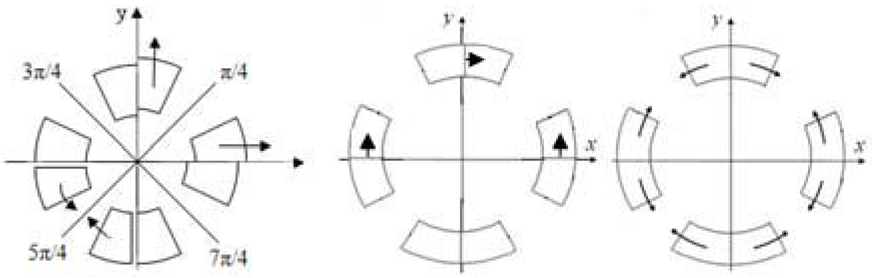

Figure 46 – Example of three of the four modes of displacements used to explain the variability of the sigma of the field error.

Analytical calculations have been carried out for each mode (see Annex F) and leads to Table 5. In this table, we expressed the field error in the whole quadrupole only in terms of $\sigma a_{1,n}$ and $\sigma b_{1,n}$ [unit] the skew and normal components of order n of the field error produced by random displacement of half-coil number one (according to the numbering system set up in Figure 45) and defined as

$$\sigma a_{1,n} = \frac{\sigma A_{1,n}}{B_2} \tag{162}$$

where $\sigma A_{1,n}$ is the spread of the field error expressed in [T] and B_2 is the main field of the quadrupole generated by the four coils and which can be considered as unchanged when half-coils are slightly displaced. According to the results shown in Table 5 one can see that:

- The four modes of random displacements of the 8 half-coils generate normal and skew harmonic of odd orders in equal quantity. This is consistent with what is observed in measurements.

- Random displacements of the 8 half-coils all independent from one another generate different normal and skew multipoles of even order. However, according to numerical simulation, the difference between sigma of normal and skew multipoles is very small.

- A coupled random displacement of the two half-coils constituting each one of the four coils so that the coil symmetry with respect to their pole line is respected generate no skew multipoles of order 6, 10, 14, … and no normal multipoles of order 4, 8, 12, …

- Random displacements of the coil mid-planes all independent from one another generate no normal multipoles of even order.

- As easily guessed, a coupled random displacement of the 8 half-coils so that the four-fold symmetry of the quadrupole is not broken generates only allowed harmonics.

Results found here enable explaining the origin of the pattern of the sigma of the field errors in superconducting quadrupoles. Note that all the results drawn here have been obtained considering coil displacement but are also valid when considering coil deformations. From this study and by means of a Monte-Carlo method similar to the one presented before, one could possibly provide an estimate of the amplitude of the displacement in each mode. This has not been done here due to lack of time. Moreover, from guessed value of the coil-blocks displacement and/or deformation one can easily, by means of formulae in Table 5, provide an estimate of the spread for each harmonic. This can be very useful tool at the early stage of a magnet design where the magnet designer has to provide a field error estimate.

Table 5 – effect of four modes of coil defect in superconducting quadrupole on the field error

Harmonics order	Standard deviation of the multipoles							
	Random defects on the position of half-coils		Random defects on coils Symmetric wrt. the pole line		Random defect on the mid-plane position		Quadrupolar-type random defects	
	Skew	Normal	Skew	Normal	Skew	Normal	Skew	Normal
n = 1, 5, 9, …	$2\sqrt{\left(\sigma a_{1,n}\right)^2+\left(\sigma b_{1,n}\right)^2}$		$2\sqrt{\left(\sigma a_{1,n}\right)^2+\left(\sigma b_{1,n}\right)^2+\rho_a\left(\sigma a_{1,n}\right)\left(\sigma b_{1,n}\right)}$		$2\sqrt{2}\sigma a_{1,n}$		0	0
n = 2, 6, 10, …	$2\sqrt{2}\sqrt{\left(\sigma a_{1,n}\right)^2}$	$2\sqrt{2}\sqrt{\left(\sigma b_{1,n}\right)^2}$	0	$4\sigma b_{1,n}$	$4\sigma a_{1,n}$	0	0	$8\sigma b_{1,n}$
n = 3, 7, 11, …	$2\sqrt{\left(\sigma a_{1,n}\right)^2+\left(\sigma b_{1,n}\right)^2}$		$2\sqrt{\left(\sigma b_{1,n}\right)^2+\left(\sigma b_{1,n}\right)^2-\rho_a\left(\sigma b_{1,n}\right)\left(\sigma b_{1,n}\right)}$		$2\sqrt{2}\sigma a_{1,n}$		0	0
n = 4, 8, 12, …	$2\sqrt{2}\sqrt{\left(\sigma a_{1,n}\right)^2}$	$2\sqrt{2}\sqrt{\left(\sigma b_{1,n}\right)^2}$	$4\sigma a_{1,n}$	0	$4\sigma a_{1,n}$	0	0	0

.

IV.5 Estimate of the amplitude of the blocks displacement in Nb3Sn magnets

IV.5.1 Analysis of the HFDA dipole

The HFDA dipole has been designed as a part of the FNAL high field magnet program in support of the R&D effort for the Very Large Hadron Collider (VLHC). It is based on the Nb_3Sn technology using the wind-and-react method and aims at producing a bore field above 10 T [59] [94] [103]. The design is based on a two layers coil with a 43.5 mm diameter bore (see Fig. 3) surrounded by a cold iron yoke. The cable width is ~15 mm, thus giving a coil width of ~30 mm. Six nearly identical 1-m-long dipole models, named HFDA02 to HFDA07, have been built and tested. The magnets have the same cross-section and same cable geometry.

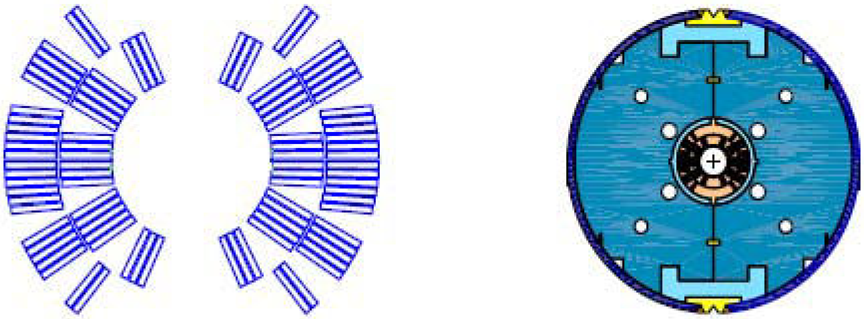

Figure 47 – Coil (left) and cold-mass (right) cross-section of the HFDA dipole cold-mass [59].

The six models use different mid-plane and radial shims to optimize the coil pre-stress (*i.e.,* to compensate for different coil sizes), which is a very sensitive when relying on Nb3Sn conductor. This obviously increases the spread in the field harmonics. This effect is subtracted by using the sensitivity tables of multipoles versus shim size evaluated through an electromagnetic model. The strand for the first three models HFDA02-04 was produced using the Modify Jelly Roll (MJR) process, while the three last models HFDA05-07 use Powder-in Tube (PIT) strands. The diameter of both strands and the cable geometry are the same and therefore it should not affect the field quality. The geometric harmonics of the six magnets, presented in Table 6 for a reference radius of 10 mm, are obtained averaging the multipole values between the current up and down ramps at 3 kA to subtract the coil magnetization and the iron yoke hysteresis effects. The magnets were pre-cycled up to a high current prior to each measurement to remove any possible magnetization history effect.

Using the Monte-Carlo method described in the previous section, we obtain an estimate of the spread in the position of the coil of 0.13 mm (see Figure 48). This number is about 2 times larger than what obtained for the Tevatron dipoles, and 5 times larger than for the LHC dipoles. Here, we have to point out that we are comparing a stable series production of a well–established technology with a new technology used in a few models. The data split according to the different families are shown in Table 7.

Unfortunately, no measurement of the spread along the axis is available and therefore we cannot separate in this 0.13 mm estimate the part coming from the spread from coil to coil from the part coming from the variation along the axis.

Table 6 – Integral harmonics of the 6 models HFDA02-07, average between up and down ramp at 3 kA, and standard deviation

HFDA	02	03	04	05	06	07	Std. dev.
b2	4.1	-7.13	0.75	4.59	-3.63	0.42	4.53
b3	-4.0	-2.36	8.28	1.16	3.78	5.52	4.71
b4	0.4	-0.19	0.16	0.79	-1.52	-0.02	0.79
b5	0.0	-0.53	-0.34	1.94	1.20	1.35	1.02
b6	0.0	0.12	0.02	0.22	-0.30	-0.06	0.18
b7	0.1	0.04	0.49	0.29	0.17	0.09	0.17
b9	-0.2	-0.01	-0.15	0.1	0.07	-0.08	0.12
a2	-9.6	1.93	12.56	-0.45	-8.22	1.57	8.04
a3	-0.2	0.81	-0.25	0.90	1.10	0.91	0.60
a4	-1.1	-0.75	0.06	-1.97	-1.31	0.67	0.96
a5	0.3	0.04	0.11	0.26	0.25	0.06	0.11
a6	0.3	0.03	-0.01	-0.28	-0.39	0.09	0.25
a7	-0.1	0.03	-0.03	0.03	0.08	0.03	0.06
a9	-0.2	0.04	-0.07	-0.01	-0.10	0.21	0.14

Table 7 – Estimate of the reproductibility of the coil positioning (in mm) in the production of superconducting dipoles for HFDA, average values and split among the different multipole families.

	b2n+1	b2n	a2n+1	a2n	all
HFDA	0.274	0.124	0.047	0.180	0.130

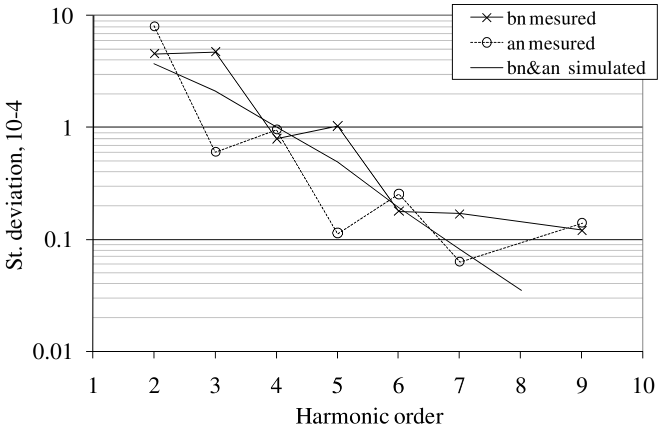

Figure 48 – Standard deviation of the multipoles of the 6 HFDA Nb3Sn dipole magnets (data points), and estimate of the standard deviation for a random movement of the blocks of 0.13 mm (solid line) (R_{ref} = 10 mm)

An indirect cross-check of this result comes from the measurement of the coils position in the HFDA02 cross-section carried out at Fermilab on a slice of the magnet using an optical system [59]. For each block, one has four measurements (one per quadrant), and average and standard deviations are computed. The standard deviations are given in Table 8. The block numbering starts from the inner layer mid-plane block, and ends at the outer layer pole block. The average random displacement for each one of the three degrees of freedom defined in Figure 40 ranges from 0.05 mm for the tilt, to 0.12 for the azimuthal movement. Summing the three values in quadrature one obtains 0.15 mm, *i.e.,* a value closes to the estimate based on the analysis of magnetic measurements.

Table 8 – Estimate of the reproductibility of the coil positioning in the production of superconducting dipoles for HFDA, average values are split among the different multipole families defined in Figure 40.

Block	Δr (mm)	$\Delta\varphi$ (mm)	$\Delta\alpha$ (mm)
1	0.110	0.173	0.061
2	0.115	0.120	0.050
3	0.076	0.090	0.035
4	0.090	0.122	0.089
5	0.062	0.129	0.047
6	0.012	0.092	0.028
average	0.078	0.121	0.052

IV.5.2 Analysis of the TQ quadrupole

Ninety-mm aperture Technological Quadrupoles (TQ) [29] [43] have been designed in the frame-work of the LARP program aiming at demonstrating the viability of Nb_3Sn quadrupole magnets for the upgrade of the LHC interaction regions. The TQ coil cross-section is made of two layers wound with a 10 mm width cable (see Figure 49).

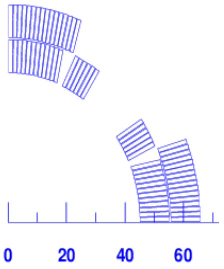

Figure 49 – Cross-section of one coil of the TQ quadrupole coil.

Two different coil support structures have been studied for the same coil cross-section: the TQS and TQC types (see Figs. 5 and 6). The TQC coil is pre-stressed and supported by round stainless steel collars, 2-piece iron yoke and stainless steel skin [43] while the TQS coil is pre-stressed by thick aluminum cylinder through 4-piece iron yoke [29]. Since the TQ program has been launched, two TQS (TQS01a/b/c and TQS02a/b/c) and two TQC (TQC01a/b and TQC02a/b/e) quadrupole magnets have been built and tested. The versioning of the magnets (a-b-c) is related to a reassembly of the magnet and replacement of coils. TQC02e denotes a quadrupole based on the collar structure that used coils which were already tested in TQS02. Since we are interested in the spread of the coil positioning caused by assembly and components, we carried out a simulation on the spread evaluated on the available data, namely four TQS and three TQC.

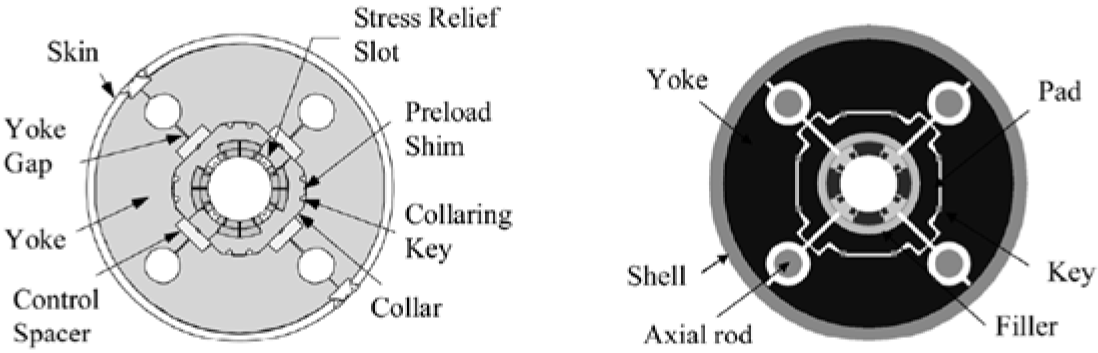

Figure 50 – Cross-section of the 90 mm aperture TQC-type (left) and TQS-type (right) quadrupole magnets [94].

TQS and TQC have a different design and cross-section of the yoke but the same coil, which cause a difference in b_6 and b_{10}. This difference is subtracted to have a homogeneous set of data. The available data and the spread are given in Table 9. The best fit of the MonteCarlo is shown in Figure 51. The corresponding spread in the coil positioning is 0.144 mm. Also in this case, this is at least a factor 5 worse than what is obtained for a mature production of Nb-Ti quadrupoles.

Table 9 – TQ integral harmonics at 45 T/m, R_{ref} = 22.5 mm. Calculated values of b_6 and b_{10} are substracted.

	TQC			TQS				
n	01a	02e	02a	01a	02a	02b	02c	St. dev.
b3	0.99	-0.01	-3.40	-1.49	1.90	0.60	-2.62	1.97
b4	-0.07	0.41	2.07	-1.13	1.28	2.38	3.26	1.53
b5	2.89	4.65	-5.33	-0.83	2.66	-0.46	-1.11	3.33
b6	-6.28	-7.12	-7.03	-6.33	-6.75	-7.25	-7.88	0.56
b7	0.13	-0.10	-0.11	0.19	0.00	0.11	-0.19	0.14
b8	-0.06	0.08	0.20	-0.05	-0.29	0.02	0.01	0.15
b9	-0.04	-0.07	0.21	0.12	0.15	-0.04	0.04	0.11
b10	0.02	0.24	0.12	0.22	0.10	0.33	0.30	0.11
a3	-1.54	0.43	-2.95	3.64	2.55	-7.02	-6.62	4.19
a4	-0.63	-2.33	4.38	-3.34	-5.87	0.73	0.85	3.33
a5	5.00	8.35	6.83	-0.78	-0.38	1.17	-1.33	3.97
a6	0.03	0.52	-1.58	-0.26	-0.08	-0.61	0.79	0.78
a7	0.07	-0.50	-0.22	-0.29	-0.15	0.06	-0.02	0.21
a8	0.12	0.26	-0.48	-0.16	-0.56	0.13	-0.08	0.31
a9	-0.04	-0.24	-0.33	-0.01	-0.05	0.04	0.00	0.14
a10	-0.01	0.04	0.03	0.02	-0.09	0.00	0.02	0.04

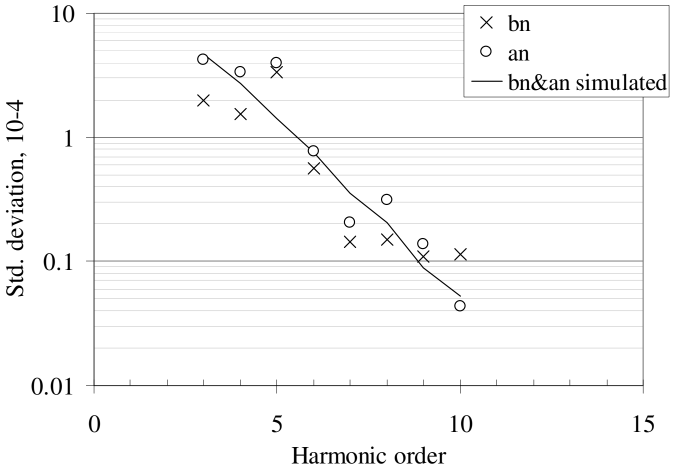

Figure 51 – Standard deviation of six TQ magnets (markers), and best fit through simulation (lines) with *d*=0.144 mm.

A few TQ models (TQS01a, TQS02a, TQC02a and TQC02e) have also been measured with 100 mm long rotating coils; in this case we have 5 measurements in consecutive positions that are in the so-called straight part of the magnet. A spread computed over five measurements can provide a rough estimate of the precision of the coil positioning along the magnet axis. Results are shown for TQC02e in Figure 52: the fit gives a spread in the coil position of 0.036 mm. For other three magnets one finds similar values, see Table 10. One can draw the following conclusions:

- The spread along the axis measured with a 100-mm long-mole in Nb3Sn quads is similar to what is measured in the main LHC dipoles with a 125-mm long-mole.
- The reproducibility of the position of 0.14 mm estimated through the spread of the integrals is dominated by the spread from coil to coil, and not from the spread along the axis. The contribution along the axis, integrated over the 0.8 straight part of the magnet, gives about 0.015 mm, *i.e.,* one order of magnitude less.

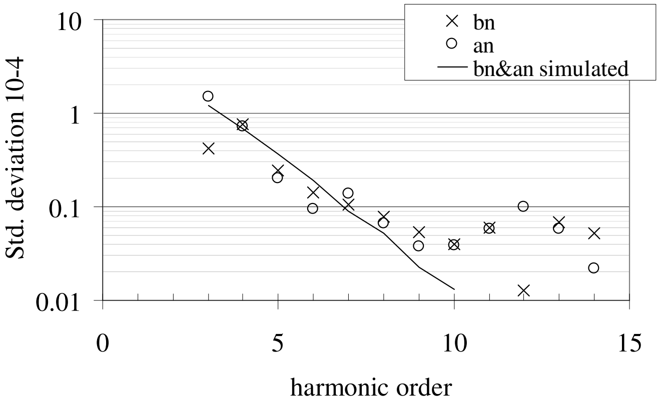

Figure 52 – Standard deviation of multipoles (data points) along the axis of TQC02e, (measurements with a 0.1 m long coil at 22.5 mm reference radius), and Monte Carlo best fit with 0.036 mm spread in the coil position (lines).

Table 10 – Estimate of the reproductibility of the coil positioning along the axis for the three TQ quadrupoles.

Magnet	d (mm)
TQS01a	0.042
TQS02a	0.045
TQC02a	0.064
TQC02e	0.036
LHC dipoles	0.030

IV.6 Uncertainty of the field errors in superconducting quadrupoles

The usual method to estimate the uncertainty in the mean due to geometric errors relies on field computations where blocks of conductors constituting the winding are radially or azimuthally displaced by 0.025-0.050 mm [50]. These errors are then added in absolute value or quadratically to obtain the uncertainty in the mean (δa_n or δb_n). This method usually tends to overestimate what we have in real magnets. Here, we investigate the values of the uncertainty in the mean obtained from integrated field errors measurements performed on 7 series of superconducting quadrupoles for the LHC and 5 series for RHIC. We only consider non-allowed harmonics so that uncertainties in the mean coincide with the mean of the field measurements. A method to estimate the expected uncertainty in the mean in a magnet series is presented.

Main geometrical features of the quadrupoles series studied here are summarized in Table 11. The mean and sigma values of the field errors of each series are given at a reference radius taken as 2/3 of the aperture diameter in Annex C and are shown in semi-logarithmic plots in Figure 53 and in Figure 54. Magnetic measurements have been performed by means of a rotating coil at room temperature for the LHC MQ, the LHC MQM, the LHC MQMC/L, and the RHIC MQ [4]. The three MQM quadrupole-types (MQM, MQMC and MQML) have the same cross-section but differ in length [63]. For the LHC MQY [57] MQXA [2] and MQXB [95] and for the RHIC Q1/2/3 [4] magnetic measurements have been performed at operational temperature (1.9 K for the LHC magnets and 4.2 K for the RHIC magnets) and at nominal current. As for the LHC MQM, the RHIC quadrupoles named Q1, Q2 and Q3 have similar cross-section but differ in length. Harmonic orders are considered up to the order 10 because of the lack of precision of the measurement system for higher order.

Table 11 – Main geometric features of the LHC and RHIC quadrupole magnets considered in our study.

	Magnet	Ap. Diameter (mm)	Magnetic length (m)	Number of magnets	Number of apertures
LHC	MQ	56	3.1	400	2
	MQY	70	3.4	12	2
	MQXA	70	6.37	19	1
	MQXB	70	5.5	9	1
	MQM /C/L	56	2.4/3.4/4.8	46/15/38	2
RHIC	Q1/2/3	130	1.44/3.40/2.10	26/27/13	1
	MQ	80	1.11	380	1

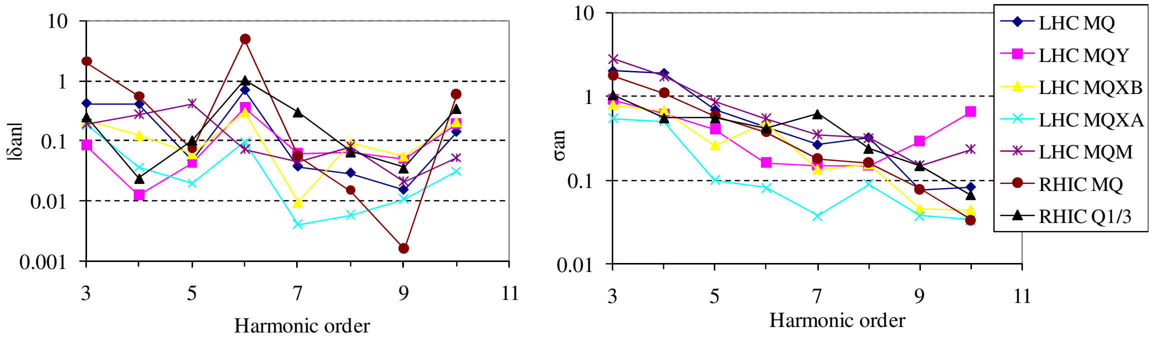

Figure 53 – Semi-logarithmic plot of the uncertainty in the mean (left), and the standard deviation (right) of the skew geometric field errors measured on 7 series of the LHC quadrupoles, and on 5 series of the RHIC quadrupoles. Harmonic have all been rescaled at a reference radius taken as 2/3 of the aperture radius.

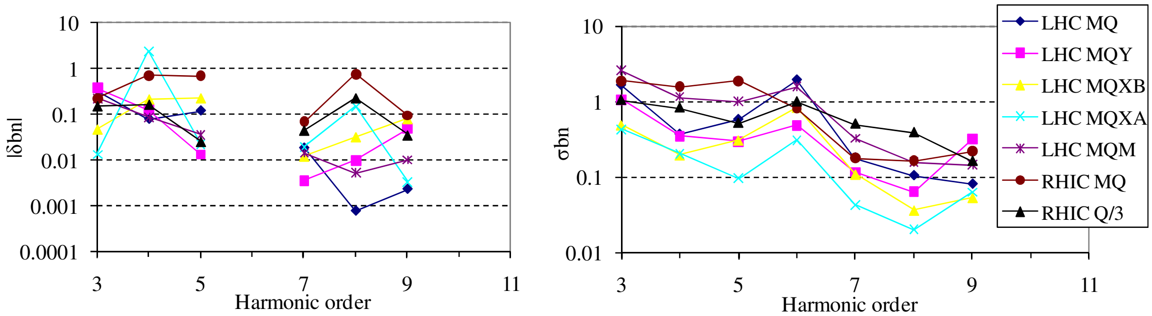

Figure 54 - Semi-logarithmic plot of the uncertainty in the mean (left), and the standard deviation (right) of the normal geometric field errors measured on 7 series of the LHC quadrupoles, and on 5 series of the RHIC quadrupoles. Note the allowed harmonic orders have been removed for |δb_n|. Harmonic have all been rescaled at a reference radius taken as 2/3 of the aperture radius.

Let us assume that each series of quadrupoles is a sample taken in a much larger series featuring a mean value of the field harmonic errors denoted by m (m_{an} and m_{bn} for the skew and normal harmonics, respectively). The mean value of the sample, denoted by δ, (δa_n and δb_n for the skew and normal harmonics, respectively) is an estimated value of m given within the range of confidence calculated by means of [56]

$$m - t\frac{\sigma}{\sqrt{N}} < \delta < m + t\frac{\sigma}{\sqrt{N}}, \tag{163}$$

where σ is the sigma of the field error of the sample, and N is the number of magnets in the sample. The parameter t is given by the Student table (since σ is calculated for the sample) for N-1 degrees of freedom and for a probability α for δ to be in the range of confidence (see expression below).

$$P\left[m - t\frac{\sigma}{\sqrt{N}} < \delta < m + t\frac{\sigma}{\sqrt{N}}\right] = \alpha. \tag{164}$$

Ideally, in a quadrupole series one should have m = 0 for all non-allowed multipoles. With this assumption, Eq. (164) becomes

$$P\left[\frac{|\delta|\sqrt{N}}{t\sigma} < 1\right] = \alpha, \tag{165}$$

i.e., the probability to have $\frac{|\delta|\sqrt{N}}{t\sigma} < 1$ is of α. Examples of measurements consistent or not with Eq. (165) are shown in Figure 55.

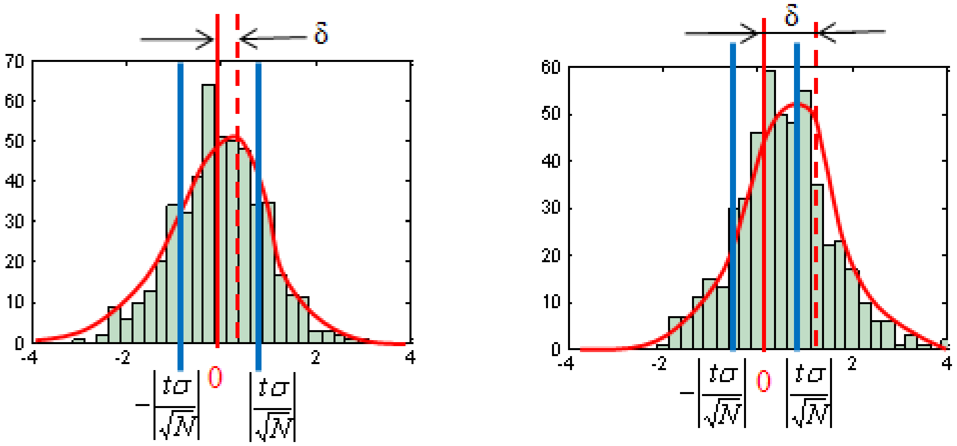

Figure 55 – Examples of measurements consistent (left) or not (right) with the hypothesis of a mean value of zero.

In Table 12 we provide, by means of the Student table [56], the t value for each magnet series and considering a probability for δ to be in the range of confidence of 99.9 %. From these values of t we calculate the quantity $\frac{|\delta|\sqrt{N}}{t\sigma}$ for each harmonic order and type (see Table 13). Ratios $\frac{|\delta|\sqrt{N}}{t\sigma}$ which are smaller than one (yellow boxes in Table 13) agree with our hypothesis of a mean value over a large number of magnets which tends to be zero (m=0). Ratios larger than one disagree with our hypothesis (red boxes in Table 13) and clearly indicate that there is a systematic defect in quadrupoles of the series resulting in systematic non-allowed harmonic errors which add up coherently.

Table 12 – Values of the parameter *t* obtained from the Student table [56] and for a probability for $\frac{|\delta|\sqrt{N}}{t\sigma}$ to be below one of 99.9 %.

	LHC							RHIC			
	MQ	MQY	MQXA	MQXB	MQM	MQM C	MQM L	Q1	Q2	Q3	MQ
Nb magnets	400×2	12×2	19	9	45×2	15×2	38×2	26	27	13	380
t	3.291	3.767	3.922	5.041	3.46	3.659	3.46	3.725	3.707	4.318	3.291

Table 13 – Ratio $\frac{|\delta|\sqrt{N}}{t\sigma}$ calculated for non-allowed harmonics of each series of quadrupoles of the LHC and RHIC. Yellow boxes means that the mean value of the harmonic is within the estimated range of confidence $\left(\frac{|\delta|\sqrt{N}}{t\sigma} < 1\right)$. Red boxes correspond to $\frac{|\delta|\sqrt{N}}{t\sigma} > 1$.

	LHC							RHIC			
Nb	400×2	12×2	9	19	45×2	15×2	38×2	26	27	13	380
Multipole	MQ	MQY	MQXB	MQXA	MQM	MQMC	MQML	Q1	Q2	Q3	MQ
a3	0.7	0.1	0.2	0.4	0.1	0.0	0.1	0.2	0.2	0.3	0.6
a4	2.0	0.0	0.1	0.1	0.1	0.2	0.1	0.0	0.3	0.2	0.3
a5	1.7	0.1	0.1	0.2	0.4	0.4	0.6	0.1	0.1	0.2	0.1
a6	12.8	2.8	0.4	1.3	0.2	0.2	0.0	3.2	0.2	1.9	7.1
a7	0.3	0.5	0.0	0.1	0.2	0.0	0.1	0.4	0.3	0.2	0.2
a8	1.4	0.5	0.4	0.1	0.2	0.2	0.3	0.3	0.1	0.1	0.1
a9	0.4	0.2	0.7	0.3	0.0	0.2	0.2	0.2	0.0	0.2	0.0
a10	13.2	0.4	2.8	1.0	0.0	0.3	0.1	4.7	1.3	2.0	9.6
b3	0.2	0.5	0.1	0.0	0.0	0.1	0.1	0.2	0.1	0.0	0.1
b4	1.0	0.5	0.6	13.4	0.0	0.2	0.0	0.2	3.4	0.3	0.2
b5	0.3	0.1	0.4	0.3	0.0	0.0	0.1	0.0	0.2	0.5	0.2
b6	26.1	14.6	0.2	4.2	4.4	4.4	4.3	1.9	0.7	6.3	5.1
b7	0.0	0.0	0.1	0.5	0.1	0.0	0.1	0.1	0.1	0.2	0.2
b8	0.9	0.2	0.5	8.1	0.0	0.1	0.0	0.4	0.8	0.0	2.6
b9	0.8	0.2	0.9	0.1	0.1	0.0	0.1	0.2	0.0	0.4	0.2
b10	23.7	5.9	0.9	2.5	1.5	0.9	1.7	0.3	2.8	5.1	9.9

One can clearly see that for the skew harmonic order different from 6 and 10, except for LHC MQ, the value of the measured uncertainty δ is compatible with the hypothesis of no systematic errors, *i.e.,* m=0. This is consistent with our assumption of a mean value of the harmonics of zero. However, for the skew harmonic of rank 6 and 10, one notices that there are several cases where δ is outside the range of confidence, thus indicating a systematic defect. This is partly due to the connection side of the coil end which produces skew harmonics of order 6 and 10 as it is the case for the RHIC [98]. For the LHC MQ quadrupoles, the integrated harmonic field errors in the straight part of the coil are available and lead to the Table 14 where we can see that the ends contribution partly explains the large δa_6 and δa_{10} values.

Table 14 – Ratio $\frac{|\delta|\sqrt{N}}{t\sigma}$ calculated for the skew harmonics errors of the LHC MQ quadrupoles series, either in the straight part (ends excluded) or over the whole magnet length (ends included).

n	ends excluded	ends included
3	0.6	0.7
4	1.1	2.0
5	0.5	1.7
6	5.7	12.8
7	0.5	0.3
8	1.4	1.4
9	0.1	0.4
10	5.7	13.2

For the normal harmonics, one notice that all mean values are within the range of confidence except for b_4 and b_8. This can be explained by the method of collaring used. Indeed, collaring a quadrupole in a dipole way tends to break the fourfold symmetry of the magnet and produce b_4 and b_8 components which add up coherently in a magnet series. This is what has been observed in the LHC MQXA and RHIC MQ where unexpected large b_4 and b_8 values have been measured [84] [98]. Note that in these magnets, collars are consistent with the fourfold symmetry but the iron yoke, which provides part of the pre-stress in the coil, is made of two pieces, *i.e.,* a dipole symmetry. Others magnets which have been collared in an asymmetric way are the LHC MQXB, the RHIC Q1/2/3 and the RHIC MQ. Therefore, for all non-allowed harmonics except a_6, a_{10} and b_4, b_8 (only for quadrupole collared in a dipole way), the hypothesis of a mean value which tends to be zero when increasing the number of magnets of the series held. In other word, the non-zero measured uncertainty δ is due to the finite size of the sample of magnets.

IV.7 Summary

In this chapter we studied the reproducibility that can be obtained in positioning the coil in superconducting magnets made with Nb_3Sn, and we compared it to the results relative to the standard technology based on Nb-Ti. This reproducibility usually sets the ultimate limit to the field quality that can be achieved in superconducting magnets for high energy particle accelerators.

The computations are based on an inverse method that makes use of a MonteCarlo analysis: the relation between the spread in the coil position and the spread in the field harmonics is evaluated with a standard code that implements the Biot-Savart law. Then, the spread in the integral field harmonics measured over a homogeneous series of magnets is associated with a spread in the coil position through a best fit. Some care must be taken to separate the component coming from the variation along the magnet axis, which depends on the magnet length, from the part that varies from coil to coil. To separate these two effects one needs to have not only the integral measurements for each magnet, but also the local measurement over a longitudinal section of the magnet.

Reference values set by the Nb-Ti technology used in high energy particle accelerators have been reviewed. For both dipoles and quadrupoles manufactured in the past 15 years the measured spread in field harmonics corresponds to a coil position reproducibility (from magnet to magnet) of 0.030 to 0.015 mm, reaching a minimum of 0.010 for the LHC MQXA. These values are obtained for a mature technology and for a stable production of several units (20 to 1000) of the same objects. Oldest magnets, namely Tevatron and HERA dipoles, have a larger spread of 0.040 to 0.065 mm. Measurements with a short mole on the LHC dipoles indicate that the contribution coming from the spread along the axis is negligible for these long magnets, and that these values do not depend on the magnet length.

For Nb_3Sn accelerator magnets, the analysis was performed on two small series of 1-m-long R&D models which include six 43.5-mm-aperture HFDA dipoles and six 90-mm-aperture TQ quadrupoles. We obtain a spread of 0.13 mm for the dipoles and 0.14 mm for the quadrupoles. In the first case, the estimate based on the magnetic measurements is in good agreement with an optical measurement carried out over a slice of the magnet. Part of the difference between the Nb-Ti and the Nb_3Sn values are due to the fact that we are comparing a few R&D short models with a mass production. Therefore, it is premature to conclude that the Nb_3Sn technology is intrinsically providing a worse field quality than the Nb-Ti. There is still the potential of an improvement of a factor 5-10.

We also analyzed the spread in the coil position along the axis of the same magnet. As for Nb-Ti long dipoles, this quantity does not affect the spread from magnet to magnet and therefore the 0.14 mm estimate does not depend on the fact that we are considering very short models. On the other hand, the 0.03 mm spread along the axis obtained with a 100 mm long mole for the TQ is very similar to what is obtained for the LHC dipole with a similar mole length (125 mm). This means that the homogeneity of the field quality along the axis of a Nb_3Sn magnet has reached the standards of the Nb-Ti technology.

We also investigated another topic related to the field quality: the uncertainty in the mean of the non-allowed harmonics of the field errors in series of superconducting quadrupoles. By design, non-allowed harmonics are zero. However, when analyzing magnetic measurements one usually finds that the mean is different from zero. This can be either due to systematic defects in the coil resulting in systematic field errors which add up coherently from magnet to magnet or to statistical effect due to the finite size of the sample. To find out whether the uncertainty in the mean is due to a systematic defect or due to a statistical bias, we used magnetic measurements performed on 11 series of Nb-Ti quadrupoles of the LHC and RHIC machines. For each series, we analyzed if the mean of the integrated field error is compatible with the hypothesis that the uncertainty is zero. We find out that in general this is the case, except for a_6, a_{10}, b_4 and b_8. We showed that for a_6 and a_{10} the mean is partly due to the asymmetry of the connection side of the magnets end. For b_4 and b_8 the uncertainty in the mean is not compatible with the hypothesis of a zero-mean only in quadrupoles which have a iron yoke made of two pieces instead of four and therefore is not consistent with the quadrupole symmetry.

V. Electromagnetic design of the quadrupole for the upgrade of the LHC interaction region

V.1 A novel method for coil optimization

V.1.1 Outline

One of the objectives during the design phase of the coil cross-section of a superconducting accelerator quadrupole magnet is to achieve a field homogeneity of the order of 10^{-4} through the optimization of several input parameters, *i.e.,* coil block dimensions and positions. Due to the complexity of the coil geometry, *i.e.* coil blocks made of cables and cables made of strands, it is usually not possible to perform a scan through all possible coil cross-sections for a given aperture, cable dimensions and number of layers. Coil optimization methods usually rely on optimization algorithms (such as genetic algorithm which allows finding local minima spread in the space of all possible solutions [74]. However, these methods cannot ensure that the derived minimum is a global one and cannot exclude the existence of better solutions.

Here, we propose a staged approach to coil design. We first approximate real coil lay-outs made of cable (see Figure 56, right) with pure sector blocks (sector delimited by lines going through the reference frame origin), having uniform current density (see Figure 56, left), so as to use explicit equations derived from the Fourier transform. This allows a very fast computation of the field harmonics, and therefore to find out rapidly the coil lay-outs which satisfy field quality requirements. The analytical knowledge of the magnetic field makes possible the computation of the short sample current and the corresponding gradient as well as the magnetic forces.

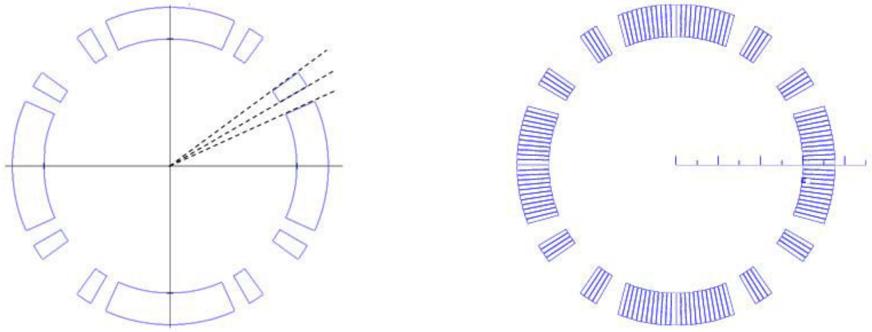

Figure 56 – Quadrupole cross-section with coils made of two pure sector blocks (left) and quadrupole with coils made of real arrangement of cables (right).

The originality of this method is that it can provide a global optimization for coils made of up to five blocks so that one can carry out an exhaustive analysis for these cross-sections, and thus easily spot the one which best fit with the specifications. The real coil is then obtained by approximating sectors with block of Rutherford cables. A further optimization on the position of the blocks by means of magnet design software such like Roxie enables the reduction of the unavoidable field harmonic distortions due to the discrete cable size. The method developed here is not aim at providing a substitute to magnet design software but is a complementary tool enabling a fast exploration of the space of possible solutions. Its limit is the number of blocks, *i.e.,* it cannot be used for more than five blocks since the number of free parameters to handle becomes too large. This method has been used to design a proposed cross-section for the new inner triplet quadrupole of the LHC.

V.1.2 Analytical model

The aim of a quadrupole is to provide a pure quadrupolar field. To reach this goal one has to cancel out the three first allowed multipoles *i.e.* b_6, b_{10} and b_{14} which are naturally not necessarily null in a quadrupole coil. Higher order multipoles can be neglected since they are naturally small. This is achieved by using coils made of more than one sector and by choosing appropriate angles for the angular position and dimension of the sectors constituting the winding.

In our model, we consider that a quadrupole with coils made of P sectors is obtained by superimposing P sub-quadrupoles defined as quadrupoles with coils made of one sector. For instance, in Figure 57 are shown the three sub-quadrupoles (pictures 1, 2 and 3 left) constituting the quadrupole with coils made of three sectors (right).

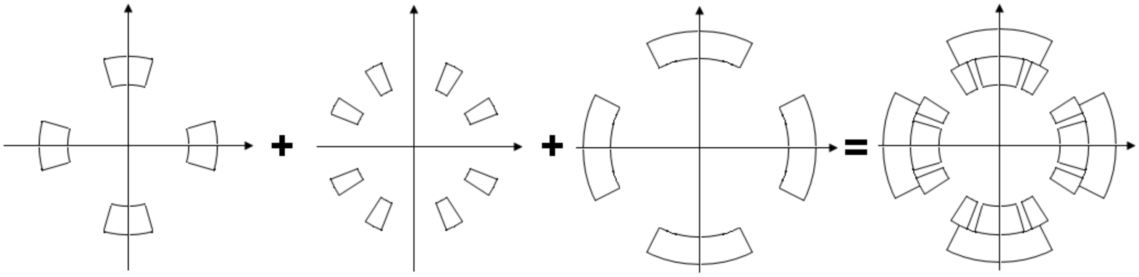

Figure 57 – Decomposition of a quadrupole with coils made of 3 sectors (right) into sub-quadrupoles with coils made of one sector.

Due to the linearity of the sum, the magnetic field produced everywhere, *i.e.,* in the coil and in the air, by the entire quadrupole is obtained summing up the contribution of each sub-quadrupole constituting the winding. This is particularly interesting if the current density is uniform in each sector (but can differ from sector to sector) since then one can use Fourier series presented in Section II.3.2 and giving the radial and azimuthal components of the magnetic field produce everywhere by a quadrupole with coils made of one sector. We recall these expressions for the quadrupole shown in Figure 58. Its coils are made of one pure sector of inner and outer radius R_1 and R_2 and delimited by the angles θ_1 and θ_2. Sectors are powered with a constant current density +/-j_0.

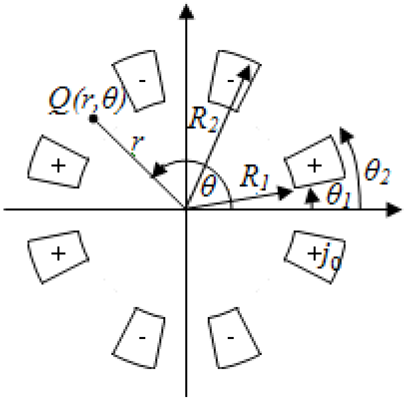

Figure 58 – Quadrupole with coils made of one pure sector.

The current density *j(θ)* flowing at the point *Q(r,θ)* of angular position *θ* and for any radius $r\epsilon[R_1, R_2]$ can be expressed through a Fourier series

$$j(\theta) = \sum_{n=1}^{\infty} j_0 \alpha_n \cos(n\theta), \tag{166}$$

where the Fourier coefficient α_n calculated for the coil shown in Figure 58 is given by

$$\alpha_n = \frac{8}{n\pi}[\sin(n\theta_2) - \sin(n\theta_1)]. \tag{167}$$

Note that due to the quadrupolar symmetry, $\alpha_n = 0$ for any order $n \neq 4k+2$, with $k\epsilon\mathbb{N}$. Therefore, expressions of the magnetic field produced in different regions delimited by the coil inner and outer radii are:

- **Magnetic field generated by the quadrupole for $r < R_1$**

For $n = 2$

$$B_r(r,\theta) = \sum_{n=2,6,10,\dots}^{\infty} -\frac{\mu_0 j_0 \alpha_2}{2} r \ln\left(\frac{R_2}{R_1}\right) \sin(2\theta) \tag{168}$$

$$B_\theta(r,\theta) = \sum_{n=2,6,10,\dots}^{\infty} -\frac{\mu_0 j_0 \alpha_2}{2} r \ln\left(\frac{R_2}{R_1}\right) \cos(2\theta) \tag{169}$$

and for $n > 2$

$$B_r(r,\theta) = \sum_{n=2,6,10,\dots}^{\infty} \frac{\mu_0 j_0 \alpha_n}{2} \frac{r^{n-1}}{(n-2)} \left(\frac{1}{{R_2}^{n-2}} - \frac{1}{{R_1}^{n-2}}\right) \sin(n\theta) \tag{170}$$

$$B_\theta(r,\theta) = \sum_{n=2,6,10,\ldots}^{\infty} \frac{\mu_0 j_0 \alpha_n}{2}\frac{r^{n-1}}{(n-2)}\left(\frac{1}{{R_2}^{n-2}} - \frac{1}{{R_1}^{n-2}}\right)\cos(n\theta) \tag{171}$$

- **Magnetic flux density generated by the quadrupole coil for *R*$_1$ < *r* <*R*$_2$**

For $n = 2$

$$B_r(r,\theta) = \sum_{n=2,6,10,\ldots}^{\infty} -\frac{\mu_0 j_0 \alpha_n}{2}\left[\frac{1}{4}\left(r - \frac{{R_1}^4}{r^3}\right) + r\ln\left(\frac{R_2}{r}\right)\right]\sin(2\theta) \tag{172}$$

$$B_\theta(r,\theta) = \sum_{n=2,6,10,\ldots}^{\infty} -\frac{\mu_0 j_0 \alpha_n}{2}\left[\frac{1}{4}\left(\frac{{R_1}^4}{r^3} - r\right) + r\ln\left(\frac{R_2}{r}\right)\right]\cos(2\theta) \tag{173}$$

and for $n > 2$

$$B_r(r,\theta) = \sum_{n=2,6,10,\ldots}^{\infty} -\frac{\mu_0 j_0 \alpha_n}{2}\left[\frac{1}{n+2}\left(r - \frac{{R_1}^{n+2}}{r^{n+1}}\right) - \frac{1}{n-2}\left(\frac{r^{n-1}}{{R_2}^{n-2}} - r\right)\right]\sin(n\theta) \tag{174}$$

$$B_\theta(r,\theta) = \sum_{n=2,6,10,\ldots}^{\infty} -\frac{\mu_0 j_0 \alpha_n}{2n}\left[\frac{1}{n+2}\left(2r + n\frac{{R_1}^{n+2}}{r^{n+1}}\right) - \frac{1}{n-2}\left(n\frac{r^{n-1}}{{R_2}^{n-2}} - 2r\right)\right]\cos(n\theta) \tag{175}$$

- **Magnetic flux density generated by the quadrupole coil for *r* > *R*$_2$**

For any n

$$B_r(r,\theta) = \sum_{n=2,6,10,\ldots}^{\infty} -\frac{\mu_0 j_0 \alpha_n}{2(n+2)}\frac{1}{r^{n+1}}\left[{R_2}^{n+2} - {R_1}^{n+2}\right]\sin(n\theta) \tag{176}$$

$$B_\theta(r,\theta) = \sum_{n=2,6,10,\ldots}^{\infty} \frac{\mu_0 j_0 \alpha_n}{2(n+2)}\frac{1}{r^{n+1}}\left[{R_2}^{n+2} - {R_1}^{n+2}\right]\cos(n\theta) \tag{177}$$

The additional magnetic field due to the presence of an infinitely permeable iron yoke of inner radius R_f set around the quadrupole coil can be calculated be means of the current image method [37] (see Figure 59).

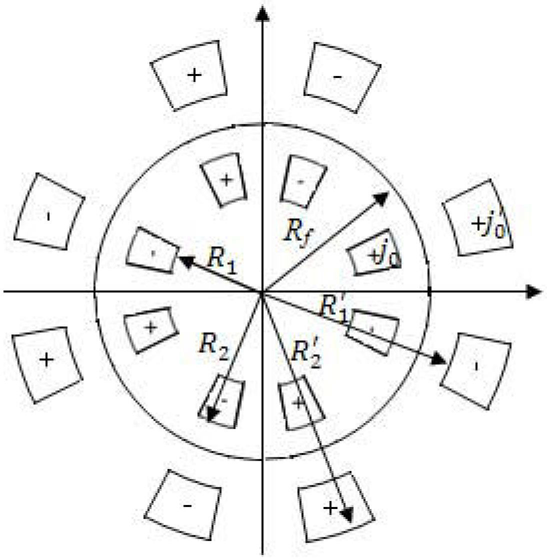

Figure 59 – Quadrupole of the Figure 58 surrounded by an infinitely permeable iron yoke of inner radius R_f. Outer coils are virtual coils obtained with the current image method.

The inner and outer radius R_1' and R_2' of the virtual coil providing the same contribution than an infinitely permeable iron yoke of inner radius R_f are given by

$$R_1' = \frac{R_f^2}{R_2} \qquad \text{and} \qquad R_2' = \frac{R_f^2}{R_1}, \tag{178}$$

and the current density j_0' flowing in the virtual coil is obtained from

$$\mathrm{j}_0' = \frac{\mu_\mathrm{r} - 1}{\mu_\mathrm{r} + 1} \frac{(\mathrm{R}_1 \mathrm{R}_2)^2}{\mathrm{R}_\mathrm{f}^4} \mathrm{j}_0 \tag{179}$$

- **Magnetic field due to the infinitely permeable iron yoke for *r* < R_f**

For *n* = 2

$$B_r(r,\theta) = \sum_{n=2,6,10,\dots}^{\infty} -\frac{\mu_0 j_0 a_2}{2} r \ln\left(\frac{R_2'}{R_1}\right) \sin(2\theta) \tag{180}$$

$$B_\theta(r,\theta) = \sum_{n=2,6,10,\dots}^{\infty} -\frac{\mu_0 j_0 a_2}{2} r \ln\left(\frac{R_2}{R_1}\right) \cos(2\theta) \tag{181}$$

and for *n* > 2

$$B_{n,r}(r,\theta) = \sum_{n=2,6,10,\ldots}^{\infty} \frac{\mu_0 j_0 a_n}{2} \frac{r^{n-1}}{(n-2)} \left(\frac{1}{{R_2}^{n-2}} - \frac{1}{{R_1}^{n-2}} \right) \sin(n\theta) \tag{182}$$

$$B_{n,\theta}(r,\theta) = \sum_{n=2,6,10,\ldots}^{\infty} \frac{\mu_0 j_0 a_n}{2} \frac{r^{n-1}}{(n-2)} \left(\frac{1}{{R_2}^{n-2}} - \frac{1}{{R_1}^{n-2}} \right) \cos(n\theta) \tag{183}$$

In Figure 60 we calculated by means of Eqs. (168) to (183) the magnetic field modulus in the air for a quadrupole with coils made of one 30º sector as shown in Figure 61, either surrounded by an iron yoke (left) or not (right). The maximal harmonic order considered in the computation is 100. Note that the calculation is fast because only harmonics of order 4*k*+1 (*k* positive integer) contribute to the magnetic field. Note also that the field computation in the yoke is not possible with the image current method.

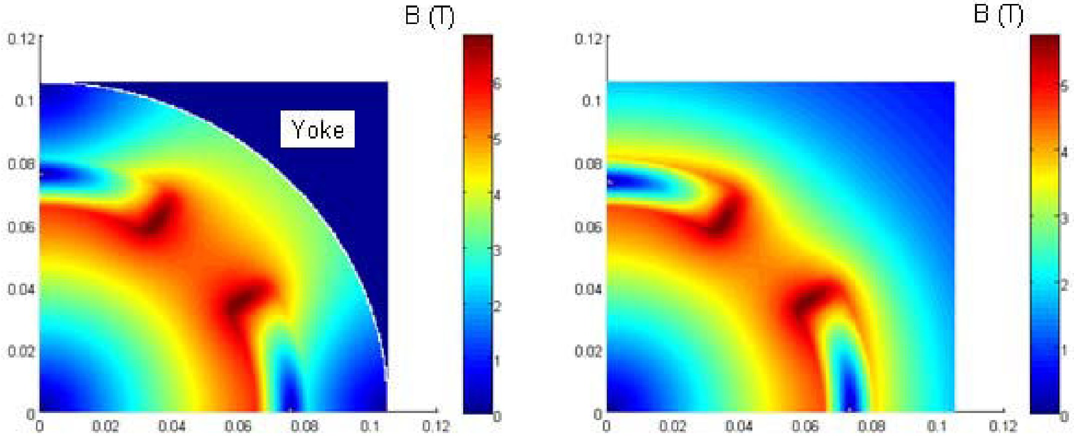

Figure 60 – Magnetic flux density computed with Matlab in the first quadrant of a quadrupole made of a single 30º sector coil surrounded by an iron yoke (left) or not (right). Expressions of the magnetic field, given from Eq. (168) to Eq.(183), have been considered up to *n* = 100. The inner radius and the width of the coil are of 60 mm and 15 mm.

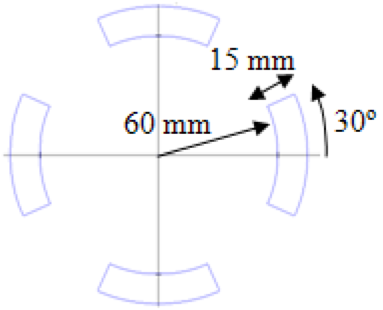

Figure 61 – Coil cross-section considered for the plot of the magnetic field modulus in Figure 60.

V.1.3 Multipoles optimization

Allowed harmonics generated in the aperture of a quadrupole composed of P sub-quadrupoles can be analytically calculated summing up the contribution of each sub-quadrupole. The sub-quadrupole number p ($p \epsilon [1; P]$) has coils made of one sector of inner and outer radius $R_{1,p}$ and $R_{2,p}$, delimited by the angles $\theta_{1,p}$ and $\theta_{2,p}$, and powered with a uniform current density j_p. The tangential component of the magnetic field produced at the reference radius $R_{ref} < R_{1,p}$ in such a quadrupole is expressed as [73]

$$B_{\theta,p}(R_{ref},\theta) = \sum_{n=1}^{\infty}\left[B_{n,p}\cos(n\theta) + A_{n,p}\sin(n\theta)\right]\left(\frac{r}{R_{ref}}\right)^{n-1}, \tag{184}$$

where $B_{n,p}$ and $A_{n,p}$ are the normal and skew harmonics of order n produced by the sub-quadrupole p and given at the reference radius R_{ref}. The expression of the harmonic coefficient $B_{n,p}$ can be obtained identifying Eqs. (169) and (171) with Eq. (184) when setting $\theta = 0$ in Eq. (184). For $n = 2$, $B_{n,p}$ writes

$$B_{2,p} = -R_{ref}\frac{\mu_0 j_p}{2} ln\left(\frac{R_{2,p}}{R_{1,p}}\right)\frac{8}{2\pi}\left[\sin(2\theta_{2,p}) - \sin(2\theta_{1,p})\right], \tag{185}$$

and for $n > 2$ it writes

$$B_{n,p} = \frac{\mu_0 j_p}{2}\frac{R_{ref}^{n-1}}{(n-2)}\left(\frac{1}{{R_{2,p}}^{n-2}} - \frac{1}{{R_{1,p}}^{n-2}}\right)\frac{8}{n\pi}\left[\sin(n\theta_{2,p}) - \sin(n\theta_{1,p})\right]. \tag{186}$$

The field harmonic B_n generated in the aperture of the quadrupole constituted of the P sub-quadrupoles is thus

$$B_n = \sum_{p=1}^{P} B_{n,p}. \tag{187}$$

The normalized multipole writes

$$b_n = 10^4\frac{B_n}{B_2} = 10^4\frac{\sum_{p=1}^{P} B_{n,p}}{\sum_{p=1}^{P} B_{2,p}}. \tag{188}$$

When designing a quadrupole coil the aperture radius, the cables width, and the number of layers are usually fixed parameters. Therefore, to find out all the possible coil layouts built with a given number of sectors and providing a good field quality, *i.e.,* b_6, b_{10} and b_{14} within 1 unit, one has to perform a scan through all the possible combinations of sector angular position and thickness. This can be achieved by implementing Eq. (188) into a numerical code like Matlab and proceeding following the staged approach proposed in Figure 62.

A quadrupole made of P sub-quadrupoles provides $2P$ angles to play with $\{\theta_1,\ldots\theta_{2p}\}$. We propose, as a first step, to fix ($2P$-1) angles and to vary, with a preliminary chosen angular step, the remaining angle within its physical limits *i.e.* sectors cannot overlap. For each analyzed coil layout we calculate the allowed multipoles of rank 6 and 10. Only the coil layout which gives the smallest quadratic sum of b_6 and b_{10} is kept and then is tested in term of field quality: the coil layout is stored if it generates multipoles b_6 and b_{10} within 1 unit. If the solution satisfies the field quality requirement on b_6 and b_{10}, then one is sure that we did not skip other good solutions obtained for different angles. Indeed, the condition for having two coil layouts allowing cancelling b_{10} and b_{14} is to have two different angles providing the same b_6 and the same b_{10}, thing which is impossible in the range where the scan is performed, *i.e.,* [0-π/4] (see Figure 63). Proceeding this way enables discarding all nearly identical coil layouts which could satisfy to the field quality requirement and to only keep the one which is the closest to the targeted field quality.

The same analysis is then repeated for all possible (2P-1) angles combinations. Note that the presence of an iron yoke around the coil is not taken into account here because it would double the computational time while having a limited impact on the multipoles. Also to reduce the computational time, the analysis of b_{14} is done only on coil layouts which already provide b_6 and b_{10} within 1 unit. Again, only coil layouts generating b_{14} within 1 unit are kept as potential solution for the magnet design.

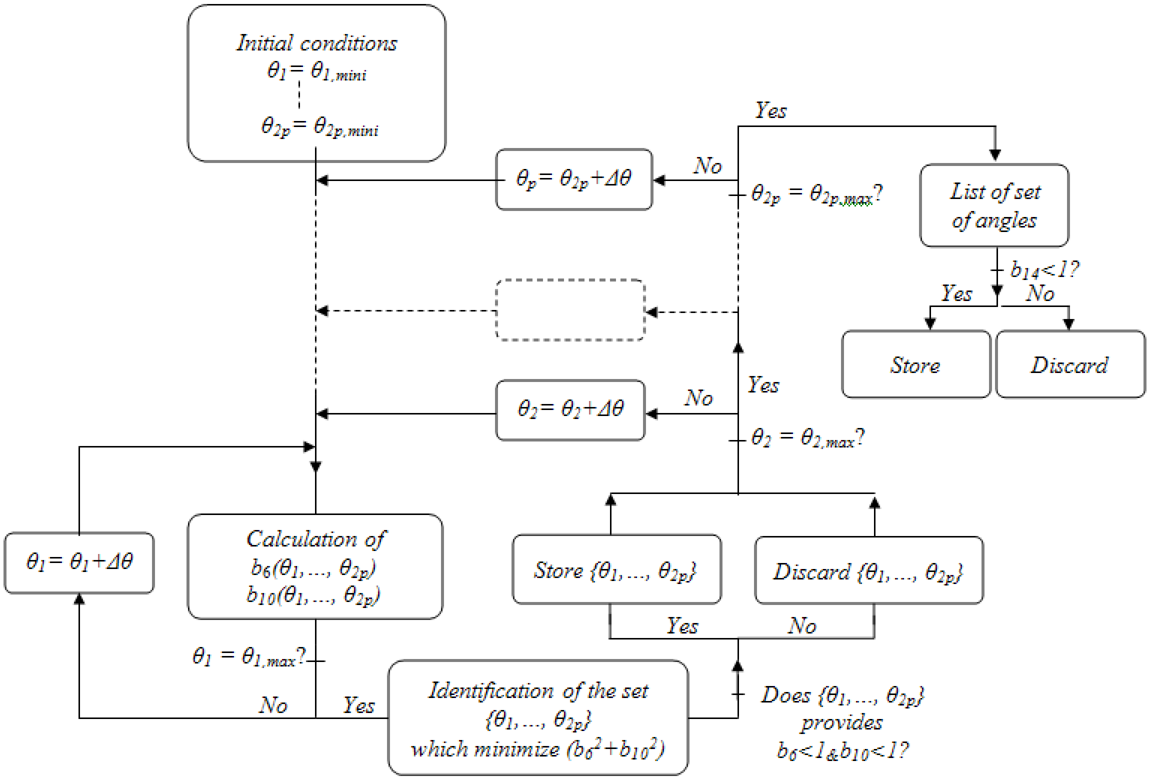

Figure 62 – Representation of the way to perform a complete scan on the sectors angles.

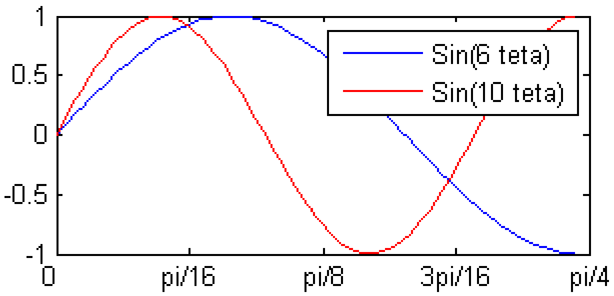

Figure 63 – Functions *sin(6θ)* and *sin(10θ)* plotted in the range where the sector angles vary.

The range within which sector angles vary can be reduced by taking into consideration that the role of a quadrupole is to provide a large gradient, and that the coil has to be feasible from the mechanical point of view. In a quadrupole, the major part of the field gradient is produced by the part of the coil located near the mid-plane. Inserting copper wedges in this area would make the gradient dropping dramatically. Therefore, we propose to close the mid-plane and to fix at 15° the minimal angular thickness of the sectors in contact with the coil mid-plane (see Figure 64). Note that closing the mid-plane allows reducing the space of the phase angles from $2P$ to $2P-q$, q being the number of layers constituting the coil. Moreover, in order to prevent damaging the cable when bended around the pole, we propose to limit the top angle of the coil at

$$\theta_{max} = \frac{\pi}{4} - \frac{S}{2R_{in}}, \tag{189}$$

where S [mm] is the azimuthal length of the inner radius of the pole nose and R_{in} [mm] the inner radius of the coil (see Figure 64). In the LHC main dipole, which uses the same cables than the new insertion quadrupole we have to design, one has S = 8.3 mm. This enables a reduction of the time computation while discarding either low field gradient solutions or impractical solutions.

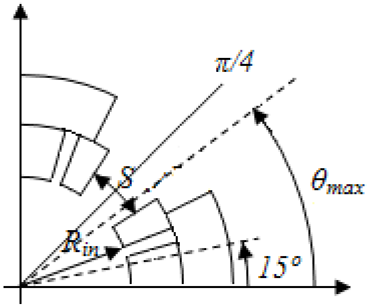

Figure 64 – Coil angles limitation allowing getting rid out of low gradient or impractical coil layouts.

Ideally, to guaranty that we did not skip coil layouts of good field quality when performing the scan one should chose an angular step $\Delta\theta$ such that the variation of the multipoles $\Delta b_6, \Delta b_{10}$ and Δb_{14} associated to $\Delta\theta$ are smaller or equal than 1 unit. The multipole variation Δb_n due to the angular variation $\Delta\theta$ can be calculated from

$$\Delta b_n(\Delta\theta) = 10^4 \frac{\Delta B_n(\Delta\theta)}{B_2 + \Delta B_2(\Delta\theta)} \sim \frac{1}{B_2} \Delta B_n(\Delta\theta) \tag{190}$$

Let us considers the worst case where (*i.e.*, B_2 is at its smallest value) B_2 is provided by a quadrupole with coils made of a 15° sector of inner radius R_1 and of coil width qw_L (q being the number of layers of width w_L) as it is shown for instance for q = 1, 2 and 3 in Figure 65. The current density is considered uniform in the coil.

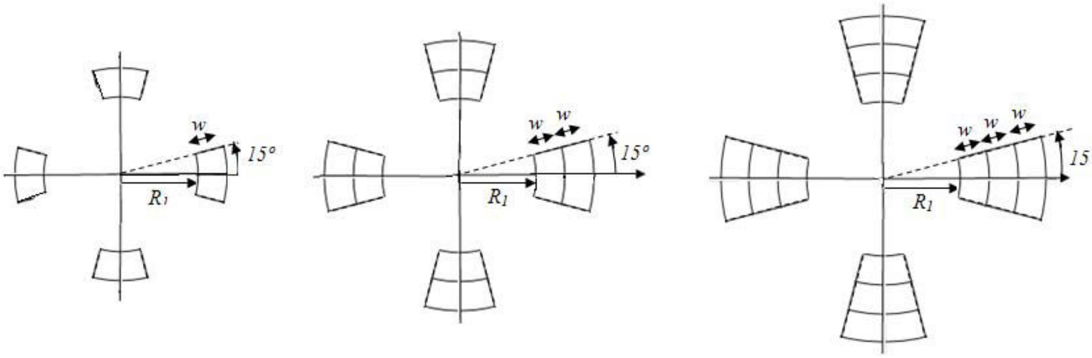

Figure 65 – Example of quadrupoles used for Eq (191) with q=1 (left), q=2 (middle) and q=3 (right).

At the first order and assuming that the variation on the multipole B_n due to an angular variation in the layer number k (k = 1 for the inner layer, and $k = q$ for the outermost layer) is at its maximum value one has (details of the calculus are given in Appendix C)

$$\Delta b_n^{(k)} \sim \Delta\theta \frac{\frac{2}{(n-2)}\left(\frac{2}{3}\right)^{n-2}}{ln\left(1 + q\frac{w_L}{R_1}\right)\sin\left(\frac{\pi}{6}\right)} \left(\frac{1}{\left(1 + k\frac{w_L}{R_1}\right)^{n-2}} - \frac{1}{\left(1 + \frac{(k-1)w_L}{R_1}\right)^{n-2}} \right) 10^4. \tag{191}$$

The reference radius is taken as 2/3 of the coil aperture radius. For given $\Delta\theta$, q and k, expression (191) depends only on a function of the layer width to aperture radius ratio (w_L/R_1). A more practical ratio defined as the coil width to aperture radius ratio (qw_L/R_1) will be considered in the following. In Figure 66 is plotted the maximal variation of $|\Delta b_6|$ versus qw_L/R_1 and for an angular step $\Delta\theta$ of 0.02°. Coils made of one (q=1) and two (q=2) layers have been considered. Only the multipole b_6 has been plotted since it is the harmonic order the most sensitive with the angular step.

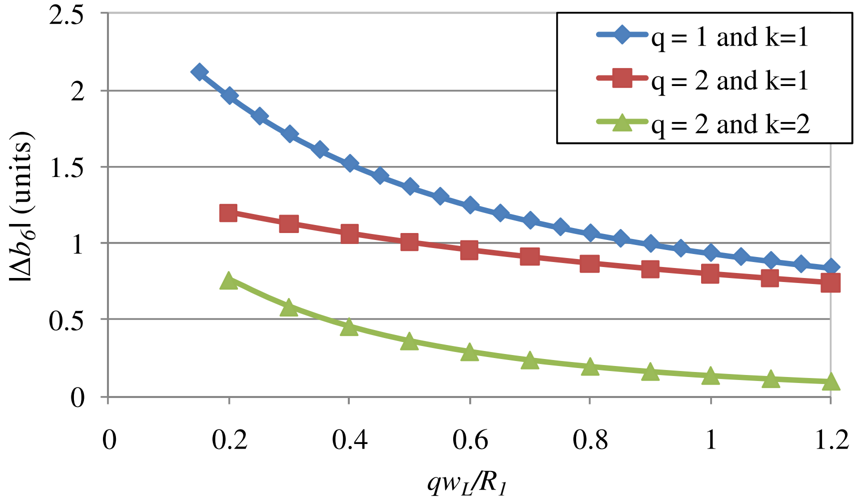

Figure 66 – Maximal variation of b_6 corresponding to an angular step of 0.02º versus coil width to aperture radius ratio. Three cases are considered: a one layer coil (q=1, blue line), and two 2-layers coils (q=2) with angular variation either in the inner layer (k=1, red line) or in the outer layer (k=2, green line).

One observes from Eq (191) and from Figure 66 that:

- For a given angular step, the largest multipole variation is on b_6 (the amplitude of the multipole variation decreases when the multipole order increases).
- For a given angular step, the maximal variation of b_6 decreases when increasing the coil width to aperture radius ratio.
- In a multi-layers coil and for a given angular step, the variation of b_6 is larger when it is generated by an angular variation in the inner layers than in the outer ones.

One can derive the following conclusions: for similar coil layouts, *i.e.*, same number of layers, it is faster to perform an angular scan when the ratio coil width/aperture radius is large. This means that RHIC quadrupoles need a finer scan with respect to the LHC dipoles. For instance, according to Figure 66, in a one-layer coil (q=1) the step corresponding to a given variation of b_6 is more than 2 times larger for a coil aspect ratio of 1.2 than that of 0.2. Moreover, in a multi-layer coil, to provide the same multipole variation, the angular step used in the outer layer has to be larger than that of the inner layer. For instance, according to Figure 67, the angular step in the outer layer of a tow-layers coil has to be from 2 to 8 times larger than that in the inner layer for coil aspect ratio ranging from 0.2 to 1.2.

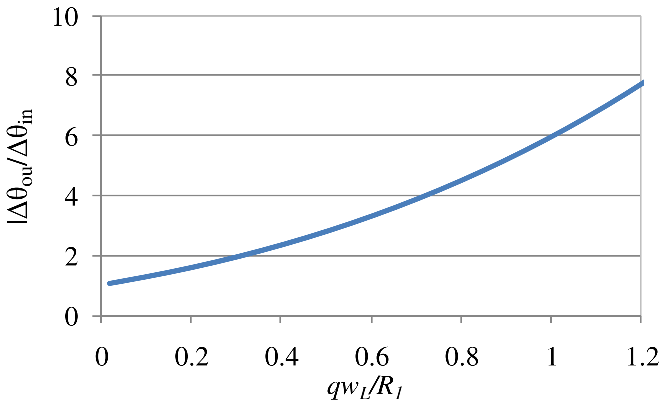

Figure 67 – Ratio between the outer and inner angular step in a two layers coil allowing generating equal maximal variation of b_6.

The angular step has to be small enough to induce multipoles variation below one unit, but not too small neither because of the long computational time it would require. Layers of quadrupole coils are usually made of one or two blocks (see for instance the coil cross-sections used for the LHC, Tevatron and HERA quadrupoles shown in Figure 68).

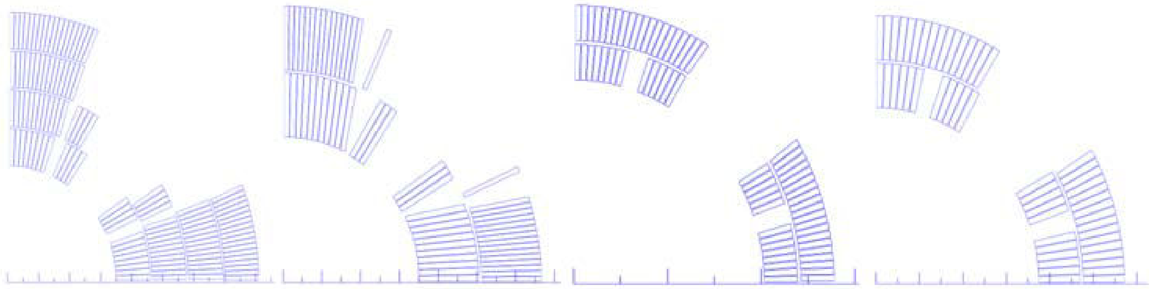

Figure 68 – Coil cross-sections of the LHC MQXA (left), LHC MQXB (second from left), Tevatron MQ (second from right), and HERA MQ (right).

The number of all the possible angles combinations in a one layer coil made of two blocks (Figure 69, left) can be calculated by means of (see Appendix E)

$$N_b = \frac{n^3}{6} + \frac{n^2}{2} + \frac{n}{3}, \tag{192}$$

where n is the number of angular sub-division in the range $[\theta_{min}; \theta_{max}]$ related to the angular step $\Delta\theta$. It is calculated from

$$n = \ Integer\left\{\frac{(\theta_{max} - \theta_{min})}{\Delta\theta}\right\}. \tag{193}$$

In Table 15 are shown estimates of the time needed to calculate for one coil configuration the multipoles b_6 and b_{10} by means of Matlab® 2009a and for the four different coil layouts shown in Figure 69. A standard PC equipped with two 2.8 GHz Pentium 4 processors was used.

Table 15 – Computational time to compute multipoles b_6 and b_{10} for one coil layout.

	2 blocks	3 blocks	4 blocks	5 blocks
Nb of angles	3	4	6	7
t (μs)	~ 25	~ 30	~ 40	~45

The computational time range from 20 μs for a 2 blocks-coil to 45 μs for a five blocks coil (the time increases by about 5 μs when adding one new free parameter, *i.e.,* angle). This is about 10^4 faster than magnets design software like Roxie [73] where the evaluation of the multipoles takes of the order of 1 s. Moreover, in contrary of Roxie where multipoles are obtained summing up the contribution of each strand of each cable forming the coil, the computational time of our method does not depend on the geometrical dimensions of the coil, *i.e.,* angular and radial dimensions. This is particularly interesting for quadrupoles with large aperture and large coil width such as for the new inner triplet quadrupoles of the LHC.

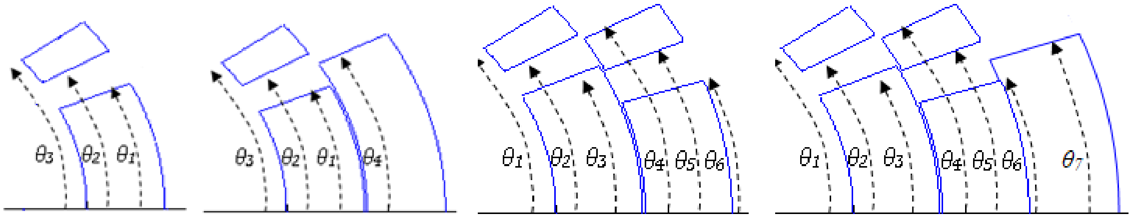

Figure 69 – From the left to the right: one layer coil made of two blocks, two layers coil made of three blocks, two layers coil made of four blocks, and three layers coil made of five blocks.

One can estimate the computational time requested to carry out an angular scan in a given coil layout (a given number of blocks) and for a given angular step by means of Eq. (192) and Table 15. In Figure 70 is plotted in blue the time needed to perform an angular scan in the four coil cross-sections shown in Figure 69 versus the angular step. The inner radius of the coil and the width of each layer are consistent with those of the coil for the new inner triplet quadrupole for the LHC, *i.e.,* coil inner radius and layer width of 60 mm and 15 mm respectively. For 2 layers coils the angular step $\Delta\theta_{ou}$ in the outer layer has been chosen so as to generate the same multipoles variation than the one caused by the angular step $\Delta\theta_{in}$ in the inner layer (Figure 67). Angular steps in the 2nd and 3rd layer of a three-layer coil have been calculated in a similar way. The range within which is performed the scan is [15°-41°].

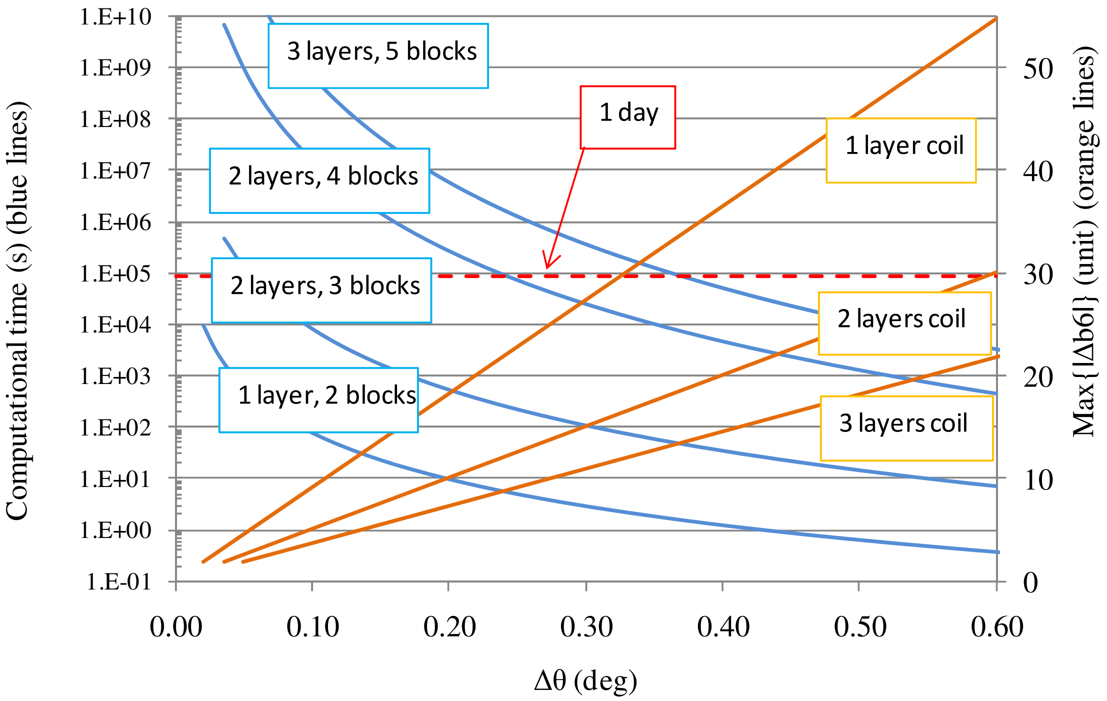

Figure 70 – Computational time versus angular step (blue lines), and maximal variation of b_6 versus angular step (orange lines). For two (q=2) and three (q=3) layers coils the angular step Δθ is the one used in the innermost layer. Steps used in other layers have been chosen so as to generate the same maximal variation on b_6 than in the innermost layer. The coil aperture radius and the layer width used here are consistent with those of the coil for the new inner triplet quadrupole of the LHC *i.e.* R_1 = 60 mm and w_L = 15 mm. The range considered is [15º-41º].

The validity of the graph shown in Figure 70 has been verified for the case of a one layer coil made of two blocks. A numerical analysis performed with Matlab with an angular step of 0.2º has been done within 10 seconds and showed that the maximal variation on the multipole b_6 associated to the step is of about 13 units (see Figure 71). These values are in good agreement with estimated values obtained from Figure 70 and predicting a computational time of 10 s and a maximal variation of the multipoles within 17 units.

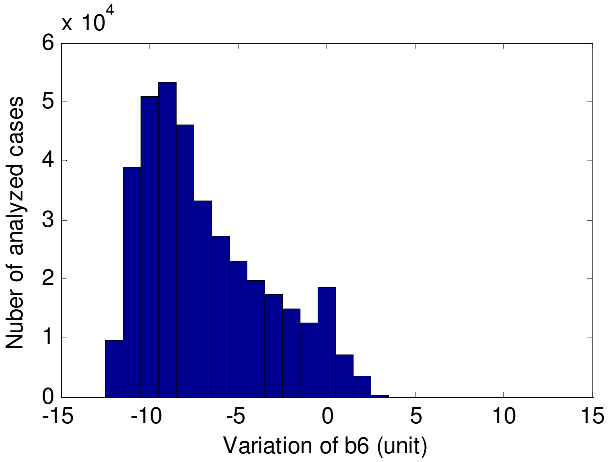

Figure 71 – Variation of the multipole b_6 due to the discrete angular step.

Despite the rapidity of the method to calculate multipoles in one cross-section (tens of micro-seconds), it appears, according to Figure 70, that the computational time needed to perform an angular scan fine enough to generate b_6 variations within 1 unit can be very long (*i.e.,* 15 hours for a two-blocks coil, 60 days for a three blocks coil, and about 8000 years for a four blocks coil!). However, a parametric study carried out for the two-block coils (see Figure 69, left) and for angular steps of 0.05°, 0.1° and 0.15° shows that a small step provides lots of nearly identical solutions but does not provide solutions in a region which cannot be explored with a larger step (see Figure 72 and Figure 73). Therefore, to get rid out of all the nearly identical cross-sections it is interesting to take an angular step generating b_6 variations larger than one unit while keeping the constraint on the field quality for a cross-section to be suitable of 1 unit. This also has the pleasant effect of substantially reducing the computational time.

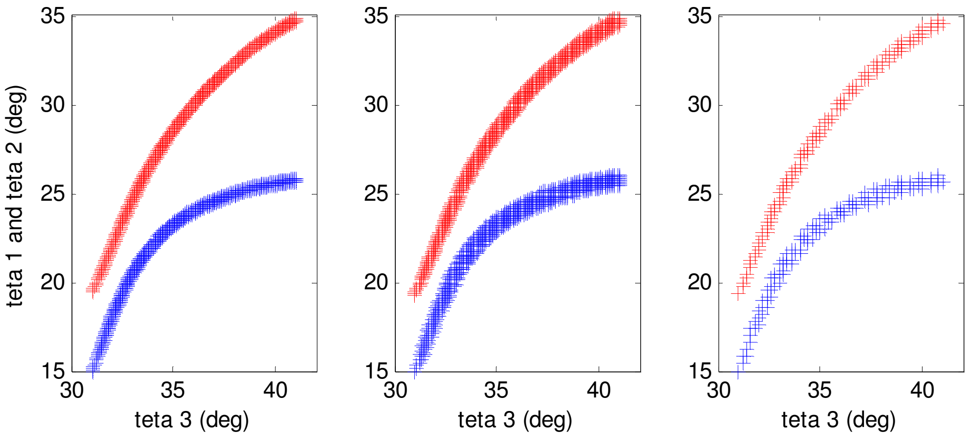

Figure 72 – Angles (defined in Figure 69, left) generating multipoles b_6 and b_{10} within one unit for an angular step of 0.05° (left), of 0.1° (middle) and of 0.15° (right).

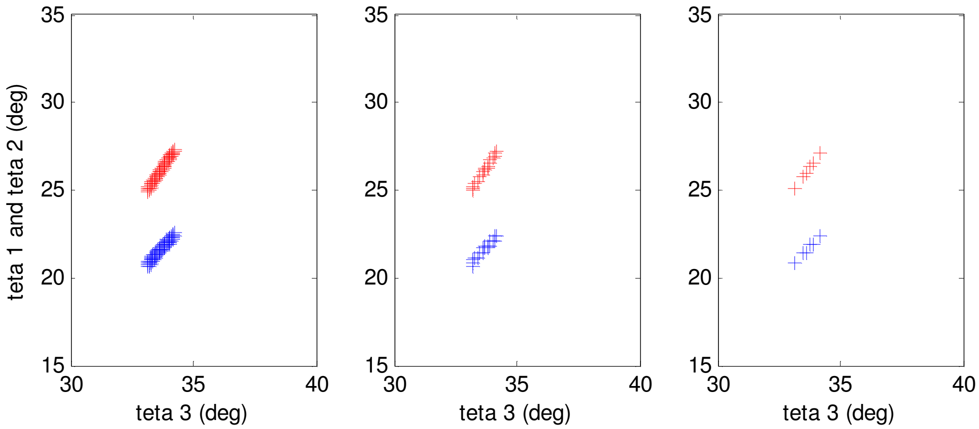

Figure 73 – Similar Figures as in Figure 72 but with the additional constraint to have b_{14} within one unit.

According to Figure 73, an angular step of 0.15° seems the most suitable for the scan in a one layer coil since it provides distinct solutions uniformly spread in the range of interest giving b_6, b_{10} and b_{14} within 1 unit. According to Figure 70, the maximal variation on $|b_6|$ associated to a step of 0.15° is of about 15 units.

Let us now verify if the choice of an angular step generating maximal variations of b_6 of 15 units is still relevant when varying the coil aspect ratio in the range [0.1-1.2]. The angular steps corresponding to a maximal variation of b_6 of 15 units as a function of the coil aspect ratio qw_L/R_1 has been calculated by mean of Eq. (191) for coils made of one, two and three layers (Figure 74).

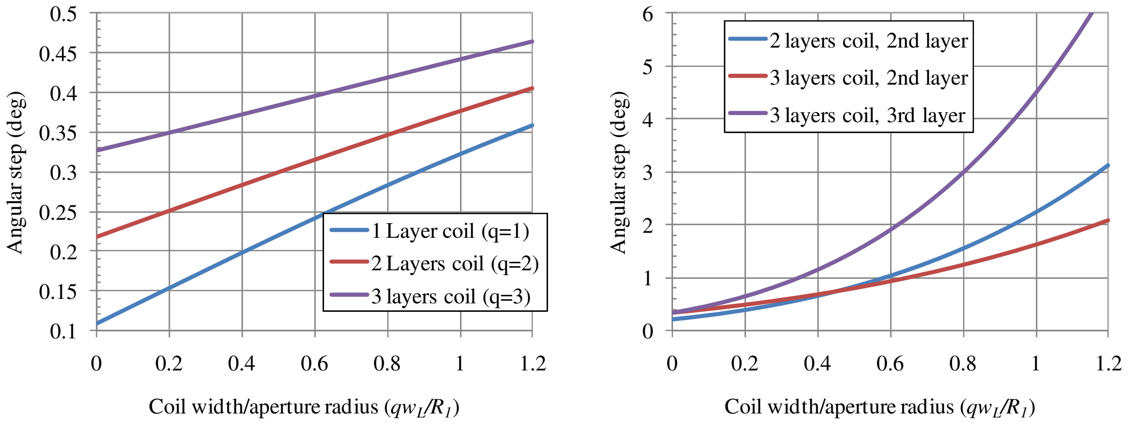

Figure 74 – Angular step allowing generating maximal variation of b_6 of 15 units. Left: step in the inner layer of coil made of 1, 2 and 3 layers. Right: step in the outer layer of a 2 layers coil, and step in the 2^{nd} and 3^{rd} layer of a three-layer coil.

We performed a numerical analysis for the one-layer case (see Figure 75). Three coil aspect ratios have been considered: 0.25, 0.5 and 1. For each case the angular step has been chosen from Figure 74. One clearly see that our method to choose the angular step works since in each case one got 6 solutions generating b_6, b_{10} and b_{14} within 1 unit.

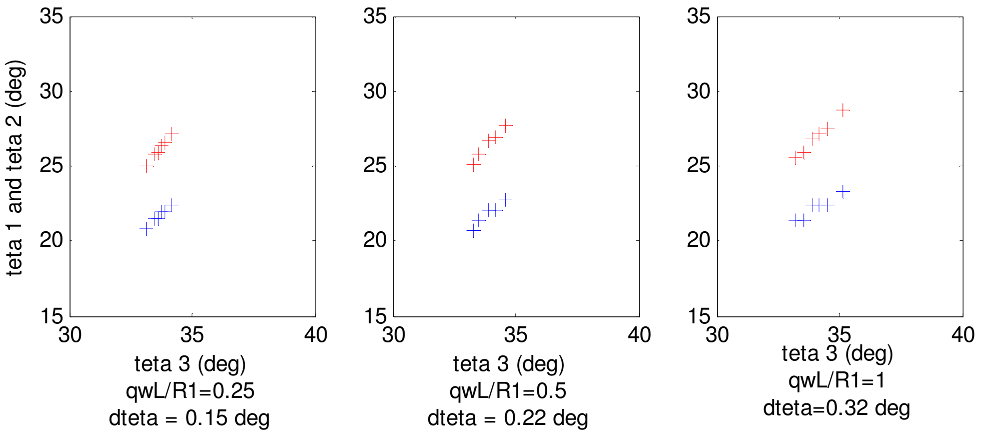

qwL/R1=0.25
dteta = 0.15 deg

qwL/R1=0.5
dteta = 0.22 deg

qwL/R1=1
dteta=0.32 deg

Figure 75 – Angular scan carried out on a one layer coil (q=1) made of two blocks and for three coil width to aperture radius ratio (0.25, 0.5, and 1). The angular step has been chosen according to the coil aspect ratio and by means of Figure 74. The number of solutions in each case is six.

Let us assume that an angular step generating a maximal variation of b_6 of 15 units allows providing distinct solutions spread in the whole range of solutions, whatever the number of layers considered. Let us verify if it is the case for a three-block coil made of two layers. According to Figure 74 (left) the step for the inner layer which generates a maximal variation on b_6 of 15 units and for a coil aspect ratio of 0.5 is of 0.3º. To generate a similar maximal variation on b_6 the step in the outer layer has to be of 0.9º (see Figure 74, right). A numerical analysis enables a validation of our assumption. Indeed, as shown in Figure 76, the solutions obtained with angular steps in the inner and outer layer of 0.3º and 0.9º (left) provides different solutions almost uniformly spread in the range of solutions obtained with smaller steps (0.2º and 0.4º for the inner and outer layer respectively). From now, we assume that the choice of the step has to be done so as to generate maximal variation of b_6 of 15 units, whatever the coil aspect ratio and the number of layers considered.

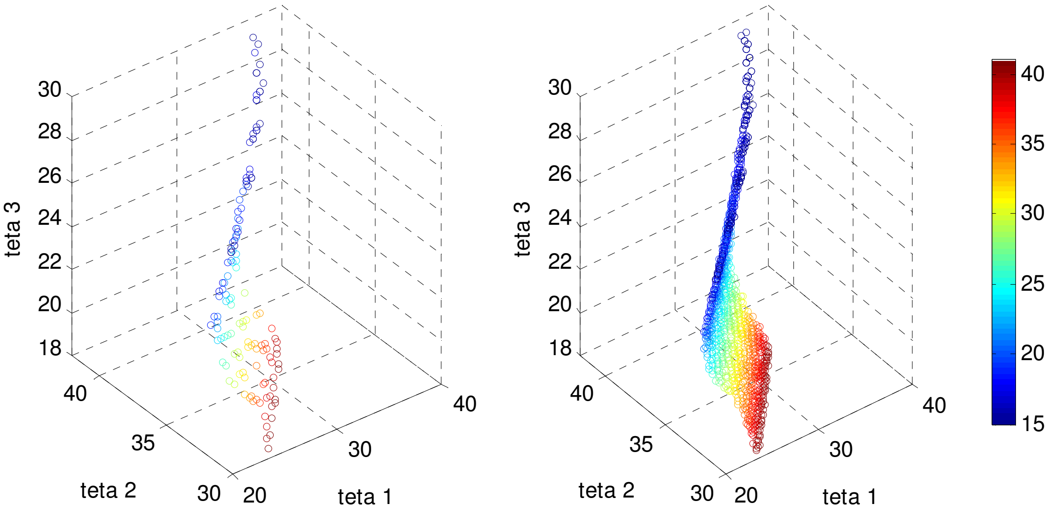

Figure 76 – 3D plot of the angles giving b_6, b_{10} and b_{14} within one unit in a three blocks coil and for a coil with to aperture radius ratio of 0.5 (like for the new inner triplet quadrupole of the LHC). Left: angular step in the inner and outer layer are of 0.3° and 0.9° respectively corresponding to a maximal variation on b_6 of 15 units. Right: angular steps of 0.2° and 0.4° providing smaller variation of b_6.

The computational time needed to perform an angular scan in a 2, 3, 4 and 5 blocks coil is plotted in Figure 77. It has been obtained from Figure 74, Table 15 and Eq. (192). For each case the angular step is such that it generates b_6 variation within 15 units. To perform a scan in a 5 blocks coil within the reasonable amount of time of 1 day one must have a coil aspect ratio larger than 0.7.

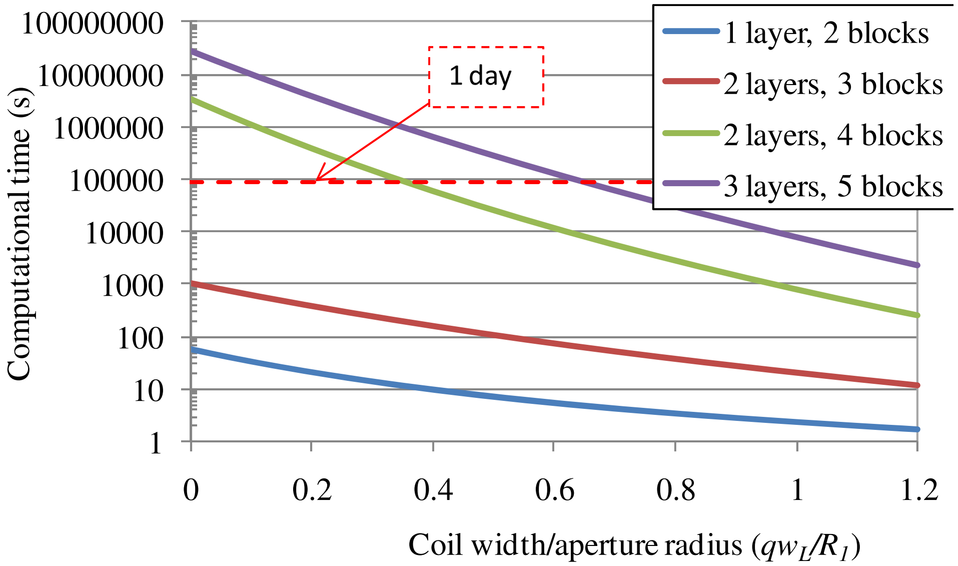

Figure 77 – Computational time needed to optimize coil layout made of 2, 3, 4, and 5 blocks.

In Table 16 we show some examples of angular analysis performed on the three quadrupole coil layouts. The inner radius (60 mm) and the width of each layer (15 mm) are consistent with that of the new inner triplet quadrupole for the LHC upgrade. Angular step has been chosen by means of Figure 74 so as to generate maximal variations of b_6 of about 15 units.

Table 16 – Example of angular analysis performed on the three coil layouts of the Figure 69. The inner radius of the coils has been taken to 60 mm and the width of each layer to 15 mm. These values are consistent with that of the new inner triplet quadrupole for the LHC. The angular scan has been done in the range [15º- 41º].

Coil layout	qw_L/R_1	Angular step inner layer (deg)	Angular step outer layer (deg)	Number of analyzed cases	Computational time	Nb of coil layouts with $\|b_6\|<1$ & $\|b_{10}\|<1$	Nb of coil layouts with $\|b_6\|<1$&$\|b_{10}\|<1$& $\|b_{14}\|<1$
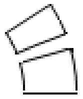	0.25	0.15	-	$0{,}9\times10^6$	22 s	286	6
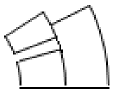	0.5	0.3	0.9	3.3×10^6	90 s	459	131
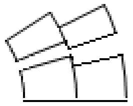	0.5	0.3	0.9	0.44×10^9	270 mins	63186	14567

The four blocks coil has 14567 coil cross-sections which generate multipoles b_6, b_{10} and b_{14} within one unit. This is too much for the next analysis consisting in calculating the short sample parameters of each coil layout. To reduce number of potential solutions one can put tighter constraint on the field quality. Since the multipoles sensitivity with the angles decreases when increasing the multipoles order we propose to keep the constraint on b_6 at one unit and to put tighter constrain only on b_{10} and b_{14}, with the constrain on b_{14} smaller than on b_{10}. For instance, the large number (14567) of coil cross-sections generating multipole b_6, b_{10} and b_{14} within one unit can be reduced to 146 by setting $|b_6|<1$, $|b_{10}|<0.2$ and $|b_{14}|<0.05$. This way of selecting coil layouts is consistent with the next part of the study consisting in fitting sectors with real cables: harmonic b_{14} will be less sensitive than b_{10} and b_6 to errors related to the impossibility of perfectly fit the sectors.

To summarize:

- The angular step has to be chosen such that the induced b_6 variation is larger than one unit (but not too large either) while the constraint on b_6 to select a cross-section is of 1 unit: this allows getting rid out of all nearly identical solutions.
- We showed for coils made of one and two layers that a maximal variation on b_6 of 15 units is a good choice for the angular step. We then assumed that it is also a good choice for any other coil layout.
- For a four blocks coil and more, the number of solutions satisfying the field quality can be very large (*e.g.* 14567 for a four blocks coil according to Table 16). To decrease the number of good solutions, thus allowing performing a more detailed study on each coil layout, one can tighten the selection constraint on b_{14} since this is the multipole the less sensitive with the angular step. If not enough one can also tighten the field constrain on b_{10}.
- Note that we did not take into account a possible current grading in the coil. This would enhance the main field, thus requiring a larger angular step than for an equivalent ungraded coil.

V.1.4 Estimate of the short sample gradient

Now we dispose of a list of several tens of set of angles corresponding to coil-layouts which provide a good field quality, *i.e.,* b_6, b_{10} and b_{14} within 1 unit. All are potentially good candidates. In order to determine which coil cross-sections fit the best with the requirements (usually high gradient and low current), we propose to calculate for each cross-section the short sample gradient and the short sample current. To do that one needs, for a given current, to calculate the maximal magnetic field modulus in each sector so as to determine their load line, which, when intercepting the critical surface of the superconductor, provides the short sample current of the sector. The smallest short sample current among all the sector-coils constituting the winding is taken as the short sample current of the magnet.

The calculation of the magnetic field modulus everywhere can be done by means of relations (168) to (183) implemented for each sector constituting the coil into a numerical code, and truncated at a sufficiently high order so as to get a sufficiently accurate value of the magnetic field. In Figure 78, we computed the magnetic field modulus generated in the first quadrant of the quadrupole of Figure 61. The order of the truncation of the Fourier series has been taken in the range from *n*= 2 (only the main harmonic) to *n*=200. One does not notice any significant change in the magnetic flux density according to the maximum harmonic order considered and for areas far from the coil. However, near and within the coil, the region of interest for us, the magnetic flux density heavily depends on the rank of the truncation. A maximal harmonic order of 100 seems to give an acceptable precision on the magnetic field while requiring a lower CPU time than for a larger order of truncation.

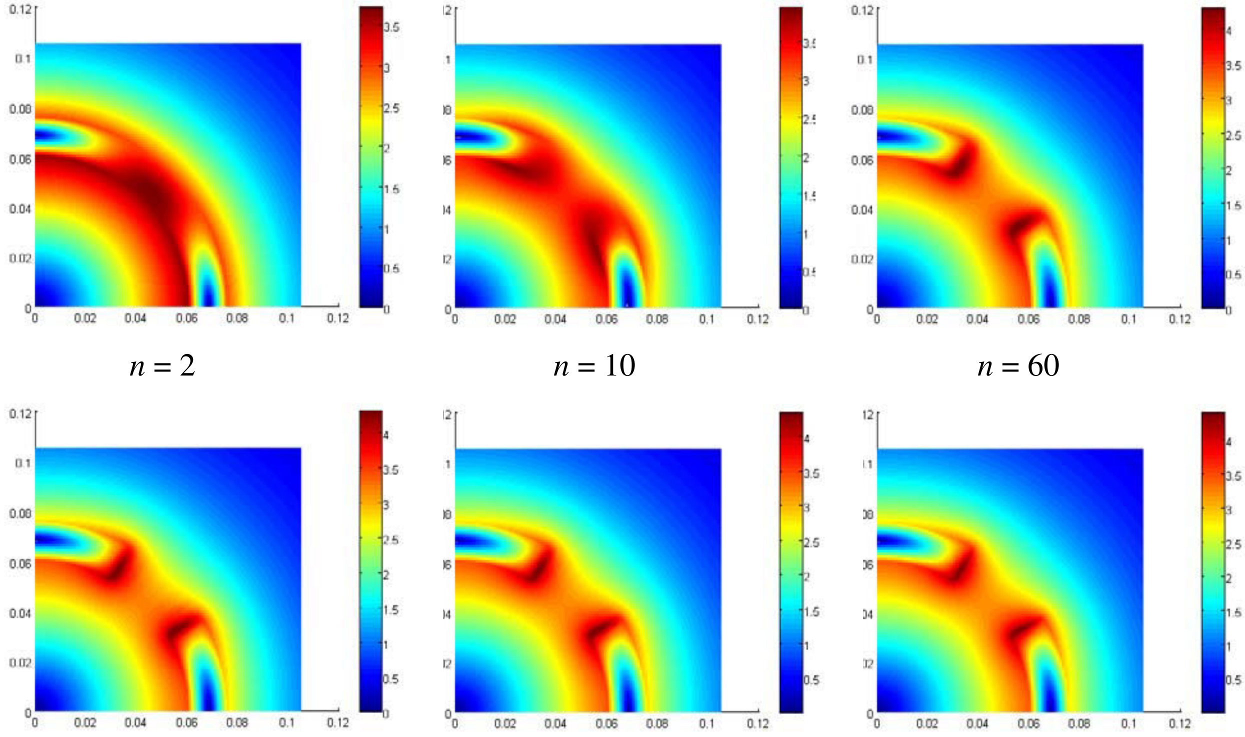

$n = 2$ $n = 10$ $n = 60$

$n = 80$ $n = 100$ $n = 200$

Figure 78 – Computation of the magnetic field modulus in the first quadrant of a quadrupole with coils made of one 30º sector by means of Eq. (168) to Eq. (177) implemented into Matlab and truncated at different order form $n = 2$ to $n= 200$.

The peak field in a sector is obtained taking the maximal value of the field modulus computed in a discrete number of points equally distributed in the sector. For instance, in the sector shown in Figure 79, one can see all the locations (points) at which the magnetic field is calculated. The step between two adjacent points has to be chosen sufficiently small so that the calculated peak field is very close to the real value. We propose here to use a step which is of the order of the distance between centers of two adjacent strands in a superconducting cable, *i.e.,* a strand diameter. This is consistent with numerical magnet design softwares like Roxie where the magnetic field is evaluated on each strand. Strands diameter in a superconducting cable is usually between 0.5 and 1 mm.

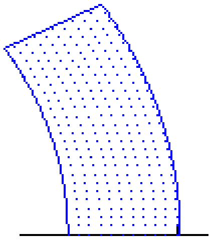

Figure 79 – Example of location where the modulus of the magnetic field is calculated (marker) in order to determined the maximum magnetic field in the coil.

This method has been used to compute the peak field in the quadrupole of the Figure 61 and varying the order of truncation from 2 to 280. Results are shown in Figure 80 and agree with our assumption that an order of truncation of 100 is enough to have a precise idea of the peak field in the coil.

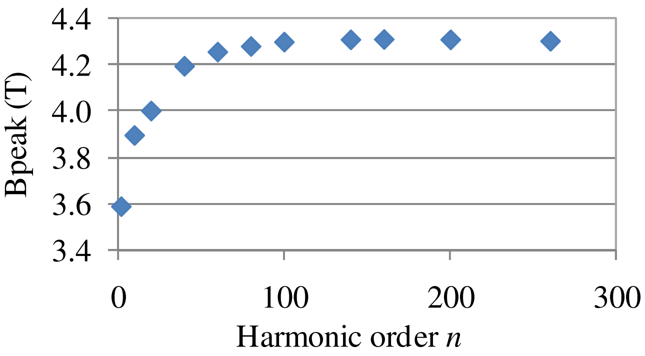

Figure 80 – Peak field in the coil of the Figure 79 versus the order of truncation.

Note that the estimate for the minimum harmonic order enabling a precise estimate of the peak field in the coil done here is only valid for a quadrupole magnet with similar dimensions than the quadrupole of Figure 61. This is the case of the MQXC magnet.

V.1.5 Estimate of the forces

The determination of the magnetic forces taking place in a sector can be done by sub-dividing sectors into nearly square sub-sectors (see Figure 81) and assuming that the magnetic force applied on a sub-sector is given by the vectorial product between the current flowing into the sub-sector and the magnetic field generated at its center. This method is easy to implement into a numerical code and gives good results (see Table 17).

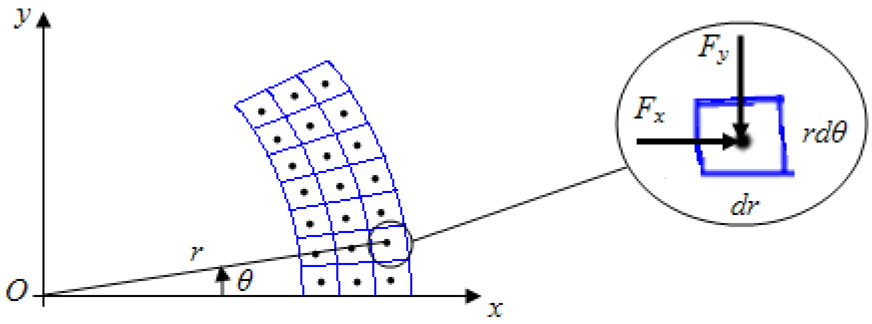

Figure 81 – Model used to calculate magnetic forces in the coil.

The x and y-components of the magnetic force applied onto a subsector (dF_x and dF_y) which center is located in (r,θ) is obtained from

$$dF_x = -j[B_\theta(r,\theta)\cos\theta + B_r(r,\theta)\sin\theta]\, jrdrd\theta \tag{194}$$

$$dF_y = -j[B_\theta(r,\theta)\sin\theta - B_r\,(r,\theta)\cos\theta]\, jrdrd\theta, \tag{195}$$

where j is the current density flowing within the sector, and $B_\theta(r,\theta)$ and $B_r(r,\theta)$ are the azimuthal and radial components of the magnetic flux density generated within the coil at the point (r,θ). The components $B_\theta(r,\theta)$ and $B_r(r,\theta)$ are analytically calculated by means of formulas introduced in section V.1.2. The total magnetic force applied on the sector is obtained summing up the contribution of all the sub-sectors

$$F_x = \sum dF_x \qquad \text{and} \qquad F_y = \sum dF_y \tag{196}$$

As an example we compare numerical computation of the magnetic force applied on the quadrupole of the Figure 61 and carried out with Roxie with values obtained with our approach. Note that the slight difference is due to the fact that the coil considered in Roxie is made of real cables and does not perfectly fit with the 30º sector. Note that since the magnetic field is known everywhere one could also have used the Maxwell stress tensor to calculate the magnetic forces.

Table 17 – Comparison between numerical computation (Roxie) and our estimate of the x and y-components of the magnetic force applied to the quadrupole of the Figure 61. In our estimate, harmonic order up to 100 and 40 subsectors have been considered.

	our approx.	Roxie
Fx	0.141	0.138
Fy	-0.312	-0.301

V.1.6 Coil cross-section with Rutherford cables

To pass from an analytical solution (see for instance Figure 82, left) which consists into a set of angles to a coil made of Rutherford cables, we first compute for each coil block the number of turns of cable which best fits with the sector coil angles (see Figure 82, middle). Then, the unavoidable field harmonic distortion due to the discrete cable size and its slight variation from a purely radial sector block are compensated by tuning the block positions and allowing small blocks tilts (see Figure 82, right). The optimization is done through sensitivity matrices built around the first guess and takes into account the saturation of the iron yoke. This is achieved by means of numerical code like Roxie [73].

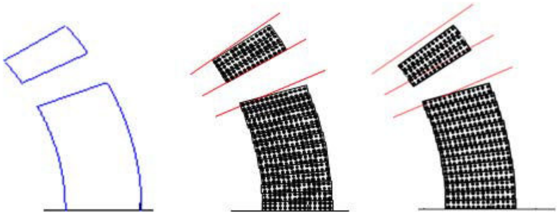

Figure 82 - Cross-section of a [0-24°; 30-36°] pure sector coil allowing cancelling b_6 and b_{10} (left). Cross-section build with real Rutherford-type cables and which best fit the pure sector (middle). The final position of the block (right) has been optimized so as to compensate for the field harmonic distortion due to the discrete cable size.

V.2 Application to the MQXC design

V.2.1 Specification of the MQXC cables

The new quadrupole for the upgrade of the interaction regions of the LHC (called MQXC) will be based on a two layers coil of 120 mm aperture diameter [67]. It will use the same 15 mm wide keystoned Rutherford Nb-Ti cables (both inner and outer layer) as in the LHC main dipole [60]. The cable insulation will probably differ from the main dipoles: a new insulation scheme, allowing a direct path to helium from the bath to the strands has been proposed. This slightly changes the expected size of the insulation [91]. The main geometric and electric features of the cables are summarized in Table 18. The cables insulation thickness are obtained from measurements performed on a stack of cables compressed at 50 MPa [49]. The inner and outer cables of the LHC main dipole are named cable 01 and cable 02 respectively, following the standard notations used for the LHC.

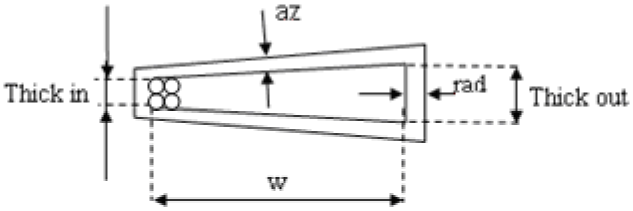

Figure 83 – Cable cross-section.

The cables 01 and 02 have a cross-sectional area (insulation included) of 33.4 mm^2 and 27.3 mm^2 respectively. Since the cables will be fed by the same current, this corresponds to having a current density in the cable 02 23% larger than in the cable 01, *i.e.,* a grading of 1.23, as in the LHC main dipoles. Cables 01 and 02 are available in unit lengths of 460 m and 780 m respectively: this constraint should be taken into account in the coil design. The superconducting performances of the cables are taken as the more pessimistic values derived from the more recent measurement performed at 1.9 K on the spare cables of the LHC main dipole (see Table 18).

Table 18 – Cables parameters, with porous insulation.

	unit	cable 01	cable 02
w	mm	15.100	15.100
thick in	mm	1.736	1.362
thick out	mm	2.064	1.598
Radial insulation	mm	0.160	0.160
Azimuthal insulation	mm	0.135	0.145
Number of strand		28	36
strand diameter	mm	1.065	0.825
Cu/Sc ratio		1.65	1.95
I_{ss}	A	14800 (10T)	14650 (9T)
$\Delta I_{ss}/\Delta B$	A/T	4680 (10T)	4050 (9T)
j_{ss}	A/mm^2	1572 (10T)	2245 (9T)
$j_{ss}/\Delta B$	A/T/mm^2	497 (10T)	620 (9T)

V.2.2 Sector coil case

Specifications we have been given on the design are that (i) allowed multipoles b_6, b_{10} and b_{14} at the reference radius (40 mm) taken as 2/3 of the aperture radius have to be below one unit, (ii) the short sample gradient has to be the largest possible, and (iii) the short sample current has to be the lowest possible.

To reach the field quality specifications, one considers a four-block coil design as for the LHC MQ or MQXB. It offers, through the 6 free parameters (θ_1, θ_2, θ_3, θ_4, θ_5, θ_6) (see Figure 84), the flexibility needed to both optimize the multipoles, the short sample gradient, and the short sample current. A three-block coil would have been too rigid from the optimization point of view since providing only four-free parameters, and a five or more blocks coil would have increased the complexity of the magnet.

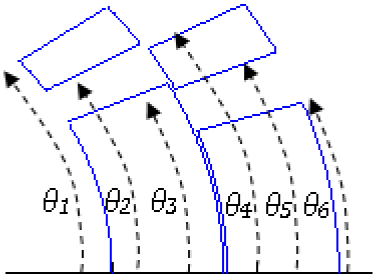

Figure 84 - Cross-section of the 4 blocks coil considered in the semi-analytical search for the optimal coil lay-out.

To determine the most adequate layout for the future quadrupole of the LHC interaction region upgrade a scan on all the possible combinations of the six-dimensional parameters space is done following the approach developed in section V.1. Parameters considered in the numerical search performed with Matlab are:

- The angular step of the 3 variables of the inner layer (θ_1, θ_2, and θ_3) is set to 0.3º.
- The angular step of the 3 variables of the outer layer (θ_4, θ_5, and θ_6) is set to 0.9º.
- The maximal angular dimension of the coil has been set to 41º, providing a collar nose thickness at least as large as what used in the LHC main dipole.
- The minimal angular thickness of the blocks in contact with the mid-plane is set to 15º.

The time needed to perform a scan on all the possible angles combinations was of about 5 hours. Multipoles are computed at 2/3 of the aperture radius and the set of angles giving the absolute value of the first three allowed multipoles (b_6, b_{10} and b_{14}) below 1 unit are kept.

The previous method has been applied to two different arrangements of the cables 01 and 02. The first arrangement is called “normal grading” and consists in winding the outer layer exclusively with the cable 02 and the inner layer exclusively with the cable 01 (Figure 85, right). The second arrangement is named “special grading” because the cable 01, which has the lowest current density (yellow cable), is not only used to wind the layer 1 but also to wind the upper block of the layer 2 (Figure 85, left). It was thought that the second arrangement, which makes a better used of the superconducting cables since increasing the current density in the block located in a low magnetic field region, would provide a larger short sample gradient than the first one.

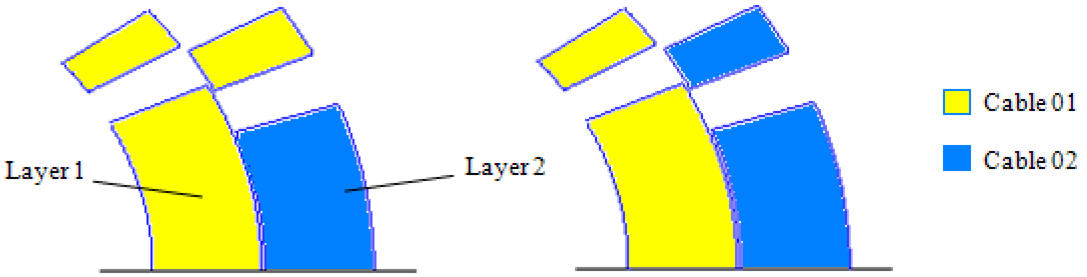

Figure 85 – Special grading (left) and normal grading (right) schemes. The color blue indicates the cable 02, and the yellow the cable 02.

Around 150 coil-layouts satisfying the field harmonic constrains ($b_6 < 1$, $b_{10} < 0.5$ and $b_{14} < 0.025$) have been found for each configuration. Then, for each one of these coil-layouts, we computed the short sample gradient and current, the magnetic forces acting on the coil, and the amount of cable used to wind a 10 m long coil (ends excluded). For this analysis, an iron yoke of infinite magnetic permeability has been set at 37 mm from the outer radius of the coil. For both the normal and the special grading cases, the short sample gradient is plotted versus the length of the cable 01 and cable 02 needed to wind one pole without taking into account the coil heads (see 3D plot in Figure 86). Each point is a cross-section satisfying the field quality requirement. 2 D plots of the same variables are shown in Figure 87.

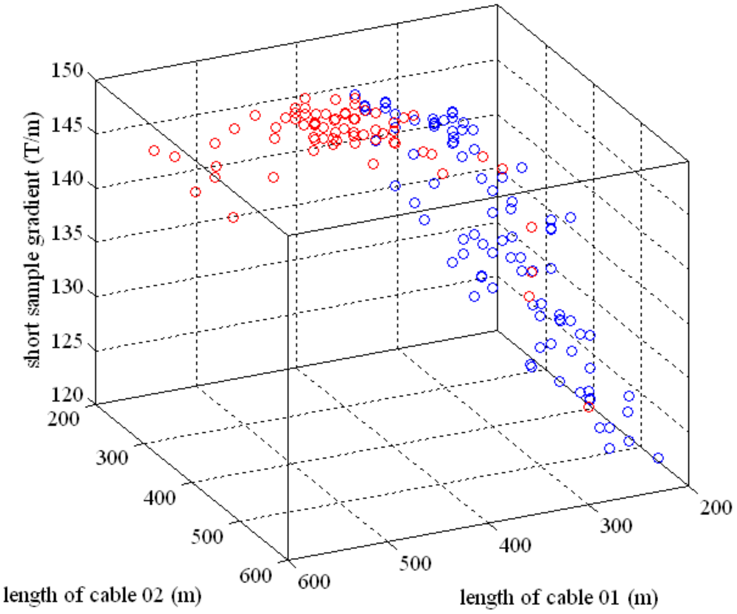

Figure 86 – Short sample gradient versus length of cables 01 and 02 needed to wind one pole. Red markers correspond to special grading cases and blue markers to normal grading cases.

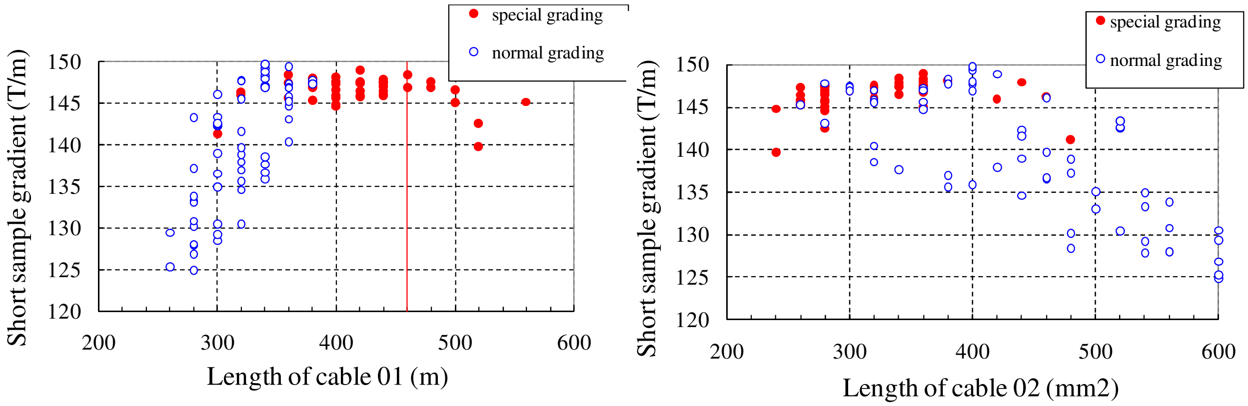

Figure 87 – Short sample gradient versus the length of the cable 01 (left) and cable 02 (right) needed to wind one pole (head excluded) for the normal grading (empty markers) and for the special grading (red marker). The red line is the unit length available.

<u>For the normal grading case:</u>

- One notices that, for a given length of cable 01, there is a disparity in the short sample gradient of about 25 T/m (*i.e.* 15 %) owing to the cables arrangements and the amount of cable 02 used.

- The maximal short sample gradient reachable for a given length of cable 01 increases with the length of the cable up to reach a maximal value of 150 T/m.

- The length of cable 01 used ranges from ~260 m, which corresponds to the smallest gradient (125 T/m), to ~380 m.

- The dependence of the gradient on the length of cable 02 is less clear. One observes, for a given length of cable 02 ranging from 260 m to 400 m, a slight increase in the gradient (~5 T/m) up to the maximal value of 150 T/m. Then, from 400 m to 600 m the maximal gradient for a given length decreases down to the minimal value of 125 T/m.

<u>For the special grading case:</u>

- For the majority of the solutions the short sample is in between 145 T/m and 150 T/m.

- The length of cable 01 used range from ~300 m to ~560 m. The gradient is almost constant and does not vary when varying the length of the cable.

- The length of cable 02 used range from ~ 240 m to ~ 480 m. The short sample gradient slightly increases with the length of cable up to reach the maximal value of 150 T/m attained for a cable length of 400 m. Above 400 m of cable 02 the gradient drops.

More generally one observes that both cables arrangement provide the same overall maximal short sample gradient of 150 T/m. The main difference between the two configurations is that the special grading case offers more coil-layouts with a short sample gradient close to the maximal value than the normal grading. The two coil layouts are equivalent from the point of view of electromagnetic performances and we selected the normal grading solution. An independent work [75] based on the genetic optimization algorithm gave a six-block configuration with a short sample gradient only 1.2 % larger. This underlines the efficiency of our method.

From here we only consider the normal grading. In Figure 88 is plotted the short sample gradient versus the short sample current. One notices that:

- There is a linear increase of the maximal short sample gradient with the current up to the maximal value of 150 T/m obtained at around 15 kA.
- For current higher than 15 kA, the maximal short sample gradient decreases when the current increases.

The interesting zone is around the point (15 kA, 150 T/m). For this current, the operational current obtained taking a 20% margin on the short sample current would be of 12 kA in case of short sample current of 15 kA. This fits the power supply of the present available hardware which can, at max, provides 14 kA. In Figure 88 we also plot the number of turns of cable 01 and cable 02 versus the short sample gradient. We see that to reach the highest gradient the number of turns of cable 01 and cable 02 tends toward similar values of 15-20 turns.

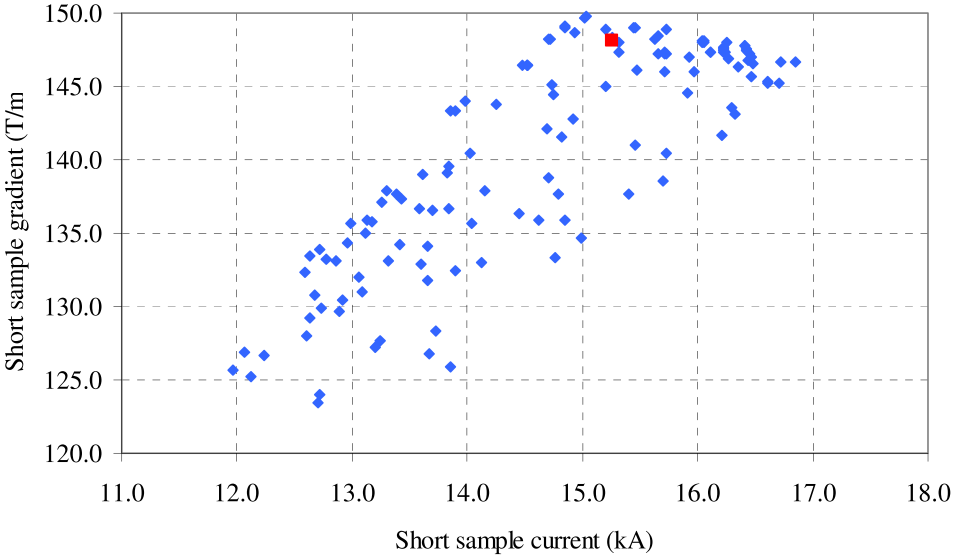

Figure 88 – Short sample gradient versus short sample current. The red point is the cross-section we choose for the MQXC quadrupole (see section below).

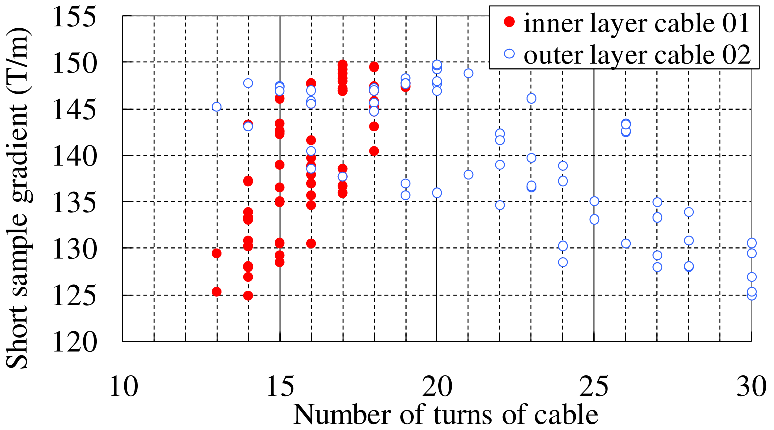

Figure 89 – Number of turns of cable 01 (red markers) and cable 02 (blue markers) versus short sample gradient.

In Figure 90 we plot the vertical and horizontal magnetic forces acting on half a coil versus the short sample gradient and considering that magnets are powered at their nominal current. Magnetic forces have been calculated using the method given in section V.1.4. We see that the force F_x pushing the coil outward is around 1 MN/m and depends barely on the gradient while the vertical force F_y which compresses the coil a the mid-plane increases continuously with the gradient from 1.2 to 1.4 MN/m. There is no cross-section providing both a high gradient and low magnetic forces.

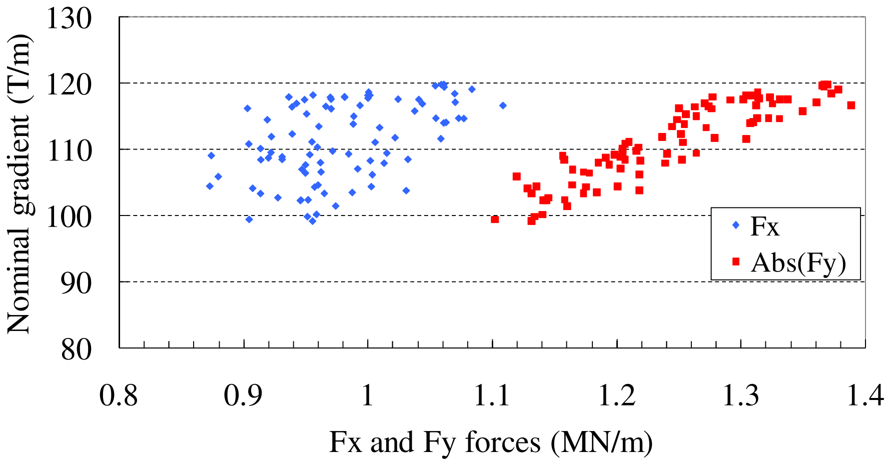

Figure 90 – Vertical and horizontal magnetic forces applied on half a magnet coil. The current is set at its nominal value.

V.2.3 Layout with Rutherford cables and iron yoke

Some promising cross-sections based on sector coil were chosen from Figure 88, in the region of high gradient and for a short sample current around 15 kA, and were realized using the LHC main dipoles cables. To pass from analytical solutions to real coils made of Rutherford cable we use the method given in section V.1.6. The coil cross-section made of pure sector blocks we selected based on the sector coil analysis is sketched in Figure 91 (left) and is identified in Figure 88 by a red marker. The coil cross-section made up of real cables and fitting the best the calculated angles is shown in Figure 91 (right). The optimization of the multipoles in presence of the iron yoke (see Section V.2.4) has been carried out with Roxie. The choice of the coil cross-section among that one maximizing the short sample gradient has been done to have radial blocks, and sufficiently large wedges for easy manufacturing and assembly.

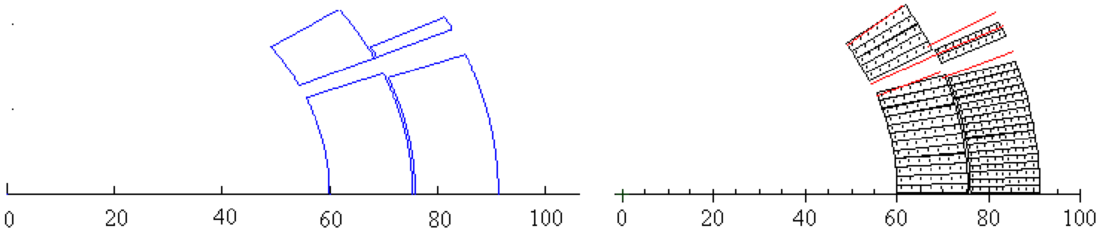

Figure 91 – MQXC coil cross-section made of pure sector blocks (left) and cross-section made of real cables and fitting the best pure sector block angles.

The proposed cross-section of the MQXC coil is presented in Figure 92 and its main features are summarized in Table 19. The short sample gradient is of 147.1 T/m for a short sample current of 15900 A (iron yoke saturation included). The nominal current taken with 20% operational margin from the short sample current is 12720 A, corresponding to an operational gradient of 118.5 T/m. The iron yoke contribution to the short sample gradient is 3.3%. For a fixed current, the yoke contribution to the gradient, excluded saturation, is of 12%. When the real geometry of the iron is taken into account, together with iron saturation, these values are reduced to 2.5% and 9% respectively.

The proposed two-layer coil is made of four blocks, and requires 17 turns of cable 01 for the inner layer and 19 turns of cable 02 for the outer layer. This corresponds to ~340 m of cable 01 and ~380 m of cable 02 for a 10-m magnet (ends excluded), that fits well the constraint on the cable length coming from the LHC dipoles (460 and 780 m respectively, (see section V.2.1)). The top angle of the coil, given by the pole angle of the inner layer (see Figure 92), is at 35º. This provides an azimuthal nose length of 21 mm. The thicknesses of the inner edges of the copper wedge located in the inner and outer layer are 4.4 mm and 2.6 mm respectively: this is larger than what we have for the thinnest copper wedge nose of the LHC main dipole (0.5 mm). The inner edge of the block 4 is totally in contact with the copper wedge of the inner layer.

The inner and outer coil are separated by a 0.5 mm thick insulation layer, and a 0.12 mm thick ground insulation is set at the mid-plane together with an additional layer, acting as a shim, of 0.1 mm. An additional insulating layer of 0.025 mm is set at the mid-plane of the outer layer and runs along the inner radius of the outer layer over a few millimeters. Its role is to improve electrical insulation between layers. The total thickness of the mid-plane is therefore 0.220 mm for the inner and 0.245 mm for the outer layer. A compression of 0.005 mm of the mid-plane is taken into account. The 0.1 mm shims can be used to fine tune the field quality during the magnet production without modifying the coil design. Similar shims can be used between the collar and the coil pole.

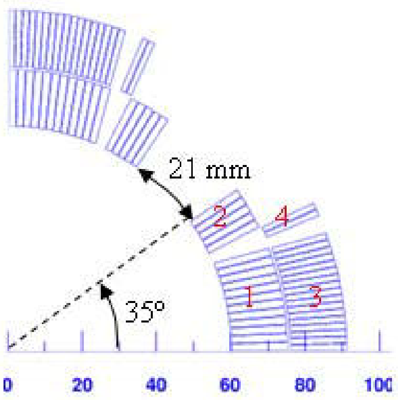

Figure 92 – Proposed cross-section of the MQXC magnet.

Table 19 – Geometric parameters of the coil.

Block N°	Nb Cond	r (mm)	φ (°)	γ (°)	cable type
1	12	60.000	0.2101	0.000	cable 01
2	5	60.000	25.728	27.757	cable 01
3	17	75.920	0.1849	0.000	cable 02
4	2	75.920	23.501	22.762	cable 02

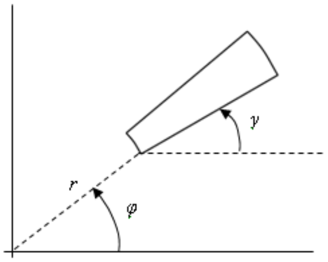

Figure 93 – Definition of the parameters used in the Table 19

V.2.4 The iron yoke

The role of the iron yoke is mainly to shield the magnet from outside magnetic field and to reduce the operational current; it also slightly increases the short sample gradient. The guidelines for the mechanical design aim at having a complete support of electromagnetic forces through the stainless steel collars [70]. This concept has the advantage of decoupling the mechanical design of the collared coils from the magnet yoke. An extensive study has been made to determine the needed thickness of the collars, based on their deformation in nominal conditions [70]: the final value of the thickness has been set to 35 mm. Taking also into account a 2-mm-gap between collars and the iron yoke, this provides a yoke inner diameter of 260 mm. Its outer diameter is set at 550 mm for tooling and tunnel limited space reasons. The yoke is a stack iron sheet whose thickness has not yet been defined. For the computation we assumed values similar to the LHC main dipoles, *i.e.*, an iron sheet thickness of 5.8 mm with a package coefficient of 0.985.

The heat exchanger has to fit in the yoke. Two possible configurations for the heat exchanger have been studied [70]. The first configuration needs two 80 mm diameter exchangers, and the second one needs one 105 mm diameter exchanger. The yoke must anyway have four holes to satisfy the four-fold symmetry of the magnet, thus avoiding unallowed multipoles. One has two possible angular positions, *i.e.,* on the midplane or at 45° (see Figure 94). From the integration point of view, the best choice would be one exchanger, and four holes of 105 mm in line with the mid-plane, but one has also to consider the field quality and the impact on the transfer function. The decrease of the short sample gradient of the 45° and of the 90° solution is around 0.40 % and 0.52 % respectively. The reduction of the transfer function at nominal current due to the iron saturation with the holes, is 1.5-3%, *i.e.,* in between what we have for the LHC MQXA (6%) and MQXB (2%) (see Figure 95) and is considered as acceptable. The impact on b_6 is 1-2 units (see Figure 96). For both solutions the position affecting less the multipole b_6 is the holes in line with the mid-planes. The impact on b_{10} and b_{14} is within 0.1 units in all cases.

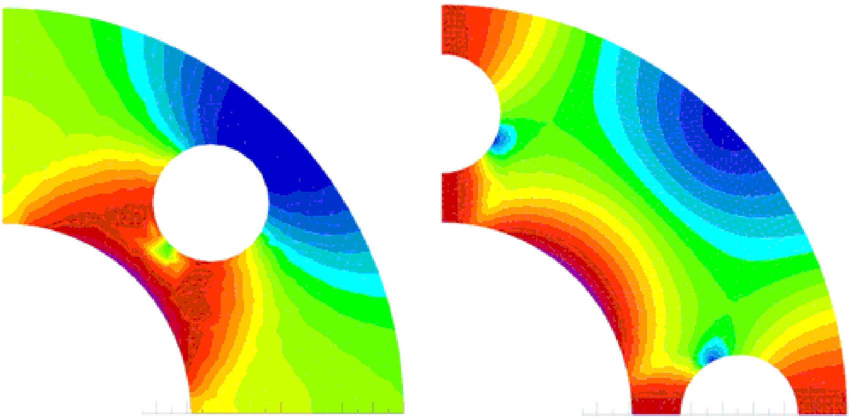

Figure 94 – Cross-sectional view of the MQXC iron yoke with either 4 holes in line with each pole (left) or 4 holes in line with each mid-plane. The configuration presented here is the 80 mm one.

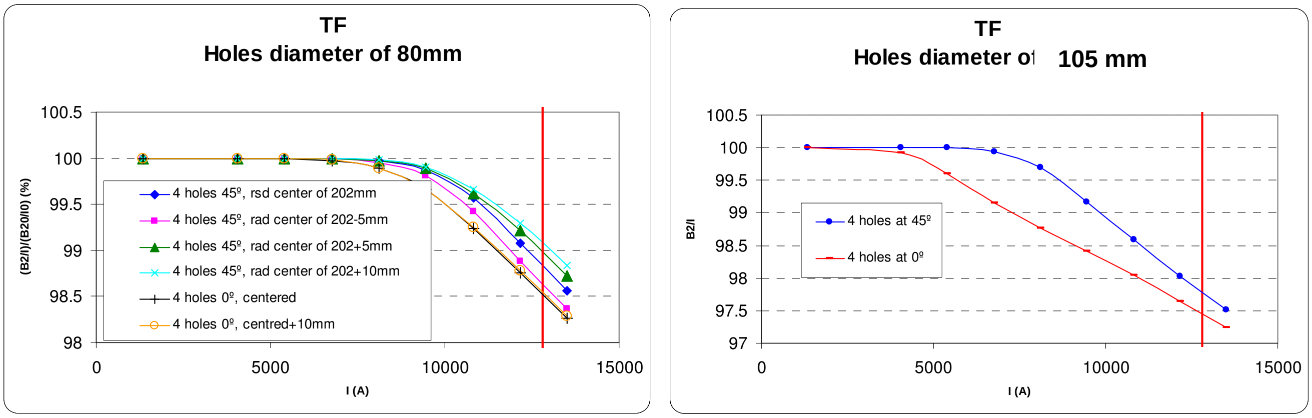

Figure 95 - Transfer function in case of the 80 mm and 105 mm hole cases.

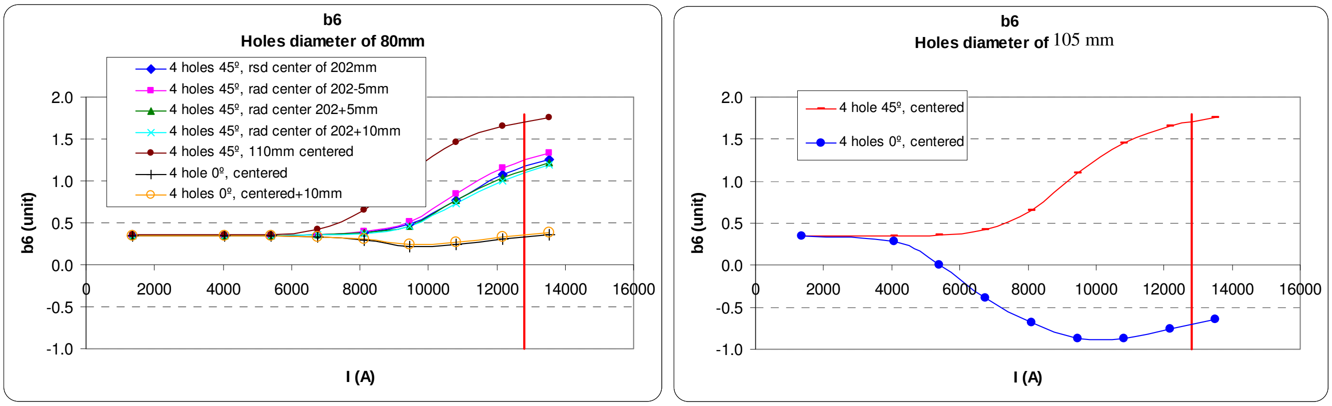

Figure 96 - Study of the impact of holes of 80 mm (left) and 105 mm (right) in the iron yoke on the multipole b_6. The vertical red line corresponds to the nominal current. The coil cross-section used here was a previous version of the MQXC.

The proposed solution is the 105 mm holes aligned with the mid-planes since this is the best configuration for the cooling system and looks as acceptable form the magnetic point of view. The cross-section of the yoke is shown in detail in Figure 97. The 105 mm holes are radially centered in the yoke in order to leave 20 mm of matter on each side. A notch (A) is set on the inner radius for the stainless-steel key which allows centering coils and collars assembly in the yoke and another one (B) is set on the outer radius to handle the magnet. Cavities of 20.5 mm diameter (C) used to house the axial iron rod are located on each pole line. Their radial location, still not defined, has to be chosen according to mechanical reasons since their impact on the field quality and on the transfer function is negligible.

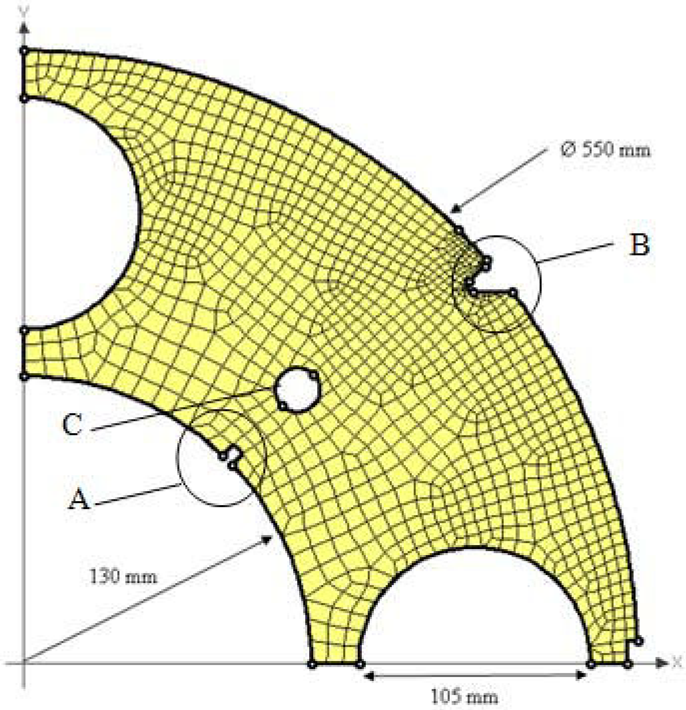

Figure 97 – Cross-section of the iron yoke.

V.2.5 Summary of the magnetic performance

The final performances of the MQXC quadrupole are summarized in Table 20. The short sample gradient is of 147.1 T/m and the nominal gradient computed at 80 % of the short sample current is of 118.5 T/m. Allowed multipoles are within 0.1 units at nominal current.

Table 20 – Main features of the MQXC magnet.

	unit	MQXC
Aperture diameter	mm	120
Inner iron diameter	mm	260
Outer iron diameter	mm	550
Short sample Gradient	T/m	147.1
Short sample current	kA	15.9
Operational gradient	T/m	118.5
Operational current	kA	12.72
Inductance	mH/ m	5.06
Reference radius	mm	40
b_6 (I = In)	unit	-0.006
b_{10} (I = In)	unit	-0.036
b_{14} (I = In)	unit	-0.076
Fx (I = In)	MN/m	0.93
Fy (I = In)	MN/m	-1.35

Load lines in blocks 1, 2, 3 and 4 (see Figure 92) are plotted in Figure 98. The magnet reaches the short sample conditions in block number 2 at a peak field of 9.8 T. Peaks field computed at short sample current in blocks 1, 3 and 4 are 8.8 T, 7.7 T and 8.2 T respectively. The current of the power supply is limited at 14000 A and therefore the MQXC magnet cannot reach on the test bench its short sample current of 15900A. The largest gradient achievable in the tunnel corresponding to a current of 14000 A is of 130 T/m. The effect of the saturation of the iron yoke on the multipoles is shown in Figure 100 and the transfer function is plotted, together with the MQXA and MQXB ones. The maximal variation on b_6 is of 0.8 units, and of 0.1 units for b_{10}.

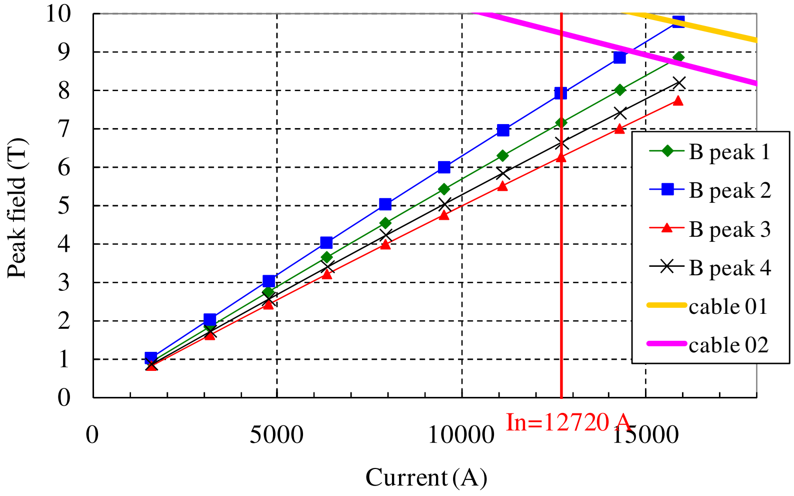

Figure 98 - Load lines in each of the four coil blocks together with the critical surface of the superconducting cables 01 and 02.

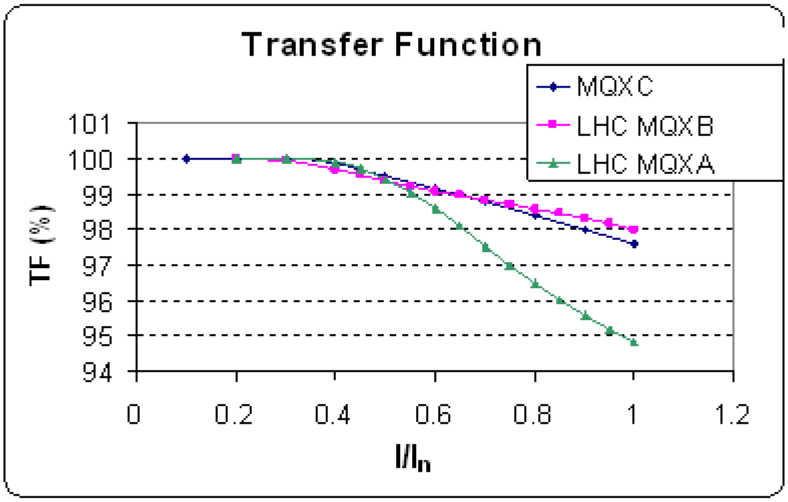

Figure 99 - Transfer functions of the MQXC, MQXA and MQXB quadrupoles.

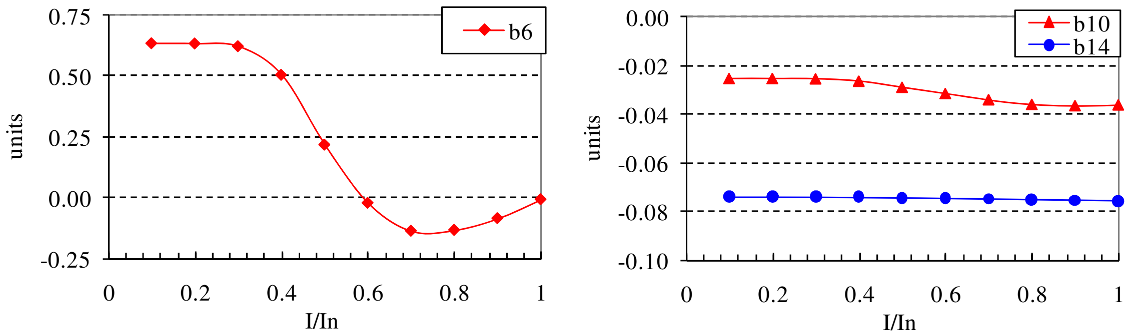

Figure 100 - Influence of the iron yoke saturation on the multipoles.

V.2.6 *Layer jump and splice*

The layer jump and the splice, sketched in Figure 101 and in Figure 102, connect electrically the inner layer to the outer layer and are located close to the connection side of the magnet. Their length is similar to what we have for the LHC main dipole since it is made from the same cable. The inner layer cable is pushed outward (layer jump) and then is overlapped by the outer layer cable (splice). In the splice the current is supposed equally shared between the two cables.

In Table 21 we present the multipoles provided by the layer jump and the associated splice. The field harmonics have been computed at points 1, 2, 3 and 4 (see Figure 101). The magnetic length of the layer jump and of the splice is of the same order than the sum of the length of each part, *i.e.,* 240 mm. The splice and layer jump contribution to the multipoles integral has been computed assuming a conservative length of the straight part of 7.25 m.

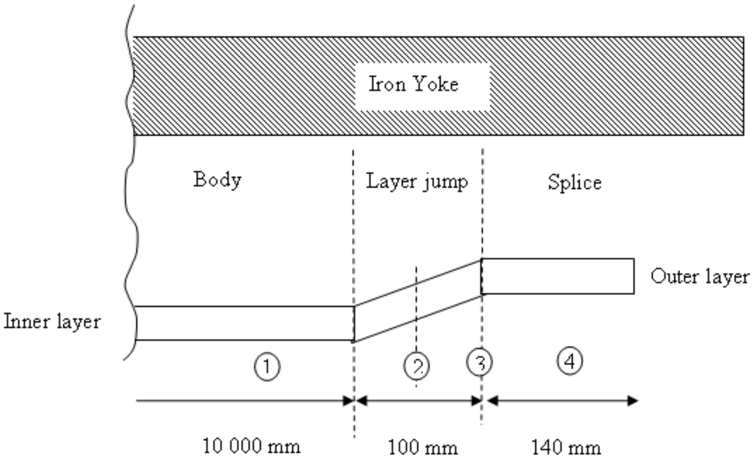

Figure 101 – Sketch of the layer jump.

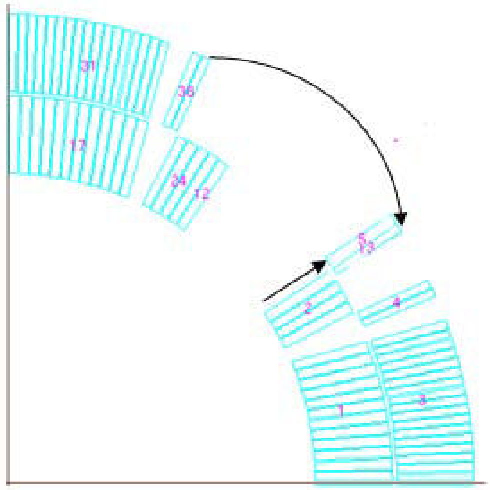

Figure 102 – Coil block numbering in the splice.

Table 21 – Field harmonic (in units) given by the layer jump and the splice and their contribution to the field integral.

Position	(1)	(2)	(3)	(4)	Contribution to the field integral
b_6	-0.01	11.11	16.31	16.10	0.43
b_{10}	-0.04	-2.30	-2.97	-2.99	-0.08
b_{14}	-0.08	0.13	0.17	0.17	0.00
a_2	0.00	35.54	61.38	62.64	1.61
a_6	0.00	-5.30	-7.78	-8.29	-0.22
a_{10}	0.00	-0.71	-0.92	-0.87	-0.02
a_{14}	0.00	0.36	0.42	0.42	0.01
G (T/m)	118.5	118.34	118.23	118.26	118.49

V.2.7 Design of the coil head

Here we present a tentative design of the non-connection side of the coil ends. A 3 D view is shown in Figure 103. We propose to split the four blocks of the coil in six blocks to reduce the peak field (see Figure 104). The coil head design is based on cables on mandrel and elliptical shape designs, using the code Roxie with the option constant perimeter. The optimization of the position and dimensions of the blocks have been done so as to cancel allowed harmonics while minimizing the peak field on the head and keeping the head as short as possible. For this optimization the Roxie code has been used. Spacers have been added to the coil end to compensate for keystoning and adjust the position of each cable in the winding. Their dimensions are similar to what have been measured on the LHC main dipole. The length of the head is of 165 mm.

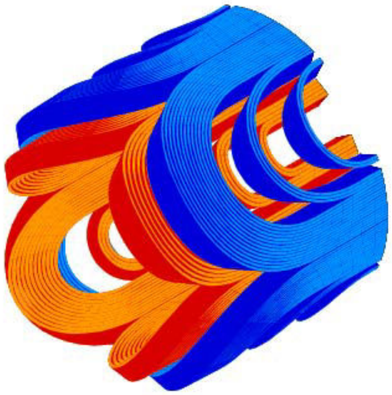

Figure 103 – 3 D view of the non connection side of the MQXC coil head.

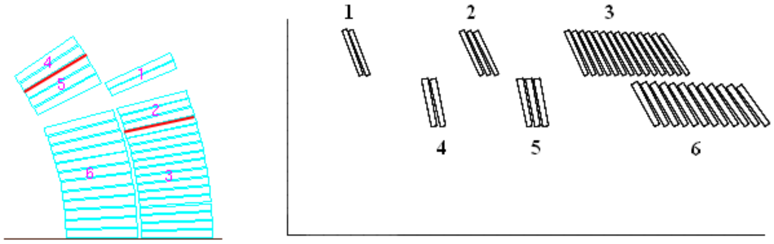

Figure 104 – Left: split of the coil blocks leading to the 6 blocks of the coil head. Right: Transverse view in the *zy*-plan of the coil head.

We first assume an iron yoke much longer than the coil: in this case, the superconductor reaches the critical surface in the head, block 4 in Figure 104, with a field value very close to what we have in the straight part of the magnet, *i.e.,* 9.8 T. This suggests that having the iron covering the heads does not significantly reduce the short sample field, and that this simpler option looks viable.

An alternative option would be to further reduce the peak field in the head, and thus to get the quench in the magnet body, by shortening the iron yoke. In Figure 105 we plotted the peak field in the coil end versus the difference between the length of the yoke and the length of the coil. Negative ΔL value means that the yoke is shorter than the coil and positive value means that the yoke is longer than the coil. When $\Delta L = 0$ the yoke edge is in line with the coil edge. Whatever the length of the yoke, the quench is always in block 4 (see Figure 104), either in the straight part when the yoke is shorter than the coil ($\Delta L < 0$) or in the head when $\Delta L > 0$. If the head is totally naked (*i.e.,* not covered by the yoke), the short sample field in the coil end is 0.2 T lower than in the straight part of the magnet, covered by the yoke, see Figure 105. This corresponds to ~0.95 kA in terms of current margin (see Figure 106). We remind the reader that the yoke only contributes to 3.2% of the gradient, for a fixed current and an unsaturated yoke, due to the large collars.

Since the margin added by a shorter iron yoke is small, the option of a yoke 50 mm longer than the coil, enabling better shielding of the magnet aperture from external magnetic field, looks viable (see Figure 107). In this case, the peak field leading to a quench would be of the same value both in the head and in the straight part, *i.e.*, 9.8 T.

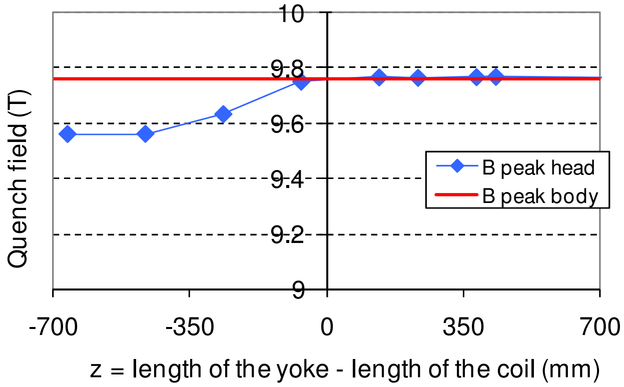

Figure 105 – Peak field leading to a quench in the coil head (blue line) versus the difference between the length of the yoke and the length of the coil. The red line shows the quench field in the straight part of the magnet.

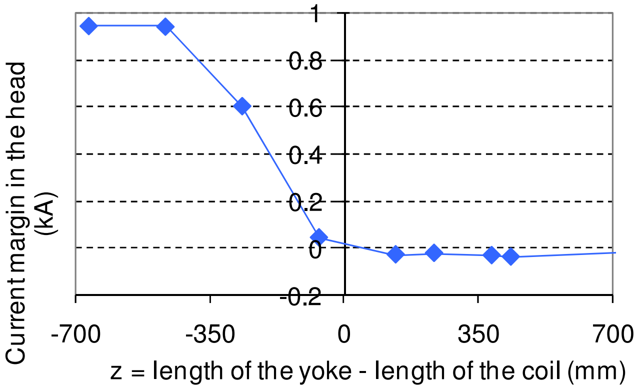

Figure 106 – Current margin in the coil head when the straight part of the magnet is fed with its short sample current, versus the difference between the length of the yoke and the length of the coil.

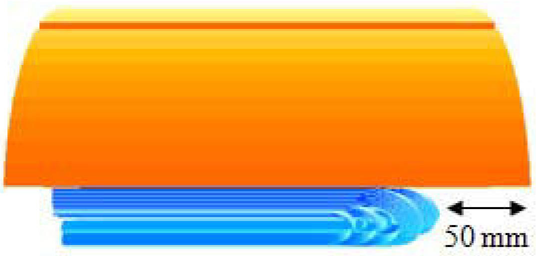

Figure 107 – Iron yoke coil in the final configuration: the yoke is 50 mm longer than the coil.

The gradient and the field harmonics along the magnet axis are plotted in Figure 108. The magnetic length of the head is of 113 mm, *i.e.*, 52 mm smaller than the physical length. Average values of the field harmonic are shown in Table 22, together with the harmonic contribution of the head to the integral, which is negligible: the head is rather close to be self compensated. The contribution to the integral is less than 0.1 units.

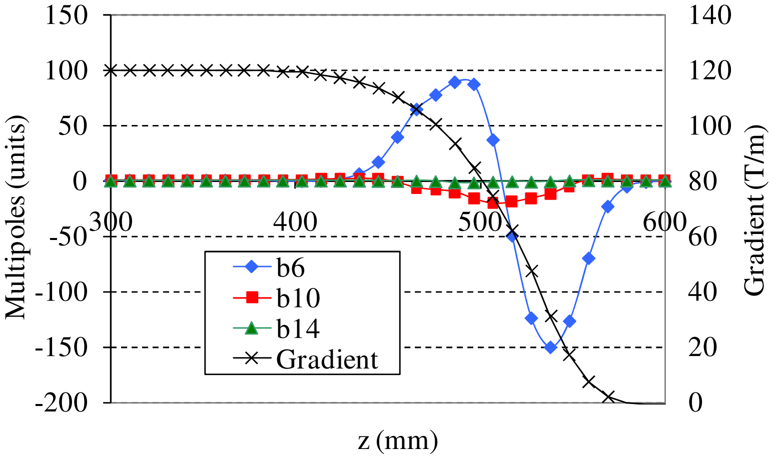

Figure 108 – Gradient and allowed field harmonics along the axis of the magnet. The iron yoke is 50 mm longer than the head.

Table 22 – Average multipole values in the coil end NCS and contribution to the field integral. Multipoles are given in units.

Multipole	average over the head	contribution to the integral
b6	-6.5	-0.10
b10	-5.5	-0.08
b14	-0.4	-0.01

V.3 Field quality study

As we explained in Section IV.3, the geometric part of the magnetic field harmonics error of a series of magnets can be defined by two components: The average and the standard deviation. In the following we will give estimates of the expected value of the standard deviation of the field error in the MQXC quadrupole series (20 magnets) which will be built in the near future. The average value for non-allowed harmonics (except a_6 and a_{10}) can be set to zero according to the study we carried out in Section IV.6. These values are very important for the beam stability study and for dimensioning corrector magnets.

The standard deviation of the field harmonic error is due to the non-reproducibility of the industrial process of the coil manufacturing and assembly. The position of the coil is the main source of the random component. Random displacements of coil blocks generate the *rms* component of the field harmonic errors. In [90], the measured standard deviation of the multipoles computed from of a set of identical magnets is used to estimate the actual *rms* blocks displacement d by means of a Monte-Carlo analysis.

Values of *rms* blocks displacement estimated in [90] for CERN LHC magnets range from 0.010 mm for the MQXA quadrupole to 0.029 mm for the MQ quadrupole. The LHC main dipole, which uses the same cables than the MQXC quadrupole, has a coil block displacements estimated at 0.025 mm. Here we used a conservative estimate of 0.030 mm.

Table 23 - Multipoles standard deviation given at 1σ caused by a *rms* coil blocks displacement of 0.030 mm. The reference radius is taken as 2/3 of the aperture radius.

	Std. dev. (unit) (1σ)	
n	bn	an
3	0.89	0.89
4	0.64	0.64
5	0.46	0.46
6	1.28	0.33
7	0.21	0.21
8	0.16	0.16
9	0.08	0.08
10	0.06	0.06
11	0.03	0.03
12	0.02	0.02
13	0.01	0.01
14	0.01	0.01

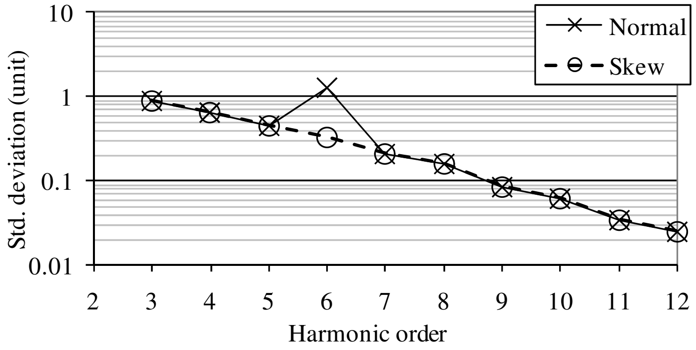

Figure 109 - Harmonic standard deviation caused by a random displacement of the blocks of rms value of 0.030 mm.

V.4 Summary

We presented a novel method to optimize the cross-section of a cos2θ-type quadrupole for accelerators. The method is based on the Fourier expressions giving the magnetic field components produced everywhere, *i.e.,* in the air and in the coil, by a quadrupole with coils made of one pure sector block, and powered with a constant current density. The general case of a quadrupole with coils made of more than one sector is then regarded as a sum of basic quadrupoles with coils made of only one sector.

The method consists in scanning all possible sector angles combinations so as to obtain a global view of the coil layouts satisfying the field quality requirements. Then for each cross-section having a “good” field quality, we calculate the peak field in the coil by means of the Fourier series truncated at a chosen order so as to determine the short sample current and the short sample gradient. This gives an overview over all cross-sections which allows to chose the one which best fits the magnet specifications. Moreover, the knowledge of the magnetic field at any point in the sectors allows calculating the magnetic forces acting on it. The effect of an infinitely permeable iron yoke can also be taken into account by means of the current image method.

Then, to pass from an analytical solution consisting of a set of sector angles to a real coil made of Rutherford cables, we first compute for each coil block the number of turns of cable which best fits the sector coil angle. Then we slightly displace the blocks so as to compensate for the unavoidable field harmonic distortion due to the discrete cable size, and due to the iron yoke saturation.

We applied this method to optimize the four-block coil of the new inner triplet quadrupole of the LHC. We performed a scan over the 6 free parameters given by the sectors angles for two different configurations of the cables arrangement. In the first configuration the inner and outer layers of the coil are exclusively wound with different cables, while in the other configuration the inner layer cable is used to wound the upper block of the outer layer. Our method allowed to find out that both configurations provided the same maximal gradient of 150 T/m (infinitely permeable iron included).

The first configuration has been chosen for our proposed coil cross-section of the MQXC. The final coil cross-section, fine tuned with Roxie and surrounded by a real iron yoke, provides a short sample gradient of 148.1 T/m. Considering a margin on the current of 20 %, the operational current is of 12.8 kA, and thus fits the present power supply hardware constraints of 14 kA. We also proposed a design for the non-connection side of the coil ends.

Conclusion

In this thesis we worked on several topics related to superconducting magnets: a semi-analytical expression for estimating the magnetic energy stored in quadrupoles [16], the precision of the coil positioning in Nb_3Sn magnets [17] and the estimate of the uncertainty in the mean of non-allowed harmonics in Nb-Ti magnets, and the design of a large aperture quadrupole for the new quadrupole for the LHC interaction regions upgrade using available tool [14] [15] and by mean of a novel a novel method to optimize quadrupole coil layouts [18] [19].

Quadrupoles magnets are essential to focus beams in particle accelerators and are often made from superconducting material. This enables providing large field gradients (which is the relevant parameter for superconducting quadrupole) and to reduce the operating cost. To operate reliably, quadrupoles have to be protected against irreparable damage which may be inflicted upon the coil during a quench. The magnetic energy stored in the magnet when operating at maximal magnetic field is a crucial parameter for dimensioning the power supply and the magnet protection system. In Chapter III we worked out a formula giving the energy as a function of the main features of a quadrupole layout (magnet aperture, coil width, grading, iron yoke dimension). The formula is very useful at the early stage of a quadrupole design where details of the coil are unknown. The formula consists in a main term giving the energy in an ironless quadrupole, and of two corrective coefficients enabling taking into account current grading in the coil (*i.e.,* a higher current density in the outer layers of the coil) and for the presence of an infinitely permeable iron yoke around the coil. The main term has been obtained from the Fourier decomposition of the current density flowing in an infinitely long quadrupole with coils made of pure sectors. The corrective coefficient accounting for the presence of the iron yoke has also been obtained analytically by means of the current image method, while the corrective coefficient accounting for current grading in the coil is a heuristic coefficient derived from a numerical study carried out on real coils. A comparison of the stored energy in real superconducting quadrupoles numerically computed and the analytical estimates of the energy showed agreement within 10 %.

We then showed that for long yoked coil (*i.e.,* transverse dimensions much smaller than the longitudinal one) the longitudinal force which tends to elongate the coil along its axis can be approximated by the stored energy per unit of meter of magnet only if the iron is infinitely permeable. We also showed, by means of the Maxwell stress tensor, that the force is necessarily smaller when the yoke is smaller than the coil.

The other important feature for magnets used for particle accelerators is the magnetic field quality. To ensure the beam stability, magnets have to provide the purest field as possible, *e.g.,* dipolar field, quadrupolar field, … The field quality is usually expressed through harmonic coefficients given in units of 10^4 times the main field. Harmonics are usually specified to be within one unit. Superconducting magnets have a field quality which is dominated by the so-called geometric errors, *i.e.*, the position of the coil. Geometric errors are badly reproducible due to tolerances in the components or in the assembly: This leads to a spread of the field harmonic errors. At the early stage of a magnet design it is of importance to give a reliable estimate of the expected sigma and mean values of the field error. In Chapter IV we first recalled the standard way, based on an inverse Monte-Carlo simulation, to estimate the reproducibility in the coil position in the transverse cross-section responsible for the sigma part of the integrated field error in a magnet series. This method has been used in the past for Nb-Ti magnets and showed reproducibility of coil position ranging from 0.030 mm to 0.010 mm. We then applied the same method for the first time on small series of Nb_3Sn magnets recently built in the frame-work of the FNAL core program (6 HFDA dipoles of 43.5 mm aperture diameter) and of the LARP program (6 TQ quadrupoles of 90 mm aperture diameter). The spread in the coil positioning has been estimated of 0.13 mm for the dipoles and of 0.14 mm for the quadrupoles. The estimation of the spread in the dipole has been shown in good agreement with optical measurement carried out on a slice of the magnet. These values are 5 to 15 times larger than what had been estimated for dipoles and quadrupoles manufactured in the past 15 years and based on the mature Nb-Ti technology. However, Nb_3Sn magnets studied here are short models at the R&D phase where the focus is more on the short sample performances than on the field quality. Therefore, one cannot conclude yet that Nb_3Sn is intrinsically providing a worst field quality than Nb-Ti.

We then analyzed the coil waviness along the axis of the TQ quadrupoles using magnetic measurements that have been done at different positions in the magnet straight part. The estimation in the spread in the coil position along the magnet axis has been found to be around 0.036 mm, a factor four times smaller than the spread from magnet to magnet. This value is similar to what has been estimated in the LHC main dipole. This means that the Nb_3Sn technology already shows a level of reproducibility, along the magnet axis, similar to that of Nb-Ti technology.

Another issue which has been opened in literature since many years is the concept of uncertainty. Following the experience of HERA, the field quality in a magnet series was expressed not only by a mean and a standard deviation, but also by a third parameter, called the uncertainty of the mean. This third number accounted for systematic components in the non-allowed multipoles (which are zero by symmetry) or for systematic differences in allowed multiupoles between magnets made by different firms. We investigated this problem in 11 series of Nb-Ti quadrupole magnets used in the LHC (7) and in RHIC (4). We showed that the non-zero of the mean measured in these series is consistent with the statistical bias related to the finite size of the sample. This holds for all harmonics, except a_6, a_{10}, b_4 and b_8. We showed that part of the non-zero mean value of a_6 and on a_{10} is due to the connection side of the magnet ends which do not respect the four-fold symmetry of the quadrupoles. We also notice that the large spread in the mean of b_4 and b_8 is only observable in quadrupoles which have been collared asymmetrically, *i.e.,* like a dipole. In conclusion we found no evidence of the need of introducing the concept of uncertainty.

Current distributions providing a pure quadrupolar field are solutions of a magneto-static inverse problem. There are an “infinite” number of solutions. This “infinity” can be reduced by taking into account of additional constrains as material properties (superconductor, iron yoke, length and dimensions of the conductors, mechanical issues, cost, …). Indeed, the phase space of solution is very large and numerical methods only manage to find out local optima. In Chapter V, we presented a novel method to optimize the electromagnetic design of superconducting quadrupole magnets based on the cos2θ design. The method is based on the Fourier series of the magnetic field produced everywhere by a quadrupole with coils made of only one sector. This simplified model can be treated semi-analytically. The more general case of a quadrupole with coils made of several sectors is regarded as a sum of quadrupoles with coils made of one sector. To find out a global solution to the inverse problem, we proposed to perform a scan over all the possible combinations of sectors angles and positions reachable with a given angular step. To diminish the computational time we suggested to reduce the range over which angles varies so as to get rid of unpractical and low gradient solutions. The number of retained solutions, consisting in sets of angles, can be then controlled by constrains on the field quality.

The cross-sections which best fit with the specifications (gradient, current,…) are then analyzed in detail through a numerical code considering real arrangements of cable, *e.g.,* Roxie [73]. The number of turns of cables is chosen to best fit the calculated angles. The unavoidable drift in the field harmonic due to the discrete size of the cable of the iron yoke saturation is compensated by slightly displacing the blocks constituting the coil.

This method has been applied to the electromagnetic design of the MQXC quadrupole aiming at replacing the actual inner triplet quadrupoles of the LHC. According to the specifications, the coil is made of 2 layers based on the spare cable of the LHC main dipole. Each layer has 2 blocks. The scan has been accomplished within 5 hours an angular step of 0.3º for the inner layer and of 0.9º for the outer layer. This provided 150 distinct coil layouts. The choice of the type of cable arrangement was chosen to have the smallest short sample current while providing the largest possible short sample gradient. The amount of cable has also been a decisional parameter. The final coil layout, iron yoke included, has a short sample gradient of 148 T/m and a short sample current of 15.9 kA. In addition to that, we also presented a tentative design of the non-connection side of the coil head, and we provided an estimate of the expected uncertainty in the magnetic field errors.

References

[1] E. Augé, et al., "*Voyage au cœur de la matière*", Paris: Belin-CNRS, 2002.

[2] Y. Ajima, et al., "*The MQXA quadrupoles for the LHC low-beta insertions*", Nucl. Instrum. Meth., Vol. A 550, pp 499-513, 2003.

[3] ALICE, *A Large Ion Collider Experiment*; http://alice.web.cern.ch/alice.

[4] M. Anerella, et al., "*The RHIC magnet system*", Nucl. Instrument. Meth., Vol. A 499, pp. 280-315, 2003.

[5] F. M. Asner, "*High field superconducting magnets*", Oxford: Clarendon Press, 1999.

[6] W. Ansorge, "*Some basic design parameters of the ISR SC quadrupole*", CERN, Geneva, Switzerland, internal note, ISR-MA/WA/rh, 1973.

[7] A. Asner, "*On a semi-analytical method for field and force calculation in coil ends of cylindrical aperture superconducting dipole and quadrupole magnets*", CERN Note 86-8, 1986.

[8] ATLAS, *A Toroidal Lhc AppartuS*; http://atlas.web.cern.ch//atlas/welcome.html.

[9] B. Bellesia, "*Correlation between magnetic field quality and mechanical components of the Large Hadron Colider main dipole*", Ph. D. Thesis, University of Clermont-Ferrand, 2006.

[10] B. Bellesia, et al, "*Field quality in low-β superconducting quadrupoles and impact on the beam dynamics for the large hadron collider upgrade*", CERN, LHC Project Report 1010, 2007.

[11] B. Bellesia, et al, "*Random Errors in superconducting dipoles*", Proceeding of European Particle Accelerator Conference, Edinburgh, Scotland, 2006.

[12] R. A. Beth, "*An Integral Formula for Two-Dimensional Fields*", IEEE Trans. Nucl. Sci., Vol. 38, No. 12, pp 4689-4692, 1967.

[13] J. Billan et al., "*Construction of a prototype superconducting quadrupole magnet for high luminosity insertion at the CERN intersecting storage ring*", CERN Yellow Report 76-16, 1976.

[14] F. Borgnolutti, et al., "*130 mm aperture quadrupoles for the LHC luminosity upgrade*", Proceeding of Particle Accelerator Conference, Albuquerque, NM, USA 2007.

[15] F. Borgnolutti, et al., "*Nouveaux quadrupoles à grande ouverture pour l'accroissement de la luminosité du LHC",* Poster présenté à Neuvièmes Journées de Cryogénie et Supraconductivité à Aussois, France, 25-27 mars 2009 .

[16] F. Borgnolutti, et al., "*Analytic Estimates of the Magnetic Energy in Superconducting Quadrupoles",* IEEE Trans. On App. Supercond., Vol. 18, No. 4, pp 1774-1780, 2008.

[17] F. Borgnolutti, et al., "*Reproductibility of the coil positioning in Nb3Sn magnet models through magnetic measurements*", IEEE Trans. On App. Supercond., Vol. 19, No. 3, pp 1100-1105, 2009.

[18] F. Borgnolutti, et al., "*A Method for Coil Design of Superconducting Quadrupole Based on Sector Coils and Fourier Transform*", To be presented at the Magnet Technology Conference to be held in Hefei (China) in October 2009.

[19] F. Borgnolutti, "*Quadrupole design study for the LHC Phase-I Upgrade*", LHC IR Upgrade Working Group 14, 15 May 2008; http://liuwg.web.cern.ch/liuwg.

[20] F. Borgnolutti, "*Update on the coil cross-section of the low-beta quadrupole*", LHC IR Upgrade Working Group 18, 15 May 2008; http://liuwg.web.cern.ch/liuwg.

[21] R. Bossert, et al., "*Construction Experience With MQXB Quadrupole Magnets Built at Fermilab for the LHC Interaction Regions*", IEEE Trans. On App. Supercond., Vol 13, No 2, pp 1297-1300, 2003.

[22] R. Bosset, et al., "*Developement of TQC01, a 90 mm Nb_3Sn model quadrupole for LHC upgrade based on SS collar*", IEEE Trans. On App. Supercond., Vol. 16, No2, pp. 370-373, 2006.

[23] L. Bottura, et al., "*Field errors decay and "snap back" in LHC model dipoles*", IEEE Trans. On App. Supercond., Vol. 7, No. 2, pp 602-605, 1997.

[24] L. Bottura, "*A practical fit for the critical surface of Nb-Ti*", IEEE Trans. On App. Supercond., Vol. 10, No. 1, pp 1054-1057, 2000.

[25] L. Bottura, "*Standard Analysis Procedures for Field Quality Measurement of the LHC Magnets*", CERN-LHC Project Document LHC-XMT-ES-0001 rev 0.2, 2001.

[26] L. Bottura, Private communication.

[27] H. Brechna, "*Superconducting Magnet Systems, Springer*", Berlin: Springer Verlag, 1973.

[28] O. Burning, et al., "*The LHC main ring*", CERN-LHC Design Report 2004-003, 2004.

[29] S. Caspi, et al., IEEE Trans. Appl. Supercond. 17 (2007) 1122.

[30] M. La China, et al.," *Comparative study of heat transfer from Nb-Ti and Nb3Sn coils to He II*", Phys. Rev. Spec. Top. Accel. Beams 11, 082401, 2008.

[31] CMS, *The Compact Muon Solenoid*; http://cmsinfo.cen.ch/welcome.html.

[32] W. Cooper, et al, "*Fermilab Tevatron Quadrupoles*", IEEE Transactions on Magnetics, Vol. 19, No. 3, pp. 1372-1377, 1983.

[33] E. D. Courant, et al., "*Theory of the Alternating –Gradient Synchrotron*", Science Direct-Annals of Physics, Volume 281, Issue 1-2, pp 360-408, 1957.

[34] W. G. Davies, "*The theory of the measurement of magnetic multipoles fields with rotating coil magnetometers*", Nuc. Instrum. Meth. Vol A311, pp 399-436, 1992.

[35] A. Devred, et al, "*Investigation of wire motion in superconducting magnets*", IEEE Trans. Magn. Vol 27 No 2, pp 2132-2135, 1991.

[36] A. Devred, "*Review of superconducting dipole and quadrupole magnets for particle accelerators*", DAPNIA/STCM 99-24, 1999.

[37] A. Devred and D. Trassart, "*Magnetic Field Produced by a Single Current Line near or within a Ferromagnetic Cylinder or Tube*", CERN Departemental Report, AT 2005-10, 2005.

[38] A. Devred, "*Practical low-temperature superconductors for electromagnets*", CERN Yellow Report, 2004-006, July 2004.

[39] *DESY;* http://zms.desy.de/research/accelerators/index_eng.html.

[40] E. Durand, "*Magnetostatique*", Masson et Cie, Paris, 1968.

[41] J. W. Ekin, "*effect of transverse compressive strain on the critical current and upper critical field of Nb3Sn*", J. Appl. Phys., Vol. 62, No. 12, 1987.

[42] J. W. Ekin, "*strain effects in superconducting compounds* ", Adv. Cryo. Eng. (Materials), Vol. 30, pp. 823-836, 1984.

[43] S. Feher, et al. "*Development and test of LARP technological quadrupole (TQC) magnet*", IEEE Trans. On. Appl. Supercond. Vol. 17,No. 2, June 2007.

[44] P. Ferracin, et al., "*Field quality analysis of the next generation IR quadrupole for the LHC*", Proceeding of Particle Accelerator Conference, Portland, Oregon, USA, 2003.

[45] P. Ferracin, et al., "*Modeling of random geometric errors in superconducting magnets with applications to the CERN Large Hadron Collider",* Phys. Rev, STAB 3 (2000) 112403.

[46] P. Fessia, et al., "*Parametric analysis of forces and stresses in superconducting quadrupole sector winding*", IEEE Trans. On App. Supercond., Vol. 17, No 2, pp 1269-1272, 2007.

[47] P. Fessia, et al., "*Parametric analysis of forces and stresses in superconducting quadrupole sector winding*", CERN-sLHC Project Report 0003, 2007.

[48] P. J. Ferry et al., "*Analysis of the Performance of the eight Superconducting Quadrupoles for the Lep Low-Beta Insertions*", CERN LEP-MA 89-67, 1989.

[49] Pier-Paolo Granieri, "*Development of the Cable Insulation for the LHC Triplet Upgrade Phase-I*", Presented in a TE seminar at CERN in July 2009: http://indico.cern.ch/conferenceDisplay.py?confId=63263.

[50] R. Gupta, "*Estimating and adjusting field quality in superconducting accelerator magnets*", Proceeding of Particle Accelerator Conference, Barcelona, Spain, 1996.

[51] R. Gupta, et al., "*Tuning shims for high field quality in superconducting magnets*", IEEE Trans. On . Appl. Supercond., Vol. 32, No. 4, pp 2069-2073, 1996.

[52] R. W. Hanft, et al., "*Studies of time dependent field distortions from magnetization currents in Tevatron superconducting dipole magnets*", IEEE Trans. Magn., Vol. 25 No. 2, pp. 1647-1651, 1989.

[53] M. Harrison et al, "*RHIC Project Overview*", Nuc. Inst. Meth., Vol. A 499, pp 235-244, 2003.

[54] J. Herrera, et al., "*Random errors in the magnetic field coefficients of superconducting magnets*", Proceeding of Particle Accelerator Conference, 1985.

[55] J. Herrera, et al., "*Random errors in the magnetic field coefficients of superconducting quadrupoles magnets*" Proceeding of Particle Accelerator Conference, 1987.

[56] J. M. Jolion, "*Probabilité et statistique* ", Cour INSA Lyon, 2006 ; http://rfv.insa-lyon.fr/~jolion/STAT/poly.html.

[57] G. A. Kirby, et al., "*Design twin aperture superconducting quadrupoles for the LHC dump insertion*", IEEE Trans. On App. Supercond., Vol. 7, No. 2, pp 562-565, 1996.

[58] K. S. Krane, "*Introductory Nuclear Physics*", John Wiley & sons, 1987.

[59] V. V. Kashikhin, et al., "*Field quality study in Nb_3Sn accelerator magnets*", Proceeding of Particle Accelerator Conference, Knoxville, Tennessee, USA, 2005.

[60] J. P. Koutchouk, et al., "*A Solution for Phase-one Upgrade of the LHC Low-Beta Quadrupoles based on Nb-Ti*", CERN LHC Project report 1000, 2007.

[61] M. J. Lamm, "*Nb_3Sn accelerator magnet development around the world*", IEEE Trans. On App. Supercond., Vol. 13, No 2, pp 1278-1283, 2003.

[62] M. J. Lamm, et al., "*Test results of Fermilb-built quadrupoles for the LHC interaction regions*", Proceeding of European Particle Accelerator Conference, Edinburgh, Scotland, 2006.

[63] *LHC design report*: http://ab-div.web.cern.ch/ab-div/publications/LHC-DesignReport.html.

[64] *LHCb, The Large Hadron Collider Beauty experiment*; http://lhcb.web.cen.ch/lhcb.

[65] A. Madur, "*Contribution à la métrologie magnétique dans les multipoles d'accélèrateurs : Les quadrupoles du Synchrotron Soleil*", Ph. D. thesis, INPL, 2006.

[66] R. Meinke, "*Superconducting magnet system for HERA*", IEEE Trans. Magn. Vol. 27 No. 2, pp. 1728-1734, 1991.

[67] R. Ostojic, et al., "*Conceptual Design of the LHC Interaction Region Upgrade: Phase-I, CERN*, LHC Project Report 1163, 2008.

[68] R. Ostojic, et al., "*The Construction of the Low-Beta Triplets for the LHC*", Proceeding of Particle Accelerator Conference, Knoxville, Tennessee, USA, 2005.

[69] R. Ostojic, et al., "*Low-Beta quadrupole designs for the LHC luminosity upgrade*", Proceeding of Particle Accelerator Conference, Knoxville, Tennessee, USA, 2005.

[70] F. Regis and P. Fessia, "*Study of the quadrupole collar structure*", LHC IR Upgrade Working Group 14, 15 May 2008; http://liuwg.web.cern.ch/liuwg.

[71] L. Rossi and E. Todesco, "*Electromagnetic design of superconducting quadrupoles*", Phys. Rev. Spec. Top. Accel. Beams 9, 102401, 2006.

[72] L. Rossi, "*Course on the LHC luminosity upgrade*", CERN academic training, 2009: http://indico.cern.ch/getFile.py/access?resId=2&materialId=slides&confId=55044.

[73] S. Russenschuck, "ROXIE: *A Computer Code for the Integrated Design of Accelerator Magnets*", CERN, LHC-Project-Report-276, 1999.

[74] S. Russenschuck, "*Electromagnetic design and mathematical optimization methods in magnet technology*", eBook,: Http://russ.home.cern.ch/russ.

[75] S. Russenschuck, Oral presentation gave in the framework of the LHC IR Upgrade Working Group, 2009.

[76] G. Sabbi, et al., "*Design studies of Nb_3Sn high-gradient quadrupole models for LARP*", IEEE Trans. On App. Supercond., Vol. 17, No. 2, pp 1051-1054, 2007.

[77] P. R. Sarma, "*General coil-shape in superconducting quadrupole magnets for generating the perfect field*", Nuc. Inst. And Meth., Vol. 568, Issue 2, Decembre 2006.

[78] P. R. Sarma, "*Coil shape of a two-fold symmetric perfect superconducting quadrupole for use in common-coil twin magnets*", Nuc. Inst. And Meth., Vol. 564, Issue 1, August 2006.

[79] W. Scandal, et al., "*Random errors induced by the superconducting winding in the LHC dipoles*", IEEE Trans. On App. Supercond., Vol. 10, No. 1, March 2000.

[80] E. E. Schmidt, et al, "*Magnetic Field Data on Fermilab Energy Saver Quadrupoles*", IEEE Trans. Nuc. Sci., Vol. NS-30, No. 4, August 1983.

[81] K.–H. Mess, et al. "*Superconducting accelerator magnets*", Singapore: World Scientific, 1996.

[82] S. Snfilippo, et al., "*Axis measurements, field quality and quench performance of the first LHC short straight sections*", IEEE Trans. On App. Supercond., Vol. 15, No. 2, June 2005.

[83] T. Sen, et al., "*Second generation of high gradient quadrupoles for the LHC interaction regions*", Proceeding of the Particle accelerator conference, Chicago, 2001.

[84] K. Sugita, et al., "*Analytical calculation of the field error due to radial coil distortions of the LHC low-beta quadrupole magnets*", IEEE Trans. On App. Supercond., Vol 12., No. 1, March 2002.

[85] L. T. Summers, et al., “*A model for the prediction of Nb_3Sn critical current as a function of field, temperature, strain and radiation damage*”, IEEE Trans. Magn., Vol. 27, No 2, 1991.

[86] *The Large Hadron Collider*; http://public.web.cern.ch/public/en/LHC/LHC-en.html.

[87] *The Superconducting Super Collider project*; http://www.hep.net/ssc/.

[88] *The standard package*; http://public.web.cern.ch/public/en/Science/StandardModel-en.html.

[89] E. Todesco, “*Field Harmonic*”, US Particle Accelerator School (unit 5), Albuquerque, New Mexico, 20090

[90] E. Todesco, et al., “*Field Quality in Low-Beta Superconducting Quadrupoles and Impact on the Beam Dynamics for the Large Hadron Collider Upgrade*”, Phys. Rev. Spec. Top. Accel. Beams 10, 062401e, 2007.

[91] D. Tommasini and D. Richter, “New *Cable Insulation Scheme Improving Heat Transfer to Superfluid Helium in Nb-Ti Superconducting Accelerator Magnets*”, Proceeding of European Particle Accelerator Conference, Genoa, Italy, 2008.

[92] F. Toral, “*Comparison of 2-D Magnetic Designs of Selected Coil Configurations for the Next European Dipole (NED)*”, IEEE Trans. On App. Supercond., Vol. 17, No. 2, June 2007.

[93] S. Turner, “*Measurement and alignement of accelerator and detector magnets*”, Cern Accelerator School, Anacapri, Italy, April 1997.

[94] G. V. Velev, et al., “*Field quality measurements and analysis of the LARP technology quadrupole models”,* IEEE Trans. Appl. Supercond., Vol. 18, No. 2, pp184-187, 2008.

[95] G. V. Velev, “*Magnetic field measurement of the LHC inner triplet quadrupole produced at Fermilab*”, Proceeding of European Particle Accelerator Conference, Lucerne, Switzerland, 2004.

[96] AA. VV., Poission-Superfish, group of codes supported by the Los-Alamos National Laboratory Under U.s. Government contract W-7405-ENG-36 [Online]. Available: http://www.vector-fields.com.

[97] AA. VV., Vector Fields [Online]. Available: http://www.vector-fields.com.

[98] J. Wei, et al., “*Field quality evaluation of the superconducting magnets for the relativistic heavy ion collider*”, Proceeding of Particle Accelerator Conference, 1995.

[99] E. Wildner, et al, “*Parametric study of energy deposition in the LHC inner triplet for the phase I upgrade*”, EPAC, Genoa, Italy, 2008.

[100] Martin N. Wilson, “*Superconducting Magnets*”, Oxford: Clarendon Press, 1983.

[101] R. R. Wilson, “*The Tevatron*”, Batavia, Illinois, FERMILAB, TM-763 (1978)

[102] R. Wolf, “*Analytical calculation of field errors due to small and random coil motion in cosine-theta type accelerator magnets*”, unpublished work.

[103] A. V. Zlobin, et al., “*Nb_3Sn accelerator magnet technology at Fermilab*”, Proceeding of Particle Accelerator Conference, Albuquerque, New Mexico, 2007.

[104] A. V. Zlobin, et al., “*Aperture limitation for 2nd generation Nb3Sn LHC IR quadrupoles*”, Proceeding of Particle Accelerator Conference, Portland, Oregon, USA, 2003.

APPENDIXIES

Appendix A

Here we mainly refer to the work done in [71] on scaling laws for the 2D electromagnetic design of superconducting quadrupoles for particle accelerators. In this paper were derived semi–analytical formulae allowing to estimate the short sample current and the short sample gradient in Nb-Ti and Nb_3Sn ironless superconducting quadrupoles based on sector coils (see Figure 110, left). These estimates can be applied to any coil, either cosθ or block, by replacing the coil width with an equivalent coil width, which is defined as the 30º sector coil having the same inner radius R_1 and cross-sectional area S than the generic coil considered (see Figure 110)

$$w_{eq} = \left(\sqrt{1+\frac{3S}{2\pi R_1^2}}-1\right)R_1. \tag{197}$$

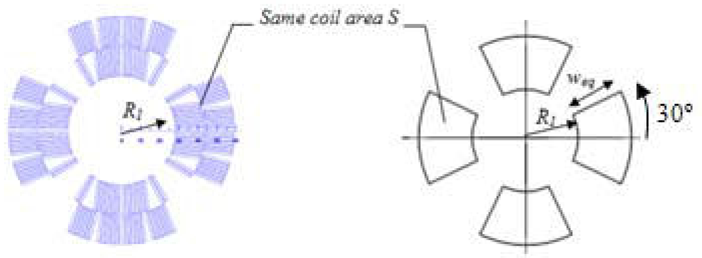

Figure 110 – Coil of the LHC MQ quadrupole (left), and equivalent quadrupole made of 30º sector coils of width w_{eq} (right).

Let us consider an ironless quadrupole coil of inner radius R_1 within which flows a uniform current density j [Am^{-2}]. Due to the linearity of the magnetic field in j, the field gradient G [Tm^{-1}] in the magnet aperture and the peak field modulus B_p [T] in the coil can be written as

$$G = j\gamma, \tag{198}$$

and

$$B_p = j\beta. \tag{199}$$

The parameter γ [TmA^{-1}] has been obtained analytically for a sector coil and is expressed as

$$\gamma = \gamma_0 log\left(1+\frac{w_{eq}}{R_1}\right), \tag{200}$$

with γ_0 = 6.93×10-7 [TmA^{-1}] for a [0-30°] sector coil, while β [Tm^2A^{-1}] has been obtained from an empirical fit

$$\beta = R_1\gamma_0\left(a_{-1}\frac{R_1}{w_{eq}}+1+a_1\frac{w_{eq}}{R_1}\right) \tag{201}$$

with $a_{-1} = 0.04$ and $a_1 = 0.11$ [71].

The engineering short sample current density j_{ss} [Am^{-2}] in the coil is reached when (j,B_p) are on the critical surface. In [71] is proposed a semi-analitycal scaling law for the j_{ss} in generic superconducting quadrupole. To this value corresponds a peak field $B_{p,ss}$ [T] and a short sample gradient G_{ss} [Tm]

The critical current density j_c of Nb-Ti material can be well fitted by a linear function of the magnetic field B for values of the magnetic field larger than 5 T at 1.9 K, and 2 T at 4.2 K:

$$j_c = c(B_{c2}^* - B), \tag{202}$$

where B_{c2}^* it the critical field. B_{c2}^* is of ~10 T at 4.2 K and ~13 T at 1.9 K, whereas the slope c ~ 6×10^8 [AT^{-1}m^{-2}] is independent of the temperature.

$$j_{ss} = \frac{kcB_{c2}^*}{1 + kcR_1\gamma_0\left(a_{-1}\frac{R_1}{w_{eq}} + 1 + a_1\frac{w_{eq}}{R_1}\right)}. \tag{203}$$

Still in [71], it has been proposed a new function to fit the critical current j_{ss} of Nb_3Sn superconductor as a function of the magnetic field B

$$j_c = c\left(\frac{b}{B} - 1\right), \tag{204}$$

where typical values for a cable having 3000 [Amm^{-2}] are $c = 4.0\times10^9$ and $b = 21$ T (at 4.2 K) or $b = 23$ T (at 1.9 K).

$$J_{ss} = \frac{kc}{2}\left(\sqrt{\frac{4b}{\beta kc} + 1} - 1\right). \tag{205}$$

The critical gradient reachable in a superconducting quadrupole is then estimated substituting Eq. (202) or Eq. (205) in Eq. (198).

Appendix B

Table 24 – Mean and standard deviation computed from measurements performed on 11 series of quadrupoles of the LHC and RHIC. Harmonic are given at a reference radius taken as 2/3 of the aperture radius.

	LHC Quadrupoles														RHIC quadrupoles							
	MQ Col		MQY Col		MQXB Col		MQXA Col		MQM		MQM C		MQML		Q1(26)	Q2 (27)	Q3 (13)	Q1	Q2	Q3	MQ	
	mean	Std. Dev.	mean	Std. Dev.	mean	Std. Dev.	mean	Std. Dev.	mean	Std. Dev.	mean	Std. Dev.	mean	Std. Dev.	mean			Std. Dev.			mean	Std. Dev.
a2	0	0	0	0	0	0	0	0	0	0	0	0	0	0	0	0	0	0	0	0	0	0
a3	0.41	2.03	0.08	0.91	0.22	0.78	0.18	0.54	0.26	1.88	-0.09	1.48	0.40	1.49	-0.25	-0.20	0.43	0.61	0.55	0.64	-1.95	1.79
a4	0.40	1.91	0.01	0.62	-0.12	0.68	-0.04	0.50	-0.27	1.02	-0.38	1.04	-0.16	0.91	-0.02	0.15	0.14	0.29	0.26	0.39	0.26	1.02
a5	0.05	0.69	0.04	0.40	0.06	0.26	-0.02	0.10	0.40	0.52	0.42	0.57	0.42	0.39	0.10	0.06	0.08	0.37	0.36	0.19	-0.32	1.70
a6	0.69	0.43	-0.35	0.16	-0.30	0.48	-0.09	0.08	-0.09	0.32	-0.14	0.36	0.01	0.26	1.02	0.12	0.37	0.17	0.37	0.10	-4.97	0.40
a7	0.04	0.26	0.06	0.15	0.01	0.13	0.00	0.04	0.08	0.22	0.02	0.19	0.04	0.20	0.30	0.19	0.13	0.43	0.33	0.28	0.08	0.19
a8	0.03	0.32	-0.06	0.15	-0.09	0.15	-0.01	0.09	-0.06	0.16	-0.08	0.21	-0.09	0.17	0.06	0.02	0.02	0.13	0.16	0.11	0.06	0.13
a9	0.02	0.08	-0.05	0.29	0.06	0.05	0.01	0.04	0.01	0.09	0.03	0.09	0.02	0.08	0.04	0.00	0.02	0.09	0.11	0.05	0.05	0.16
a10	0.14	0.08	0.19	0.64	0.21	0.04	-0.03	0.03	0.01	0.10	0.13	0.20	0.01	0.06	0.34	0.09	0.15	0.04	0.04	0.04	0.65	0.07
a11	0.00	0.04	0.31	1.18	-0.03	0.05	-0.02	0.06	0.00	0.00	0.00	0.00	0.00	0.00							0.00	0.04
a12	0.00	0.06	-0.44	1.37	-0.05	0.18	-0.01	0.09	0.00	0.00	0.00	0.00	0.00	0.00								
a13	0.01	0.04	-0.75	1.74	-0.01	0.15	0.01	0.11	0.00	0.00	0.00	0.00	0.00	0.00								
a14	0.00	0.02	-0.20	0.82	-0.17	0.08	0.02	0.12	0.00	0.00	0.00	0.00	0.00	0.00								
a15	0.00	0.01	-0.04	0.72	0.00	0.00	-0.13	0.33	0.00	0.00	0.00	0.00	0.00	0.00								
b3	-0.32	1.64	0.37	1.05	0.05	0.49	-0.01	0.42	-0.13	1.67	-0.21	1.27	-0.34	1.49	0.15	-0.09	0.01	0.48	0.47	0.79	-0.22	1.89
b4	-0.08	0.37	-0.13	0.35	0.21	0.20	2.45	0.20	0.06	0.88	0.22	0.53	-0.01	0.52	-0.16	1.46	0.40	0.52	0.22	0.60	-0.69	1.58
b5	0.12	0.58	0.01	0.30	0.22	0.31	-0.02	0.10	0.03	0.59	-0.04	0.58	0.12	0.58	0.03	0.10	0.29	0.32	0.28	0.29	0.69	1.91
b6	5.27	1.93	5.40	0.48	0.29	0.84	1.16	0.30	7.58	0.92	8.36	0.99	6.45	0.80	2.96	0.73	2.30	0.81	0.52	0.18	7.38	0.80
b7	-0.02	0.18	0.00	0.12	0.01	0.11	-0.02	0.04	-0.02	0.19	0.01	0.19	-0.02	0.18	0.04	0.03	0.10	0.33	0.28	0.25	0.07	0.18
b8	0.00	0.10	0.01	0.06	-0.03	0.04	0.15	0.02	0.00	0.09	-0.01	0.09	-0.01	0.10	0.23	0.23	0.00	0.29	0.15	0.21	-0.77	0.16
b9	0.00	0.08	0.05	0.32	-0.08	0.05	0.00	0.06	-0.02	0.09	0.00	0.07	-0.01	0.09	0.04	0.00	0.09	0.09	0.09	0.11	0.09	0.22
b10	-0.39	0.12	-4.23	0.93	0.24	0.16	-0.17	0.08	0.46	0.16	0.53	0.31	0.46	0.14	0.19	0.70	0.59	0.32	0.13	0.06	-2.41	0.13
b11	0.01	0.04	-0.22	0.90	0.10	0.11	-0.01	0.10	0.00	0.00	0.00	0.00	0.00	0.00							0.00	0.04
b12	-0.01	0.03	-0.73	1.76	-0.04	0.05	-0.05	0.09	0.00	0.00	0.00	0.00	0.00	0.00								
b13	0.00	0.04	0.32	1.75	0.18	0.20	0.02	0.12	0.00	0.00	0.00	0.00	0.00	0.00								
b14	-0.53	0.08	1.52	1.98	-0.42	0.15	0.14	0.16	0.00	0.00	0.00	0.00	0.00	0.00								
b15	0.00	0.01	-0.15	0.50	0.00	0.00	0.14	0.26	0.00	0.00	0.00	0.00	0.00	0.00								

Appendix C

Let us consider a quadrupole of coil inner and outer radius R_1 and R_2. The current density flowing within the coil is denoted by j and is assumed uniform. The variation of the normalized field harmonic Δb_ndue to a small variation of the block angular dimension of position can be well approximated by

$$\Delta b_n = 10^4 \frac{\Delta B_n}{B_2 + \Delta B_2} \sim \frac{1}{B_2} \Delta B_n, \tag{206}$$

where B_n is the field harmonic of rank n provided by the quadrupole at the reference radius R_{ref}, and B_2 is the main field.

$$\Delta B_n = \frac{\mu_0 j}{2} \frac{8}{n\pi} \frac{R_{ref}^{n-1}}{(n-2)} \left(\frac{1}{{R_2}^{n-2}} - \frac{1}{{R_1}^{n-2}} \right) [\sin[n(\theta_2 + \Delta\theta)] - \sin[n(\theta_1)]] \tag{207}$$

A the first order one has

$$\Delta B_n = -n\Delta\theta \frac{\mu_0 j}{2} \frac{8}{n\pi} \frac{R_{ref}^{n-1}}{(n-2)} \left(\frac{1}{{R_2}^{n-2}} - \frac{1}{{R_1}^{n-2}} \right) \cos(n\theta_2) \tag{208}$$

Assuming that the coil layout is such that the angle θ_2 maximize the variation

$$\Delta B_n = -n\Delta\theta \frac{\mu_0 j}{2} \frac{8}{n\pi} \frac{R_{ref}^{n-1}}{(n-2)} \left(\frac{1}{{R_2}^{n-2}} - \frac{1}{{R_1}^{n-2}} \right) \tag{209}$$

And therefore

$$\Delta b_n \sim 10^4 \frac{\Delta\theta \frac{2R_{ref}^{n-2}}{(n-2)} \left(\frac{1}{{R_2}^{n-2}} - \frac{1}{{R_1}^{n-2}} \right)}{ln\left(\frac{R_2}{R_1}\right) [\sin(2\theta_2) - \sin(2\theta_1)]} \tag{210}$$

The variation Δb_n is maximized when B_2 is at its smallest value: in our case when B_2 is provided by a quadrupole with coils made of a single [0-15°] sector. The variation Δb_n becomes

$$\Delta b_n \sim \Delta\theta \frac{\frac{2R_{ref}^{n-2}}{(n-2)}}{ln\left(\frac{R_2}{R_1}\right) \sin\left(\frac{\pi}{6}\right)} \left(\frac{1}{{R_2}^{n-2}} - \frac{1}{{R_1}^{n-2}} \right) 10^4 \tag{211}$$

Let us now assume that the coil is made of q layers of width w_L. The current density is assumed to be the same in each layer. Therefore, the multipole variation $\Delta b_n^{(k)}$ due to an angular variation in the layer number k (k = 1 for the inner layer and k = q for the outermost one) writes

$$\Delta b_n \sim \Delta\theta \frac{\frac{2R_{ref}^{n-2}}{(n-2)}}{ln\left(1+\frac{qw_L}{R_1}\right)\sin\left(\frac{\pi}{6}\right)}\left(\frac{1}{(R_1+kw_L)^{n-2}} - \frac{1}{(R_1+(k-1)w_L)^{n-2}}\right)10^4. \tag{212}$$

Finally, substituting R_{ref} by $2/3R_1$ gives

$$\Delta b_n \sim \Delta\theta \frac{\frac{2}{(n-2)}\left(\frac{2}{3}\right)^{n-2}}{ln\left(1+\frac{qw_L}{R_1}\right)\sin\left(\frac{\pi}{6}\right)}\left(\frac{1}{\left(1+k\frac{w_L}{R_1}\right)^{n-2}} - \frac{1}{\left(1+(k-1)\frac{w_L}{R_1}\right)^{n-2}}\right)10^4. \tag{213}$$

Appendix E

Let us consider a quadrupole coil made of one layer made of two blocks. This provides three angles for the parametric study (see Figure 111).

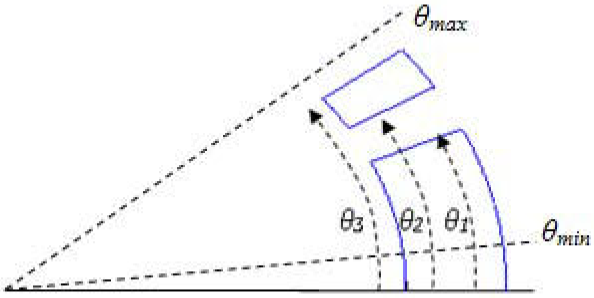

Figure 111 – Angles to play with when performing the parametric scan.

We assume that the angular step used for the parametric study provides *n* subdivisions between the angles θ_{min} and θ_{max}. Therefore there are n+1 angular positions to visit. Moreover, we assume that the angle θ_2 can never been equal to θ_3. All possible angular combinations are shown in the table below.

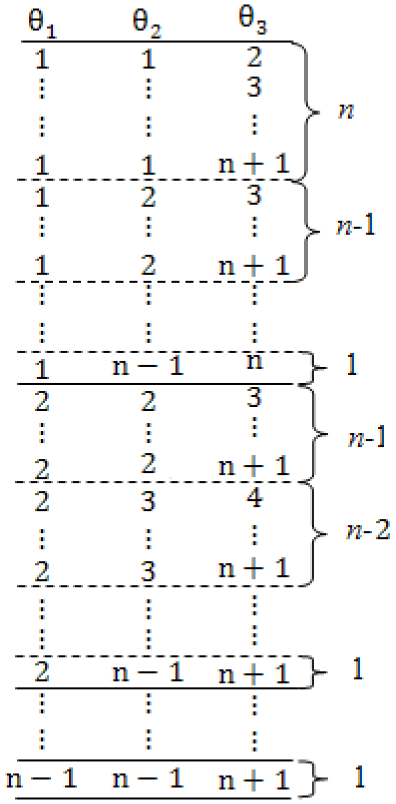

θ_1	θ_2	θ_3	
1	1	2	n
⋮	⋮	3	
⋮	⋮	⋮	
1	1	n + 1	
1	2	3	n-1
⋮	⋮	⋮	
1	2	n + 1	
⋮	⋮	⋮	
⋮	⋮	⋮	
1	n − 1	n	1
2	2	3	n-1
⋮	⋮	⋮	
2	2	n + 1	
2	3	4	n-2
⋮	⋮	⋮	
2	3	n + 1	
⋮	⋮	⋮	
⋮	⋮	⋮	
2	n − 1	n + 1	1
⋮	⋮	⋮	
⋮	⋮	⋮	
n − 1	n − 1	n + 1	1

From the above table one can derive the following formula allowing to calculated the number of possible angles combinations

$$N_b = \sum_{n=1}^{n} n + \sum_{n=1}^{n-1} n + \cdots + \cdots + \sum_{n=1}^{2} n + n. \tag{214}$$

Expression (214) can be re-written

$$N_b = \sum_{p=0}^{n-1} \frac{(n-p)(n-p+1)}{2}. \tag{215}$$

Developing expression (215) one has

$$N_b = \frac{n^3}{2} + \frac{n^2}{2} - n \sum_{p=0}^{n-1} p + \frac{1}{2} \sum_{p=0}^{n-1} (p^2 - p). \tag{216}$$

Simplifying and developing again Eq. (216) becomes

$$N_b = \frac{n^3}{6} + \frac{n^2}{2} + \frac{n}{3}. \tag{217}$$

Appendix F

- **Particularities of the field harmonic in a quadrupole**

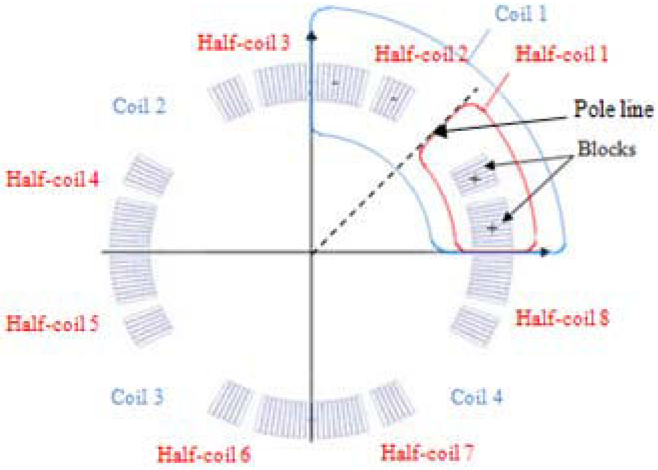

Figure 112 – definition of the quadrupole numbering considered in the section.

Let us consider a quadrupole magnets made up of eight half-coils (see for instance Figure 112). Half-coils can be made up of as many blocks as needed to cancel allowed harmonics. We call $\bar{C}_{m,n}$ the complex harmonic coefficient of order n, of real and imaginary part $B_{m,n}$ and $A_{m,n}$, and provided by half-coil number m alone and defined as

$$\bar{C}_{m,n} = B_{m,n} + iA_{m,n}, \tag{218}$$

It is well know that the complex multipole $C_{m,n}$ can be express in terms of the complex multipole generated by any other half-coil of the winding. In annex A we set up a formula allowing to express the $\bar{C}_{m,n}$coefficient in terms of $\bar{C}_{1,n} = B_{1,n} + iA_{1,n}$, the complex harmonic coefficient provided by coil number 1. The formula is similar, through slightly different, than the one given in [102]. For half-coil number m one has

$$\bar{C}_{m,n} = (i)^{m-1}\bar{C}_{1,n}e^{-i(m-1)n\frac{\pi}{4}} \qquad for\ m = 1,3,5,7, \tag{219}$$

and

$$\bar{C}_{m,n} = (i)^{m}\left(\bar{C}_{1,n}\right)^{*}e^{-imn\frac{\pi}{4}} \qquad for\ m = 2,4,6,8. \tag{220}$$

Note that half-coils number m = 1, 3, 5, 7 are obtained from a pure rotation of half-coil 1, while half-coils number m = 2, 4, 6, 8 are obtained from a symmetry plus a rotation of half-coil 1.

As an example of the use of formulae (219) and (220), we express the normal and skew multipoles $B_{2,n}$ and $A_{2,n}$ provided by half-coil 2, derived by a rotation of π/2 of the symmetric of half-coil 1 with respect to the x-axis, in terms of the multipoles $B_{1,n}$ and $A_{1,n}$

$$B_{2,n} + iA_{2,n} = -\left(B_{1,n} - iA_{1,n}\right)e^{-in\frac{\pi}{2}} \tag{221}$$

One can distinguish four sets of harmonic order where $A_{2,n}$ and $B_{2,n}$ assume different values:

- For n = 1, 5, 9, … one has $A_{2,n} = B_{1,n}$ and $B_{2,n} = A_{1,n}$
- For n = 2, 6, 10, … one has $A_{2,n} = -A_{1,n}$ and $B_{2,n} = B_{1,n}$
- For n = 3, 7, 11, … one has $A_{2,n} = -B_{1,n}$ and $B_{2,n} = -A_{1,n}$
- For n = 4, 8, 12, … one has $A_{2,n} = A_{1,n}$ and $B_{2,n} = -B_{1,n}$

The same method has been applied to half-coils 3, 4, 5, 6, 7 and 8 to build up Table 25. Note that this table is not new but has been worked out in [102]. Rows correspond to the harmonic coefficients provided by each of the eight half-coils forming the quadrupole. Columns are divided into four set of harmonic orders. Each set is divided into two columns corresponding to the real and imaginary parts of $\bar{C}_{m,n}$, *i.e.*, $B_{m,n}$ and $A_{m,n}$. For instance, the normal and skew harmonics of order n = 3, 7, 11,… generated by the coil number 3 (m = 3) are $B_{3,n} = A_{1,n}$ and $A_{3,n}$ = - $B_{1,n}$.

Table 25 – Real and imaginary parts of the harmonic coefficient $\bar{C}_{m,n}$ provided by the half-coil m and express in terms of the nomal and skew harmonic coefficients provided by the half-coil number 1. For four sets of multipole order values are considered.

	n = 1, 5, 9, …		n = 2, 6, 10, …		n = 3, 7, 11, …		n = 4, 8, 12, …	
m	$B_{m,n}$	$A_{m,n}$	$B_{m,n}$	$A_{m,n}$	$B_{m,n}$	$A_{m,n}$	$B_{m,n}$	$A_{m,n}$
1	$B_{1,n}$	$A_{1,n}$	$B_{1,n}$	$A_{1,n}$	$B_{1,n}$	$A_{1,n}$	$B_{1,n}$	$A_{1,n}$
2	$A_{1,n}$	$B_{1,n}$	$B_{1,n}$	-$A_{1,n}$	-$A_{1,n}$	-$B_{1,n}$	-$B_{1,n}$	$A_{1,n}$
3	-$A_{1,n}$	$B_{1,n}$	$B_{1,n}$	$A_{1,n}$	$A_{1,n}$	-$B_{1,n}$	-$B_{1,n}$	-$A_{1,n}$
4	-$B_{1,n}$	$A_{1,n}$	$B_{1,n}$	-$A_{1,n}$	-$B_{1,n}$	$A_{1,n}$	$B_{1,n}$	-$A_{1,n}$
5	-$B_{1,n}$	-$A_{1,n}$	$B_{1,n}$	$A_{1,n}$	-$B_{1,n}$	-$A_{1,n}$	$B_{1,n}$	$A_{1,n}$
6	-$A_{1,n}$	-$B_{1,n}$	$B_{1,n}$	-$A_{1,n}$	$A_{1,n}$	$B_{1,n}$	-$B_{1,n}$	$A_{1,n}$
7	$A_{1,n}$	-$B_{1,n}$	$B_{1,n}$	$A_{1,n}$	-$A_{1,n}$	$B_{1,n}$	-$B_{1,n}$	-$A_{1,n}$
8	$B_{1,n}$	-$A_{1,n}$	$B_{1,n}$	-$A_{1,n}$	$B_{1,n}$	-$A_{1,n}$	$B_{1,n}$	-$A_{1,n}$

- **Coil displacement**

Let us consider now that half-coil number m is slightly displaced by the quantity δ in a given direction q. Let us call $\bar{C}_{m,n}(0)$ and $\bar{C}_{m,n}(\delta)$ the complex field coefficients provided by the coil m in its initial and displaced position, respectively. The multipole variation associated to the half-coil displacement can be written

$$\Delta\bar{C}_{m,n}(\delta) = \bar{C}_{m,n}(\delta) - \bar{C}_{m,n}(0). \tag{222}$$

In first approximation, $\Delta\bar{C}_{m,n}$ is given by

$$\Delta\bar{C}_{m,n}(\delta) = \delta \left. \frac{\partial \bar{C}_{m,n}}{\partial q} \right|_0 . \tag{223}$$

Similarly to the formulae enabling the expression of the complex multipole of any half-coils constituting the quadrupole winding in terms of the complex multipoles of half-coil number one, one can expressed $\Delta\bar{C}_{m,n}$ as a function of $\Delta\bar{C}_{1,n}$, the multipole variation generated by a displacement of coil number 1 of the same amplitude and direction than coil number m

$$\Delta\bar{C}_{m,n}(\delta) = k(i)^{m-1}\Delta\bar{C}_{1,n}(\delta)e^{-i(m-1)n\frac{\pi}{4}} \qquad for\ m = 1,3,5,7, \tag{224}$$

and

$$\Delta\bar{C}_{m,n}(\delta) = k(i)^{m}\left(\Delta\bar{C}_{1,n}(\delta)\right)^{*} e^{-imn\frac{\pi}{4}} \qquad for\ m = 2,4,6,8, \tag{225}$$

where k = 1 if, after being displaced, the position of half-coils 1 and m are still consistent with the quadrupolar symmetry (see for instance Figure 113, left). Conversly, k = -1 if the final position of half-coils 1 and m breaks the fourfold symmetry. In terms of normal and skew coefficient $\Delta\bar{C}_{m,n}(\delta)$ wrtites

$$\Delta\bar{C}_{m,n}(\delta) = \Delta B_{m,n}(\delta) + i\Delta A_{m,n}(\delta) \tag{226}$$

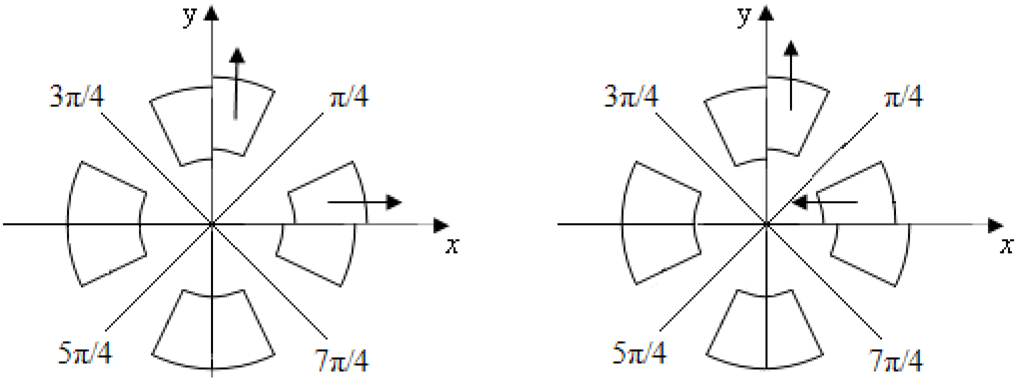

Figure 113 – Example of radial and azimuthal displacements with k = 1 (left) and with k = -1 (right).

In

Table 26, are expressed the multipoles variation $\Delta A_{m,n}(\delta)$ and $\Delta B_{m,n}(\delta)$ in terms of the multipoles variation $\Delta A_{1,n}(\delta)$ and $\Delta B_{1,n}(\delta)$ in the particular case where k = 1. For k = -1, one has to add a sign minus for normal and skew multipoles variations provided by the half-coils 2 to 8. In order to make equations more readable we use the notation $\Delta A_{m,n}$ instead of $\Delta A_{m,n}(\delta)$.

Table 26 – Variation of the multipoles $A_{m,n}$ and $A_{m,n}$ of the coil number *m* expressed in terms of the variation of the multipoles $A_{1,n}$ and $B_{1,n}$ provided by the coil 1 when slightly displaced. Coils are displaced such that the quadrupole symmetry stands (*k*=1).

	n = 1, 5, 9, …		*n* = 2, 6, 10, …		*n* = 3, 7, 11, …		*n* = 4, 8, 12, …	
m	$\Delta B_{m,n}$	$\Delta A_{m,n}$	$\Delta B_{m,n}$	$\Delta A_{m,n}$	$\Delta B_{m,n}$	$\Delta A_{m,n}$	$\Delta B_{m,n}$	$\Delta A_{m,n}$
1	$\Delta B_{1,n}$	$\Delta A_{1,n}$	$\Delta B_{1,n}$	$\Delta A_{1,n}$	$\Delta B_{1,n}$	$\Delta A_{1,n}$	$\Delta B_{1,n}$	$\Delta A_{1,n}$
2	$\Delta A_{1,n}$	$\Delta B_{1,n}$	$\Delta B_{1,n}$	$-\Delta A_{1,n}$	$-\Delta A_{1,n}$	$-\Delta B_{1,n}$	$-\Delta B_{1,n}$	$\Delta A_{1,n}$
3	$-\Delta A_{1,n}$	$\Delta B_{1,n}$	$\Delta B_{1,n}$	$\Delta A_{1,n}$	$\Delta A_{1,n}$	$-\Delta B_{1,n}$	$-\Delta B_{1,n}$	$-\Delta A_{1,n}$
4	$-\Delta B_{1,n}$	$\Delta A_{1,n}$	$\Delta B_{1,n}$	$-\Delta A_{1,n}$	$-\Delta B_{1,n}$	$\Delta A_{1,n}$	$\Delta B_{1,n}$	$-\Delta A_{1,n}$
5	$-\Delta B_{1,n}$	$-\Delta A_{1,n}$	$\Delta B_{1,n}$	$\Delta A_{1,n}$	$-\Delta B_{1,n}$	$-\Delta A_{1,n}$	$\Delta B_{1,n}$	$\Delta A_{1,n}$
6	$-\Delta A_{1,n}$	$-\Delta B_{1,n}$	$\Delta B_{1,n}$	$-\Delta A_{1,n}$	$\Delta A_{1,n}$	$\Delta B_{1,n}$	$-\Delta B_{1,n}$	$\Delta A_{1,n}$
7	$\Delta A_{1,n}$	$-\Delta B_{1,n}$	$\Delta B_{1,n}$	$\Delta A_{1,n}$	$-\Delta A_{1,n}$	$\Delta B_{1,n}$	$-\Delta B_{1,n}$	$-\Delta A_{1,n}$
8	$\Delta B_{1,n}$	$-\Delta A_{1,n}$	$\Delta B_{1,n}$	$-\Delta A_{1,n}$	$\Delta B_{1,n}$	$-\Delta A_{1,n}$	$\Delta B_{1,n}$	$-\Delta A_{1,n}$

Let us now assume that δ is a random variable taking on values in the set $\{\delta_1,\ldots.,\delta_p\}$. The standard deviation (or sigma) of the skew field harmonic error caused by random displacements of the half-coil *m* is obtained from

$$\sigma_{A_{m,n}} = \sqrt{\frac{1}{P}\sum_{x=1}^{P}\left[\Delta A_{m,n}(\delta_x)\right]^2 - \left[\frac{1}{P}\sum_{x=1}^{P}\Delta A_{m,n}(\delta_x)\right]^2} \tag{227}$$

One has a similar expression for the sigma of the normal field error $\sigma_{B_{1,n}}$

$$\sigma_{B_{m,n}} = \sqrt{\frac{1}{P}\sum_{x=1}^{P}\left[\Delta B_{m,n}(\delta_x)\right]^2 - \left[\frac{1}{P}\sum_{x=1}^{P}\Delta B_{m,n}(\delta_x)\right]^2} \tag{228}$$

- **Random displacements of half-coils**

Let us consider a series of identical quadrupoles which differ only by the precision in the positioning of the 8 half-coils constituting the winding. We assume that the precision in the half-coil positioning in a magnet and from magnet to magnet are uncorrelated. Therefore, the sigma of the field harmonic errors of the series is obtained from the quadratic sum of the sigma of the field error provided by half-coils alone

$$\sigma A_n = \sqrt{\sum_{m=1}^{8}\left(\sigma A_{m,n}\right)^2} \quad \text{and} \quad \sigma B_n = \sqrt{\sum_{m=1}^{8}\left(\sigma B_{m,n}\right)^2} \tag{229}$$

According to

Table 26 and to Eqs. (227) and (228) one can expressed $\sigma A_{m,n}$ and $\sigma B_{m,n}$ in terms of $\sigma A_{1,n}$ and $\sigma B_{1,n}$. For instance for the harmonics of order n=1,5,9,.. one has

$$\begin{aligned}\Delta B_{1,n} &= \Delta B_{1,n}\\ \Delta B_{2,n} &= \Delta A_{1,n}\\ \Delta B_{3,n} &= -\Delta A_{1,n}\\ \Delta B_{4,n} &= -\Delta B_{1,n}\\ \Delta B_{5,n} &= -\Delta B_{1,n}\\ \Delta B_{6,n} &= -\Delta A_{1,n}\\ \Delta B_{7,n} &= \Delta A_{1,n}\\ \Delta B_{8,n} &= \Delta B_{1,n}\end{aligned} \tag{230}$$

Substituting expressions of Eq. (230) in Eq. (227) allows writing

$$\begin{aligned}\sigma B_{1,n} &= \sigma B_{1,n}\\ \sigma B_{2,n} &= \sigma A_{1,n}\\ \sigma B_{3,n} &= \sigma A_{1,n}\\ \sigma B_{4,n} &= \sigma B_{1,n}\\ \sigma B_{5,n} &= \sigma B_{1,n}\\ \sigma B_{6,n} &= \sigma A_{1,n}\\ \sigma B_{7,n} &= \sigma A_{1,n}\\ \sigma B_{8,n} &= \sigma B_{1,n}\end{aligned} \tag{231}$$

The sigma of the field error in the magnet series can be calculated substituting expression of Eq. (231) in Eq. (229)

$$\sigma B_n = \sqrt{4\left(\sigma A_{1,n}\right)^2 + 4\left(\sigma B_{1,n}\right)^2} \tag{232}$$

The same method has been applied to skew and normal harmonics of the four families of harmonic orders to work out the.Table 27

Table 27 – Standard deviation of the normal and skew multipoles due to random displacements of the 8 half-coil forming a quadrupole expressed in terms of the sigma of the field error due to the coil number 1 alone.

Harmonic order	σA_n	σB_n
n = 1, 5, 9, …	$2\sqrt{\left(\sigma A_{1,n}\right)^2 + \left(\sigma B_{1,n}\right)^2}$	
n = 2, 6, 10, …	$2\sqrt{2}\left(\sigma A_{1,n}\right)$	$2\sqrt{2}\left(\sigma B_{1,n}\right)$
n = 3, 7, 11, …	$2\sqrt{\left(\sigma A_{1,n}\right)^2 + \left(\sigma B_{1,n}\right)^2}$	
n = 4, 8, 12, …	$2\sqrt{2}\left(\sigma A_{1,n}\right)$	$2\sqrt{2}\left(\sigma B_{1,n}\right)$

- **Coupled displacements within coils**

Practically, a magnet is made-up of 4 coils wounded separately and then assembled together to form the final winding. Here we assume that the two half-coils forming a coil can randomly moved but only in coupled mode. The coupling is such that the coil symmetry with respect to the pole line is always respected (see Figure 114). Here we derived expressions of the sigma of the field harmonic errors generated by such coil displacements in a series of nearly identical quadrupole magnets. Details of the calculations are given for skew multipoles and then are derived straightforwardly for normal multipoles.

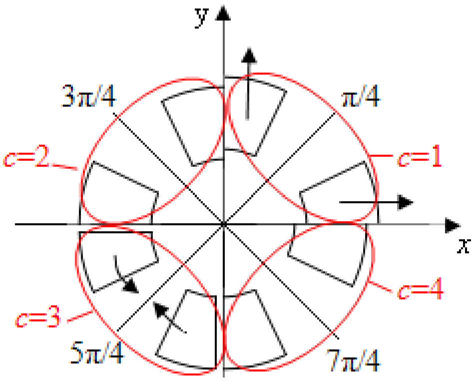

Figure 114 – Example of half-coil displacement respecting the proposed symmetry (coils are symmetric with respect to their pole line)

Let us call $A_n^{(c)}$ and $B_n^{(c)}$ the skew and normal multipoles generated by the coil *c* alone. The field errors $\Delta A_n^{(c)}(\delta)$ and $\Delta B_n^{(c)}(\delta)$ generated by correlated displacements of the two half-coils (number 2*c*-1 and 2*c*) forming the coil *c* writes

$$\Delta A_n^{(c)}(\delta) = \Delta A_{2c-1,n}(\delta) + \Delta A_{2c,n}(\delta) \tag{233}$$

and

$$\Delta B_n^{(c)}(\delta) = \Delta B_{2c-1,n}(\delta) + \Delta B_{2c,n}(\delta) \tag{234}$$

with *c* = 1,2,3 or 4. Therefore, the sigma of the field error generated by the coil *c* alone is obtained from

$$\sigma A_n^{(c)} = \sqrt{\left(\sigma A_{2c-1,n}\right)^2 + \left(\sigma A_{2c,n}\right)^2 + 2\rho\sigma A_{2c-1,n}\sigma A_{2c,n}} \tag{235}$$

and

$$\sigma B_n^{(c)} = \sqrt{\left(\sigma B_{2c-1,n}\right)^2 + \left(\sigma B_{2c,n}\right)^2 + 2\rho\sigma B_{2c-1,n}\sigma B_{2c,n}} \tag{236}$$

The perfect coupling (correlation coefficient equal to -1 or 1) of half-coils number 2*c*-1 and 2*c* within coil number *c* leads to a correlation coefficient ρ [in Eq. (235)] either equals to 1 or -1. Let us now, with the help of

Table 26, express $\sigma A_n^{(c)}$ and $\sigma B_n^{(c)}$ in terms of only $\sigma A_{1,n}$ and $\sigma B_{1,n}$.

- For n = 1, 5, 9, …

From

Table 26, one notice that

$$\Delta A_n^{(c)}(\delta) = \left(\Delta A_{1,n}(\delta) + \Delta B_{1,n}(\delta)\right) \text{ for } c = 1 \text{ and } 2 \tag{237}$$

and

$$\Delta A_n^{(c)}(\delta) = -\left(\Delta A_{1,n}(\delta) + \Delta B_{1,n}(\delta)\right) \text{ for } c = 3 \text{ and } 4 \tag{238}$$

From Eqs. (237) and (238) and from Eqs. (235) and (236)

One has for c=1,2,3,4

$$\sigma A_n^{(c)} = \sqrt{\left(\sigma A_{1,n}\right)^2 + \left(\sigma B_{1,n}\right)^2 \pm 2\left(\sigma A_{1,n}\right)\left(\sigma B_{1,n}\right)} \tag{239}$$

Similar calculations on normal multipoles lead to

$$\sigma A_n^{(c)} = \sigma B_n^{(c)} \text{ for c} = 1,2,3,4 \tag{240}$$

- For n = 2, 4, 6, …

The sigma of the harmonic generated by the coil number c is

$$\sigma A_n^{(c)} = \sigma A_{1,n}\sqrt{2 + 2\rho} \tag{241}$$

$$\sigma B_n^{(c)} = \sigma B_{1,n}\sqrt{2 + 2\rho} \tag{242}$$

Where according to

Table 26

$$\frac{\Delta A_{2c-1,n}(\delta)}{\Delta A_{2c,n}(\delta)} = -1 \quad \text{and} \quad \frac{\Delta B_{2c-1,n}(\delta)}{\Delta B_{2c,n}(\delta)} = 1 \tag{243}$$

for c = 1,2,3 or 4. This means that ρ=-1 in Eq.(241) and ρ=1 in Eq. (242). Therefore, Eqs. (241) and (242) becomes

$$\sigma A_n^{(c)} = 0 \tag{244}$$

$$\sigma B_n^{(c)} = 2\sigma B_{1,n} \tag{245}$$

- For n = 3, 7, 11, …

One has for c

$$\sigma A_n^{(c)} = \sigma B_n^{(c)} = \sqrt{\left(\sigma A_{1,n}\right)^2 + \left(\sigma B_{1,n}\right)^2 + \rho\left(\sigma A_{1,n}\right)\left(\sigma B_{1,n}\right)} \qquad (246)$$

- For $n = 4, 8, 12, \ldots$

According to Eqs. (225) and (226) and to Table 25, the sigma of the harmonic generated by the coil number *c* is

$$\sigma A_n^{(c)} = \sigma A_{1,n}\sqrt{2+2\rho} \qquad (247)$$

$$\sigma B_n^{(c)} = \sigma B_{1,n}\sqrt{2+2\rho} \qquad (248)$$

From the

Table 26, one shows

$$\frac{\Delta A_{2c-1,n}(\delta)}{\Delta A_{2c,n}(\delta)} = 1 \quad \text{and} \quad \frac{\Delta B_{2c-1,n}(\delta)}{\Delta B_{2c,n}(\delta)} = -1 \qquad (249)$$

Therefore, the coefficient of correlation ρ = 1for Eq. (247) and ρ = -1 in Eq, (248). This allows re-writing Eqs. (247) and (248)

$$\sigma A_n^{(c)} = 2\sigma A_{1,n} \qquad (250)$$

$$\sigma B_n^{(c)} = 0 \qquad (251)$$

Since the four coils constituting the quadrupoles can all move independently from one another the sigma of the field error in the quadrupole is obtained from the quadratic sum of the contribution of the four coils

$$\sigma A_n = \sqrt{\sum_{c=1}^{4}\left(\sigma A_n^{(c)}\right)} \quad and \quad \sigma B_n = \sqrt{\sum_{c=1}^{4}\left(\sigma B_n^{(c)}\right)} \qquad (252)$$

- For $n = 1, 5, 9, \ldots$

Substituting Eq. (239) in Eqs. (252) allows expressing the sigma of the field error in the quadrupole in terms of the sigma of the field error provided by the coil 1 alone

$$\sigma A_n = \sigma B_n = 2\sqrt{\left(\sigma A_{1,n}\right)^2 + \left(\sigma B_{1,n}\right)^2 \pm 2\left(\sigma A_{1,n}\right)\left(\sigma B_{1,n}\right)} \qquad (253)$$

- For $n = 2, 4, 6, \ldots$

Substituting Eqs. (244) and (245) in Eqs. (252) and allow expressing the sigma of the field error in the quadrupole

$$\sigma A_n = 0 \tag{254}$$

$$\sigma B_n = 4\sigma B_{1,n} \tag{255}$$

- <u>For $n = 3, 7, 11, \ldots$</u>

Substituting Eq. (246) in Eq. (252) allows writing

$$\sigma A_n = \sigma B_n = 2\sqrt{(\sigma A_{1,n})^2 + (\sigma B_{1,n})^2 + \rho(\sigma A_{1,n})(\sigma B_{1,n})} \tag{256}$$

- <u>For $n = 4, 8, 12, \ldots$</u>

Substituting Eqs. (250) and (251) in Eq. (252) allows writing

$$\sigma A_n = 4\sigma A_{1,n} \tag{257}$$

$$\sigma B_n = 0 \tag{258}$$

Table 28 - Standard deviation of the normal and skew multipoles due to random displacements of the 4 coils forming a quadrupole expressed in terms of the sigma of the field error due to the coil number 1 i.e. $\sigma A_{1,n}$ and $\sigma B_{1,n}$. Displacements are such that the coils are always symmetric with respect to their pole line.

Harmonic order	σA_n	σB_n
$n = 1, 5, 9, \ldots$	$2\sqrt{(\sigma A_{1,n})^2 + (\sigma B_{1,n})^2 \pm 2(\sigma A_{1,n})(\sigma B_{1,n})}$	
$n = 2, 6, 10, \ldots$	0	$4\sigma B_{1,n}$
$n = 3, 7, 11, \ldots$	$2\sqrt{(\sigma A_{1,n})^2 + (\sigma B_{1,n})^2 \pm 2(\sigma A_{1,n})(\sigma B_{1,n})}$	
$n = 4, 8, 12, \ldots$	$4\sigma A_{1,n}$	0

- **<u>Error on the position of the mid-plane</u>**

Let us call $A_n^{(d)}$ and $B_n^{(d)}$ the skew and normal multipoles generated by the set number *d* of two adjacent half-coils.

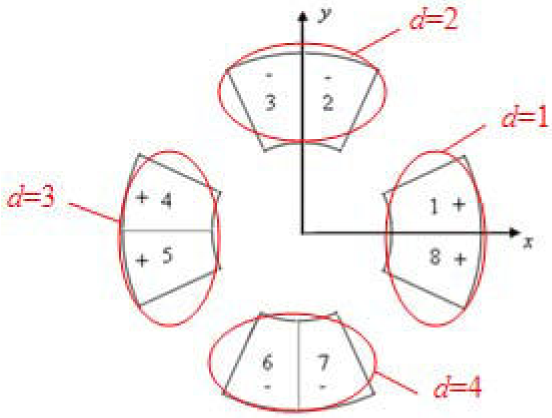

Figure 115 – Group of half-coils considered for the study of the effect of displacements of the mid-planes on the field error.

The field errors $\Delta A_n^{(d)}(\delta)$ and $\Delta B_n^{(d)}(\delta)$ generated by correlated displacements of the set number *d* of two half-coils (number 2*d*-1 and 2*d*) forming the coil *c* writes

$$\Delta A_n^{(d)}(\delta) = \Delta A_{2d-1,n}(\delta) + \Delta A_{2d-2,n}(\delta) \tag{259}$$

and

$$\Delta B_n^{(d)}(\delta) = \Delta B_{2d-1,n}(\delta) + \Delta B_{2d-2,n}(\delta) \tag{260}$$

with *d* = 1,2,3 or 4 (note that *d*=0 correspond in fact to the coil number 8). The sigma of the field error of the two adjacent half-coils *d* is

$$\sigma A_n^{(d)} = \sqrt{\left(\sigma A_{2d-1,n}\right)^2 + \left(\sigma A_{2d-2,n}\right)^2 + 2\rho\sigma A_{2d-1,n}\sigma A_{2d-2,n}} \tag{261}$$

According to

Table 26 one can write

- <u>For *n* = 1, 5, 9, …</u>

The sigma of the harmonic generated by the coil number *d* is

$$\sigma A_n^{(d)} = \sigma A_{1,n}\sqrt{2+2\rho} \tag{262}$$

$$\sigma B_n^{(d)} = \sigma B_{1,n}\sqrt{2+2\rho} \tag{263}$$

Where according to

Table 26 and for *d*= 1 and 3

$$\frac{\Delta A_{2d-1,n}(\delta)}{\Delta A_{2d-2,n}(\delta)} = 1 \quad \text{and} \quad \frac{\Delta B_{2d-1,n}(\delta)}{\Delta B_{2d-2,n}(\delta)} = -1 \tag{264}$$

And for *d*= 2 and 4

$$\frac{\Delta A_{2d-1,n}(\delta)}{\Delta A_{2d-2,n}(\delta)} = -1 \quad \text{and} \quad \frac{\Delta B_{2d-1,n}(\delta)}{\Delta B_{2d-2,n}(\delta)} = -1 \tag{265}$$

Therefore, for *d*= 1 and 4 one has

$$\sigma A_n^{(d)} = \sigma\Delta B_n^{(d)} = 0 \tag{266}$$

and for *d*= 2 and 3

$$\sigma A_n^{(d)} = \sigma\Delta B_n^{(d)} = 2\ \sigma A_{1,n} \tag{267}$$

- For *n* = 2, 4, 6, …

  One has whatever *d* =1 ,2, 3, 4

$$\sigma A_n^{(d)} = 2\ \sigma A_{1,n} \tag{268}$$

$$\sigma\Delta B_n^{(d)} = 0 \tag{269}$$

- For *n* = 3, 7, 11, …

  Similar calculations that for *n* = 1, 5, 9,… lead to

$$\sigma A_n^{(d)} = \sigma\Delta B_n^{(d)} = 2\ \sigma A_{1,n} \tag{270}$$

- For *n* = 4, 8, 12, …

$$\sigma A_n^{(d)} = 2\ \sigma A_{1,n} \tag{271}$$

$$\sigma\Delta B_n^{(d)} = 0 \tag{272}$$

Since coils are independent all from one another the sigma of the field error in the quadrupole is

$$\sigma A_n = \sqrt{\sum_{d=1}^{4}\left(\sigma A_n^{(d)}\right)^2} \tag{273}$$

And for normal multipoles

$$\sigma B_n = \sqrt{\sum_{d=1}^{4}\left(\sigma B_n^{(d)}\right)^2} \tag{274}$$

Therefore, when performing the sum given in Eqs. (273) and (274)

- For n = 1, 5, 9, …

$$\sigma A_n = \sigma B_n = 2\sqrt{2}\sigma A_{1,n} \tag{275}$$

- For n = 2, 4, 6, …

$$\sigma A_n = 4\,\sigma A_{1,n} \tag{276}$$

$$\sigma B_n = 0 \tag{277}$$

- For n = 3, 7, 11, …

$$\sigma A_n = \sigma B_n = 2\sqrt{2}\,\sigma A_{1,n} \tag{278}$$

- For n = 4, 8, 12, …

$$\sigma A_n = 4\,\sigma A_{1,n} \tag{279}$$

$$\sigma B_n = 0 \tag{280}$$

Table 29 – Effect of random displacement of mid-planes on the field quality

Harmonic order	σA_n	σB_n
n = 1, 5, 9, …	$2\sqrt{2}\sigma A_{1,n}$	
n = 2, 6, 10, …	$4\,\sigma A_{1,n}$	0
n = 3, 7, 11, …	$2\sqrt{2}\sigma A_{1,n}$	
n = 4, 8, 12, …	$4\,\sigma A_{1,n}$	0

- **Symmetric coil displacement**

Let us now consider that all half-coils constituting the quadrupole winding are displaced by the same quantity δ and in chosen directions such that the quadrupolar symmetry is always respected. See for instance the Figure 116 where half-coils are azimuthally and radially displaced such that the fourfold symmetry is always verified.

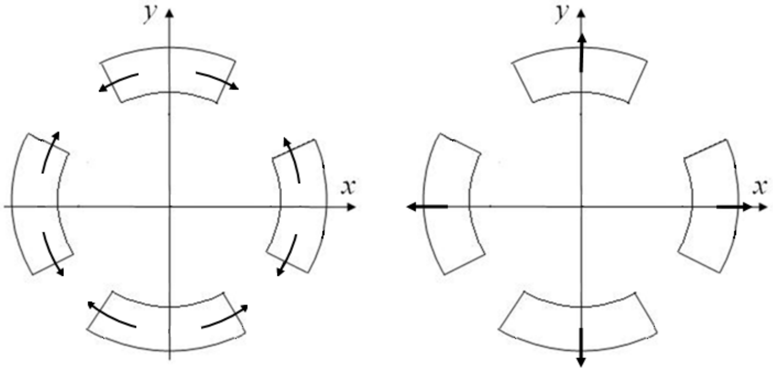

Figure 116 – Example of displacements, azimuthal (left) and radial (right), of all the half-coils constituting the winding such that the quadrupolar symmetry of the magnet is always respected.

Because of the four-fold symmetry, non-allowed multipoles are zero. Therefore

$$\sigma A_n = 0 \text{ whatever the harmonic order} \tag{281}$$

and

$$\sigma B_n = 0 \text{ for n} \neq 2, 6, 10, \dots. \tag{282}$$

According to

Table 26 one has for allowed harmonics

$$\sigma \Delta B_n = 8 \Delta B_{1,n}. \tag{283}$$

Nomenclature

ROMAN LETTERS

$\vec{A}$	Magnetic vector potential
A_n	Skew harmonic coefficient of order n
A_n^L	Integrated skew harmonic coefficient
A_n^{coil}	Skew harmonic generated by a coil
A_n^{iron}	Skew harmonic generated by an iron yoke
a_n	Normalized value of A_n
a_n^L	Integrated value of A_n^L
a_x	Constant
A_z	z-component of $\vec{A}$
$A_{z,n}$	Harmonic of order n of A_z
a	Constant, fitting parameter in the energy formula
a_{-1}	Constant
a_1	Constant
A_c	Vector potential due to a coil alone
A_i	Supplementary vector potential due the iron yoke
$A_{i,n}$	A_i of rank n
$<a_n>$	Mean of $\mathrm{a_n}$
$a_{i,n}$	Skew harmonic of order n provided by the magnet i
a_n^e	Expected field harmonic error of order n
$A_{m,n}$	Skew harmonic of rank n provided by the coil/half-coil number m
$A_{n,p}$	Harmonic of rank n due to the sub-quadrupole number p
$A_n^{(c)}$	Skew multipole generated by the group of coils number c alone
$A_n^{(d)}$	Skew multipole generated by the group of coils number d alone
$\vec{B}$	Magnetic induction vector
B	Modulus of $\vec{B}$
B_x	x-component of $\vec{B}$
B_y	y-component of $\vec{B}$
B_z	z-component of $\vec{B}$
$\bar{B}^L$	Integrated magnetic induction
$\bar{B}_x^L$	x-component of $\bar{B}^L$
$\bar{B}_y^L$	y-component of $\bar{B}^L$
B_n	Normal harmonic coefficient of order n
B_n^L	Integrated value of B_n
B_n^{coil}	Normal harmonic generated by a coil
B_n^{iron}	Normal harmonic generated by an iron yoke
b_n	Normalized value of B_n
b_n^L	Integrated value of B_n^L
B_N	Normal harmonic coefficient of a $2N$-poles magnet
b	Constant, fitting parameter in the Nb_3Sn critical surface
b	Fitting parameter for the energy
$B_{n,r}$	Radial component of order n of the magnetic field
$B_{n,\theta}$	Azimuthal component of order n of the magnetic field

B_s	Field saturation of the iron
B_c	Upper critical field
B_{c2}	Critical magnetic field
B_{c20}	Critical magnetic field at zero temperature
B_{c2m}	Critical magnetic field at zero temperature and zero strain
B_{c2}^{*}	Critical magnetic field at zero temperature and zero current
B_{ss}	Short sample magnetic field
B_{op}	Operational magnetic field
b_n^e	Expected field harmonic error of order n
$B_{m,n}$	Normal harmonic of rank n provided by the coil/half-coil number m
$B_{\theta,p}$	Azimuthal magnetic field due to the sub-quadrupole number p
$B_{n,p}$	Harmonic of rank n due to the sub-quadrupole number p
B_p	Peak field in the coil
$B_n^{(c)}$	Normal multipole generated by the group of coils number c alone
$B_n^{(d)}$	Normal multipole generated by the group of coils number d alone
$\bar{C}_n$	Complex harmonic
$\bar{C}_n^{EU}$	European notation of $\bar{C}_n$
$\bar{C}_{n-1}^{US}$	American notation of $\bar{C}_n$
$\bar{C}_n^{l}$	Complex harmonic coefficient
$\bar{c}_n$	Normalized value of $\bar{C}_n$
c	Constant, slope of the critical surface in the (j_c, B_c) plane
c	Fitting parameter for the energy formula
c	Coil numbering
$\bar{C}_{m,n}$	Complex harmonic of order n provided by the coil/half-coil m
$D_n(r)$	Function of order n depending only on r
$D_{Nb\text{-}Ti}$	Constant used in the critical surface equation of Nb-Ti
d_x	Elementary displacement in x
d_y	Elementary displacement in y
d	Fitting parameter, *rms* value of a coil block displacement
d	Numbering for groups of two adjacent coils
dS	Elementary surface element
dS_k	Elementary surface element number k
dFx	x-component of the magnetic force applied on a subsector
dFy	y-component of the magnetic force applied on a subsector
$d\Omega$	Elementary volume element
E	Beam energy
e	Exponential function
e	Thickness of the iron yoke
$\vec{f}$	Lorentz force applied on a particle
f_x	x-component of $\vec{f}$
f_y	y-component of $\vec{f}$
f_z	z-component of $\vec{f}$
F_m	Real part of $\overline{W}^{L}$
$F_m{}^{L}$	Integral of F_m
f_{rev}	Beam revolution frequency
F	Geometric luminosity reduction factor
f_n	Function associated to the harmonic n
f_2	Function associated to the harmonic n

F_z	Net magnetic force applied on a coil end
$\vec{F}_m$	Net magnetic force applied on a conductor
$\vec{F}_k$	Net magnetic force applied on a conductor
$F_{z,k}$	z-component of $\vec{F}_k$ applied on the surface S_k
$\vec{F}_z^{(1)}$	F_z in the presence of an infinitely long iron yoke
$\vec{F}_z^{(2)}$	F_z in the presence of an iron yoke of finite size
F_x	x-component of the magnetic force applied on a sector coil
F_y	y-component of the magnetic force applied on a sector coil
G	Magnetic induction gradient
g	Integer
g	Current grading factor
$\vec{H}$	Magnetic field vector
h	Integer, function depending on t
h	Function depending on t
I_{ss}	Short sample current
I_{op}	Operational current
$\vec{j}$	Current density vector
j_z	z-component of $\vec{j}$
j	Current density
j_n	Fourier coefficient of order n of j
j_0	Current density
j_c	Critical current density in superconducting material
j_{cref}	Reference value for the critical current density of Nb-Ti material
j_{sc}	Current density in the superconductor
j_{ss}	Short sample current density
$k_{np}^{S/N}(z)$	Function giving the longitudinal dependence of the magnetic field
$k_n^{S/N}$	z-integrated value of $k_{n0}^{S/N}(z)$
k	Layer number
k	Rutherford cable filling factor
k	Parameter equal to 1 or -1
L_m	Magnetic length
L	Luminosity, magnet length
L	Number of magnet in a series
$\vec{M}$	Magnetization vector
N	Half number of pole, number of magnet in a series
m	Current margin
m	Assumed mean value of the field harmonic error
m	Coil and half-coil numbering
n	Harmonic order
n	Number of angular sub-division
n_b	Number of bunch of particle per beam
N_b	Number of particle per bunch
N_b	Number of possible angles combination
$\vec{n}$	Unitary normal vector to a surface
O	Origin of the reference frame
P	Running parameter
q	Elementary charge, number of layer in a quadrupole coil
Q_x	Number of betatron oscillation in the horizontal plane

Q_y	Number of betatron oscillation in the vertical plane

R	Radius of a circular accelerator
r	Radius in the cylindrical coordinate system
R_{ref}	Reference radius
r_p	Radial coordinate of the point P
r_1	Coil inner radius
r_2	Coil outer radius
R_1	Coil inner radius
R'_1	Inner radius of a virtual coil
R_2	Coil outer radius
R'_2	Outer radius of a virtual coil
R_{ir}	Iron yoke inner radius
$R_{1,p}$	Inner radius of the coil block number p
$R_{2,p}$	Outer radius of the coil block number p
R_{in}	Inner radius of the coil
s	Curvilinear coordinate
S_{strand}	Cross-sectional area of a strand
S_{cable}	Cross-sectional area of a cable
S	Coil cross-sectional area
S_1	Surface
S_2	Surface
S_k	Surface number k
t_i	Temps
T_c	Critical temperature
T_{c0}	Critical temperature at zero magnetic field
T_{c0m}	Critical temperature at zero magnetic field and at zero strain
T_m	Temperature margin
T_{op}	Operational temperature
t	Coil width to coil inner radius ratio
t	Student's parameter
U_t	Magnetic energy
U	Magnetic energy per meter
U_n	Magnetic energy due to the current harmonic of rank n
U_2	Magnetic energy due to the current harmonic of rank 2
U_{ng}	Magnetic energy in non-graded coil
U_g	Magnetic energy in graded coil
U_c	Magnetic energy due to the coil alone
U_i	Supplementary magnetic energy due to the iron yoke
U_{tot}	Sum of U_c and U_i
V_m	Magnetic scalar potential
V_m^L	Integrated magnetic potential scalar
$\vec{v}$	Particle velocity
v_x	x-component of $\vec{v}$
v_y	y-component of $\vec{v}$
v_z	z-component of $\vec{v}$
$\overline{W}^L$	Potential complex
w	Coil width
w_{eq}	Equivalent coil width

W_m	Total stored energy in a quadrupole magnet
w_L	Layer width
x	Position along the x-axis, factor for the current grading
x_0	Real component of $\bar{z}_0$
y_0	Imaginary component of $\bar{z}_0$
z_i	Positions along the z-axis of a reference frame
$\bar{z}$	Complex position
$\bar{z}_0$	Position of a current line
$\bar{z}'_0$	Position of a virtual current line

GEEK LETTERS

α_n	Coefficient of order n
β	Dimensionless parameter, Beta function, Ratio B_p/j
β^*	Beta function at a collision point
β_x	Beta function in the horizontal plane
β_1	Constant
β_2	Constant
β_3	Constant
γ	Relativistic factor, Ratio G/j
γ_0	Constant
δ	Mean value of the field error in a magnet series
δ	Amplitude of the displacement of a coil/half-coil
δa_n	Uncertainty in the mean of a_n
δb_n	Uncertainty in the mean of b_n
ΔT_m	Variation of the temperature margin
Δr	Radial coil block displacement
$\Delta \varphi$	Azimuthal coil block displacement
$\Delta \alpha$	tilt of a coil block around its center of gravity
ΔA_n	Skew multipole variation
$\Delta A_{m,n}$	Variation of $A_{m,n}$
ΔB_n	Normal multipole variation
$\Delta B_{m,n}$	Variation of $B_{m,n}$
Δb_n	Normalized value of ΔB_n
$\Delta b_n^{(k)}$	Δb_n due to an angular variation in the layer number k
$\Delta\theta$	Angular variation
$\Delta\bar{C}_{m,n}$	Variation of $\bar{C}_{m,n}$
$\Delta A_n^{(c)}$	Variation of $A_n^{(c)}$
$\Delta B_n^{(c)}$	Variation of $B_n^{(c)}$
$\Delta A_n^{(d)}$	Variation of $A_n^{(d)}$
$\Delta B_n^{(d)}$	Variation of $B_n^{(d)}$
$\Delta\vec{P}$	Momentum variation
ΔP_x	x-component of $\Delta\vec{P}$
ΔP_y	y-component of $\Delta\vec{P}$
ε	Strain
ε_n	Normalized transverse beam emittance

ε_i	Dimensionless random variable (i=1, 2 and 3)
θ	Angular position
θ_p	Angular position of the point P
$\theta_{1,p}$	Lower angle of the coil block number p
$\theta_{2,p}$	Top angle of the coil block number p
θ_{min}	Minimal angle
θ_{max}	Maximal top angle in a quadrupole coil
μ_0	Magnetic permeability of free-space
$\bar{\bar{\mu}}$	Magnetic permeability tensor
μ_r	Magnetic relative permeability
$\upsilon_{cu\text{-}sc}$	Copper to superconductor ratio
ρ	Correlation coefficient
σa_n	Dispersion of a_n
$\sigma A_{m,n}$	Dispersion of $A_{m,n}$
$\sigma a_{m,n}$	Normalized dispersion of $A_{m,n}$
σb_n	Dispersion of b_n
$\sigma B_{m,n}$	Dispersion of $B_{m,n}$
$\sigma b_{m,n}$	Normalized dispersion of $B_{m,n}$
$\sigma A_n^{(c)}$	Dispersion of $A_n^{(c)}$
$\sigma B_n^{(c)}$	Dispersion of $B_n^{(c)}$
$\sigma A_n^{(d)}$	Dispersion of $A_n^{(d)}$
$\sigma B_n^{(d)}$	Dispersion of $B_n^{(d)}$
σ	Dispersion of the magnetic field error
φ_x	Phase advance in the horizontal plane
φ_x^0	Constant
χ	Magnetic susceptibility
Ω	Winding domain
Ω_∞	Whole space

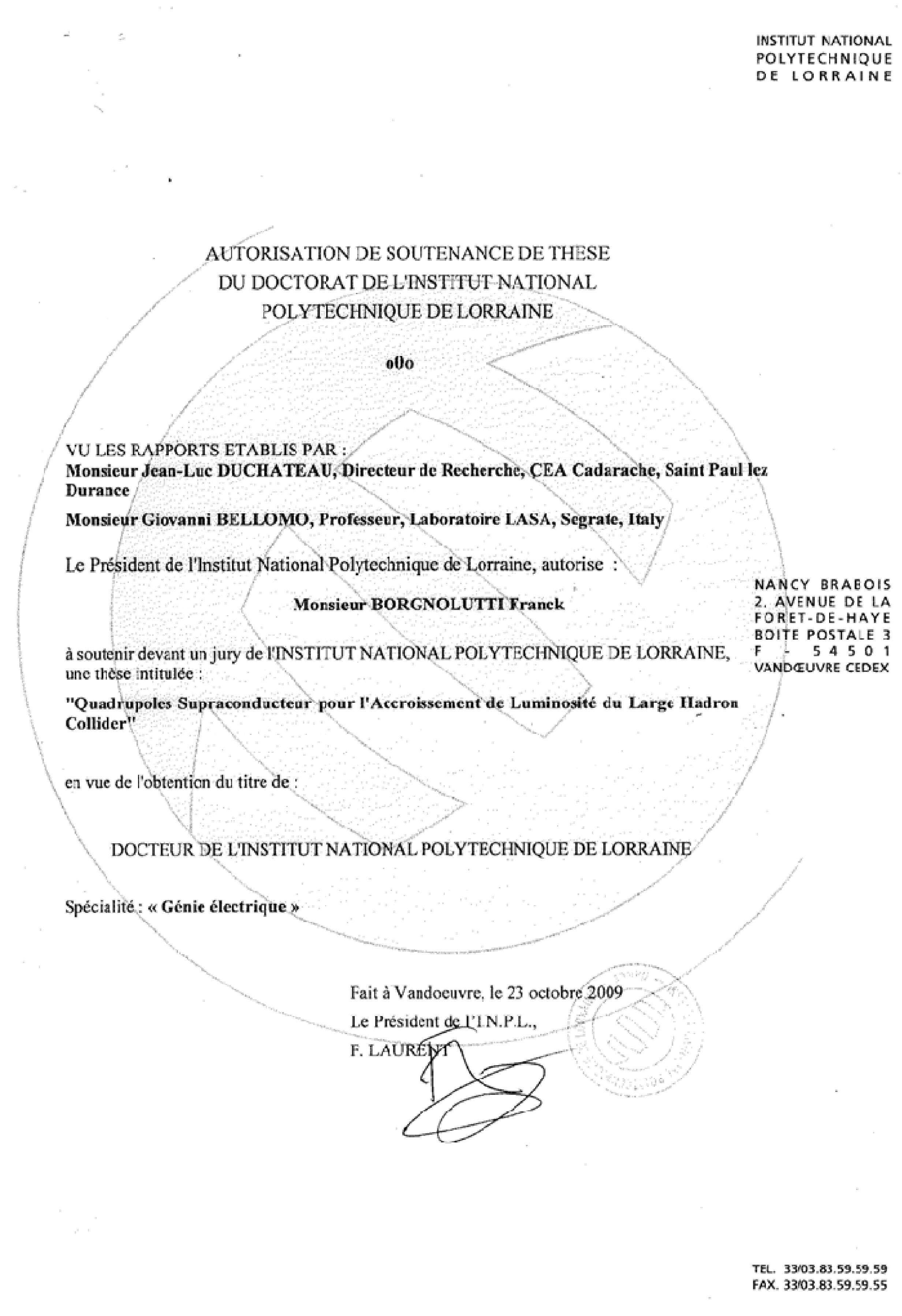

INSTITUT NATIONAL
POLYTECHNIQUE
DE LORRAINE

AUTORISATION DE SOUTENANCE DE THESE
DU DOCTORAT DE L'INSTITUT NATIONAL
POLYTECHNIQUE DE LORRAINE

o0o

VU LES RAPPORTS ETABLIS PAR :
Monsieur Jean-Luc DUCHATEAU, Directeur de Recherche, CEA Cadarache, Saint Paul lez Durance

Monsieur Giovanni BELLOMO, Professeur, Laboratoire LASA, Segrate, Italy

Le Président de l'Institut National Polytechnique de Lorraine, autorise :

Monsieur BORGNOLUTTI Franck

à soutenir devant un jury de l'INSTITUT NATIONAL POLYTECHNIQUE DE LORRAINE, une thèse intitulée :

"Quadrupoles Supraconducteur pour l'Accroissement de Luminosité du Large Hadron Collider"

en vue de l'obtention du titre de :

DOCTEUR DE L'INSTITUT NATIONAL POLYTECHNIQUE DE LORRAINE

Spécialité : **« Génie électrique »**

NANCY BRABOIS
2, AVENUE DE LA
FORET-DE-HAYE
BOITE POSTALE 3
F - 5 4 5 0 1
VANDŒUVRE CEDEX

Fait à Vandoeuvre, le 23 octobre 2009
Le Président de l'I.N.P.L.,
F. LAURENT

TEL. 33/03.83.59.59.59
FAX. 33/03.83.59.59.55

Résumé

Le travail effectué dans cette thèse a pour thème central la conception d'un aimant quadripolaire supraconducteur en Nb-Ti destiné à remplacer à l'horizon 2014 les aimants d'insertions actuellement utilisés dans le grand collisionneur de Hadrons (LHC) du CERN de Genève. Ce nouveau quadripôle, caractérisé par un diamètre d'ouverture encore jamais atteint (120 mm), ouvre la voie vers les quadripôles à grandes ouvertures. Tout d'abord, pour rapidement estimer l'énergie magnétique stockée dans un quadripôle de type cos2θ, une formule analytique basée sur la décomposition en série de Fourier du courant et permettant d'estimer l'énergie avec une précision de 10 % est développée. Le design magnétique de la section transverse de la bobine du quadripôle est ensuite réalisé en utilisant une nouvelle méthode d'optimisation basée sur les équations analytiques du champ magnétique. Puis, pour la première fois, une estimation de la reproductibilité dans le positionnement des blocs de conducteurs dans des aimants Nb$_3$Sn est faite. Elle a été réalisée à l'aide d'une méthode existante et grâce à la production récente de deux séries d'aimants Nb$_3$Sn. Une comparaison avec les valeurs obtenues pour des aimants en Nb-Ti est présentée. Ensuite, une méthode analytique basée sur les statistiques et permettant d'expliquer certains phénomènes observés sur la dispersion des mesures magnétiques dans une série de quadripôles est développée. Enfin, on montre que l'incertitude sur la moyenne des harmoniques de champ est due pour la majorité des harmoniques à un phénomène statistique lié au nombre limité d'aimants dans la série et non à des erreurs systématiques.

Mots clefs

Aimants d'accélérateurs, aimants quadripolaires supraconducteurs, énergie magnétique, optimisation de bobinages, qualité du champ magnétique, aimant Nb$_3$Sn.

Summary

The main objective of the work presented in this thesis is the design of a quadrupole magnet based on Nb-Ti. It aims at replacing the current insertion quadrupoles used in the Large Hadron Collider (LHC) at CERN by 2014. This new quadrupole features an unprecedented large aperture (120 mm) and opens the way toward large aperture quadrupoles. First, to rapidly estimate the magnetic energy stored in a cos2θ-type quadrupole, an analytical formula based on the Fourier transform of the current is developed. It allows estimating the energy with a precision of 10 %. Secondly, the magnetic design of the quadrupole coil cross-section is realized using a novel optimization method based on analytical equations of the magnetic field. Subsequently, for the first time, an estimate of the reproducibility in the coil-blocks positioning in Nb$_3$Sn magnets is given. The estimate has been obtained by using an existing method and from tow recently built Nb$_3$Sn magnet series. A comparison with values obtained for Nb-Ti magnets is also presented. Following this, an analytical method based on statistics is developed. It makes possible to explain some phenomenon observed on the dispersion of the magnetic measurement in a quadrupole series. Finally, we show that the uncertainty in the mean of the magnetic field errors is for most of the harmonics related to statistical errors due to the limited number of magnets in the series, and not because of systematic defects in the coil.

Key-words

Accelerator magnets, superconducting quadrupole magnets, magnetic energy, coil optimization, magnetic field quality, Nb$_3$Sn magnets.